Structure – Functional Analyses of Bacterial Cell Agglutinating Antimicrobial Peptides

Sheetal Sinha

Interdisciplinary Graduate School
Nanyang Environment & Water Research Institute

2018

Structure – Functional Analyses of Bacterial Cell Agglutinating Antimicrobial Peptides

Sheetal Sinha

Interdisciplinary Graduate School
Nanyang Environment & Water Research Institute

A thesis submitted to the Nanyang Technological University in partial fulfillment
of the requirement for the degree of
Doctor of Philosophy

2018

Statement of Originality

I hereby certify that the data and findings in this thesis is the result of original research and has not been submitted for a higher degree to any other University or Institution.

. . . .
Date

. . . .
Sheetal Sinha

Acknowledgement

I would like to express my sincere gratitude to my supervisor, Assoc. Prof. Surajit Bhattacharyya for continuously guiding me throughout my research. His motivation and guidance has helped me grow as a researcher. I would also like to thank my co-supervisor Prof. Ng Wun Jern for always believing in me and giving me the freedom to explore my field of interest. I am also highly thankful to my mentor, Prof Liu Yu for being there when I needed him.

I am grateful for my funding sources that made my research possible. I was offered a research scholarship by Interdisciplinary Graduate School (IGS) and Nanyang Environment & Water Research Institute (NEWRI).

I would like to sincerely thank Dr. Harini Mohanram for helping me throughout my research and for being patient in answering all my queries. I am grateful to Areetha D'souza for her invaluable inputs and help. I would also like to thank my labmates Dr. Deepak Chatterjee and Lewis Lu for their research inputs whenever I needed them.

I find myself extremely lucky to be a part of IGS, NTU. My PhD journey in IGS has been a delightful experience with a good balance of student life and research. I am extremely thankful to my research centre NEWRI (AEBC), for giving me this wonderful opportunity and for extending any academic or administrative help whenever I needed. I was a part of IGS student club throughout my PhD. I am sincerely thankful to IGS and the club to help me achieve a lot of interpersonal skills and self-confidence.

I am highly indebted to all my friends with whom I had a memorable time over past few years.

- Saurabh, Raja and Nikitha, thank you for being like a family to me in Singapore and for constantly encouraging me and helping me through all the bad times.
- Abhishek, Sumedh, Nishanth, Kaushik, Supriya and Vikram, thank you for all the festivities that we celebrated together and for being a continuous source of happiness.
- Abhijit and Ashish, thank you for innumerable fun weekends and for awesome home-cooked food and dessert.

- Antareep and Manisha, thank you for making the last year of my PhD so interesting and memorable.
- Arun and Varsha, thank you for constantly supporting me and for always being there in the time of need.

To my brother Anmol, thank you for always staying by my side, for putting up with my craziness and for the most fun Skype sessions. Most importantly, I would like to thank my parents for their unlimited love and support and for always emphasizing the importance of good education. Thank you for all your patience and countless prayers.

Table of Contents

Abstract

Innate antimicrobial peptides have served as the first line of defense against pathogens throughout human history. Host defense cationic AMPs are broad spectrum antimicrobials that can kill bacteria, viruses and fungi. On the basis of their modes of action, AMPs can be broadly classified into three categories – membrane permeabilizing AMPs, AMPs having intracellular targets and cell agglutinating AMPs. Bacterial cell death by membrane permeabilization has been well perceived. In the recent years, increasing number of studies are conducted on AMPs targeting intracellular components. However, very few AMPs are known to agglutinate bacterial cells. Moreover, the mechanism is of agglutination is poorly understood. Multiple binding sites in AMPs for outer membrane lipopolysaccharides or cell wall peptidoglycans are pivotal for agglutination. However, a complete understanding of the mechanism is required to develop novel antimicrobials with agglutination as a mode of action.

In this thesis, the first atomic resolution structure of thanatin, a cell agglutinating peptide in complex with LPS has been reported. Thanatin assumes a four stranded antiparallel β-sheet conformation in a 'head-tail' dimeric topology. In contrast, thanatin in free solution assumes an antiparallel β-hairpin conformation. Dimerization of thanatin provides multiple LPS binding sites needed to facilitate agglutination. Furthermore, dimeric thanatin displays higher cationicity and hydrophobicity. Various gain-in function and loss-in function mutation were synthesized to determine the structure-activity correlation. Biophysical analyses of thanatin and mutant peptides were conducted to determine LPS/peptide binding constant. Perturbation of LPS micelles in the presence of these peptides was also analysed using biophysical and NMR experiments. Finally, MD simulations were conducted on thanatin dimer/LPS complex to understand the mode of LPS recognition and agglutination. Structural changes in thanatin in presence of zwitterionic DPC micelles were also analysed. Unlike in complex with LPS, thanatin adopts a monomeric topology in presence of DPC micelles. Paramagnetic relaxation enhancement experiments were carried out to examine the interaction of thanatin with DPC micelles. The mechanistic insights on bacterial cell agglutination can be utilized to develop antimicrobials with alternative mode of action.

Furin is a serine endoprotease which is ubiquitously found in mammals. Its prodomain is known to possess anti-cancerous properties. In this report, the antimicrobial property of a furin prodomain derived peptide has been reported and elucidated for the first time. Various truncations from furin prodomain were screened for their antimicrobial activity. YR26, derived from the central region of the prodomain displays a broad spectrum of activity against both Gram-positive and Gram-negative bacteria. To determine the structure-activity correlation, various truncations were made from the C-terminus of the peptide. YR26 completely loses its activity on truncating more than six residues from C-terminus. Furthermore, the active peptides were found to be non-hemolytic and non-toxic to mammalian cells *in vitro*. To gain insights on the mode of action, membrane permeabilization assays and other biophysical experiments were conducted. The active AMPs were found to completely permeabilize outer membrane but were not potent in permeabilizing the inner membrane of *E. coli* cells. Moreover, the experiments indicated a higher order of association of *E. coli* cells/LPS micelles in the presence of these peptides. Interaction studies of POPC-POPG and POPC liposomes with the active prodomain derived peptides strongly indicate agglutination as a mode of action. In order to gain further insights on the mechanism of agglutination, 3D structure of YR26 in presence of SDS micelles was determined using solution state NMR spectroscopy. YR26 adopts an anti-parallel α-helical conformation with two distinct helices attached with an extended loop. The two anti-parallel α-helical region provides multiple LPS binding site to facilitate cell agglutination. YR26 can be further used a template for the discovery of novel antimicrobial drug.

List of Figures

List of Tables

Abbreviations

ATCC - American Type Culture Collection
AMP - Antimicrobial Peptides
MDR - Multi Drug Resistance
FDA - Food and Development Authority
LB - Luria-Bertanii broth
MHB - Mueller-Hinton broth
MIC - Minimum Inhibitory Concentration
RBC - Red Blood Cells
LPS - LipoPolySaccharides
EDTA - EthyleneDiamineTetraAcetic acid
DPC - DodecylPhosphoCholine
SDS - Sodium Dodecyl Sulfate
FITC-LPS - Fluorescein IsoThioCyanate LPS
NPN - 1-N-Phenyl Naphtylamine
POPC - 1-palmitoyl-2-oleoyl-sn-glycero-3-phosphocholine
POPG - 1-palmitoyl-2-oleolyl-sn-glycero-3-phosphoglycerol
HPLC - High Performance Liquid Chromatography
TFA - TriFluoroAceticacid
ITC - Isothermal Titration Calorimetry
DLS - Dynamic Light Scattering
NMR - Nuclear Magnetic Resonance spectroscopy
STD - Saturation Transfer Difference
NOESY - Nuclear Overhauser SpectroscopY
TOCSY - TOtal Correlation SpectroscopY
tr-NOESY - Transferred NOESY
^{1}H - Proton
NOE - Nuclear Overhauser Effect
DSS - 2,2-Dimethyl-2-Silapentane 5-Sulfonate sodium salt
E. coli - *Escherichia coli*
K_d - Dissociation constant
HBD - Human Beta Defensins
PBS - Phosphate Buffered Saline

List of Publications

- Sinha, S., Zheng, L., Mu, Y., Ng, W.J., Bhattacharjya, S. *Structure and Interactions of Host Defense Antimicrobial Peptide Thanatin in Lipopolysaccharide Micelles Reveal Mechanism of Bacterial Cell Agglutination*. Nat. Sci. Rep. DOI : 10.1038/s41598-017-18102-6

- Chin, J.S.F., Sinha, S., Nalaparaju, A., Yam, J.K.H., Qin, Z., Ma, L., Liang, Z.-X., Lu, L., Bhattacharjya, S., Yang, L. *Pseudomonas aeruginosa Psl exopolysaccharide interacts with the antimicrobial peptide LG21*. Water. DOI: 10.3390/w9090681

- Lu, S., Du, Q., Sinha, S., Subrata, A., Bhattacharjya, S., Xing, B., Yeow, E.K.L. *Lipopolysaccharide-affinity copolymer exploits the rapid motility of swarmer bacteria to trigger antimicrobial drug release.* Nature Comm. [under review]

- Lau, Q.Y.[1], Li, J. [1], Sani, M.-A. [1], Sinha, S. [1], Li, Y. [1], Ng, F.M., Kang, C., Bhattacharjya, S., Separovic, F., Verma, C., Chia, C.S.B. *Elucidating the bactericidal mechanism of action of the linear antimicrobial tetrapeptide: BRBR-NH2*. BBA Biomembranes. DOI: 10.1016/j.bbamem.2018.05.004

- Sinha, S., Harioudh, M.K., Dewangan, R.P., Ng, W.J., Ghosh, J.K., Bhattacharjya, S. *Cell Selective Pore Forming Antimicrobial Peptides of the Prodomain of Human Furin: A Conserved Aromatic/Cationic Sequence Mapping, Membrane Disruption and Atomic-resolution Structure and Dynamics.* Journal of Med. Chem. [under review]

Chapter 1

Overview

Discovery of new antimicrobials is crucial to combat emerging multi-drug resistant bacteria. In this chapter, the motivation behind the study is discussed. Specific objectives and key contributions made by this study to the area are highlighted. Finally, an overview of all the chapters in this thesis is delineated.

1.1 Motivation

An excessive use of antibiotics and disinfectants in our daily lives has led to an exponential rise of drug resistant and multi drug resistant pathogens in the past few decades[2-4]. Evolution due to positive selection has armed bacteria with resistant genes against these antibiotics[4, 5]. The resistant genes even in commensal bacteria are harmful because these bacterial species can disseminate their resistant genes to virulent strains by means of horizontal gene transfer[6]. The situation is further aggravated by the decline in discovery of new antibiotics. Hundred- thousands of people die annually due to the emergence of antimicrobial resistance and lack of new antibiotics[7]. Therefore, it is imperative to study new antimicrobials with alternate modes of action. Antimicrobial peptides (AMPs) serve as the forefront of defense against pathogens in nature[8-10]. They are an integral component of the host defense system and are evolutionarily evolved as a part of the innate immunity since millions of years[11-13]. Hence, understanding the mechanisms of antimicrobial action of these peptides can aid in discovery of new drugs against infectious diseases. Broadly, on the basis of their antimicrobial action, these peptides can be classified in three categories namely, pore-forming AMPs, AMPs targeting intracellular components and bacterial cell agglutinating AMPs. There are a lot of studies on the first two classes of AMPs[14, 15]. However, specific mechanisms of bacterial cell agglutination by the third class of AMPs are not well evaluated. A major drawback of the membrane permeabilizing AMPs is their toxicity towards host cells and low selectivity[16, 17]. Hence, a cognizance of the structural-function correlation of the AMPs is crucial to modify their hydrophobicity and cationicity and improve their selectivity. Furthermore, a knowledge of non-membranolytic mode of action is important to develop new antimicrobial drugs with diverse killing mechanisms. Very few antimicrobial peptides and proteins are known to agglutinate bacterial cells as their primary mode of action. Understanding the structural requirements and specific mechanism of action for agglutination can either help in modification of existing AMPs to improve their selectivity or in designing new antimicrobials.

1.2 Objectives

Overall objective of this thesis is to study the non-membrane permeabilizing antimicrobial peptides. Specific objectives are:

- To study the mechanism of bacterial cell agglutination by AMPs by employing NMR as a means to characterize their structure in free state, presence of lipopolysaccharide (LPS) and zwitterionic DPC micelles.
- To identify critical residues involved in interaction with LPS and to design new mutations which either facilitate in the understanding of the mode of action or improve the activity and cell selectivity of these AMPs.
- To study their activity against a wide range of bacterial strains and to test their toxicity to mammalian cells.
- To use various biophysical techniques such as fluorescence spectroscopy and isothermal calorimetry to further understand the mode of antimicrobial action.
- To design new AMPs that have high antimicrobial activity and less toxicity to mammalian cells.

1.3 Findings & Contributions

In this thesis, I have worked with two different systems of bacterial cell agglutinating antimicrobial peptides. I have strived to understand various mechanisms by which these peptides agglutinate the bacterial cells and critical residues involved in cell agglutination. Specific contributions are:

- Determined the structure of thanatin in presence of LPS. Interestingly, thanatin dimerizes in presence of LPS and provides multiple binding sites to facilitate agglutination.
- Designed various loss-in function mutants in order to discover the critical residues necessary to bind LPS.
- Improved the activity of thanatin by mutating one of the residues in β-sheet and increasing the overall stability of the β-hairpin.
- Understood and elucidated the mechanism of agglutination by thanatin and prepared a mechanistic model to illustrate the mechanism.
- Determined the activity and cytotoxicity of various truncations in furin pro-domain.
- Discovered the antimicrobial and non-cytotoxic region in furin pro-domain.

- Elucidated the structure and multiple binding sites of YR26 (derived from furin pro-domain) in presence of an anionic micelle, SDS.
- Determined the mode of action of YR26 by means of various biophysical characterizations and discovered that the peptide works by agglutination.

1.4 Thesis Overview

The aim of this thesis is to study various cell agglutinating antimicrobial peptides and to delineate the underlying mechanism that facilitates agglutination. In this chapter the motivation behind the project, specific objectives of this thesis and significant contributions made in the area are discussed.

In the second chapter, the overall history of antimicrobials starting with the discovery of penicillin is elucidated. The mode of action of antibiotics and the resistance development in bacteria are explained. The exponential rise in the multi-drug resistant bacteria is a strong motivation behind the discovery of new antimicrobials. Moreover, different types of AMPs based on their structure are illustrated. Furthermore, various modes of action of antimicrobial peptides are discussed in the chapter which paves a pathway for understanding agglutination as a mode of action of antimicrobial peptides and proteins.

In the third chapter, all descriptive list materials used is mentioned. Furthermore, a detailed account of all the experimental methods done in this thesis is elucidated.

In the fourth chapter, few cell-agglutinating antimicrobial peptides are illustrated and an overview of the work already done on thanatin is discussed. Dissociation constant and ED_{50} is calculated to study the binding of thanatin with LPS. Thermodynamic parameters for binding are determined and the structural changes imparted by thanatin on LPS micelles is elucidated. Finally, the differences in the structures of thanatin in presence of zwitterionic DPC micelles and anionic LPS are revealed and an energy minimized model of thanatin dimer binding with multiple LPS units is illustrated.

In the fifth chapter, various gain-in function and loss-in function mutants of thanatin are designed by identifying the critical residues involved in interaction with LPS. The structures of these mutants were determined in free solution and in presence of LPS. The antimicrobial activity for the mutant peptides was assessed. In order to gain deeper insights on the mechanism of agglutination, various biophysical experiments were done to compute the dissociation constant, binding affinity for these peptides with LPS and the underlying thermodynamic parameters. Furthermore, structural changes made by these mutant peptides in LPS micelles were assessed using fluorescence and ^{31}P NMR spectroscopy. Finally, modelling of thanatin dimer/LPS complex was done using MD simulation and an illustrative model explaining he mechanism of agglutination was prepared.

In the sixth chapter, an overview of furin pro-domain is discussed and an account of other protein pro-domains having antimicrobial activity is illustrated. Various truncated forms of furin pro-domain are designed and a region which is most active against bacteria and least cytotoxic is elucidated. In order to understand the mode of antimicrobial action, the active truncated derivative peptides from furin pro-domain were analysed using fluorescence spectroscopy. The chapter elucidates the inefficiency of these truncated peptides to permeabilize the inner membrane of bacterial cells and their efficacy in agglutinating the LUVs (mimicking bacterial cells) in larger clumps. Finally, the structure of YR26, an active derivative from furin pro-domain was determined in presence of anionic SDS micelles. Interestingly, multiple LPS binding sites were also observed in YR26 to facilitate agglutination.

In the seventh chapter, a summary and conclusion of the work is provided. Moreover, possible future applications of the active peptides are also listed.

Chapter 2

Literature Review

In this chapter, a brief history of the discovery of antimicrobials is discussed and the crucial need for development of new antimicrobial drugs is emphasized. Furthermore, various modes of action of different antibiotics and the mechanisms of resistance development in bacteria are discussed. Finally, structural diversity and different modes of antimicrobial action of AMPs are discussed. Pore formation and targeting intra-cellular components by antimicrobial peptides are well studied. However, not much work is done on the mechanism of bacterial cell agglutination. This chapter lays a foreground for the study of the mechanism of agglutination by AMPs.

Antimicrobial peptides are ubiquitously found in both prokaryotes and eukaryotes as a part of their host defense mechanisms. They are evolutionarily conserved components of the innate immune systems and can be traced back to a few hundred million years ago. One of the earliest studies on the phylogeny of AMPs investigated the evolutionary relationship between AMPs from hylids of South America and Australia and from ranids of Europe, Asia and North America[11]. The study concluded that the precursor proteins from various hylids and ranids belonged to a single family, the pre-prodermaseptins[11]. The historical reconstruction and phylogenetic analyses showed that the pre-prodermasptin genes originated from an ancestral gene, over 150 million years old[12, 13]. Defensins from invertebrates, fungi, plants and mammals were proposed to have emerged from a common ancestor atleast 2.6 billion years old[18, 19]. Big defensins which is present in invertebrates but not in vertebrates can be traced back to their common ancestor, Bilateria which is more than 500 million years old[20-22]. Over time, AMPs have evolved by means of positive selection leading to structural and functional diversity in both vertebrates and invertebrates[23, 24]. Such evolution has rendered the AMPs an ability to combat new or altered pathogens.

Although AMPs have served as the first line of defense against pathogens throughout human history, investigations into anti-microbials were commenced only in the early 20th century with the discovery of lysozyme. Alexander Fleming reported its activity in hen's egg white, saliva and nasal mucus[25]. He also discovered penicillin in 1928 and later on established its therapeutic use[26, 27]. With the discovery of penicillin, streptomycin and other antibiotics, research into the innate immune defense mechanisms died down. However, with the increase in resistant and multi-drug resistant bacteria in 1960s and 1970s, studies on cationic proteins from neutrophils that utilize oxygen-independent killing mechanism started gaining interest[28, 29]. However, the research was overshadowed by studies on oxidative microbial killing components of phagocytes until Hans Boman's group in 1981, isolated an inducible cationic antimicrobial peptides, cecropins from the moth *Hyalophora cecropia*, a non-human source[30]. In 1987, Zasloff, *et al* isolated magainins from the African clawed frog, *Xenopus laevis*[31]. In 1985, Lehrer's group isolated and identified human neutrophil derived defensins 1-3 (HNP 1-3) from human polymorphonuclear leukocytes[32]. These and other extensive studies on AMPs from plants[33], insects[34] and other vertebrates lacking an adaptive immune system[35] established that these peptides play a crucial role in immune systems of mammals, including humans who possess innate and adaptive immune system. Moreover, these studies indicated that their induction in response to an infection is a highly conserved innate immune response. Till date more than 2000 AMPs have been identified and the number of peptides being reported is increasing rapidly[36, 37].

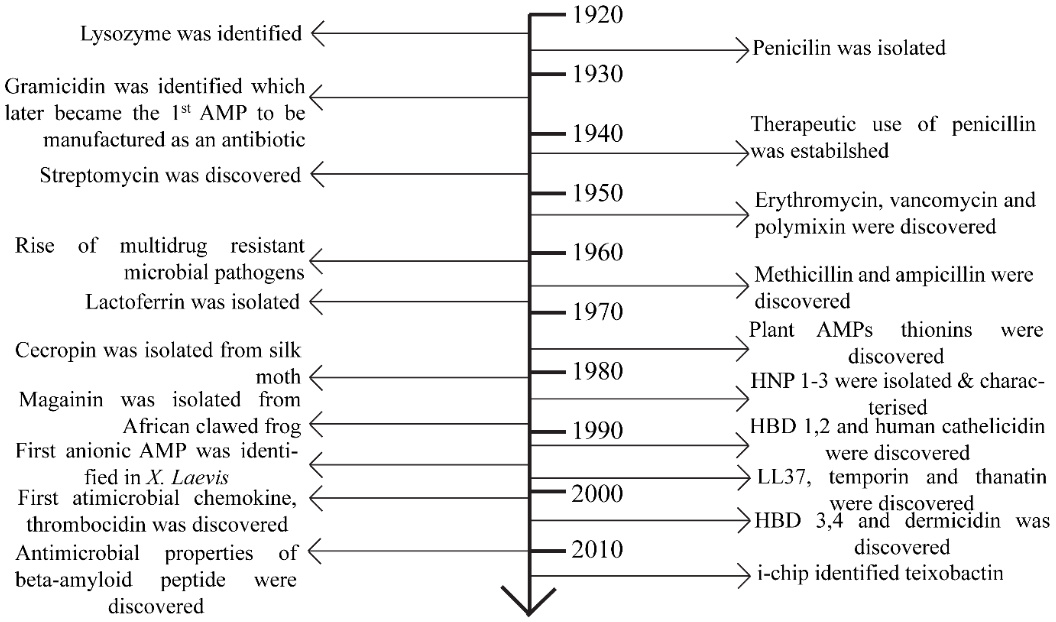

Figure 2.1| A brief history of the discovery of antimicrobials. The figure summarizes the advent of the global age of antibiotics with the discovery of penicillin and streptomycin, rise of multi-drug resistant bacteria leading to an increase in interest in AMPs and discovery of new AMPs both from human and non-human sources[1].

2.1 Antibiotics

The end of the golden age of antibiotics witnessed an exponential rise in drug resistant and multi drug resistant bacteria. Due to positive selection in evolution, the antimicrobials in nature and development of resistance against these antimicrobials in microorganisms co-exist and co-evolve. Hence, to be able to combat with these superbugs, we need to be cognizant of the mechanism by which they develop resistance and the mode of antibiotic action.

2.1.1 Mode of Action of Antibiotics

Bactericidal action of the antibiotics is a complex process which starts with their interaction with various intra-cellular targets. Antibiotics may interact with nucleic acids or essential enzymes to inhibit RNA synthesis, DNA-replication and protein synthesis or to hinder cell wall and cell membrane synthesis[38].

The quinolone class of antibiotics interacts topoisomerase II and topoisomerase IV and entraps them at the site of DNA cleavage. Thus, a stable interaction complex between cleaved DNA and drug bound topoisomerases prevent DNA strand re-joining[39, 40]. As a result of the blocked replication forks, DNA machinery gets arrested leading to inhibition of DNA synthesis[41].

Rifamycin class of antibiotics binds to the β-subunit of a DNA-bound RNA polymerase and sterically inhibits RNA strand initialization[42, 43]. The β-subunit of the DNA-RNA polymerase complex is situated in a channel from where a newly synthesized RNA strand emerges[44]. Hence, Rifamycin is able to completely inhibit RNA synthesis provided the RNA synthesis has not progressed beyond the addition of two ribonucleotides[45].

β-Lactams interact with the active sites of transpeptidases and hamper them to catalyse the cross-linking of peptidoglycan units in the cell membrane[46, 47]. The mechanical strength offered by the peptidoglycan layer is vital to survive harsh environmental conditions and any changes in osmotic pressure. Inhibition of cell wall synthesis may result in induction of cell stress responses and premature cell lysis[48].

50S and 30S ribosome inhibitors prevent protein synthesis either by physically blocking initiation of protein translation[49] or translocation of peptidyl tRNAs[50] or by interfering with the stability of peptidyl tRNAs[51]. Most of the ribosome inhibitors are typically bacteriostatic. However, aminoglycosides is the only class of ribosome inhibitors that is broadly bactericidal[38]. It interacts with 30S subunit if ribosome and incorporates wrong amino acids into elongating peptide strands, thus promoting protein mistranslation. When incorporated into the cell envelope, mistranslated and misfolded membrane proteins lead to an increased drug uptake, resulting in cell death[52].

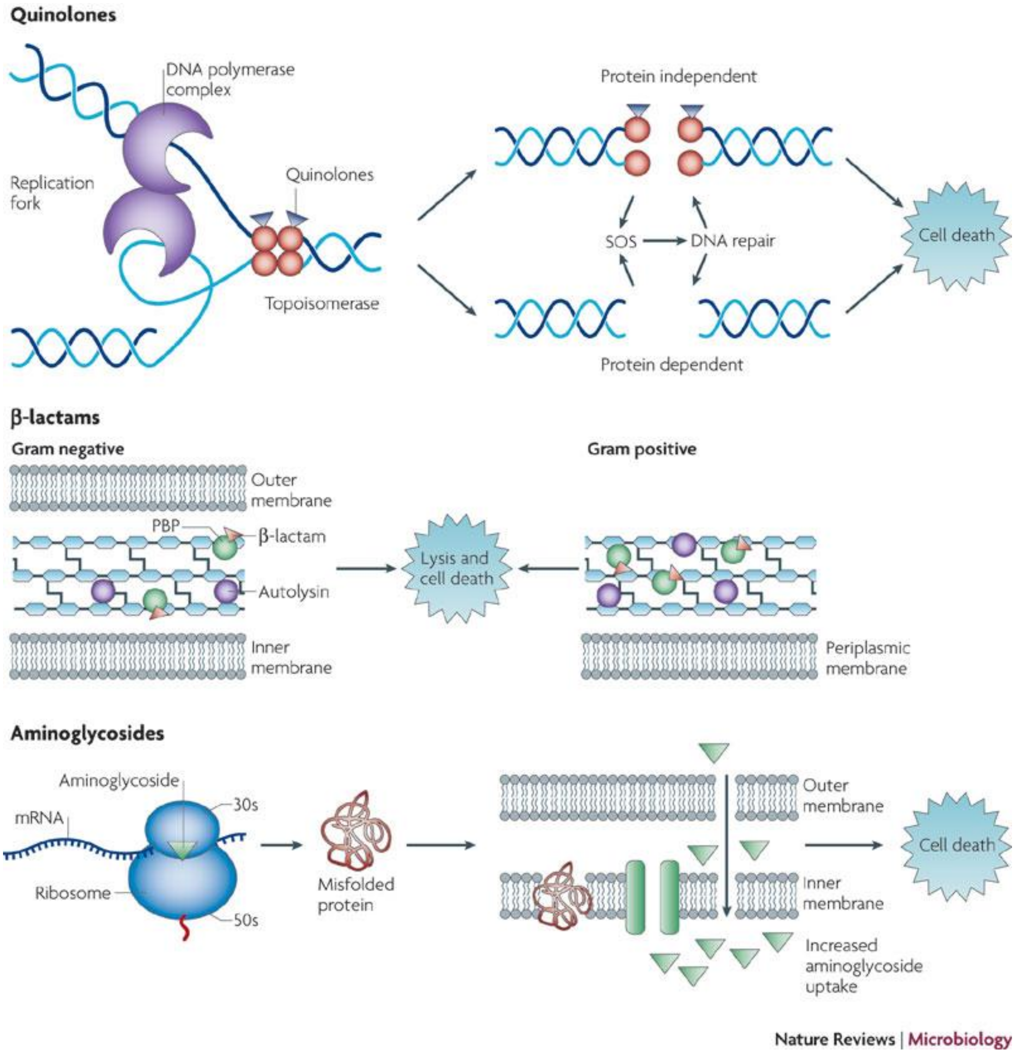

Figure 2.2| An illustration of different mode of action of various classes of antibiotics. Quinolones hinder the replication of DNA, β-lactams interact with PBPs and inhibit cross-linking of peptidoglycan units and aminoglycosides promote mistranslation of membrane proteins.

Figure taken from ref.[38]

2.1.2 Mechanisms of Antibiotic Resistance in Bacteria

Natural antibiotics were produced by certain bacterial strains for billions of years[53]. This gave them a selective benefit over other strains competing for resources[54]. Antibiotic resistant genes are also as archaic as natural antibiotics. Resistance in bacteria can occur either by mutation or by acquisition of these resistant genes via horizontal gene transfer. A number of pathways contribute to antibiotic resistance in bacteria by mutation.

Some resistant strains retain their sensitive target but enzymatically modify or inactivate the drug molecule. The four-membered ring of β lactam is cleaved enzymatically by β lacatamase rendering the drug inactive[55].

Preventing the drug molecules to enter the bacterial cell or forcing them out faster than they can enter is also a potent way to protect themselves against antibiotic action. A well-known mechanism of resistance to tetracyclines is attributed to an increased efflux using an energy-requiring transport pump[56].

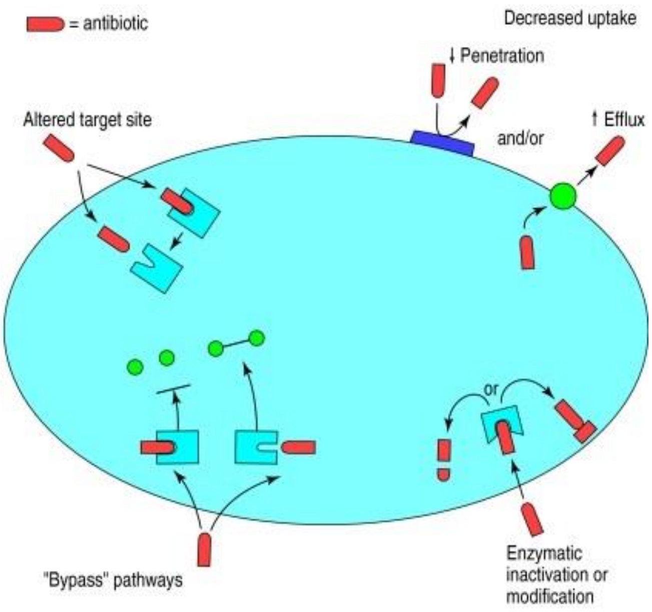

Figure 2.3| A Schematic of various biochemical mechanisms of antibiotic resistance. Antibiotic resistant strains either enzymatically inactivate or modify the drug molecules or alter the target site, decrease the drug uptake or completely bypass the pathway for antibiotic action.

Figure taken from ref.[55]

Enterococci produces PBPs to have inherently low affinity to the antibiotic cephalosporins, which renders them completely inactive to inhibit cell-wall synthesis. Thus, the antibiotic can penetrate the cell and reach the target but is unable to inhibit the activity because of alterations in the primary site of action[57]. Certain strains produce alternative targets resistant to an antibiotic to bypass its effect altogether. MRSA produces an alternative penicillin binding protein PBP2a, which is not inhibited by drugs such as flucoxacillin and thus they do not affect the structural integrity of the cell membrane[58].

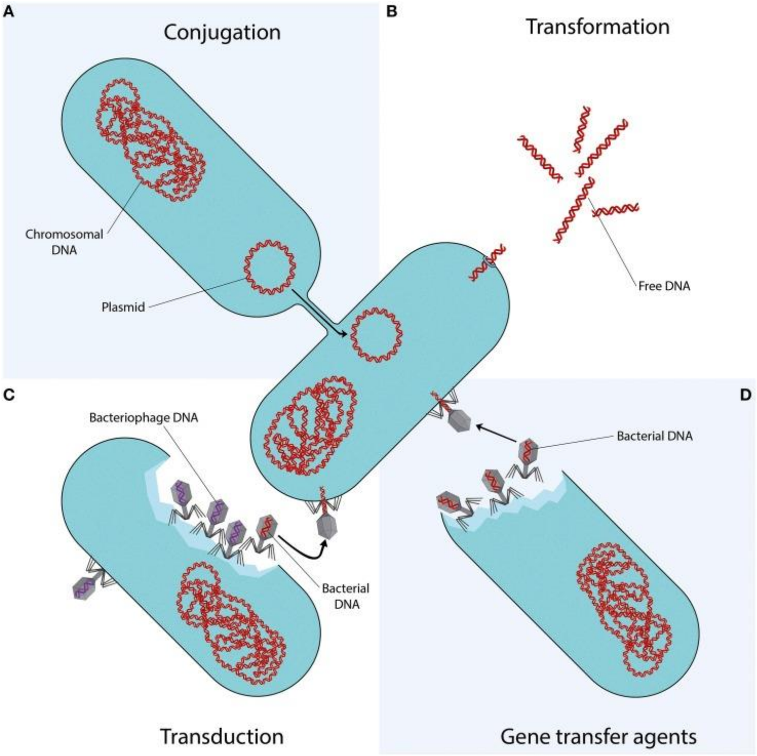

Figure 2.4| Resistant species disseminate their resistant genes to other strains via horizontal gene transfer by four classical mechanisms. Bacterial strains may uptake foreign DNA by surface contact with other cells, or by integrating naked fragment of extra-cellular DNA or via bacteriophages and gene transfer agents.

Figure taken from ref.[6]

The antibiotic resistance found in environmental and commensal bacterial species is also of relevance. These bacterial species disseminate their resistant genes to pathogenic strains via horizontal gene transfer (HGT)[6]. Resistance genes in many clinically relevant pathogenic bacterial strains have originated from nonpathogenic sources, underlining the significance of HGT in overcoming the antibiotic barrier. Horizontal gene transfer can occur by conjugation, transformation, transduction or via gene transfer agents[6].

In conjugation, cells contact via cell surface pili or adhesins to transfer DNA[59, 60]. Certain strains of bacteria uptake, integrate and functionally express naked fragments of extracellular DNA. This process of horizontal gene transfer is called transformation[61, 62]. Through transduction, bacteriophages can transfer genes that are advantageous to their microbial hosts. The transferable genes range from chromosomal DNA to plasmids and antibiotic resistant genes[63, 64]. Gene transfer agents are host cell produced particles capable of transferring genetic material.

Using antibiotics in personal care products in our day to day lives has expedited the development of resistance in bacterial strains. According to the review on antimicrobial resistance, 2014 there are around 700,000 deaths annually caused due to antimicrobial resistance. If major steps towards development of new antimicrobials are not taken, the death toll due to AMR will rise to 10 million by the year 2050. The resistant superbugs would kill more people than cancer. Hence, exploiting other methods to combat with these superbugs is imperative.

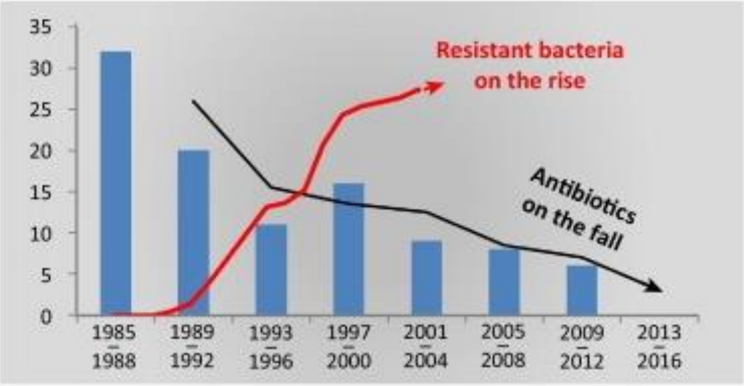

Figure 2.5| Increasing resistant bacterial strains vs declining development of new antibiotics. The figure illustrates the % of bacterial strains that have become resistant to the last resort drug, vancomycin (red) in US hospital ICUs and a diminishing trend in the launch of new antibiotics in the depicted period.

Figure taken from ref.[7]

2.2 Antimicrobial Peptides (AMPs)

AMPs have been the first line of defense against invading pathogens in hosts for millions of years[11]. Unlike antibiotics which have intracellular targets, most antimicrobial peptides work by interacting with components of bacterial cell membrane. These antimicrobial peptides are rich in cationic and hydrophobic residues and hence, can interact with the negatively charged bacterial cell membranes electrostatically and hydrophobically. Most AMPs are unstructured in aqueous solution, however to exert their activity, they fold into a structural motif in membranous environment[14]. On the basis of structural diversity, they can mainly be classified either as α-helical, β-sheet or extended AMPs[65].

2.2.1 Structural Diversity of Antimicrobial Peptides

- α-helical antimicrobial peptides

  Linear peptides that assume amphipathic α-helical structure is widespread in nature. They are generally broad-spectrum antibiotics and are active against both Gram-negative and Gram-positive bacteria. During the lipid-peptide interaction, amphipathicity of the AMPs is sorted out along the axis of the helical structure parallel to the membrane plane. These peptides also often have proline or glycine induced kink in the middle of the helix. The charged side of the peptide face towards the phospholipid head groups of the membrane, whereas the hydrophobic side of the α-helical AMP gets embedded into the hydrophobic acyl tail core[66, 67]. Magainin, isolated from the skin of the African clawed frog, is one of the most extensively studied AMPs. It is known to exert a detergent-like action, translocate to the inner leaflet and permeabilize the cell membrane[68]. LL37, derived from human cathelicidin family is another example of α-helical antimicrobial peptides that break the integrity of bacterial cell membranes[69]. Cathelicidin family of polypeptides are usually found in keratinocytes, polymorphonuclear leukocytes and lysozymes of macrophages. Unlike most α-helical AMPs, Buforin II isolated from the histones of the Asian toad *Bufobufo gargarizans* do not compromise the cell membrane integrity. Instead, it accumulates in the cytoplasm and adapt a polyproline II conformation to interact with nucleic acids[70, 71].

- β-sheet antimicrobial peptides

  In addition to defensins, that are found ubiquitously throughout plant and animal kingdoms, this class of AMPs also include several β-hairpin peptides such as thanatin, protegrin 1 and bovine lactoferrin. The hairpin structure is stabilized by one or more disulphide bridges between cysteine residues and multiple backbone hydrogen bonds laterally connecting two β-strands. Most of the pore forming β-sheet antimicrobial peptides like porcine protegrin 1, adapt an oligomeric transmembrane β-barrel conformation in presence of anionic membranes. They are known to disrupt the bacterial membrane by forming toroidal pores. However, in presence of zwitterionic mammalian cell membranes, these peptides form β-sheet aggregates on the surface of the membranes[72]. Although pore formation is the most established mode of action, some β-sheet antimicrobial peptides also employ non-lytic mechanisms against bacteria. Bovine lactoferrin localizes in the cytoplasm, following translocation and interact with nucleic acids and inhibit protein synthesis. It can also act synergistically with other antimicrobials to affect transmembrane potential and proton-motive force, ultimately inhibiting ATP dependent multi-drug efflux pumps[73]. Thanatin, an insect defense peptide derived *Podisus maculiventris* does not employ pore formation as its mode of action against bacteria. It is instead known to agglutinate the bacterial cells[74].

- Extended antimicrobial peptides

  Although these peptides do not fold into any regular secondary structure elements, they adapt a defined amphipathic conformation in presence of a membrane. Most of these peptides are not membrane active and contain high proportions of proline, arginine or tryptophan residues[14]. Proline rich insect-derived peptides like pyrrhocoricin, drosocin and apidaecin penetrate across the cell membrane and interact with the heat-shock protein DnaK to hinder the DnaK ATPase activity and with GroEL to inhibit chaperone-assisted protein folding[10]. Arg and Trp rich short hexapeptide WRWYCR inhibits DNA-repair and is known to have a broad spectrum bactericidal activity[75]. Indolicin is a 13-residue Arg and Trp rich AMP which is derived from bovine leukocytes. It has a complex mode of action, with a number of mechanisms contributing to its activity. It is known to target oxidized phospholipids, activate phospholipase A_2 to hydrolyze anionic membrane[10], act as a small anion carrier across membrane and segregate lipids to cause membrane leakage[76, 77]. Additionally, it also interacts with DNA, interferes with DNA-binding enzymes and induces filamentation in *E. coli*[78]. However, which of these modes of actions contributes most to its *in vivo* activity is still unclear.

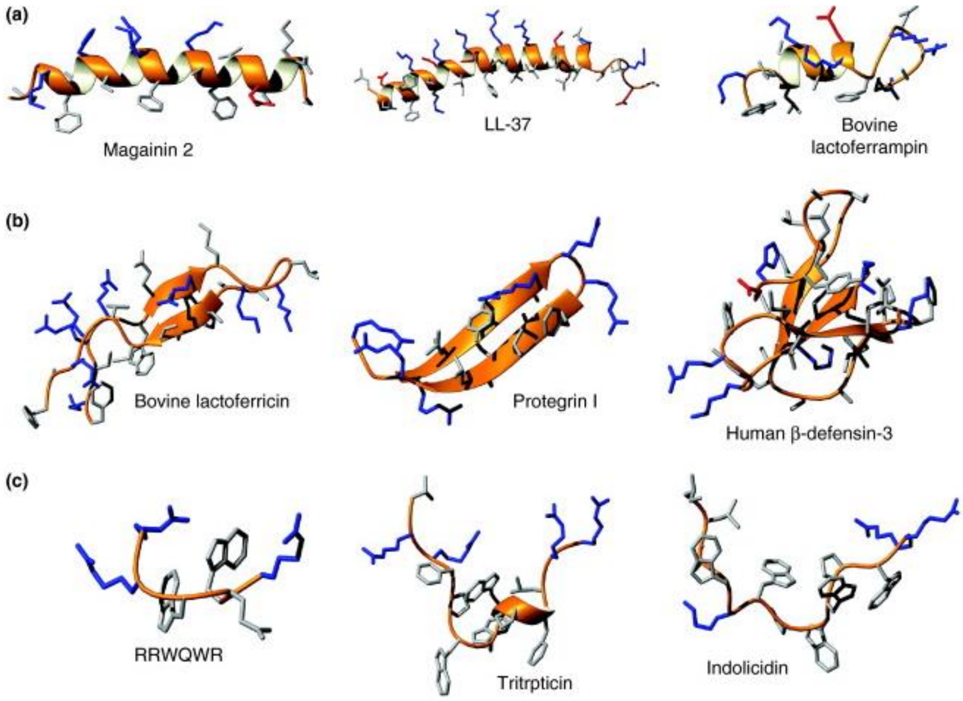

Figure 2.6| Structural diversity of antimicrobial peptides. a. α-helical AMPs: Magainin 2 (PDB ID: 2MAG), LL-37 (PDB ID: 2K6O) and Bovine lactoferrampin. **b.** β-sheet AMPs: Bovine lactoferricin (PDB ID: 1LFC), Protegrin 1 (PDB ID: 1PG1) and Human β-defensin 3 (PDB ID: 1KJ5). **c.** Extended AMPs: Hexapeptide RRWQWR, Tritrpticin (PDB ID: 1D6X) and Indolicidin (PDB ID: 1G89).

Figure taken from ref.[14]

Certain proline and arginine rich peptides are not able to adapt to an amphipathic conformation in presence of membranous environment because of the overexpression of proline residues. They instead adopt a polyproline helical type-II structure[79]. Gramicidin A dimerizes in a head-to-head conformation to form a β-helix loop inside the hydrophobic interior of lipid bilayer. Naturally occurring cyclic peptides like gramicidin S and θ-defensins also show broad spectrum activity against both Gram-positive and Gram-negative bacteria. Such structural diversity in AMPs improves the host's innate defense system against a variety of pathogens and helps in a better synergy.

2.2.2 Mode of Action of Antimicrobial Peptides

Within and beyond the aforementioned conformational classes, the antimicrobial peptides exhibit modes of action that are highly diverse and complex. An awareness of these mechanisms will provide us with an insight on how these molecules act to defend against infections. Moreover, it would facilitate us to develop new antimicrobials to enhance immune mechanisms and subdue their ability to develop resistance against these mechanisms. In order to exert antimicrobial activity, majority of the peptides interact with the outer membrane components of pathogens. A pivotal facet of their potential as a therapeutic drug is the degree to which these antimicrobial peptides distinguish between microbial and mammalian cells. High selectivity towards microbial cells implies less toxicity against host cells. Hence, it is crucial to understand the differences between biomembranes of bacterial and mammalian cells.

2.2.2.1 Study of bacterial and mammalian cell membranes

The elementary constituent of all biomembranes is the amphipathic phospholipid bilayer. However, based on specific composition, prokaryotic and eukaryotic cell membrane is remarkably different. Zwitterionic phospholipids such as phosphatidylcholine (PC), phosphatidylethanolamine (PE) and sphingomyelin (SM) are found in abundance in mammalian cell membranes. In contrast, bacterial cell membranes are rich in anionic phospholipids such as phosphatidylglycerol (PG), cardiolipin (CL) and phosphatidylserine (PS). Sterols having no net charge such as cholesterol and ergesterol are found in mammalian cells but are absent in bacterial cell membranes[80]. Hence, cationic AMPs can interact both hydrophobically and electrostatically with bacterial cell membranes but only hydrophobically with mammalian cell membranes. Therefore, tweaking the hydrophobicity and cationicity of AMPs can lead to an improved toxicity towards bacterial cells. Another fundamental contrast between prokaryotic and eukaryotic cell membrane is the difference in their transmembrane potential

(Δψ). A typical mammalian cell exhibits a transmembrane potential ranging from -90 to -110 mV. However, bacterial cells in their mid-log phase exhibit Δψ between -130 to -150 mV[81]. Self-promoted uptake of antimicrobial peptides is influenced by membrane electrochemistry. Therefore, such significant differences in the transmembrane potential serve as additional guiding parameters for selective toxicity of these peptides[81].

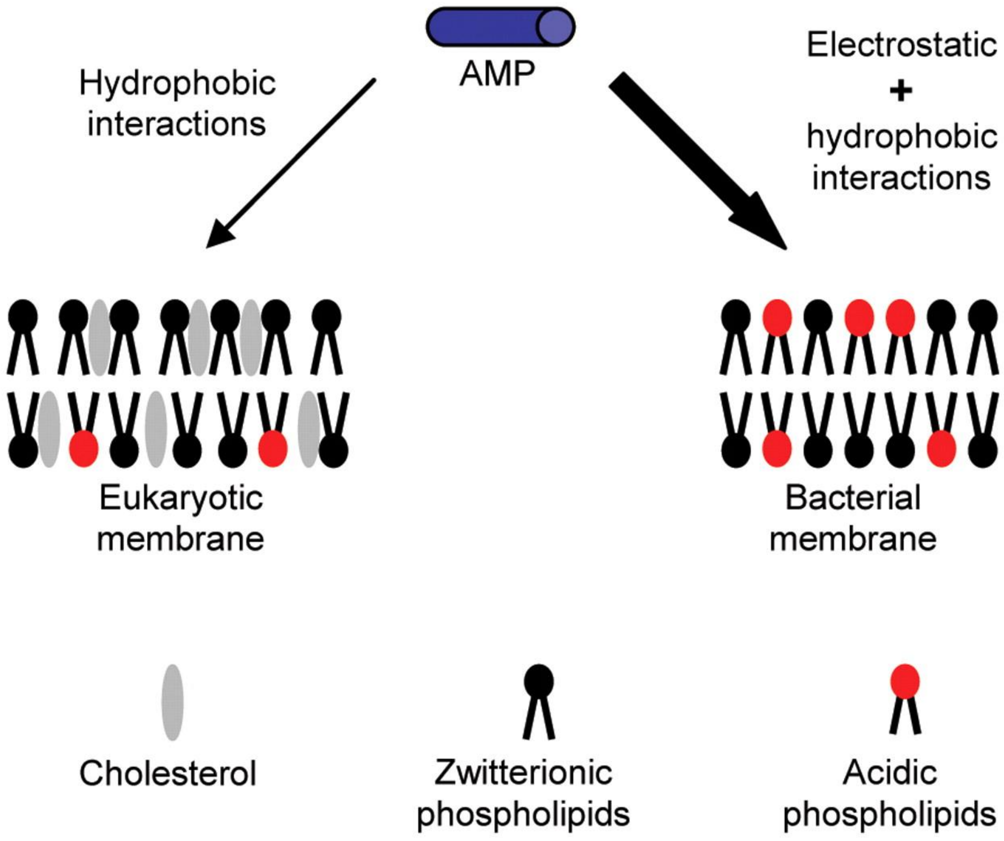

Figure 2.7| Interaction of antimicrobial peptides with biomembranes. Cationic AMPs have strong electrostatic interactions with negatively charged bacterial cell membranes. However, only a weak interaction is present between hydrophobic pockets of these peptides and zwitterionic mammalian cell membranes. Moreover, cholesterol present in eukaryotic cell membranes provide additional strength and protection from AMP activity.
Figure taken from ref.[82]

Cell wall is the first barrier that an antimicrobial agent needs to overcome to exert its activity. Contrary to Gram-positive bacteria, Gram-negative bacteria possess an additional membrane, known as the outer membrane (OM), encompassing cytoplasmic membrane and peptidoglycan layer. Phospholipids are located in the inner leaflet and Lipopolysaccharide in the outer leaflet of the OM[83]. Gram-positive bacteria possess a much thicker peptidoglycan layer compared to their Gram-negative counterparts. Lipoteichoic acids are present in the entire cell envelop. Their lipid component penetrates into the outer leaflet of cytoplasmic membrane, whereas the teichoic acid portion penetrates inserts into the peptidoglycan layer[83]. LPS and lipoproteins (LP) are the most important pathogenicity factors (PF) of Gram-negative and Gram-positive bacteria, respectively. Release of PF into the extracellular milieu, frequently results in bacterial sepsis[84]. Hence, an ideal antimicrobial agent should have a potent ability to bind and neutralize PF, in addition to high antimicrobial activity and low host cell toxicity.

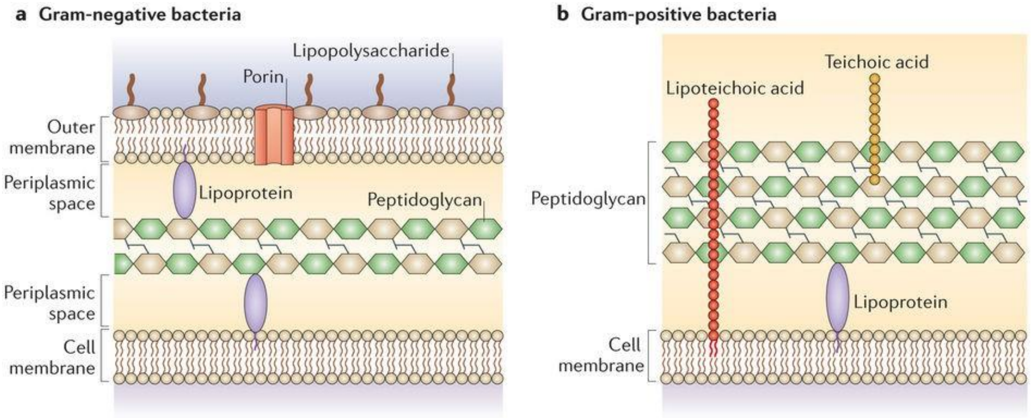

Figure 2.8| Cell wall of Gram-positive and Gram-negative bacteria. Gram-negative bacterial cell wall consists of a thin peptidoglycan layer between inner and outer membranes. Outer membrane consists of LPS in its outer leaflet. Gram-positive bacteria possess a thick peptidoglycan layer and lipoteichoic acid and lacks outer membrane.

Figure taken from ref.[85]

2.2.2.2 Mechanism of antimicrobial action

Mechanism of antimicrobial action of AMPs on pathogens is a series of complex steps which may involve either interacting with membrane targets or translocating through the cell membrane without compromising the membrane integrity and interacting with intracellular targets such as nucleic acids and enzymes. The mode of antimicrobial action of cationic AMPs can be broadly categorized in three different groups: pore formation, intracellular targets and agglutination.

Pore forming antimicrobial peptides

Numerous models for antimicrobial membrane permeabilization have been proposed. Moreover, a given peptide may act via different mechanisms in variable membrane environments. Most membrane active AMPs have both cationic and hydrophobic faces. The cationic part ensures initial attraction towards the negatively charged bacterial cell membrane. The hydrophobic domain helps insert the AMP inside the cell membrane. There are three classical killing mechanisms by which AMPs interact and form pores in bacterial cell membrane.

- Barrel-Stave mechanism

  In the mechanism, AMPs are inserted perpendicularly to the membrane bilayer plane. A number of channel-forming peptides form a ‘barrel-like’ ring around an aqueous pore. The term ‘stave’ represent transmembrane spokes comprised of peptides/peptide complexes. The hydrophobic face of the AMP face towards the acyl chains of the membrane while the hydrophobic face forms the pore-lining[86, 87]. Initially, peptides bind to the membrane surface in monomeric state. Peptides might then undergo a conformational phase transition, pushing the polar phospholipid head groups aside which leads to an induction of localized membrane thinning. This facilitates the hydrophobic domain of the AMPs to insert into the membrane. Cationic AMPs facing the phospholipid head group also assist in this process. After achieving the threshold concentration, the bound peptides self-aggregate and insert deeper into the hydrophobic membrane core[86, 87]. In transmembrane configuration, aggregation results in a minimum exposure of peptide hydrophilic residues to the hydrophobic interior of the membrane. Likewise, continued acceleration of peptide monomer leads to further expansion of membrane pores. Upon successful phospholipid translocation, the peptides are transported from outer membrane to the inner membrane leaflet due to concentration gradient of surface bound AMPs and a negative transmembrane potential. Alamethicin has been deduced to conform to the Barrel-Stave model[86, 87].

- Carpet mechanism

  Like aforementioned mechanism, peptides initially bind to the surface of the target membrane via electrostatic interactions. However, it does not involve channel-formation. Rather, displacement of phospholipids, changes in membrane fluidity and reductions in membrane-barrier properties subsequently lead to membrane disruption in a dispersion-like manner. In the carpet model, peptides accumulate on the membrane surface and when the density reaches a threshold concentration, the membrane is subjected to unfavourable energetics and its integrity is lost[86, 87]. Cecropin P1, derived from moth hemolymph, initially orients parallel to the membrane as a concentrated layer of peptide monomers on the surface. It does not insert into the hydrophobic milieu of the membrane but destabilizes the phospholipid packing and causes membrane disruption.

- Toroidal Pore or Wormhole mechanism

  The wormhole model has been mainly deduced from experiments using a-helical peptides like magainins. The hydrophobic residues of the bound peptides displace the negatively charged phospholipid head groups introducing a positive curvature strain in the membrane and membrane thinning[86, 87]. At the threshold peptide to lipid ratio, peptides orient perpendicular to the membrane and begin to self-associate to ensure minimum exposure of their polar residues to the membrane hydrophobic domain. Thus, the aggregated monomers form dynamic peptide-lipid supramolecular or toroidal pore complex. Contrary to the Barrel-Stave model, in toroidal pore model, lipids are intercalated with the peptides in transmembrane channel and the supramolecular complex constitutes of a membrane-pore lined with phospholipid head groups and polar peptide residues[86, 87].

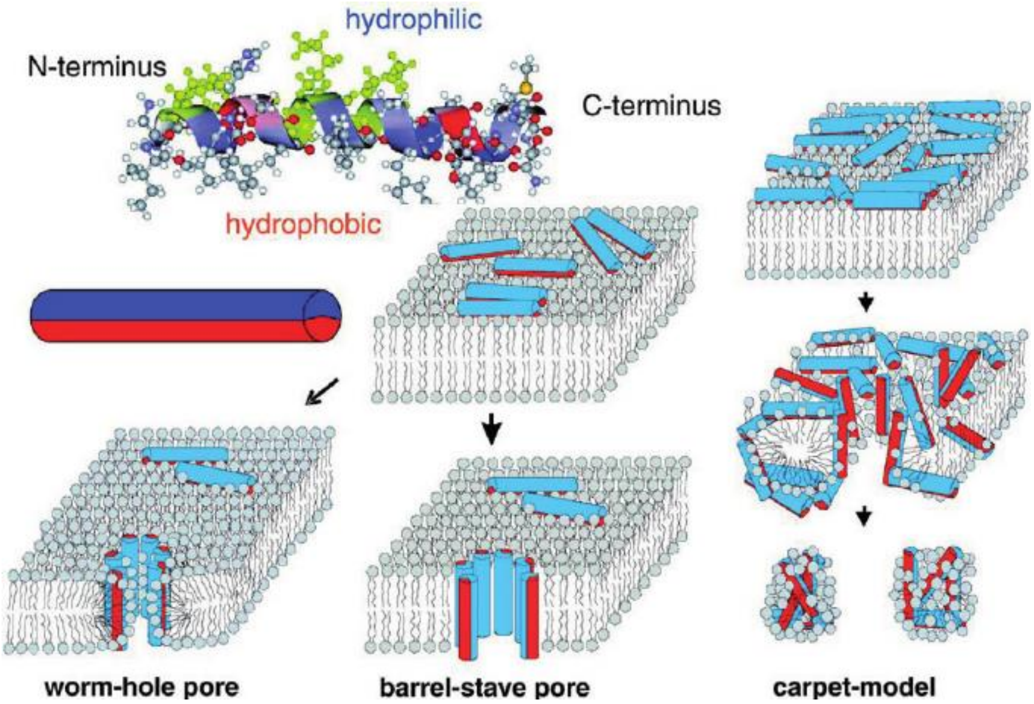

Figure 2.9| Classical mechanisms of membrane permeabilization. Wormhole pore model as proposed for magainin and Barrel-Save model as proposed for alamethicin. Hydrophobic face of the AMPs is oriented towards the hydrophobic core of the membrane bilayer. In carpet model, the AMP accumulate at a high concentration on the surface, subsequently leading to micellation.

Figure taken from ref.[86]

Antimicrobial peptides having intracellular targets

Most cationic AMPs have some degree of affinity towards bacterial cell membrane. Hence, there are very few examples where AMPs do not lyse cell membrane under any circumstances. Hence, it is critical to analyse the cell membrane integrity at their MIC values. For example, at near MIC concentrations, Bac7 binds to intracellular targets without compromising the membrane integrity. However, at several folds its MIC value, it permeabilizes the cell membrane[88]. AMPs get internalized inside the bacterial cell membranes and inhibit DNA replication/transcription, cytokinesis, protein or cell wall synthesis. However, the precise mechanism by which AMPs enter a bacterial cell is unclear. The most accepted mechanism is spontaneous translocation, whereby peptides insert into the membrane breaking up lipid-chain associations and forming transient pores. Upon disintegration of these transient pores, some peptides become spontaneously translocated to the inner leaflet of the membrane[89]. The proline-rich group of AMPs show a different mechanism in which they get translocated via a bacterial protein[90].

Proline-rich AMP, Oncocin112 binds to 70S ribosome and blocks access to the peptidyl transferase centre and peptide exit tunnel of the 50S ribosomal subunit. This inhibits the transition of the protein synthesis to elongation phase[91]. The tetrapeptide GE81112 binds to 30S ribosome subunit and blocks translation initiation[92]. Buforin II derived from *Bufo bufo gargarizans* binds to DNA but does not damage the cell membrane[93]. CRAMP, a helical lytic peptide works in part by inhibiting cytokinesis. It was found to impair the cell division of *Salmonella* leading to long filamentous structures[94]. Lantibiotics are a class of post transitionally modified bacteriocins which are produced by Gram-positive bacteria. target the membrane-bound cell wall precursor lipid II and form a complex with it, thereby resulting in inhibition of cell wall biosynthesis. Certain type B lantibiotics like mersacidin, bind to lipid II without compromising the cell membrane integrity. However, other lantibiotics such as plantaricin C, gallidermin and epidermin bind to lipid II, hampering cell wall synthesis and also induce pore formation in a strain-specific manner[95]. Several PR-AMPs such as apiaecin, pyrrhocoricin and drosocin interact with the heat shock protein DnaK in a stereospecific manner. They inhibit DnaK by a dual mode of action wherein, they sterically block the chaperone folding activity and compete with other proteins for the natural substrate-binding site. These interactions also lead to a decreased ATPase activity[96-98]. Upon binding to cell membrane, the synthetic model hexapeptide MP196, delocalizes the peripheral membrane proteins vital for cell wall synthesis and respiration, limiting cellular energy and weakens the integrity of cell wall[99]. Thus, antimicrobial peptides with intracellular targets have diversified modes of action. To increase their chances as potential new drugs in the future, it is pivotal to understand their modes of membrane translocation, active concentration in cytoplasm and their interactions with intracellular targets.

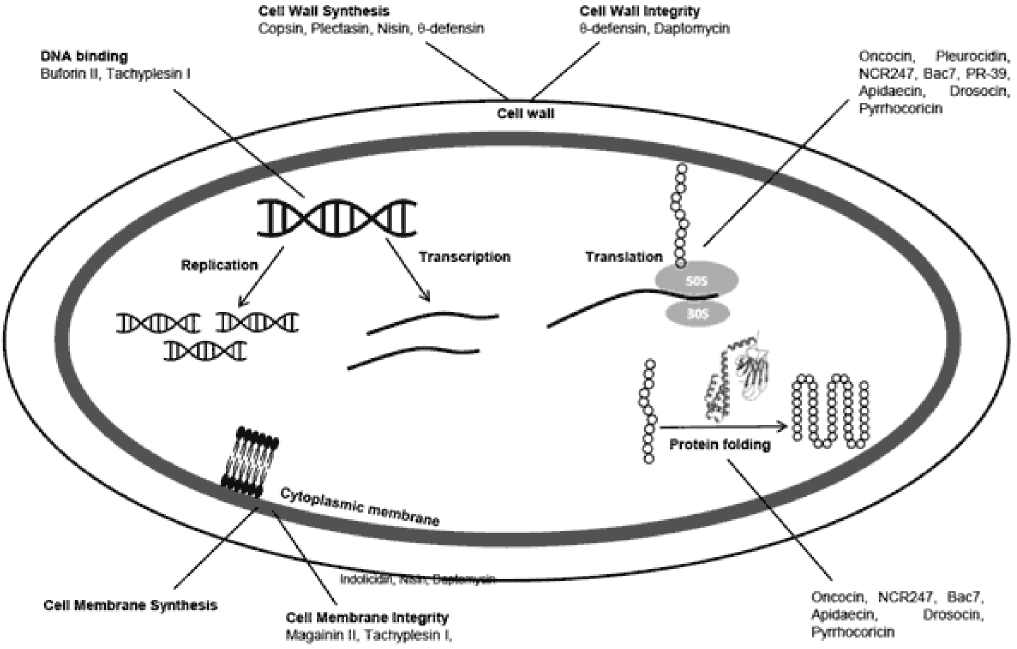

Figure 2.10| Intracellular targets of AMPs. Certain non-membranolytic AMPs work by inhibiting cell wall and cell membrane biosynthesis, protein synthesis or by binding to essential enzymes or nucleic acids, inhibiting DNA replication/transcription.
Figure taken from ref.[95]

Bacterial cell agglutinating antimicrobial peptides

Cell agglutination is the least understood mode of antimicrobial action. Moreover, very few AMPs have been discovered which exert their antimicrobial activity through agglutination. A crucial characteristic of these AMPs is that they have multiple binding sites which can interact with the negatively charged components of the microbial cell membrane like phosphate groups in lipopolysaccharides in Gram-negative bacteria and lipoteichoic acid in Gram-positive bacteria. Therefore, these peptides bind to multiple bacterial cells at a time, eventually leading to agglutination.

Macin family of proteins within the superfamily of scorpion toxin-like proteins consists of three members, namely theromacin and neuromacin from leeches and hydramacin-1 from *Hydra*. Hydramacin-1 and neuromacin exert antimicrobial activity by aggregating bacteria. The proteins become sandwiched as a belt of positive charges between two hydrophobic bacterial cell membranes. Therefore, they interact hydrophobically and electrostatically with two bacterial cells in parallel and each cell can interact with several other antimicrobial proteins leading to the formation of huge cell aggregates. At MIC, neuromacin employs a non-membranolytic mechanism of action by agglutinating bacterial cells. However, at concentration several folds higher than MIC and at slightly acidic pH, it also permeabilizes the cell membranes[100].

Amyloid-β (Aβ) peptides are the major constituents of the plaques found in the brains of patients with Alzheimer's disease. On treatment with several bacterial strains, the amyloidogenic peptides $A\beta_{x\text{-}42}$ ($A\beta_{1\text{-}42}$, $A\beta_{2\text{-}42}$ and $A\beta_{3p\text{-}42}$) form large agglutinates of bacterial cells and kill most of the pathogens within 6h of incubation[101].

GL-13 is a synthetic peptide derived from parotid secretory protein (PSP). The peptide has a moderate bactericidal activity. However, it agglutinates bacterial cell to bigger aggregates and increases bacterial clearance by macrophages[102].

Thanatin is a 21-amino acid host defense peptide, derived from *Podisus maculiventris*. This AMP is known to exert its antimicrobial activity via agglutination. In presence of LPS, dimerizes to achieve multiple binding sites necessary for bacterial agglutination[74].

Eosinophil Cationic Protein (ECP) is an eosinophil secreted protein which has a broad spectrum of antimicrobial activity against both Gram-positive and Gram-negative bacteria. It has a very high affinity towards LPS and it exerts its antimicrobial activity distinctively via agglutination[103].

Anionic antimicrobial peptides

Since the discovery of first anionic AMPs in the early 1980s, they have been increasing identified in nature including vertebrates, invertebrates and plants. Hence, it is evident that AAMPs are also a crucial and integral part of innate defense system. AAMPs generally have a net charge from -1 to -7. The mode of action of AAMPs is still unclear, however some AAMPs make use metal ions to make cationic salt bridges with negatively charged bacterial membrane[104]. This facilitates them to interact with their targets and exert antimicrobial action. Sheep and cattle AAMPs (SAAPs) use Zn^{2+} to form cationic salt bridge between SAAPs and the anionic components of the cell membrane. This results in translocation of these peptides into the cytoplasm where they can interact with their intracellular targets[104]. Dermcidin (DCD) is an AAMP which is secreted by the human sweat glands and transported to the epidermal surface of the human skin.

The processed form of DCD, anionic DCD-1(L) undergoes Zn^{2+} dependent formation of an oligomeric complex upon interaction with anionic bacterial cell membrane. This results in ion channel formation leading to membrane depolarization and cell death[105].

2.2.3 Synergy among antimicrobial peptides

The essence of synergism between two drugs is in the fact that the combined action of both the antimicrobials is more than the sum of action of each antimicrobial drug when taken alone. Synergism is effective when an optimal concentration of one antibiotic cannot be achieved due to toxicity at that concentration or site of the infection. Moreover, a number of AMPs in synergic combinations with conventional antibiotics are being used in clinical trials as a last resort against multi-drug resistant (MDR) pathogens like methicillin-resistant *Staphylococcus aureus* (MRSA), *Klebsiella pneumoniae*, *Pseudomonas aeruginosa*, etc[106]. In nature, there is an evidence of synergy among antimicrobial peptides in a lot of anatomic sites. In insects, a repertoire of eight to ten antimicrobial peptides act synergistically against broad range of pathogens acting via various specific mechanisms of action. Protegrin and indolicin can act synergistically against *E. coli* and *P.aeruginosa* via cooperative membrane action[106]. Colistin with the antibiotic imipenem can act against *K.pneumoniae*[106]. There are many more examples of antimicrobials acting in synergy which has reached to the stage of clinical trials. Moreover, due to a scarcity of new antimicrobials, synergy is rapidly gaining attention as an antimicrobial therapy against MDR pathogens and infectious diseases.

2.3 Conclusion

The emergence of multi drug resistant pathogens has rendered antibiotics inefficient in treating infectious diseases. Development of new antimicrobials is pivotal to win this war against resistant bacteria.in contrast to most antibiotics, AMPs have evolved with innate immunity since millions of years to work against microbes in the host environment. However, there are major drawbacks in their use as a pharmacological drug. AMPs are usually larger than antibiotics and are strongly cationic resulting in a poor bio-distribution. AMPs are fairly toxic and have high decomposition rates. However, careful modifications in the peptide structure can eliminate or improve these pharmacological parameters. Hence a sound knowledge of the structural – function correlation of the peptide in question is crucial.

In the following chapters, I have studied novel mechanisms of action of non-membrane permeabilizing antimicrobial peptides and have analysed the role of crucial residues in its activity against pathogens.

Chapter 3

Materials and Methods

In this chapter, a summary of all the materials used in this thesis work is given. A detailed discussion of all the NMR and biophysical experiments conducted for this work is delineated. Moreover, a description of boundary conditions and parameters used during MD simulation of LPS/thanatin complex is explained. Finally, a detailed protocol of YR26 expression and purification is discussed.

3.1 Materials

LPS from *E. coli* 0111:B4, FITC-LPS from *E. coli* 055:B5, MH broth, SDS and fluorescent dyes like NPN and calcein were purchased from Sigma Aldrich. The fluorescent probes, SYTOX green amd BODIPY TR Cadaverine were purchased from Invitrogen. DPC, POPC and POPG and the extruder used for the preparation of liposomes were obtained from Avanti Polar lipids (Alabaster, AL). NMR reagents such as DSS, D_2O, DPC-d_{38} and SDS-d_{25} were purchased from Cambridge Isotope Laboratories, Inc (Massachusetts, USA). Thanatin, mutated thanatin peptides and dansyl labelled thanatin peptides were purchased from GL Biochem. (Shanghai, China). Furin prodomain derived peptides were purchased from Synpeptide Co. Ltd. (Shanghai, China). Plasmid for YR26 expression was procured from Shanghai ShineGene Molecular Biotech, Inc. All other fine chemicals were of analytical grade.

3.2 Methods

3.2.1 Minimum Inhibitory Concentration

Minimum Inhibitory Concentration (MIC) of thanatin and analogs was measured using broth dilution method. Mid-log phase cultures of four Gram-negative (*Escherichia coli*, *Pseudomonas aeruginosa* ATCC 27853, *Klebsiella Pneumoniae* ATCC 13883, *Salomonella enterica* ATCC 14028) and four Gram-positive (*Bacillus subtilis*, *Staphylococcus aureus* ATCC 25923, *Streptococcus pyogenes* ATCC 19615, *Enterococcus faecalis* ATCC 29212) bacteria were diluted in MHB to a final concentration of 5×10^5 CFU/ml. In a 96-well plate 50 µl of peptides at final concentrations ranging from 25 µM to 0.25 µM were prepared and another 50 µl of the diluted bacterial solutions were added to each of the wells. The plate was incubated at 37^{o}C for 18 hrs. OD_{600} was measured and the concentration at which there is complete inhibition of bacterial growth was recorded as the MIC of the peptide.

3.2.2 Hemolysis Assay

1 ml of fresh blood sample was taken from a heathy volunteer. The erythrocytes were washed with PBS (10 mM sodium phosphate buffer, 150 mM NaCl, pH 7) and 5% blood solution was prepared in PBS. In a 96 well plate, 50 µl of varying

concentrations of peptide were prepared. Another 50 µl of 5% blood solution was added to each well. The plate was incubated for 1 hr at 37°C. The plate was centrifuged and the OD_{540} of the supernatant was measured. 1% triton-X was taken as positive control and PBS was taken as negative control. % hemolysis was calculated as:

$$\% \text{ hemolysis} = \frac{\text{OD}-\text{ODnegative}}{\text{ODpositive}-\text{ODnegative}} * 100$$

Where,

OD: OD_{540} for any well
ODnegative: OD_{540} for negative control
ODpositive: OD_{540} for positive control

3.2.3 Cytotoxicity Test

NIH3T3 cell line was used to test the toxicity of the AMPs towards mammalian cells. 10,000 cells were added per well in a 96-well plate and the plate was incubated overnight at 37°C and 5% CO_2. Next day, media was removed and 100 µl of desired concentration of peptides in fresh media were added. The plate was incubated for 4 hours at 37°C and 5% CO_2. Media was again replaced by fresh media. 10 µl of MTT was added in each well. The plate was again incubated for 4 hours at 37°C and 5% CO_2. Finally, media was removed from every well and 100 µl of DMSO was added to each well to solubilize the crystals. The plate was again incubated for 10 minutes. Each well was mixed thoroughly and OD was taken at 540 nm. For negative control, no peptide was added and for positive control, no cells were added. % cell viability was calculated as:

$$\% \text{ Cell Viability} = \frac{\text{ODnegative}-\text{OD}}{\text{ODnegative}-\text{ODpositive}} *100$$

Where,

OD: OD_{540} for any well
ODnegative: OD_{540} for negative control
ODpositive: OD_{540} for positive control

3.2.4 Calculation of Dissociation Constant of thanatin and mutated peptides

To study the binding affinity of the peptides to LPS, peptides were dansylated at the N-terminus and the fluorescence measurements were carried out with Cary Eclipse fluorescence spectrophotometer (Varian inc). 50 µM dansylated peptides were excited at 330 nm wavelength and their emission fluorescence were monitored from 450–650 nm followed by the addition of increasing concentration of LPS. ΔFmax was calculated as (F − Fo)/(Fmax − Fo) and was plotted against concentration of LPS, where, F is the fluorescence intensity at maxima for any LPS concentration. Fo is the basal fluorescence intensity at maxima. Fmax is the fluorescence intensity at maxima for maximum LPS concentration. To calculate the dissociation constant, the data were fitted using Hill's equation.

3.2.5 BODIPY Cadaverine Displacement Assay

Relative affinities of thanatin and its analogs to LPS were examined in terms of their ability to displace BODIPY TR cadaverine (BC) from LPS-BC mixture. BC has a high affinity to LPS and its displacement from LPS by the peptides results in dequenching of its fluorescence. 5 µM BC and 50 µg/ml LPS mixture was prepared in 50 mM Tris buffer, pH 7.4. In a 96-well plate, 50 µl of peptides were prepared at final concentrations ranging from 500 µM to 0.01 µM by serially diluting in 50 mM Tris buffer, pH 7.4. Another 50 µl of the aforementioned LPS-BC mixture was added to the wells and fluorescence was measured by exciting samples at 580 nm and emission was recorded from 604-650 nm. BC occupancy factor was calculated as: BC Occupancy Factor = (F_{max} – F)/ (F_{max} - F_{min})

Where,

F = Fluorescence intensity at maxima at a particular mediator concentration,
F_{max} = Fluorescence intensity at maxima at maximum mediator concentration,
F_{min} = Fluorescence intensity at maxima at minimum mediator concentration.

Occupancy factor was plotted against concentration of peptides and ED_{50} was calculated using the following equation:

$$y = 1 - B + \frac{T - B}{\left\{1 + \left(\frac{x}{ED50}\right)^{-H}\right\}}$$

Where, B is the minimum occupancy factor and T is the maximum occupancy factor.

3.2.6 Outer Membrane Permeabilization Assay

The ability of the peptides to permeabilize the outer membrane was examined using 1-N-Phenylnaphthylamine (NPN) dye. *E. coli* cells were grown to mid log phase and were diluted to OD $_{600}$ 0.5 in 10 mM phosphate buffer, pH 7.0. 10 μM NPN was added to the cells from 5 mM NPN stock solution and basal fluorescence was recorded. This was followed by the addition of increasing concentrations of peptides and recording the emission spectra. Excitation wavelength was set as 350 nm and emission wavelength was recorded from 390 nm to 450 nm. The fluorescence measurements were carried out on Cary Eclipse fluorescence spectrophotometer (Varian Inc) equipped with dual monochromators. Finally, the fluorescence intensity at 410 nm was plotted against concentration of each peptide to examine the effect of the AMPs on the outer membrane of the *E. coli* cells.

3.2.7 Inner Membrane Permeabilization Assay

E. coli cells were grown to mid log phase in LB media and were diluted to OD_{600} of 0.5 in 10 mM phosphate buffer, pH 7.0. 2.5 μM of SYTOX green dye was added to the cells from 5 mM stock solution and the mixture was incubated in dark for 15 mins. Basal fluorescence was recorded by setting the excitation wavelength at 485 nm and recording the emission wavelength from 490 nm to 550 nm. Furthermore, increasing concentrations of peptides were added and fluorescence was measured. An increase in fluorescence intensity of the dye indicates that the inner membrane of the *E. coli* cells is permeabilized. The fluorescence measurements were carried out on Cary Eclipse fluorescence spectrophotometer (Varian Inc) equipped with dual monochromators.

3.2.8 Intrinsic Tryptophan Fluorescence Assay

Basal fluorescence of the furin prodomain derived peptides was measured by exciting the peptides at 280 nm and recording the emission spectra frim 300 nm to 400 nm. Change in the wavelength of emission intensity maxima was observed by addition of increasing concentrations of LPS, SDS or DPC. To examine the binding affinity, the normalized change in fluorescence intensity maxima was calculated as:

Normalized value = $\frac{\text{Fmax (basal)} - \text{Fmax}}{\text{Fmax(basal)}}$

Where,

Fmax (basal) = Basal fluorescence intensity at maxima,
Fmax = Fluorescence intensity at maxima at a particular micelle concentration,

This normalized value of change in fluorescence intensity was then plotted against micelle concentration and the plot was fitted with Hill's equation to get dissociation constant. To study the interaction of AMPs with liposomes, basal intrinsic tryptophan fluorescence spectrum was recorded. Following this tryptophan fluorescence emission intensity spectra were recorded in presence of increasing liposome concentrations. Change in wavelength at fluorescence intensity maxima in presence of higher liposome concentration was then analysed to examine the AMP/liposome binding. The fluorescence measurement was carried out in Cary Eclipse fluorescence spectrophotometer using a 0.1 cm path length quartz cuvette.

3.2.9 Isothermal Titration Calorimetry

The thermodynamic aspect of the thanatin and mutant peptides binding to LPS was studied using a microcal ITC 200 calorimeter. 50 µM LPS (MW: 10 kDa) in phosphate buffer, pH 7 was loaded into the sample cell and 1 mM peptide stock was loaded into the syringe. The reference cell was filled with buffer. 25 injections of 1.5 µl peptides were made into the sample cell at 25°C and the stirring speed was set at 900 rpm. The raw data obtained was fitted using single site binding model in Microcal origin 5.0 software to get the association constant (K_a) and enthalpy change (ΔH). Dissociation constant (K_d), Gibbs free energy (ΔG) and entropy change ($T\Delta S$) were calculated as:

$K_d = 1/K_a$

$\Delta G = - RT \ln K_a$

$T\Delta S = \Delta H - \Delta G$

In case of furin prodomain derived peptides 500 µM peptide stock solution was titrated into the sample cell having 50 µM LPS at 37 °C. The raw data was fitted using single site binding model in MicroCal PEAQ-ITC analysis software.

3.2.10 FITC-LPS Fluorescence Assay

The relative ability of the antimicrobial peptides to interact with FITC-LPS micelles was studied by measuring the fluorescence of 500 nM FITC-LPS in 10 mM sodium phosphate buffer, pH 7 followed by addition of increasing concentrations of peptide samples. Fluorescence intensity was recorded at an excitation wavelength of 480 nm and emission wavelength of 500-550 nm. % reduction in intensity with respect to free FITC-LPS was calculated as:

$$\frac{Fluorescence\ intensity\ of\ FITC-LPS\ in\ presence\ of\ peptide\ at\ maxima}{Flourescence\ intensity\ of\ free\ FITC-LPS\ at\ maxima}*100$$

3.2.11 Zeta Potential Measurement

E. coli grown to mid-log phase in LB media were diluted to an OD_{600} of 0.2. Zeta potential of 700 μl of the bacterial cells was first measured. Furthermore, increasing concentrations of peptides were added and zeta potential was measured. The measurements were made in disposable zeta cells with gold electrodes. For each concentration, a total of 3 measurements of 100 runs each was carried out. The experiments were carried out on a zeta sizer Nano ZS (Malvern Instruments, Worcestershire, UK) equipped with a 633 nm He laser.

3.2.12 Preparation of liposomes

Bacterial cell mimicking POPC-POPG (3:1) liposomes and mammalian cell mimicking POPC liposomes were prepared to study their interaction with the AMPs. Dry weights of the appropriate lipids were measured in glass vials. Chloroform and methanol in the ration of 3:1 was added to the vials to dissolve the lipids. The solvent was then evaporated under a stream of nitrogen gas. This leads to the formation of a thin film on the sides of the vials. The vials were then freeze dried for 2 hours to completely remove any trace of the solvent. The film was then dissolved in 10 mM phosphate buffer, pH 7. The mixture was frozen and thawed repeatedly for atleast 10 times. The liposomes were made unilamellar by extruding the lipid through 100 nm membranes. The lamellarity of the liposomes was confirmed by analysing their particle size by dynamic light scattering technique.

In case of calcein-bound liposomes, the film was dissolved in 10 mM phosphate buffer consisting of 70 mM calcein. After extrusion, the unbound calcein was separated from the calcein-bound liposomes using PD-10 desalting column.

3.2.13 Calcein Leakage Assay

Membrane permeabilizing ability of the AMPs was determined by examining the release of calcein from the calcein-bound liposomes using Cary Eclipse fluorescence spectrophotometer (Varian Inc). Basal fluorescence of the calcein-bound liposomes was measured by exciting the vesicles at 490 nm and recording the emission fluorescence from 500 nm to 550 nm. Fluorescence emission spectra in presence of increasing peptide concentration was also recorded. Change in emission intensity maxima was then plotted against peptide concentration to examine the calcein leakage in presence of AMPs. The measurements were carried out using 0.1 cm path length quartz cuvette.

3.2.14 DLS Particle Size Analysis

Agglutination ability of the furin prodomain derived AMPs was examined by analysing the particle size of 1 μM POPC-POPG and POPC liposomes in presence of increasing peptide concentrations. Mean diameter of free liposomes was first determined in 10 mM phosphate buffer, pH 7 using dynamic light scattering instrument (Brookhaven Instruments Corp., Holtsville, NY). DLS measurements were then made for liposome:peptide ratios of 1:1, 1:2 and 1:4. Scattering data was analysed using the particle sizing software provided with the instrument.

3.2.15 Transmission Electron Microscopy

Agglutination of bacterial cells by the antimicrobial peptides were visualized using TEM. Midlog phase *E.coli* cells were treated with 10 μM active peptides for one hour. The samples were concentrated to 10 times in phosphate buffer and were loaded onto the copper grids. 0.5% uranyl acetate was used for negative staining of the dye. T12 ICor TEM was used to collect the images. *E.coli* cells without any peptide treatment were used as control.

3.2.16 NMR Spectroscopy Experiments for Thanatin and its Analogs

All the NMR spectra were recorded on a Bruker DRX 600 spectrometer, equipped with a cryo-probe and pulse field gradients. Data acquisition and processing were performed with topspin software running on Linux workstation. 0.4 mM peptides in aqueous solution containing 10% D2O at pH 5 were used to acquire two dimensional TOCSY (total correlation spectroscopy) and NOESY (nuclear Overhauser effect spectroscopy) spectra at 298 K. Mixing times of 80 ms for TOCSY and 300 ms for NOESY were used. DSS (2,2-dimethyl-2-silapentane 5-sulfonate sodium salt) was used as an internal reference for chemical shift. NOESY experiments were performed with 400 increments in t1 and 64 transients. WATERGATE procedure was used for water signal suppression. A total of 2 K data points was used in t2 and NMR data was analysed in SPARKY (T.D. Goddard and D.G. Kneller, University of California, San Francisco, CA, USA) program. In order to study interaction of thanatin with DPC micelles, two dimensional TOCSY and NOESY spectra of 0.28 mM thanatin dissolved in 125 mM perdeuterated DPC were recorded at 308 K. Mixing times of 80 ms for TOCSY and 150 ms for NOESY were used. Paramagnetic relaxation experiments were carried out to gain insights on thanatin/DPC interaction. 0.15 mM thanatin and 62.5 mM perdeuterated DPC were dissolved in 100% D_2O. TOCSY spectrum was recorded with the same experimental parameter. 2 mM of 5-DSA or 16-DSA, dissolved in deuterated methanol was added and TOCSY spectrum was recorded. Intensity changes in $H\alpha$/NH correlations were estimated. For proline residues, $H\alpha/H\delta$ correlations were considered. Remaining amplitude (RA) for each residue (calculated as NMR peak intensity with paramagnetic probe/intensity without probe) was determined to estimate its interaction with DPC.

Two-dimensional transferred NOESY spectra were acquired in aqueous solution, 10% D_2O containing 30 μM LPS and 0.4 mM peptides at pH 5. The experiment was performed with the same parameters as the NOESY experiment except that the mixing time was 75 ms. In order to study the interaction of peptides with LPS, one dimensional ^{31}P NMR spectra of 400 μM LPS in water, pH 6 was recorded on a Bruker DRX 400 spectrometer. Following this, a series of one-dimensional ^{31}P NMR spectra were recorded for LPS:peptide ratios of 4:1, 2:1 and 1:1. Two-dimensional STD TOCSY spectra of thanatin-LPS complex in D_2O, pH 5 were recorded with 330 t1 increments and 72 transients using MLEV-17 spin lock field of 80 ms. LPS was saturated at −2.5 ppm (on resonance) and 40 pm (off resonance) for 2 s. Subtraction of the two spectra by phase cycling leads to the required STD spectra. Saturation transfer was achieved by using 40 selective Gaussian 270 pulses with a duration of 50 ms. Relaxation delay of 2.1 s was used. One dimensional STD experiments were carried out by saturating LPS at −3 ppm (on resonance) and 40 ppm (off resonance) with a series of 40 selective Gaussian- shaped pulses (49 ms each) with 1 ms interval leading to a total saturation time of 2 s.

3.2.17 NMR-Derived Structure Calculations for Thanatin and its Analogs

3D structures of thanatin and its analogs were calculated using CYANA program. Distance restrains were estimated from two dimensional NOESY spectra on the basis of NOE intensities. Strong, medium and weak NOEs were translated to upper bound distance limits of 2.5, 3.5 and 5.0 Å, respectively. While calculating structure, a disulphide bond constraint was used between cys11 and cys18. SHIFTY was used to calculate the dihedral angle constraint using Hα chemical shift deviation of individual amino acids. Calculations of dimeric structure of thanatin were carried out by adding eleven Gly residues connecting two thanatin molecules. Out of 100 structures calculated, 20 lowest energy structures were kept for further analysis. PROCHECK[107] was used to produce Ramachandran plot, which was in turn used to validate the structures calculated.

3.2.18 Molecular Dynamics (MD) Simulation

MD simulations were carried out in collaboration with A/P Yuguang Mu and Liangzhen zheng at SBS, NTU. All atom molecular dynamics simulations were performed based on a periodic boundary condition (PBC) box with 120 1,2-Dipalmitoyl-sn-glycero-3-phosphoethanolamine (DPPE) (in lower leaflet), 48 LPS (in upper leaflet) molecules and the thanatin dimer, in a 84 × 84 × 120 cubic box with around 11000 TIP3P water molecules and 192 Ca^{2+} ions, as well as Cl^{-} ions. This LPS/DPPE hybrid bilayer lipid initial model was adopted and modified from the long equilibrium lipid model by Kirschner *et al*[108]. The schematic diagram of LPS model used in this study has been depicted in Supplementary Fig. 9. The Glycam based force field was used for lipid system. As for two thanatin dimer, NMR model was utilized for simulations, using Amber 99SB-ILDN force field. We adopted the Amber99SB force field parameters for TIP3P explicit water model and ions in all the simulations. Once the simulation boxes were constructed, the systems went through a 1000-steps energy minimization to eliminate possible close contacts among atoms, followed by 100 ps equilibrium in NVT ensemble with restraints added to the heavy atoms of DPPE and LPS molecules. 10 ns equilibrium was employed in NPT ensemble simulations with similar restraints akin to NVT equilibration. Thanatin dimer was randomly inserted into the simulation box replacing water molecules. At 310 K, 100 ps NVT and 10 ns NPT equilibriums, heavy atoms of the thanatin dimer were also imposed by position restraints of 1000 kJ/(mol.nm2). Finally, three repeat runs for 400 ns each, with different initial velocities, were carried out under temperature 310 K. All the simulations were performed with Gromacs package together with Plumed package. The time step for all simulations was 2 fs, while the coordinate data were stored every 2 ps. In NVT and NPT ensembles, temperature coupling was realized using velocity rescaling thermostat scheme updating velocities every 0.1 ps, whereas in NPT ensemble simulations, semi-isotropic pressure coupling method Parrinello-Rahman was utilized to maintain the lipid bilayer structure. SHAKE algorithm and LINCS algorithm were applied, to restrict the bonds between hydrogen-heavy atoms and the heavy-heavy atoms covalent bonds, respectively, to an equilibrium value. Furthermore, PME scheme enabled the long range electrostatic interactions. For both long range electrostatic and van der Waals interactions, the distance cutoff was 1.2 nm. During simulations, dimeric structure of thanatin was maintained by applying eight distance restraints using a quadratic bias potential (force constant 1000) according to Gromacs manual 5.0. It may be noted that structure of dimeric thanatin in water is not favourable due to repulsion among cationic sidechains. The dimer structure is only stabilized in complex with LPS. The minimum distance and center of mass distance between LPS and thanatin dimer were calculated using Gromacs g_mindist and g_dist respectively. The coordination number (*CN*) of LPS/thanatin was defined as

$$CN = \sum_{i=1}^{N_L} \sum_{j=1}^{N_T} C(d_{ij})$$

and

$$\mathrm{C(d_{ij})} = \begin{cases} 1, & d_{ij} \leq cutoff \\ 0, & d_{ij} > cutoff \end{cases}$$

whereas, N_L and N_T are the total number of atoms in LPS and thanatin dimer respectively, and dij is the distance between atom i in LPS and atom j in thanatin dimer, a distance cutoff = 0.4 nm was used. The thanatin-LPS residue contact probability matrix ($NRes_{LPS} \times NRes_{than}$) was calculated using a distance cutoff = 0.4 nm by counting and normalizing through all the frames in the trajectories, whereas $NRes_{LPS} = 15$ and $NRes_{than} = 42$ were the number of residues in the LPS and the thanatin dimer. For each frame of thanatin-LPS complex, 0 or 1 was assigned to each bin according to the abovementioned equation with cutoff = 0.4 nm to have a contact matrix for all residue-residue pairs and all the matrices summed up and normalized by dividing by the total number of frames.

3.2.19 Expression and Purification of YR26

Synthetic gene of YR26 was cloned as fusion protein in a pET14b vector containing hydrophobic KSI at the N-terminus. The pET14b vector contains six His-tag at the N-terminus for affinity purification. An Asn-Pro sequence was introduced between KSI and hydrophilic YR26 for chemical cleavage by formic acid. The recombinant plasmid (containing ampicillin resistance) was transformed into Rosetta *E. coli* cells (having chloramphenicol resistance). A single isolated colony was picked and cultured in LB medium with ampicillin (100 μg/ml) and chloramphenicol (32 μg/ml) overnight as a starter culture. Seed culture was transformed to 1L M9 media (containing ampicillin and chloramphenicol) in 1:100 ratio by volume and was allowed to grow for in a shaker incubator at 37°C and 180 rpm for 6-7 hours till its OD_{600} reached 0.6-

0.8. The M9 media used consisted of ^{15}N ammonium chloride, necessary for ^{15}N labelling. The culture was then induced with 1mM IPTG and was allowed to grow overnight at 37°C and 180 rpm. Cells were harvested at 7000 rpm (JA 10 rotor). Expression was checked using SDS-PAGE gel electrophoresis. As the fusion protein is localized to inclusion bodies, protein purification was carried out in denaturing conditions (8 M urea). The cells were re-suspended in binding buffer (8 M urea, 50 mM phosphate buffer, 300 mM NaCl), pH 8.0 and the mixture was incubated for 1 hour while shaking at room temperature. The cells were then lysed by sonication. To eliminate cell debris, the translucent cell suspension was centrifuged at 15000 rpm (JA 25.5 rotor) for 30 mins at 4ºC. The supernatant containing the fusion protein was then loaded on the Nickel-NTA column (QIAGEN) and eluted using 8 M urea buffer containing 500mM imidazole. Eluent containing pure protein was kept for dialysis against water for 36 – 48 hours to remove urea and salts. The dialyzed mixture was then treated with 50% formic acid at 45-50°C for 24 hours in dark. Formic acid cleaves the peptide bond between Asp and Pro residues and separates the ^{15}N-YR26 from KSI tag. Formic acid was removed using rotary evaporator and the obtained film was re-dissolved in water. KSI being very hydrophobic, precipitated out leaving behind a solution of ^{15}N YR26. The peptide was further purified using HPLC and the major peak was confirmed by MALDI-TOF and NMR.

3.2.20 NMR Experiments for Furin Prodomain Derived YR26

All the NMR spectra were recorded on a Bruker DRX 600 spectrometer, equipped with a cryo-probe and pulse field gradients. Data acquisition and processing were performed with topspin software running on Linux workstation. To determine the structure of YR26 in presence of SDS micelles, 0.3 mM peptides and 150 mM SDS in aqueous solution containing 10% D2O at pH 5 were used to acquire 2D ^{1}H-^{1}H TOCSY and NOESY spectra at 298 K. Mixing times of 80 ms for TOCSY and 150 ms for NOESY were used. DSS (2,2-dimethyl-2-silapentane 5-sulfonate sodium salt) was used as an internal reference for chemical shift. NOESY experiments were performed with 400 increments in t1 and 64 transients. WATERGATE procedure was used for water signal suppression. A total of 2 K data points was used in t2 and NMR data was analysed in SPARKY (T.D. Goddard and D.G. Kneller, University of California, San Francisco, CA, USA) program. Synthetic unlabelled YR26 was used to acquire ^{13}C-^{1}H HSQC (natural abundance) spectrum in 100% D_2O at 298 K. 0.4 mM YR26 and 200 mM SDS were used for the experiment with 1024 increments in t1 and 56 transients. ^{15}N-^{1}H HSQC experiment was conducted for 0.44 mM ^{15}N YR26 and 220 mM SDS at 298 K, pH 5. The experiment was performed with 96 increments in t1 and 8 transients. ^{15}N-^{1}H Heteronuclear NOE relaxation experiment conducted with 128 increments in t1 and 8 transients. The relaxation delay was set at 3 s and the spectral widths in F2 and F1 were set at 15.02 and 35 ppm, respectively. The spectrum was split into saturated and unsaturated spectra of ^{1}H resonances. Heteronuclear ^{15}N-^{1}H NOEs were determined as the ratio of the peak intensities with and without proton saturation. The ^{15}N longitudinal (R_1) and transverse (R_2) relaxation rate constants were determined by collecting a time series of ^{15}N-^{1}H HSQC spectra with sensitivity enhancement. For R_1 measurements, the spectra were acquired at relaxation delays of 0.2, 0.6, 0.9, 1.2, 1.5, 2.0 and 2.5 s, with repeat experiment at 1.5 s for error estimation. For R_2 measurements, data were collected at 10, 30, 50, 70, 90 and 110 ms, with repeat experiment at 70 ms for error measurement. For relaxation experiments, 2K data points were used in t2 with 90 increments in t1. The relaxation constants were determined by fitting the crosspeak intensities to a mono-exponential function. To study the localization of YR26 in SDS micelles, ^{15}N-^{1}H HSQC spectra were recorded for YR26 in presence of SDS micelles and in presence of spin labelled doxyl lipids, 5-DSA and 16-DSA. Intensity changes in the HSQC peaks were estimated and remaining amplitude (RA) for each residue (calculated as NMR peak intensity with paramagnetic probe/intensity without probe) was determined to estimate its interaction with SDS micelles.

3.2.21 NMR-Derived Structure Calculations for YR26 in Presence of SDS

3D structure of YR26 in presence of SDS was calculated using CYANA program. Distance restrains were estimated from two dimensional NOESY spectra on the basis of NOE intensities. Strong, medium and weak NOEs were translated to upper bound distance limits of 2.5, 3.5 and 5.0 Å, respectively. Hα chemical shift deviation of individual amino acids from NOESY spectrum, ^{13}C chemical shift deviation from ^{13}C-^{1}H HSQC spectrum and ^{15}N chemical shift deviation from ^{15}N-^{1}H HSQC spectrum were incorporated in SHIFTY to calculate dihedral angle constraint. Out of 100 structures calculated, 20 lowest energy structures were kept for further analysis. PROCHECK was used to produce Ramachandran plot, which was in turn used to validate the structures calculated.

Chapter 4

Structure and Interactions of Thanatin in LPS Reveal Mechanism of Bacterial Cell Agglutination

In this chapter, first atomic-resolution 3D structure of thanatin in complex with LPS is reported. Furthermore, interaction of thanatin in LPS is analysed by means of various biophysical and NMR techniques. Dissociation constant and binding affinity of thanatin/LPS complex are determined by means of fluorescence spectroscopy. Moreover, structural changes in LPS micelles in presence of thanatin are examined using ^{31}P *NMR and fluorescence spectroscopy. The differences in the structures of thanatin in free solution and in presence of DPC and LPS micelles are analyzed. Interestingly, in free solution and in presence of DPC micelles, thanatin assumes a monomeric* β*-hairpin conformation. However, in presence of LPS, thanatin adopts a four stranded anti-parallel* β*-sheet conformation with a 'head-tail' topology. The dimeric structure of thanatin provides multiple LPS binding sites, facilitating agglutination.*

4.1 Introduction

Understanding the mechanism of action of antibiotics and antimicrobial peptides and proteins is pivotal in the development of new antimicrobial drugs and to combat MDR strains of pathogens[109]. Pore formation and targeting intra-cellular components are two major modes of action that are widely studied. However, specific mechanism of agglutination of bacterial cells by antimicrobial peptides is still unclear. Mechanistically, it is likely that agglutinating antimicrobial peptides may contain multiple LPS/LTA binding sites necessary to interact with more than one bacterial cell at a time. Furthermore, one bacterial cell can bind to multiple agglutinating AMPs. This results in clumping of bacterial cells into big aggregates. A simplistic illustration of agglutination is shown in Figure 4.1.

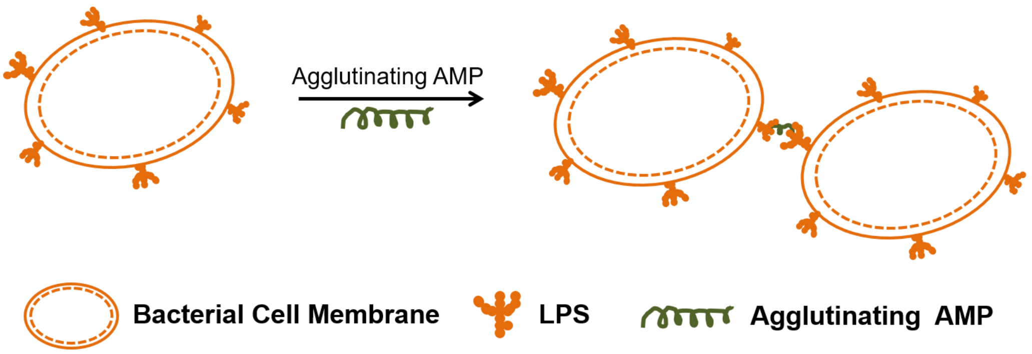

Figure 4.1| Agglutination Action by AMP. Multiple LPS binding sites in cell agglutinating AMPs allow agglutination.

A majority of the AMPs discovered have membranolytic mode of action. Studies on AMPs having an intracellular target have taken pace in the last decade[109]. However, very few antimicrobial peptides and protein are known to have agglutination as their primary mode of action. Comprehending their structural-function correlations and mechanism of LPS interaction could be the key to the development of new drugs with alternate mechanism of action.

GL-13, derived from PSP has a moderate bactericidal action. Instead, it agglutinates bacterial cells into larger aggregates, thereby increasing the chance of bacterial clearance by macrophages[102]. On treatment with human RNase 3/ECP, *E. coli* cells aggregate without damaging the cytoplasmic membrane. Cell death and global cell damage is observed at a later time point[103].

Hydramacin-1, derived from *Hydra* exerts its antimicrobial action by bacterial cell agglutination. Hydramacin-1 adopts a knottin fold consisting of a α-β motif stabilized by disulphide bonds (PDB ID: 2k35). It has a ring-like arrangement of cationic residues and two oppositely situated hydrophobic hemispherical patches. These hydrophobic hemispheres are sandwiched between two anionic membranes of different bacterial cells, thereby clumping the bacterial cells together[100]. The barnacle model illustrating the antimicrobial action of hydramacin-1 is elucidated in figure 4.2.

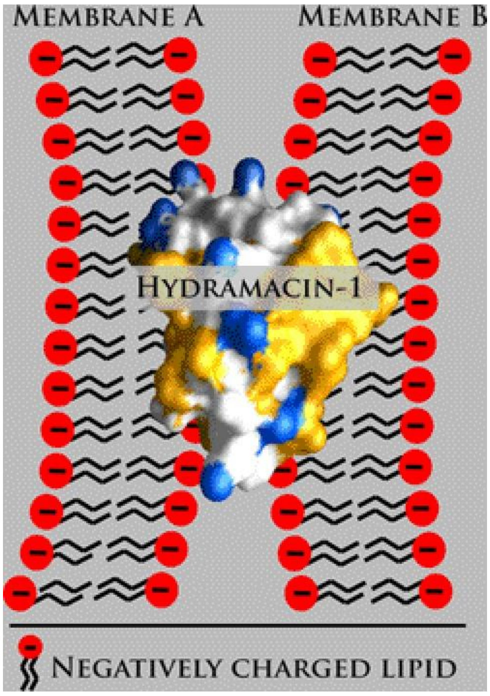

Figure 4.2| Mechanism of cell agglutination by hydramacin-1. Hydrophobic patches of hydramacin-1 (yellow) are sandwiched between two anionic membranes A & B. The cationic surface areas of hydramacin-1 are shown in blue.

Figure taken from ref.[100]

Another member of the macin family, neuromacin from leeches also shows bacterial cell aggregation. However, the mechanism of antimicrobial action for moth the macins is significantly different. Unlike hydramacin-1, neuromacin also demonstrates a pH dependent pore forming activity. The membrane permeabilization is mediated through the protonation and deprotonation of the four histidine residues which are absent in hydramacin-1. However, the pH dependent pore formation activity is moderate in comparison to a classical membrane permeabilizing AMP such as alamethicin. Hence, it can be assumed that neuromacin does not form stable pores and agglutination is the primary mechanism of its antimicrobial action[100].

Thanatin is a 21-residue inducible host defense peptide which is derived from the hemipteran insect *Podisus maculiventris*. The term thanatin is derived from 'Thanatos', which means death in Greek. Thanatin has a wide spectrum of antimicrobial action, including activity against Gram-negative and Gram-positive bacteria a well as fungi[74]. Minimum inhibitory concetration (MIC) values shown in table 4.1 illustrates that the peptide is highly potent against bacteria as well as fungi.

Table 4.1| Minimum Inhibitory Concentrations of thanatin. MICs are expressed as the interval a-b, where a is the highest test concentration at which bacterial cells are growing and b is the lowest test concentration at which there is 100% inhibition in bacterial growth. Table taken from ref.[74]

Micro-organism	MIC (μM)
Gram-positive bacteria	
A. viridans	0.6-1.2
M. luteus	1.2-2.5
B. megaterium	2.5-5
B. subtilis	2.5-5
P. acidolactici	20-40
Gram-negative bacteria	
E. coli D31	0.3-0.6
S. typhimurium	0.6-1.2
K. pneumoniae	0.6-1.2
E. cloacae	1.2-2.5
Fungi	
N.crassa	0.6-1.2
B.cinerea	1.2-2.5
N. haematococca	1.2-2.5
T. Viride	1.2-2.5
A. brassicola	2.5-5

The primary sequence of thanatin (GSKKPVPIIYCNRRTGKCQRM) is not homologous to other insect defense peptides. Rather, it is strikingly similar to brevinins, AMPs isolated from frog skin. Furthermore, in contrast to insect defensins, thanatin is not a pore-forming peptide. Instead, it first arrests the motility of bacterial cells which is followed by agglutination of the cells into large aggregates as observed by a decrease of light diffusion at 600 nm above a threshold concentration of thanatin (minimum agglutination concentration)[74]. To further understand the agglutination effect of thanatin, large unilamellar vesicles (LUVs) mimicking Gram-positive bacteria, Gram-negative bacteria and mammalian cells were prepared and their mean diameter was observed in absence and presence of 100 μM thanatin using dynamic light scattering technique[110]. In presence of thanatin, LUVs mimicking bacterial cells aggregated to particles few thousands nanometres large. However, in presence of 150 mM NaCl, these aggregates were significantly smaller (Figure 4.3), further corroborating the fact that aggregation is related to the antimicrobial activity of thanatin[110]. Moreover, no such change was observed in LUVs simulating mammalian cells which is consistent with the fact that no erythrocyte agglutination was observed for thanatin.

The structure of thanatin in free state was calculated at 278 K and pH 3.3 using NMR[111]. Thanatin adopts an anti-parallel β- sheet conformation at its C-terminus and a random coil structure at its N-teminus from residues Gly1 to Pro7. The two strands of β-sheet include residues from Ile8 to Asn12 and Lys17 to Met 21. The region is stabilized by a disulphide bond between residues Cys11-Cys18 and hydrogen bonds between residues Tyr10 – Gln19 and Asn12 – Lys17. The six-membered turn connecting the two strands has a standard $\beta\alpha\alpha\gamma\alpha_L\beta$ conformation which is stabilized by hydrogen bonds between residues Asn12 – Lys17, Asn12 – Thr15 and Arg13 – Gly16. There is a γ-turn at the N-terminus from Lys4 to Val6 which is stabilized by a bond C=O(4) – NH(6)[111]. The solution structure of thanatin is illustrated in the Figure 4.4.

In the present chapter, LPS/thanatin interactions have been elucidated by means of various techniques such as NMR, fluorescence spectroscopy and ITC. In order to gain insight on the specific mechanism underlying its agglutination activity,

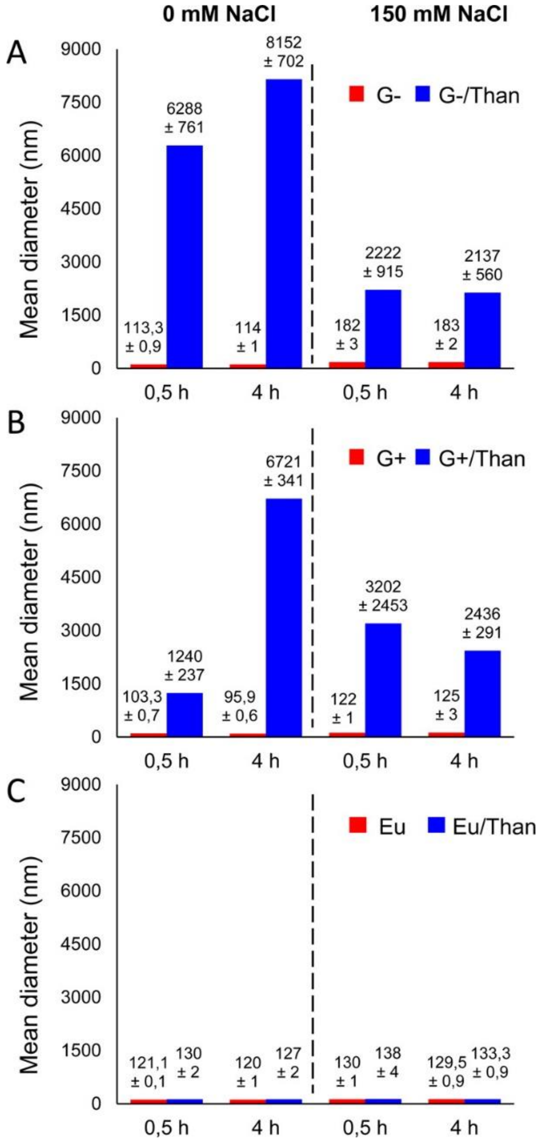

Figure 4.3| Thanatin agglutinates LUVs mimicking bacterial cells. G- model: LUVs were synthesized to mimic Gram-negative bacteria (POPE:POPG 7:3), G+ model: LUVs were synthesized to mimic Gram-positive bacteria (POPG:TOCL 6:4) and Eu model: LUVs were synthesized to mimic mammalian cells (POPC:Chol 8:2).
Figure taken from ref.[110]

the first atomic-resolution 3D structure of thanatin in complex with LPS has been determined and specific structural changes adopted by thanatin in presence of LPS have been delineated. The current chapter aims to provide a better comprehension of the structural requirements of the bacterial cell agglutinating antimicrobial peptides and insights on specific steps leading to cell agglutination by thanatin.

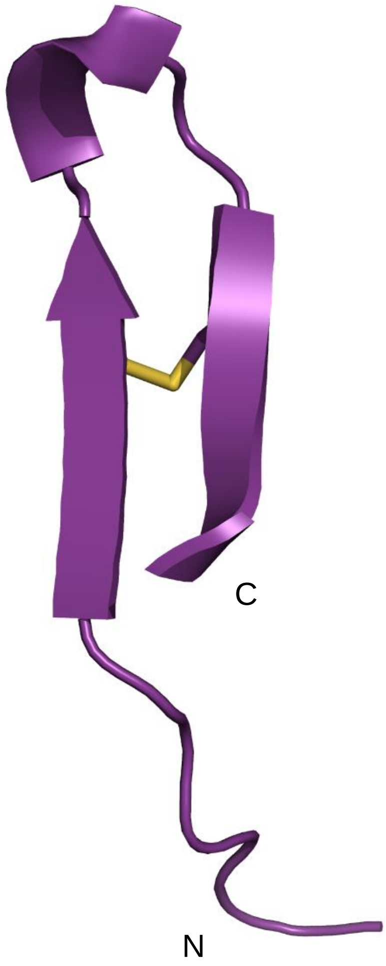

Figure 4.4| Structure of thanatin in free solution. Solution structure of thanatin in H_2O:D_2O 90:10 at 278 K, pH 3.3. Thanatin adopts a β-sheet conformation at its C-terminus with 7-residue long random coil at its N-terminus. Structure PDB ID: 8TFV.

4.2 Results

4.2.1 Minimum Inhibitory Concentration

Thanatin is a highly potent antimicrobial peptide with a wide spectrum of antimicrobial activity. MIC for thanatin was determined against four Gram-positive bacteria and four Gram-negative bacteria. Low MIC values, as illustrated by Table 4.2 underlines the high efficiency of thanatin in inhibiting the growth of bacterial cells.

Table 4.2| Antimicrobial activity of thanatin. Minimum inhibitory concentration (µM) of thanatin against EC: *Escherichia coli*; PA: *Pseudomonas aeruginosa*; SE: *Salmonella enterica*; KP: *Klebsiella pneumoniae*; SA: *Staphylococcus aureus*; BS: *Bacillus subtilis*; SP: *Streptococcus pyogenes*; EF: *Enterococcus faecalis*.

Peptide	**MIC (µM)**							
	Gram-Negative				**Gram-Positive**			
	EC	**PA**	**SE**	**KP**	**SA**	**BS**	**SP**	**EF**
Thanatin	0.5	1	1	1	1	2	0.5	0.5

4.2.2 Interactions of Thanatin and LPS by Fluorescence

Thanatin does not have an intrinsic fluorophore such as Trp. Therefore, N-terminal dansylated thanatin or dans-thanatin was used to examine its interaction with *E. coli* 0111:B4 LPS. The increase in intensity of the fluorescence emission spectrum and a concomitant blue shift in $\Delta\lambda_{max}$ (wavelength at maxima) on addition of increasing concentrations of LPS suggests that the fluorophore has been incorporated into the hydrophobic environment of LPS micelles.

The change in fluorescence intensity (ΔF) at λ_{max} was then plotted as a function of concentration of LPS. This plot was fitted with Hill’s equation to yield dissociation constant (K_d). The fluorescence emission spectra and Hill’s plot are shown in Figures 4.5 and 4.6 respectively. LPS/thanatin interactions are cooperative in nature with K_d of 8.6 µM and a Hill’s Coefficient of 2. This indicates that two molecules of LPS simultaneously bind to thanatin.

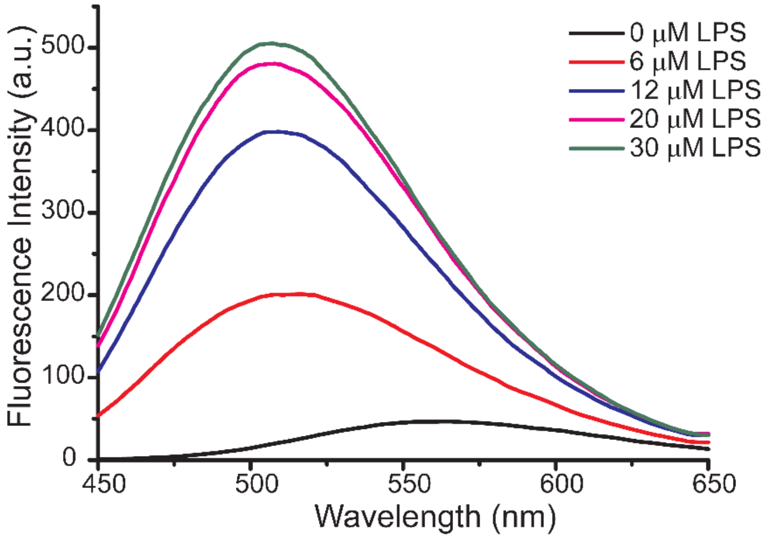

Figure 4.5| Fluorescence emission spectra of dans-thanatin. Increase in fluorescence intensity and blue shift of the emission maxima in presence of higher concentrations of LPS indicate a hydrophobic environment around the fluorophore.

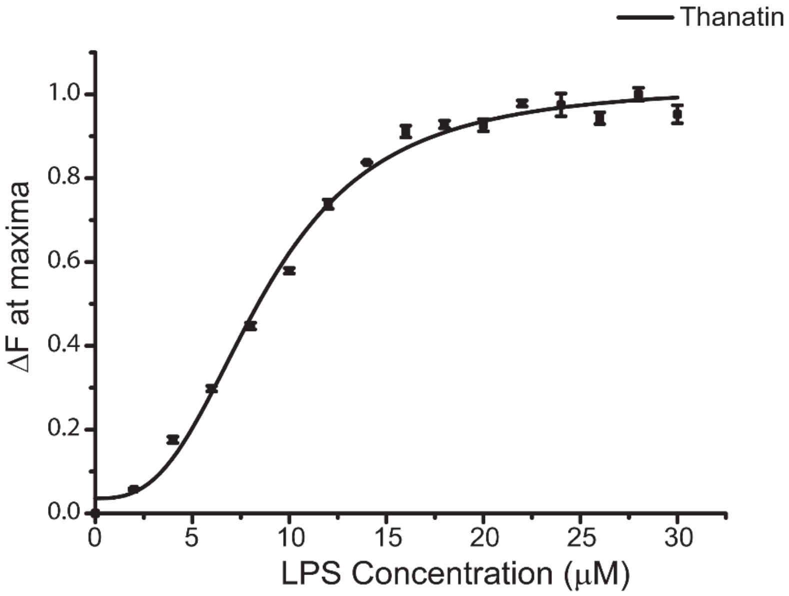

Figure 4.6| Hill's plot to calculate dissociation constant. Changes in fluorescence emission intensity of N-terminal dansylated thanatin in presence of varying concentrations of LPS reveal that thanatin/LPS interaction is cooperative in nature.

4.2.3 BODIPY- Cadaverine Displacement Assay

BODIPY-cadaverine (BC) is a fluorescent probe that binds to the lipid A domain of LPS through electrostatic interactions between cationic amid groups of the fluorescent probe and the anionic phosphate groups of lipid A. Effective dose 50 or ED_{50} is the concentration of the drug which replaces 50% of the fluorescent probe from lipid A. Hence, lower the ED_{50} value for a particular peptide, higher is its affinity to interact with LPS. Figure 4.7 demonstrates that thanatin binds more efficiently to LPS, with an estimated ED_{50} of 0.87 μM, as compared to polymyxin B, an archetype LPS binding peptide, displaying a higher ED_{50} of 3.7 μM.

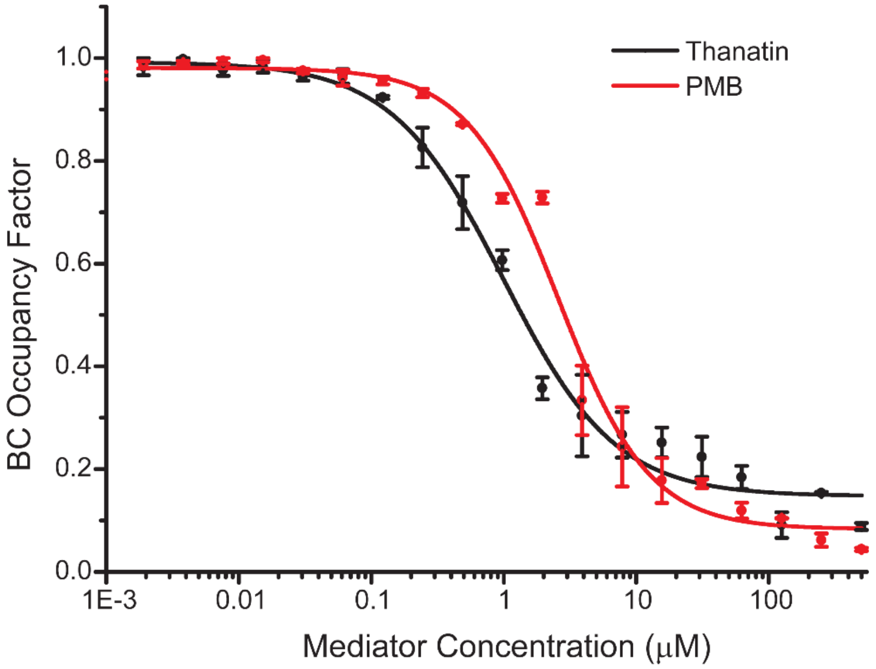

Figure 4.7| BC occupancy factor. Comparison of BC probe displacement by thanatin and PMB. A lower BC occupancy factor at a particular mediator concentration indicates a more efficient binding of the mediator to LPS.

4.2.4 Isothermal Titration Calorimetry

To further understand LPS/thanatin interactions, binding affinity and thermodynamic parameters were analysed using ITC. The downward position of the titration peaks and integrated heat values (Figure 4.8) suggest that LPS/thanatin interactions are exothermic in nature with enthalpy driven binding. ITC derived LPS/thanatin binding parameters are shown in Table 4.3.

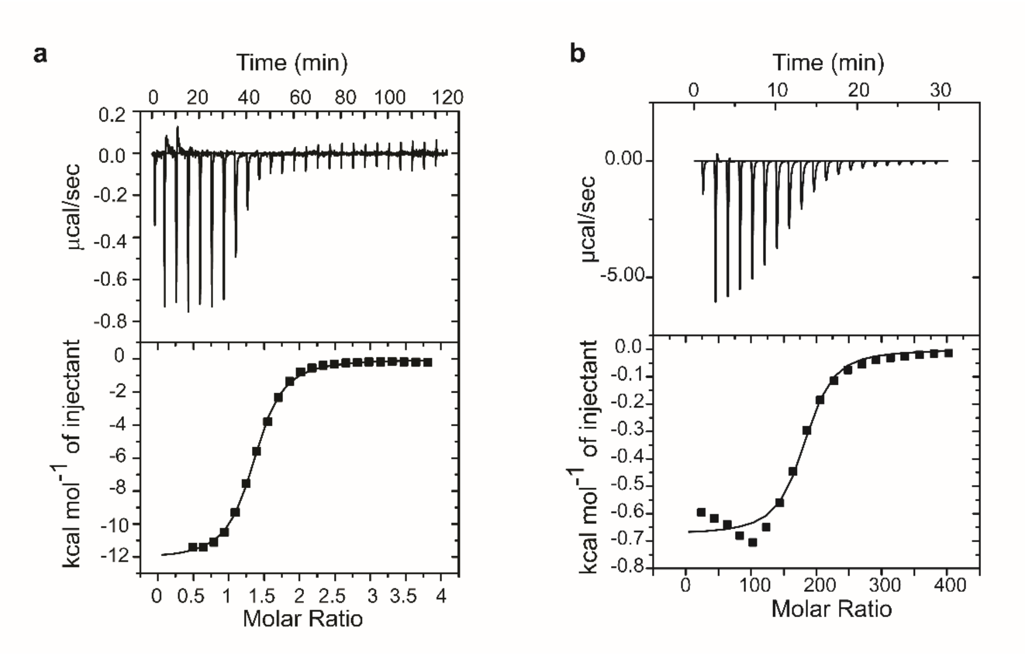

Figure 4.8| ITC thermogram. a, thanatin/LPS interaction and **b,** thanatin/DPC interaction. ITC data reveals that thanatin/LPS binding is exothermic in nature. Thanatin interacts much more strongly with LPS than DPC.

Table 4.3| Themodyamic parameters. ITC derived binding parameters of thanatin titrated against 50 μM LPS and 40 mM DPC in 10 mM phosphate buffer, pH 7.

	K_d (μM)	**ΔH (Kcal/mol)**	**TΔS (Kcal/mol)**	**ΔG (Kcal/mol)**
Thanatin/LPS	1.55	-12.16	-4.24	-7.92
Thanatin/DPC	52.08	-0.68	5.15	-5.83

High K_d values for thanatin/DPC interaction indicate that thanatin interacts with the zwitterionic DPC micelles much weakly than with LPS. As opposed to thanatin/LPS interaction, its interaction with DPC is entropy driven.

4.2.5 Zeta Potential Measurements

Surface charge neutralization of *E. coli* 0111:B4 in presence of increasing thanatin concentrations was studied by measuring its zeta potential. Anionic LPS-outer membrane leads to a negative zeta potential of the *E. coli* cells. On addition of increasing concentrations of cationic pore-forming AMPs, zeta potential would first neutralize and then further reach to a plateau at a higher positive value of ~ 5mV. Similarly, on addition of 5 μM of thanatin, the zeta potential dramatically increases from -50 mV to -5 mV. However, on further increasing concentrations of thanatin, the zeta potential reaches a plateau at ~ 0-1 mV (Figure 4.9). The data suggests that thanatin interacts with the bacterial cell membrane via electrostatic interactions. The zeta potential of the cells does not increase to a higher positive value in presence of high thanatin concentration, as in case of cationic pore forming antimicrobial peptides. However, thanatin is able to effectively neutralize the surface charge of the outer membrane of *E. coli* cells.

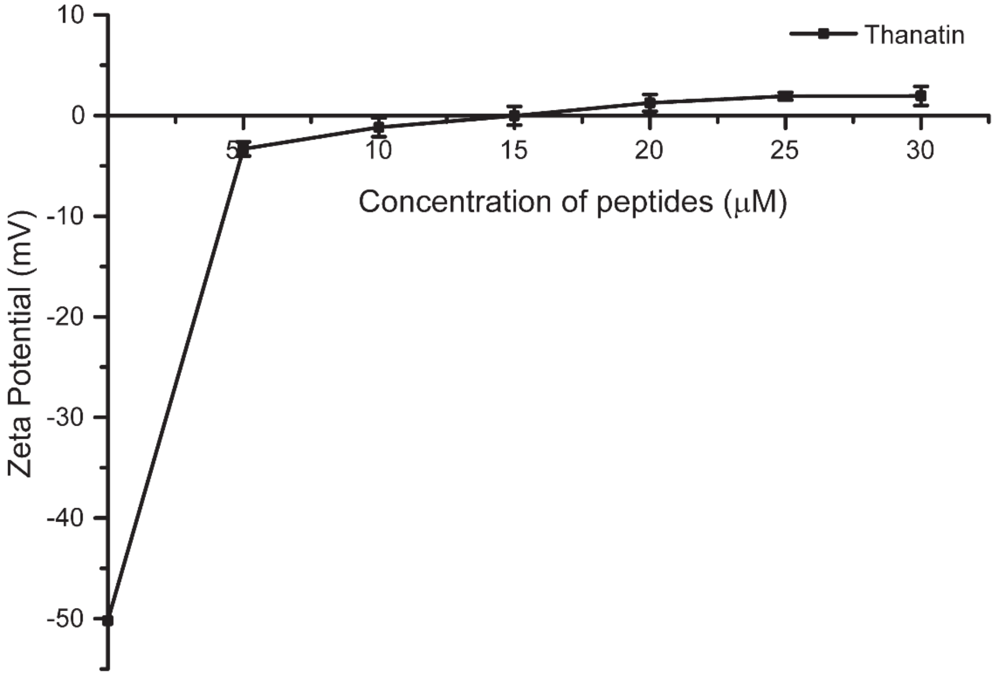

Figure 4.9| Zeta potential measurement. Thanatin neutralizes the zeta potential of mid-log phase *E. coli* cells indicating electrostatic interactions between thanatin and bacterial cell membrane

4.2.6 FITC-LPS Fluorescence Assay

In order to examine the structural changes in LPS micelles when in complex with thanatin, LPS labelled with FITC or FITC-LPS was examined in presence of varying concentrations of thanatin in fluorescence spectrometer. Dissociation of LPS micelles on binding with pore forming antimicrobial peptides results in FITC emission intensity. On the other hand, the emission intensity of FITC-LPS is quenched due to FRET among the fluorophore in an aggregated LPS micelle structure[112]. As can be observed from Figure 4.10, there is a significant quenching in emission intensity of FITC-LPS in presence of increasing thanatin concentrations. Such diminution in the fluorescence intensity of FITC-LPS in complex with thanatin suggests a higher degree of FRET amongst the fluorophore FITC. Hence, from the FITC-LPS fluorescence data it can be concluded that LPS micelles undergo a higher order of association upon binding with thanatin. The slight blue shift upon addition higher concentrations of thanatin indicate that the LPS micelles are interacting with thanatin.

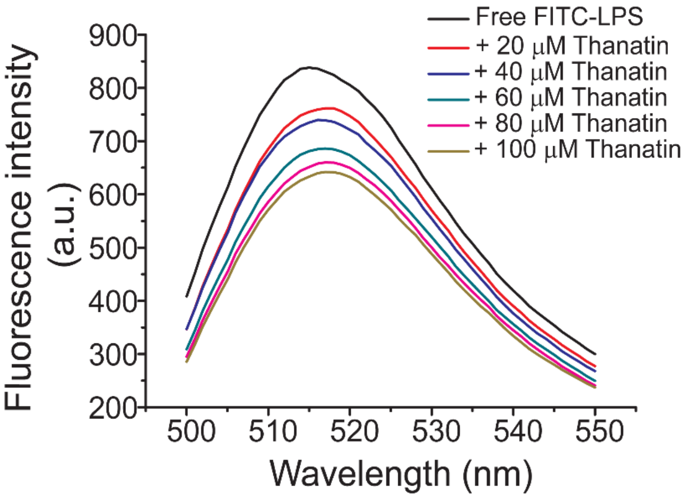

Figure 4.10| Emission intensity spectra of FITC-LPS. Unlike in presence of pore forming AMPs, emission intensity spectra of FITC-LPS demarcates a marked quenching in presence of increasing concentrations of thanatin.

4.2.7 Transmission Electron Microscopy

TEM images were done in presence and absence of 10 μM thanatin to directly visualize the effect of the agglutinating peptide on *E.coli* cells. Figure 4.11 clearly demonstrates that the bacterial cells agglutinate in presence of thanatin as opposed to free E. coli cells.

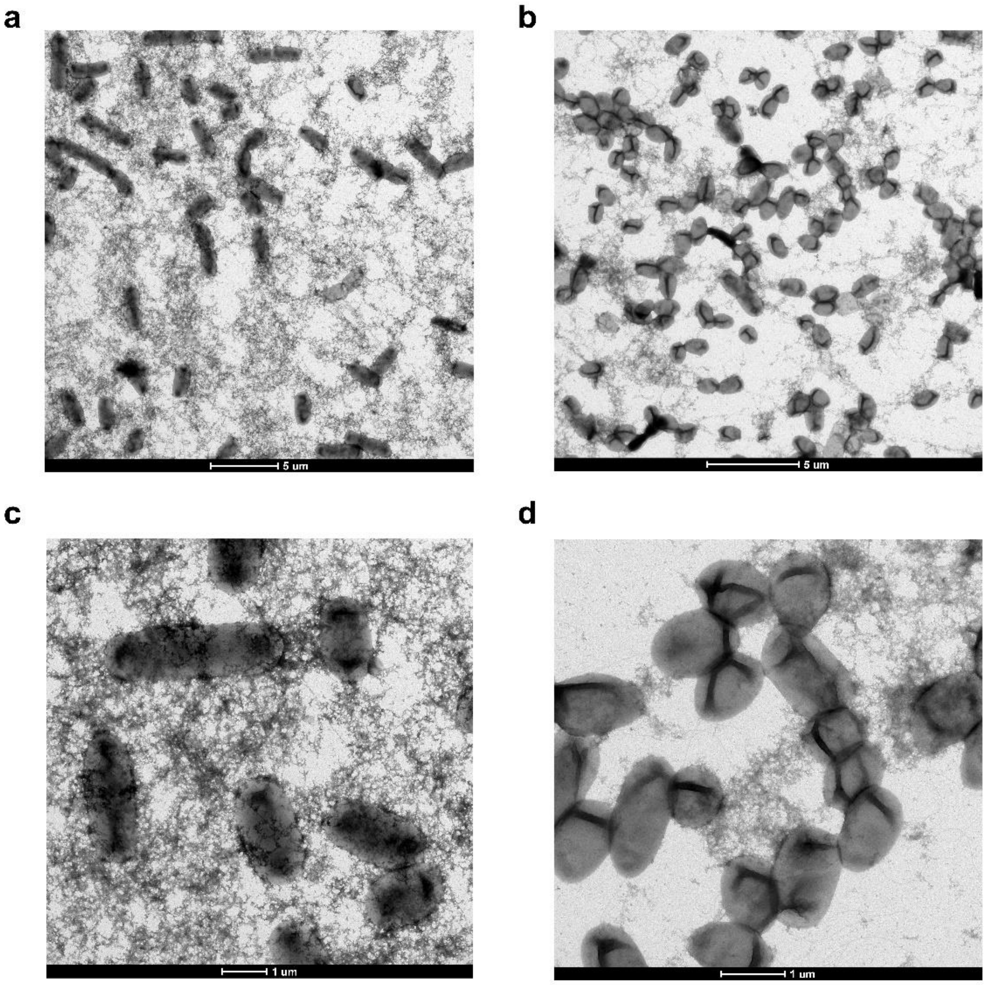

Figure 4.11| TEM images of *E.coli* cells. Bacterial cells as viewed under TEM in absence of (a,c) and in presence of thanatin (b,d).

4.2.8 ^{31}P NMR Spectroscopy of LPS

Perturbation of LPS micelle structure by thanatin was further examined by ^{31}P NMR experiments. ^{31}P NMR spectra of LPS were acquired in free solution and at three different molar ratios of LPS:thanatin, that is, 4:1, 2:1 and 1:1 (Figure 4.12). Free LPS micelles produce two well resolved NMR signal at ~ -1.00 ppm and -2 ppm, respectively[112]. As illustrated in the figure, both the phosphate groups demonstrate extensive line broadening and changes in chemical shifts when in complex with thanatin. This suggests involvement of the phosphate head groups in binding with thanatin. As evident, at higher concentration of thanatin, at 1:1 molar ratio, ^{31}P NMR signals of LPS appear to be extremely broadened. Such resonance broadening effect may potentially arise from slower tumbling motion of aggregated LPS micelles in complex with thanatin. Thus, the results indicate that LPS micelles undergo structural rearrangements and an association to larger LPS aggregates when in complex with thanatin.

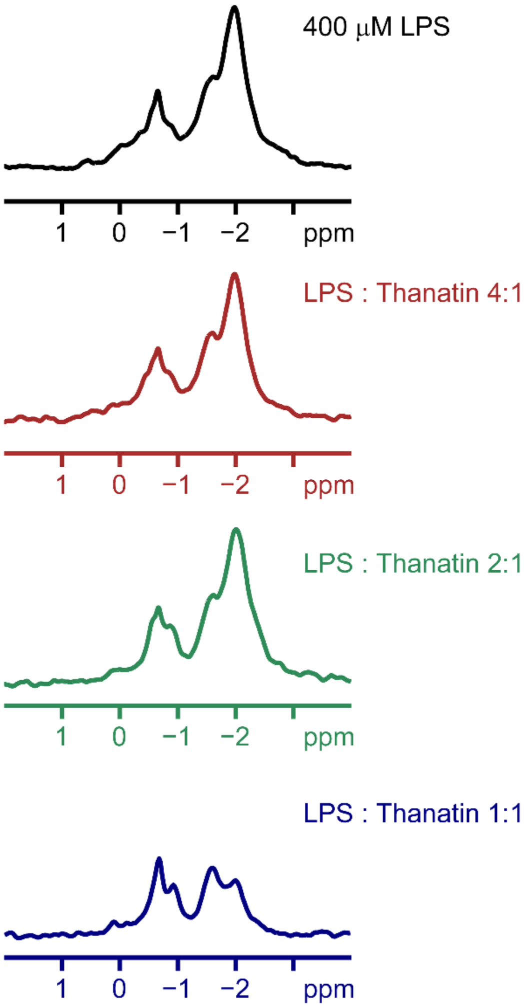

Figure 4.12| ^{31}P NMR spectra of LPS in complex with thanatin. Extensive line broadening and changes in chemical shift indicate interaction of mono- and di-phosphate groups with thanatin.

4.2.9 Saturation Transfer Difference (STD) NMR

STD-NMR method is used to map contact residues of ligands in complex with receptor molecules at atomic resolution, within a fast chemical exchange regime[113, 114]. STD-NMR has been utilized to determine contact residues of potent pore forming AMPs in LPS micelle[115, 116]. One-dimensional ^{1}H STD and two-dimensional ^{1}H-^{1}H STD-TOCSY experiments were carried out to identify residues of thanatin in contact with LPS micelle (Figures 4.13 & 4.15 respectively). Due to better resolution, two-dimension STD-TOCSY spectra were analysed and residues of thanatin in contact with LPS micelle were identified. Figure 4.15 illustrates STD-TOCSY spectrum of thanatin correlating CαH resonances with aliphatic sidechain resonances and sidechain/sidechain resonances. As reported in earlier works, resonances demonstrating cross-peaks in the STD-TOCSY spectra receive a high degree of saturation from the binding partners due to their close proximity[113, 114]. The STD-TOCSY spectrum of thanatin showed cross-peaks arising from CαHs to sidechains and among sidechain/sidechain resonances for a number of residues. STD-TOCSY correlations appear to be more intense among the sidechains resonances compared to that of backbone CαH to sidechain resonances, indicating closest proximity of sidechains to LPS micelle. In particular, conspicuous STD-TOCSY correlations could be detected for the basic residues including K3, K4, R13, R14, K17 and R20, indicating their proximity with LPS micelle. Residues P5, V6, P7 also delineated STD effect. Note, these N-terminal residues K3, K4, P5 and V6 have experienced large conformational change in complex with LPS micelle. The single aromatic residue Y10 displayed strong STD effect involving ring protons and CαH/CβH protons, indicating its association with LPS micelle (Figure 4.13 & 4.15 inset). The non-polar sidechains of residues I8, I9 and M21 remain in a close contact with LPS micelle as demonstrated by the strong STD-TOCSY correlations. Taken together, STD analyses suggest that most of the residues, including cationic, aromatic and non-polar, of thanatin are essentially embedded with LPS micelle. Figure 4.14 shows residues of thanatin demonstrating STD effects in complex with LPS. As can be seen, almost all of the residues of thanatin were found to be in contact with LPS outer membrane, suggesting intimate association of thanatin/LPS. In particular, sidechain proton resonances of a number of amino acids displayed strong STD effects compared to the backbone protons, signifying their closest proximity to LPS.

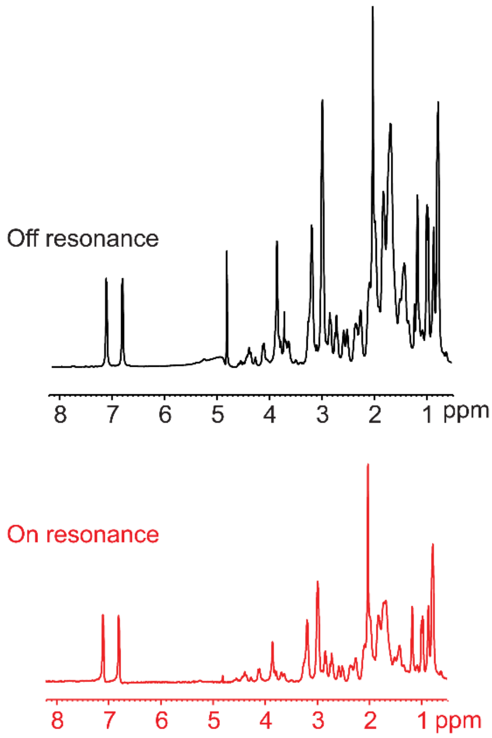

Figure 4.13| One-dimensional ^{1}H Saturation Transfer Difference NMR. STD of thanatin in presence of LPS at off resonance at 40 ppm and on resonance at -3 ppm.

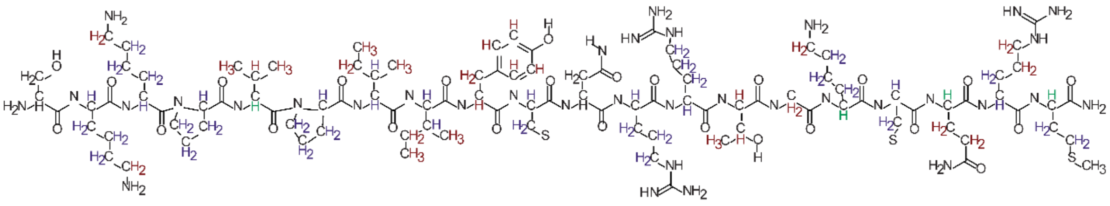

Figure 4.14| STD NMR experiment of thanatin in complex with LPS. A strong (red) or medium (blue) STD effect suggests that the proton is interacting more closely to LPS as compared to a weak (green) STD effect.

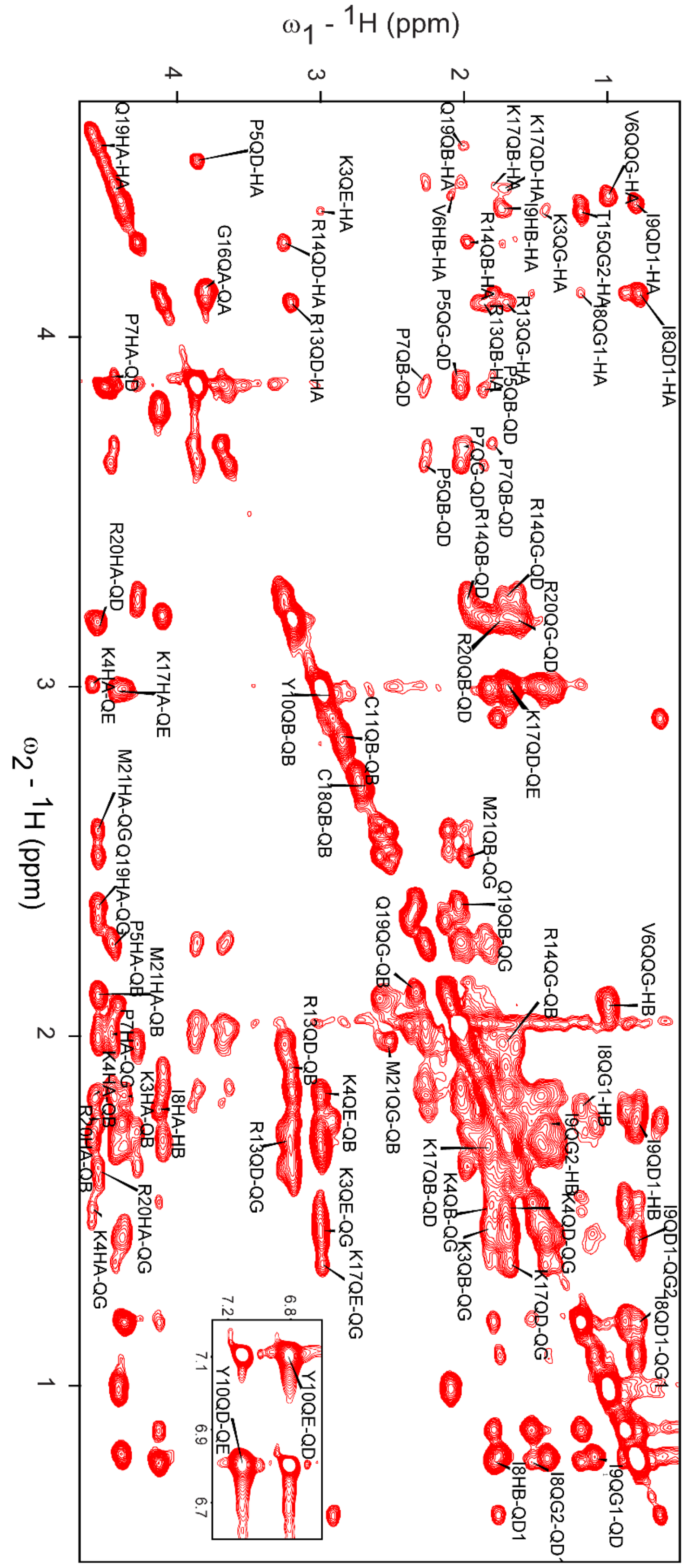

Figure 4.15| 2D STD NMR spectra of thanatin in complex with LPS. Two dimensional ^{1}H-^{1}H STD TOCSY spectra suggest that there is an intimate association of thanatin with LPS.

4.2.10 Structure of thanatin in free solution

3D structure of thanatin in free solution at 298K and pH 5 was determined using NMR. Two-dimensional ^{1}H-^{1}H TOCSY and NOESY spectra were analysed to determine the solution structure of thanatin at 298 K. Figures 4.16 and 4.17 illustrate NMR derived 3D structure of thanatin in aqueous solution and an ensemble of twenty energy minimized structures, respectively. The structure was determined based on 140 NOE driven distance constraints and dihedral angle constraints. Thanatin assumes an extended conformation for N-terminal residues G1-P7, followed by a beta hairpin like structure containing two stranded antiparallel β-strands comprising residues I8-N12 and residues K17-M21. The two antiparallel β-strands are connected by a loop consisting of residues R13-G16. The β-hairpin structure is stabilized by a single disulfide bond involving residues C11 and C18 (Figure 4.17). The 3-D structure of thanatin determined here at 25^{o}C is akin to the structure previously determined at 5^{o}C. A list of long range NOEs for β-hairpin structure is shown in Table 4.4.

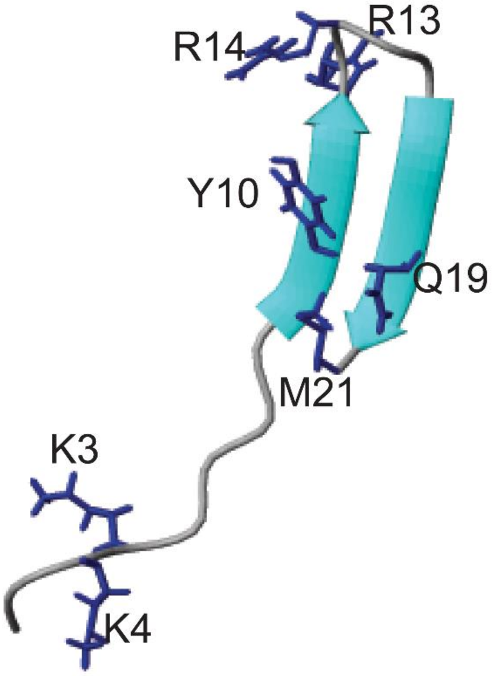

Figure 4.16| Representative structure of thanatin in aqueous solution. NMR derived 3D structure of free thanatin at 298K, pH 5. Thanatin assumes a β-hairpin structure with an extended coil at its N-terminus.

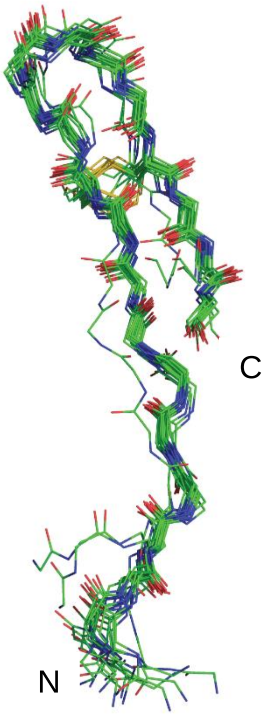

Figure 4.17| NMR derived structure of free thanatin. Superposition of backbone atoms of twenty lowest energy structures of thanatin in aqueous solution.

4.2.11 Thanatin structure in DPC micelles

Dodecylphosphocholine (DPC) detergent is a membrane mimic which is frequently used for NMR structural determination of AMPs in zwitterionic environment. 3D structure of thanatin in presence of DPC micelles was determined at 308 K and pH 5 by analysing two dimensional ^{1}H-^{1}H TOCSY and NOESY spectra. NMR derived 3D structure of thanatin in presence of DPC micelles and an ensemble of twenty energy minimized structures are shown in Figures 4.18 and 4.19. Thanatin assumes a β-hairpin conformation at its C-terminus and an extended coil structure at its N-terminus in presence of zwitterionic DPC micelles. This conformation is similar to the one adopted by thanatin in free solution. However, a lot more long range NOEs are visible between the two β-strands of thanatin in the ^{1}H-^{1}H NOESY spectrum of thanatin presence of DPC micelles (Table 4.4). Furthermore, αH chemical shift deviation illustrated in Figure 4.20 also suggests that thanatin has more β-sheet characteristics in presence of DPC micelles as opposed to in free solution.

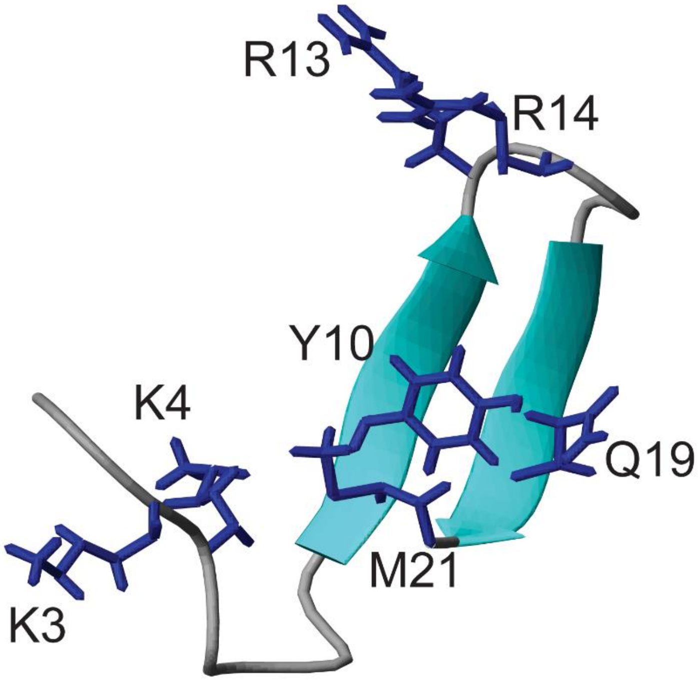

Figure 4.18| Representative structure of thanatin in presence of DPC micelles. Thanatin assumes a monomeric β-hairpin structure with an extended N-terminus in presence of zwitterionic DPC micelles at 308 K, pH 5.

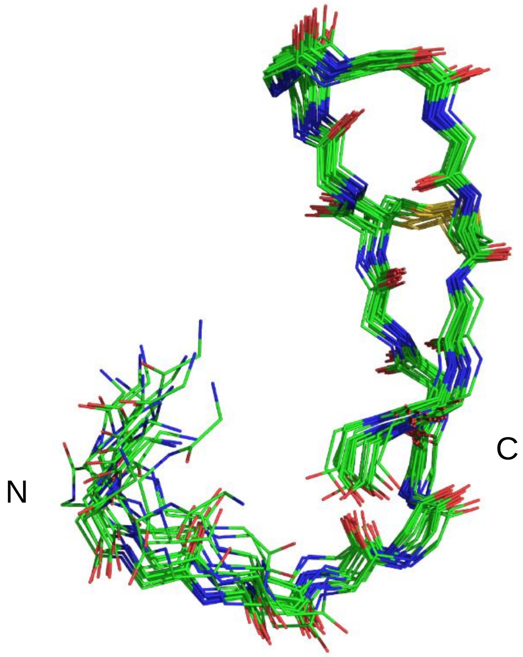

Figure 4.19| NMR derived structure of thanatin in presence of DPC. Superposition of backbone atoms of 20 lowest energy structures of thanatin in presence of zwitterionic DPC micelles.

Table 4.4| Long range connectivities of thanatin. A comparison of long range NOE connectivities observed in ^1H-^1H NOESY spectra of thanatin in free solution and thanatin in presence of DPC micelles. 14 long range connectivies were used to determine the 3D structure of free thanatin as opposed to 26 long range connectivities that were incorporated to calculate the structure of thanatin in presence of DPC micelles.

Free Thanatin	**Thanatin in presence of DPC**
21 MET QG – 10 TYR QD	19 GLN QB – 10 TYR H
19 GLN QG – 10 TYR QD	19 GLN QG – 10 TYR H
19 GLN QB – 10 TYR QD	19 GLN H – 10 TYR H
10 TYR HA – 19 GLN H	21 MET QG – 10 TYR H
20 ARG HA – 9 ILE H	19 GLN QB – 10 TYR QD
21 MET HA – 8 ILE H	19 GLN QG – 10 TYR QD
9 ILE QD1 – 20 ARG HE	21 MET QB – 10 TYR QD
18 CYSS HA – 11 CYSS H	21 MET QG – 10 TYR QD
18 CYSS HA – 12 ASN H	19 GLN QB – 10 TYR QE
18 CYSS QB – 12 ASN H	21 MET H – 10 TYR QE
11 CYSS HA – 19 GLN H	21 MET QB – 10 TYR QE
11 CYSS QB – 19 GLN H	18 CYSS HA – 11 CYSS H
12 ASN QB – 16 GLY H	18 CYSS HA – 12 ASN H
12 ASN QB – 17 LYS H	12 ASN QB – 16 GLY H
	12 ASN QB – 17 LYS H
	12 ASN H – 18 CYSS HA
	9 ILE QD1 – 18 CYSS H
	11 CYSS HA – 18 CYSS H
	9 ILE QD1 – 19 GLN H
	10 TYR H – 19 GLN H
	11 CYSS HA – 19 GLN H
	12 ASN H – 19 GLN H
	9 ILE QD1 – 20 ARG H
	8 ILE QD1 – 21 MET H
	10 TYR QD – 21 MET H
	10 TYR QE – 21 MET H

4.2.12 Paramagnetic Relaxation Enhancement

Interaction of thanatin with the DPC micelles was further studied by analyzing the resonance perturbation caused by the spin-labeled doxyl lipids, 5-doxyl stearic acid (5-DSA) and 16-doxyl stearic acid (16-DSA). Two dimensional ^1H-^1H TOCSY spectra was obtained in absence and in presence of 2 mM doxyl lipids

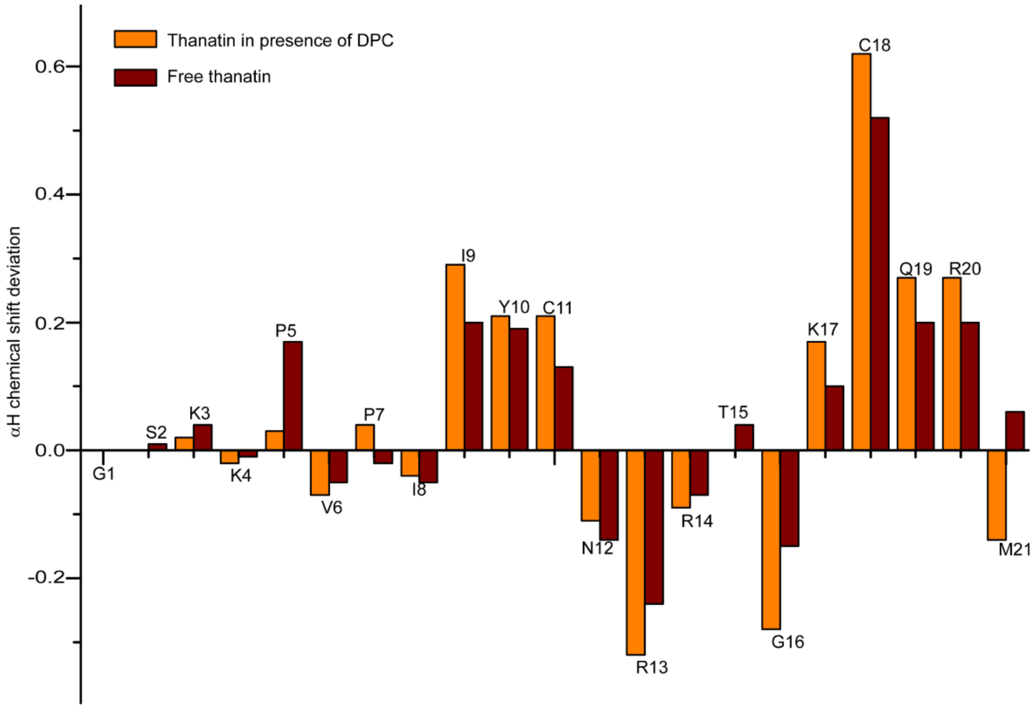

Figure 4.20| αH Chemical shift deviation. Thanatin has more β-sheet characteristic in presence of zwitterionic DPC micelles.

and the intensity changes in Hα/NH correlations (remaining amplitude) were estimated. For proline residues, Hα/Hδ correlations were considered. Figure 4.21 elucidates the remaining altitudes (RA) for each residue in presence of 5-DSA and 16-DSA. Most of the residues have high RA values in presence of both the doxyl lipids, suggesting that they are not localized on the micelle surface or in the hydrophobic core of the micelles. C11, R13 and C18 have low RA values in case of both 5-DSA and 16-DSA. Furthermore, Y10, K17 and Q19 have lower RA values for 16-DSA when compared to 5-DSA. Taken together, it can be suggested that these residues are localized in the hydrophobic region but above the micelle centre. Residues V6 and I8 are largely perturbed by 16-DSA. However, they have higher RA values in presence of 5-DSA. This indicates that these residues are interacting with the non-polar domain of DPC micelles. Henceforth, it can be concluded that thanatin has minimum interactions with the zwitterionic DPC micelle and it does not insert well into the hydrophobic core of the micelle. This further corroborates the high selectivity of thanatin towards anionic membranes.

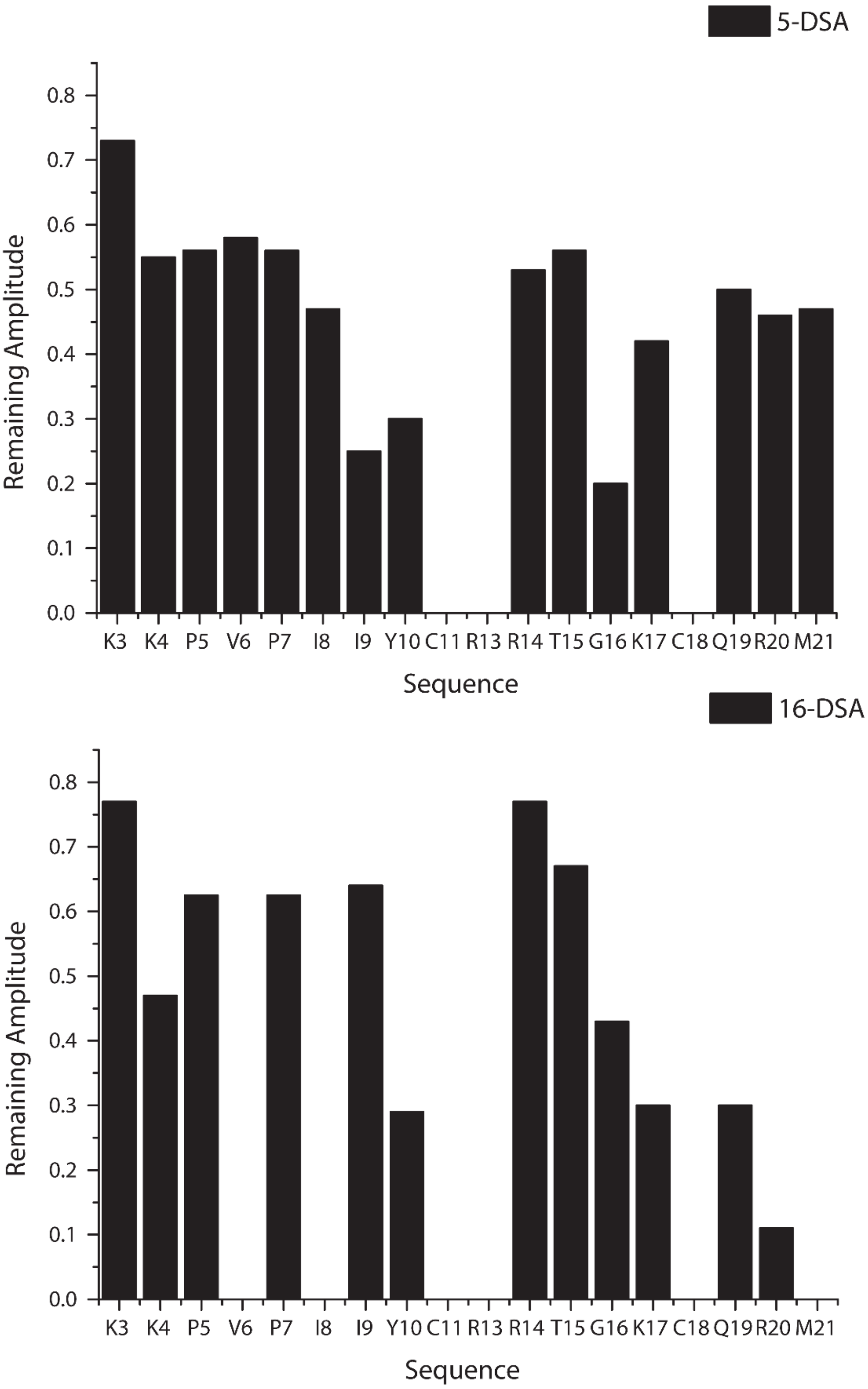

Figure 4.21| Paramagnetic relaxation enhancement. Resonance perturbations in two dimensional TOCSY spectrum of thanatin in presence of DPC micelles by spin-labelled doxyl lipids, 5-DSA and 16-DSA.

4.2.13 NMR Analyses of thanatin in LPS micelles

Transferred nuclear Overhauser effect spectroscopy (tr-NOESY) can be utilized to determine atomic-resolution structures of AMPs and LPS neutralizing peptides in presence of LPS micelle[117-119]. Owing to the low critical micelle concentration (<1 μM), LPS readily forms micelles in solution of high molecular weight[120]. AMPs undergoing fast chemical exchange between free and LPS bound states yield tr-NOEs permitting determination of bound conformations[117-119]. Binding induced resonance perturbation of thanatin in one-dimensional NMR spectra suggests that there is a fast chemical exchange (Figure 4.22). Two-dimensional tr-NOESY spectra of thanatin in presence of LPS micelle has yielded more number of NOE connectivity in comparison to thanatin in free solution involving sidechain/sidechain and backbone/sidechain resonances (Figure 4.23).

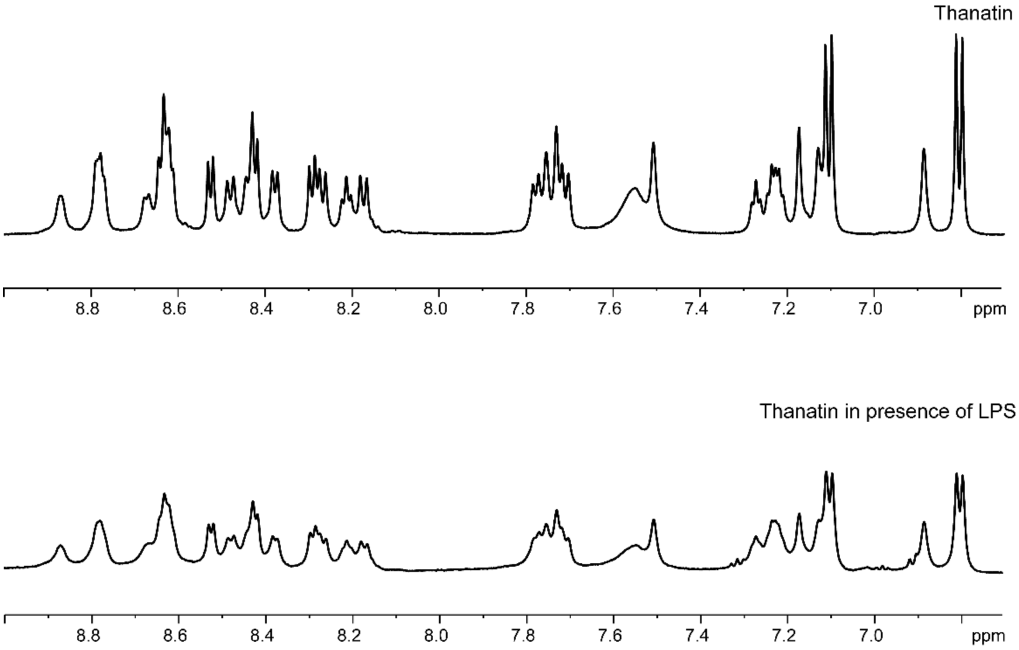

Figure 4.22| 1D NMR spectra of thanatin in presence of LPS micelles. One dimensional NMR spectra of 0.4 mM thanatin in free solution and 0.4 mM thanatin in presence of 30 μM LPS at 298 K, pH 5. Resonance perturbation in presence of LPS indicates a fast chemical exchange.

Moreover, there are several new long range NOEs detected for residues, V6, I8, Y10, R14, K17 of thanatin in LPS micelles (Figure 4.24). Notably, residue Y10 has demonstrated as many as ~40 NOEs in complex with LPS micelle (Figure 4.24). Interestingly, a number of unique long-range NOEs are detected among residues e.g. V6/C11, I8/N12, I8/R13, I8/R14 while analysing the NOESY spectra of thanatin in complex with LPS (Table 4.5, Figure 4.25). These NOEs indicate that there is a close proximity among residues at the extended N-terminus and residues at the β-turn of the β-sheet structure of thanatin.

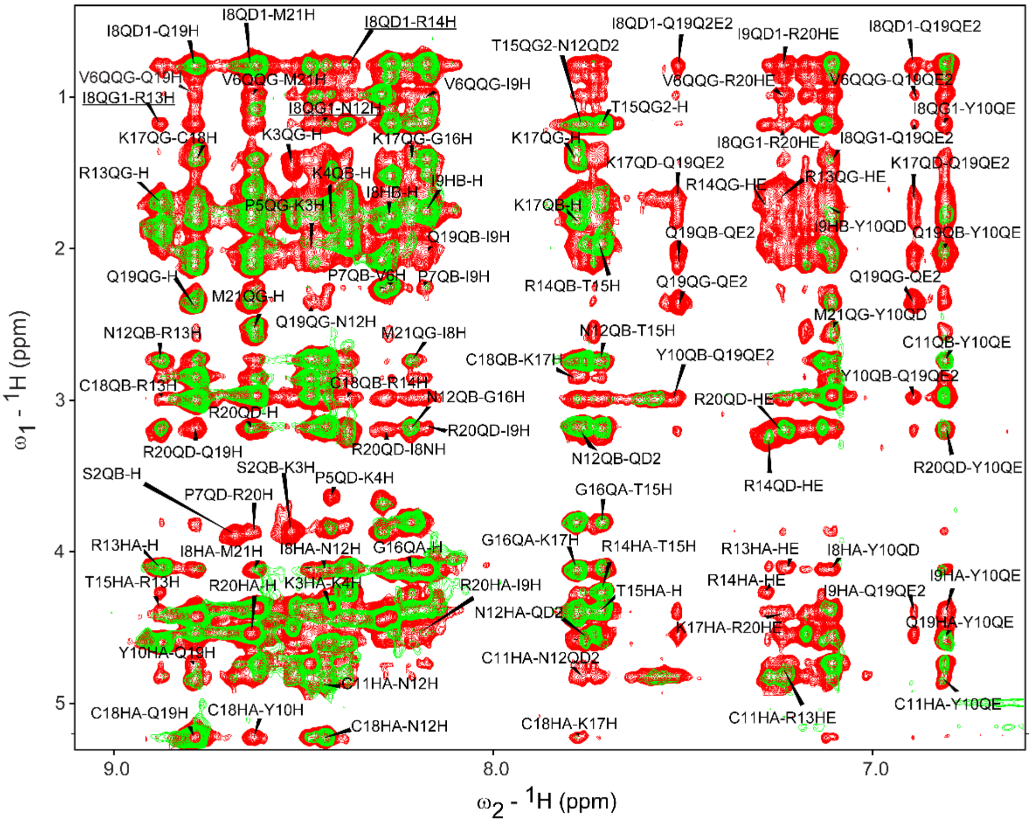

Figure 4.23| Tr-NOESY: Thanatin in presence of LPS. Two dimensional tr-NOESY spectrum of thanatin in presence of LPS (red) has more long range NOE connectivities as compared to two dimensional NOESY spectrum of free thanatin (green). Furthermore, certain unique NOE cross peaks (underlined) which are present only in tr-NOESY spectrum of thanatin/LPS complex are incompatible to the β-hairpin structure of monomeric thanatin and are used as inter-monomeric NOEs for structure determination.

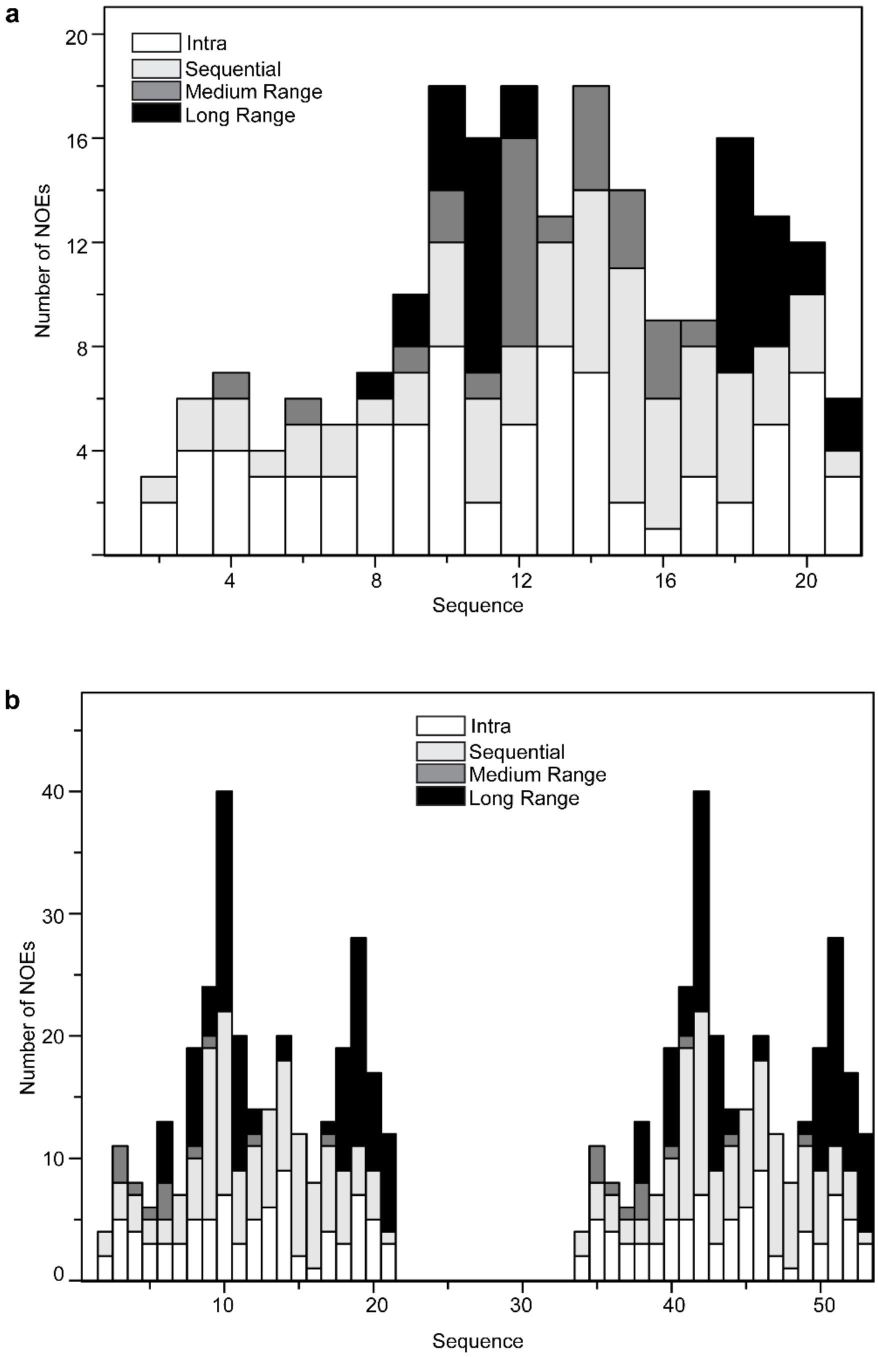

Figure 4.24| No. of NOE connectivities per residue. Bar diagrams showing number and type of NOE constraints for a, free thanatin and b, thanatin in presence of LPS. Thanatin/LPS complex has a lot more long range NOE constraints than free thanatin.

Table 4.5| Inter-monomer long range NOEs for thanatin dimer. A list of long range NOEs that were deemed incompatible with the monomeric structure and were further used as inter-monomeric NOEs for structure calculation.

Thanatin dimer in complex with LPS
6 VAL QQG – 11 CYS’ H
14 ARG H – 8 ILE’ QD1
6 VAL QQG – 11 CYS’ H
8 ILE QD1 – 13 ARG’ H
8 ILE QD1 – 12 ASN’ H
6 VAL’ QQG – 11 CYS H
14 ARG’ H – 8 ILE QD1
6 VAL’ QQG – 11 CYS H
8 ILE’ QD1 – 13 ARG H
8 ILE’ QD1 – 12 ASN H

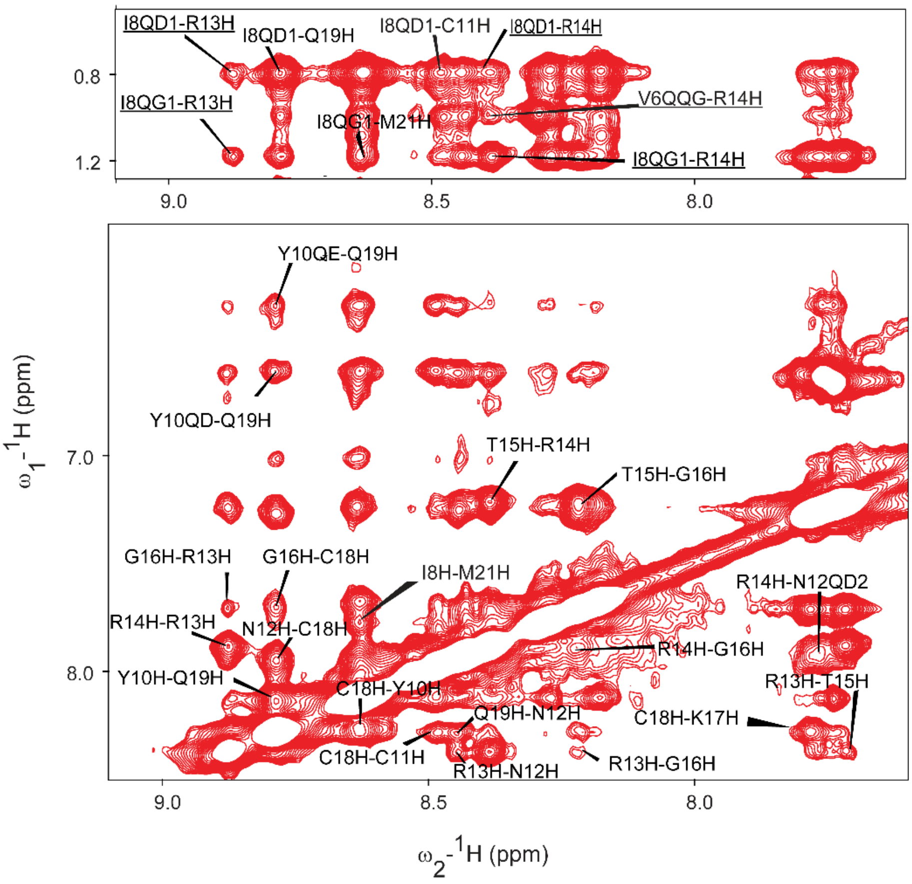

Figure 4.25| Two dimensional NOESY spectra of thanatin in presence of LPS. Underlined NOEs are incompatible with the monomer structure and is incorporated while determining the structure of thanatin dimer.

4.2.14 Three-dimensional structure of thanatin in LPS micelle

Figure 4.26 shows superposition of backbone atoms (Cα, N and C') of twenty low energy structures of dimeric thanatin in complex with LPS. NOE driven distance constrains for residues V6/C11, I8/N12, I8/R13, I8/R14 (Table 4.5) were found to be incompatible to a monomeric β-sheet structure and were utilized as inter-monomeric or dimeric NOEs for structure determination. The ensemble of dimeric structures of thanatin was determined utilizing 386 NOE driven distance constrains including 78 long range and 10 inter subunit NOEs. The structural statistics and RMSDs are provided in Table 4.6.

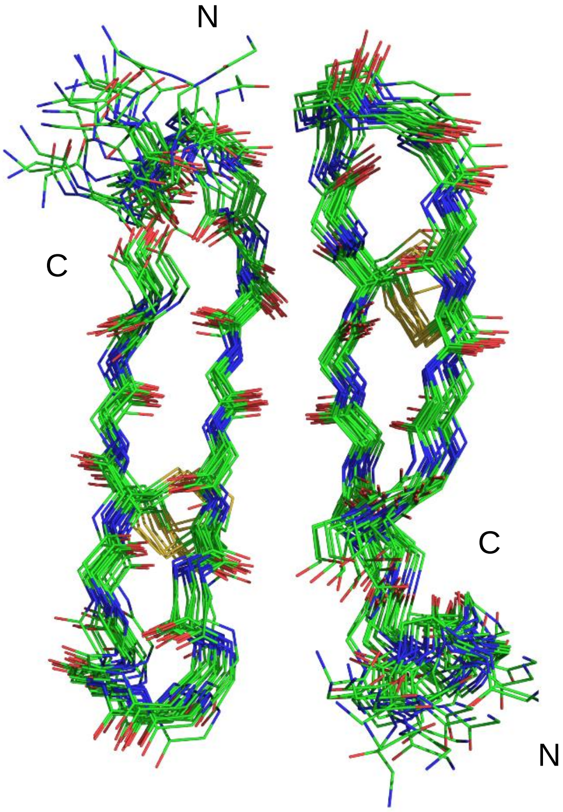

Figure 4.26| 3D structure of thanatin in presence of LPS. Superposition of backbone atoms of lowest energy dimeric structure of thanatin in complex with LPS. The long N-terminus regions of the two monomers are oriented in an anti-parallel fashion to each other.

Table 4.6| Structural statistics. A summary of structural statistics for free thanatin, thanatin in presence of zwitterionic DPC micelles and thanatin dimer in presence of anionic LPS micelles.

	Thanatin	**Thanatin in presence of DPC**	**Thanatin in presence of LPS**
Distance constraints			
Sequential [|i-j|= 1]	33	52	118
Medium range [1 <|i-j|< 4]	11	12	8
Long range [|i-j|≥ 4]	14	26	78
Inter monomer	-	-	10
Total	140	158	386
Dihedral-angle constraints	32	32	64
Deviation from mean structure (Å)			
All backbone atoms	0.66	0.77	1.42
All heavy atoms	1.16	1.29	1.93
Ramachandran plot for the mean structure (%residues)			
Most favoured region	87.5	68.8	75
Additional allowed region	12.5	31.2	25
Generously allowed region	0	0	0
Disallowed region	0	0	0

The 3-D structure of dimeric thanatin in complex with LPS revealed a four stranded β-sheet topology, whereby the residues at the long N-terminal region (residues 1-13) of the two monomers are engaged in a non-covalent interface in an antiparallel fashion. The two subunits of the dimer sustained close packing interactions between sidechains of aromatic and hydrophobic residues, Y10/Y10', M21/M21' and Q19/Q19' (Figure 4.27). Further, a number of cationic residues, namely R13, R14 at the β-turn region and K3 and K4 at the N-terminus, in the dimeric structure of thanatin are situated in spatially proximal orientation (Figure 4.27).

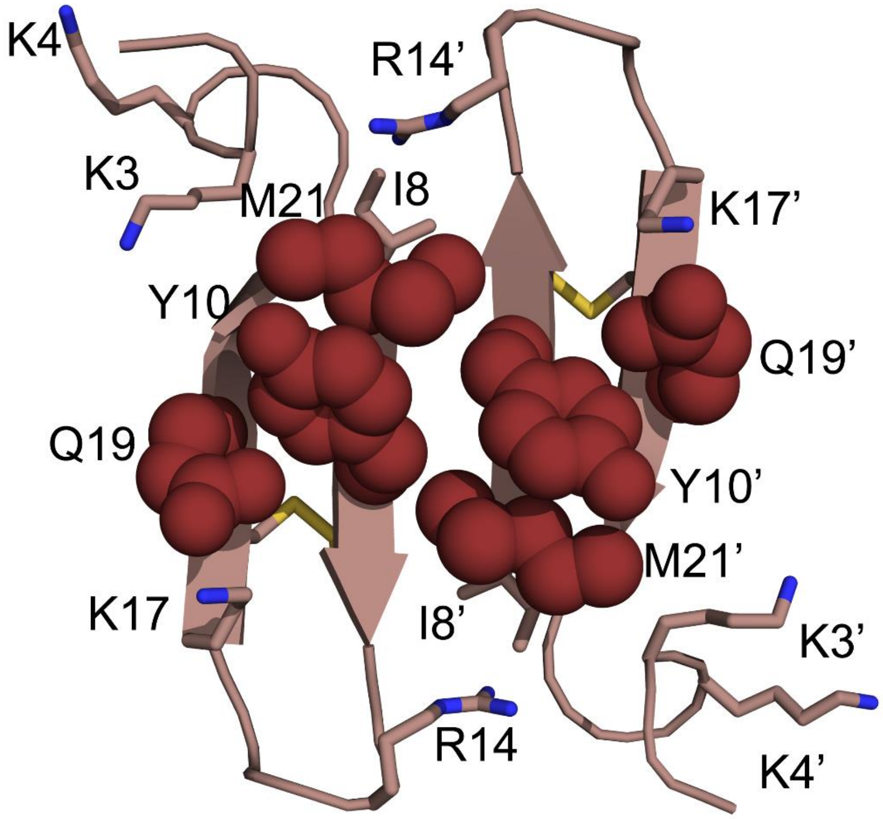

Figure 4.27| Thanatin dimerizes in presence of LPS. Hydrophobic and aromatic residues in each subunit of the dimer interact closely with each other.

The superposition of structures of free thanatin and in complex with LPS (for one of the subunit) is illustrated in figure 4.28. As seen, there are significant differences between the LPS bound structure and free structure of thanatin both in backbone and sidechain dispositions. The RMSD values for backbone atoms and all heavy atoms were estimated to be 5.1 Å and 6.2 Å, respectively. Strikingly, in complex with LPS micelle, the cationic N-terminal segment, residues G1-P7, of thanatin acquires a define conformation and folds back towards the β-hairpin structure. In particular, residues K^3KPV^6 adopt a β-turn conformation centring residues K4 and P5 at i+1 and i+2 positions, respectively, with a potential hydrogen bond between C=O of residue K3 and N-H of residue V6 (Figure 4.29).

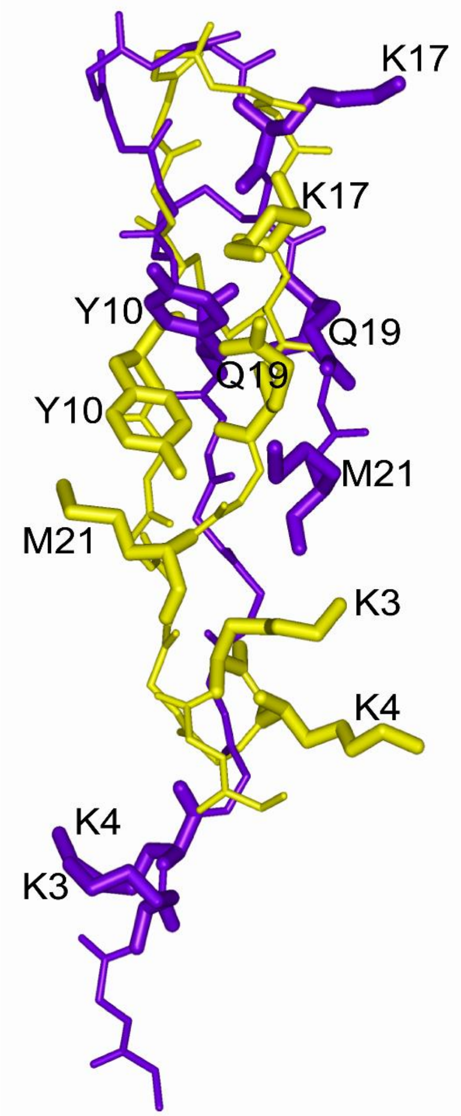

Figure 4.28| A comparison of thanatin structures in free solution and in presence of LPS. Superposition of one sub-unit of thanatin dimer in presence of LPS (yellow) and thanatin monomer in free solution (violet) with an RMSD of 5.1 Å for backbone atoms and 6.2 Å for heavy atoms.

The electrostatic potential surfaces of dimeric and monomeric thanatin are shown in Figure 4.30. The dimeric structure of thanatin in LPS demonstrates large cationic patches at the distal ends and an extended non-polar surface at the centre of the four stranded β-sheet. Therefore, in comparison to the monomeric structure, the dimeric structure of thanatin possesses higher cationicity and hydrophobicity.

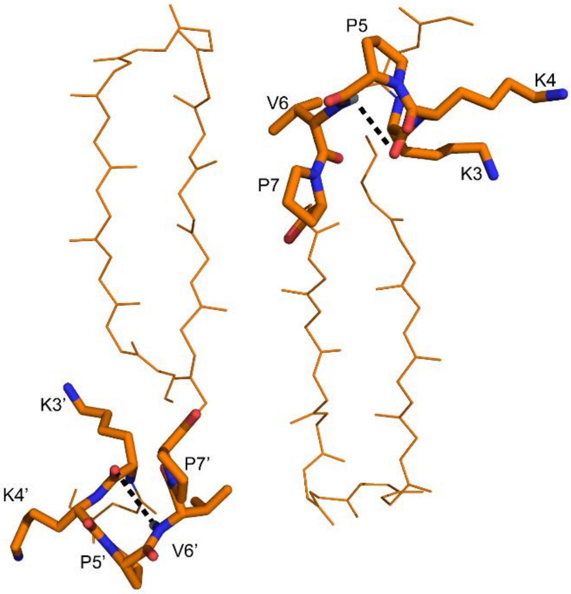

Figure 4.29| N-terminus of thanatin in presence of LPS. N-terminal segment of thanatin folds back toward the β-hairpin structure to adopt a β-turn conformation centring residues K4 and P5 at i+1 and i+2 positions with a potential H-bond between C=O of the residue K3 and N-H of the residue V6.

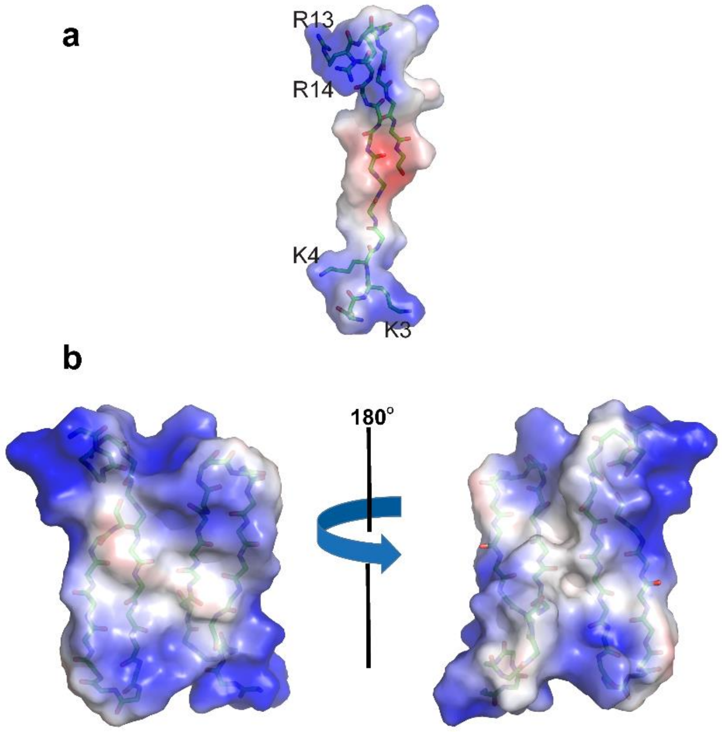

Figure 4.30| Electrostatic surface potential of **a,** free thanatin and **b,** thanatin dimer in presence of LPS. Large cationic patches at the distal ends of thanatin dimer interact with the negatively charged LPS. Therefore, in contrast to the monomer, each thanatin dimer can interact with more than one bacterial cell which is critical for agglutination.

4.2.15 Docking thanatin dimer in LPS micelles

Energy calculations were performed in Discover module of Insight II (Biosym). Constraints were set between cationic residues of thanatin (K3, K4, R20, K17, R13 & R14) and anionic phosphate groups in LPS unit. It is interesting to note that the distance between R13/R14 from one sub-unit and K3/K4/R20 from the other sub-unit is around 10-15 Å. This distance is similar to the distance between two phosphate groups in LPS unit. Moreover, the distance between K17 and R20 from one sub-unit is also around 16 Å. Therefore, the aforementioned residue pairs might serve as the perfect binding pockets for the LPS unit. Dielectric constant was set to 30. To start, initial constraints were set between one binding pocket and one unit of LPS. The system was then subjected to Steepest Descent energy minimization. In order to release the initial model from bad contacts, Conjugated energy minimization was further used. Similarly, energy minimization was done for other binding pockets. Figure 4.31 elucidates plausible LPS binding sites in thanatin dimer.

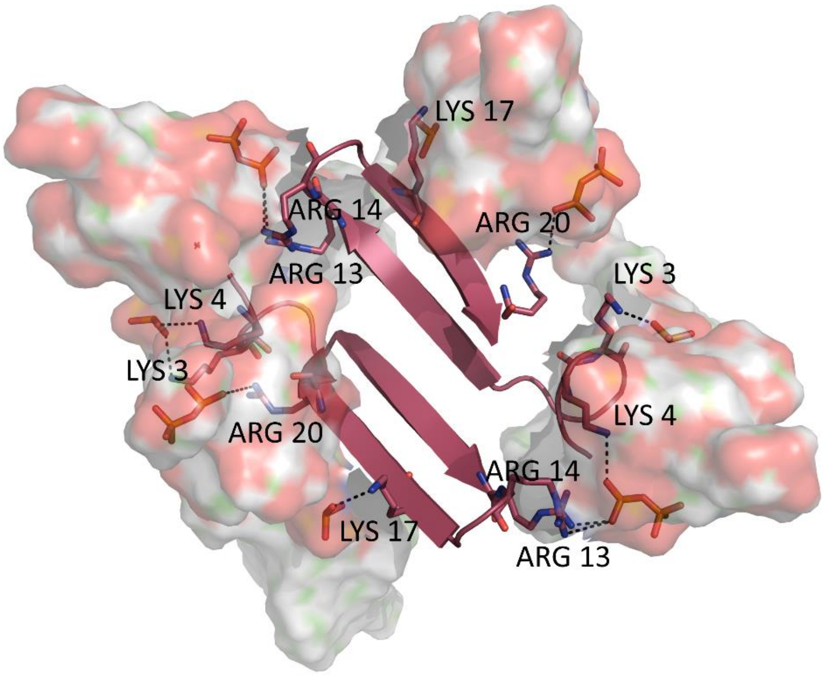

Figure 4.31| Docked model of thanatin/LPS complex. Multiple possible binding sites in thanatin dimer facilitates agglutination.

4.3 Discussion

The outer member LPS in Gram-negative bacteria acts as a permeability barrier against bactericidal agents and thus, plays an important role in its survival[121]. Sometimes following the treatment for bacterial infection, free LPS attaches to a circulating LPS binding protein causing septic shock in humans and other animals[122]. Currently, there are no drugs of therapeutic modality against sepsis or septic shock[123]. LPS being a strong inflammatory molecule, is also associated with other diseases[124]. Therefore, atomic-resolution structures and interaction analyses of AMPs in complex with LPS would not only yield mechanistic insights on bacterial outer membrane disruption, but structural scaffolds can be utilized for the generation of antibiotics and endotoxin neutralization drugs. Towards this, 3D structures of several pore forming AMPs in complex with LPS have been reported in past and recent years[112, 115, 116]. Opposed to pore formation which requires AMPs to disrupt inner membrane, bacterial cell agglutinating AMPs target outer membrane components. Bacterial cell killing by agglutination has been reported for a number of antimicrobial peptides, proteins and recently for amyloid-β peptides[101-103, 111]. However, the mechanism of cell agglutination is yet to be elucidated. One of the key steps in cell agglutination of Gram-negative bacteria is the binding of AMPs with the outer membrane LPS. In order to glean knowledge in agglutination process, we have determined the first 3D structure of a host defence cell agglutinating AMP, thanatin, in complex with LPS micelle and investigated its interactions. Biophysical and optical spectroscopic studies demonstrated characteristic interactions and helped in estimating thanatin-LPS binding parameters. Dansyl fluorescence emission of dans-thanatin indicated potential inclusion of thanatin into a non-polar environment of LPS micelles (Figures 4.5 and 4.6). On the other hand, enthalpy driven binding interactions suggested that LPS-thanatin complex may be stabilized by ionic and/or hydrogen bonding (Figure 4.8, Table 4.3). Whereas, negative entropy change appears to suggest more ordering of the LPS-thanatin complex (Table 4.3). Furthermore, thanatin mediated efficient release of BC probe from LPS (Figure 4.7) and *E. coli* surface charge neutralization (Figure 4.9) indicated predominant ionic interactions with the lipid A head groups and outer membrane LPS, respectively. STD-NMR analyses demonstrated that thanatin is intimately associated with LPS micelle utilizing many of the cationic and non-polar and aromatic residues

(Figure 4.15). Further, interaction of thanatin with LPS micelle yielded changes in LPS micellar structure as observed from ^{31}P NMR (Figure 4.12) and FITC-LPS fluorescence studies (Figure 4.10). Such interactions and complex formation between LPS-thanatin would contribute to the outer membrane binding and cell agglutination process.

In order to better correlate, atomic resolution structures of thanatin are determined in free solution and in complex with LPS micelle. Free thanatin assumed a β-hairpin structure for the central sequence (residues I8-M21) along with an N-terminal extended region (Figures 4.16 and 4.17). Thanatin in presence of zwitterionic DPC micelles also adopted a similar conformation (Figures 4.18 and 4.19). By contrast, thanatin in complex with anionic LPS micelles demonstrated a higher order structural assembly of a dimeric four stranded β sheet (Figures 4.26 and 4.27). Notably, 3D structures of pore forming β-sheet antimicrobial peptides determined in complex with LPS reveal monomeric topology for β-sheet AMPs. This conformation may be necessary for outer membrane permeabilization. As seen, the dimeric structure of thanatin has resulted in close proximity of the N-terminal β-strand of one subunit and C-terminal β-strand of another subunit in antiparallel manner (Figure 4.28). Hydrophobic and aromatic residues Y10 (Y10') and M21 (M21') are found to be engaged in close packing interactions across the two β-strands in the dimeric structure of thanatin (Figure 4.27). These hydrophobic residues and potentially their mutual packing interactions appear to be important for the antibacterial activity and LPS interactions. The basic residues K3, K4, R13, R14, K17 and R20 belonging to the cationic patches are found to be primarily involved in LPS recognition (Figures 4.30 and 4.31).

The atomic-resolution structure of thanatin solved in complex with LPS micelles thus provides mechanistic insights on bacterial cell agglutination. Clearly, the antiparallel topology of the dimeric structure of thanatin allows binding of another LPS at the distal end (Figure 4.31). The dimeric structure of thanatin can bind to multiple LPS molecules and enable bacterial cells proximity in a carpet mode. Further, surface charge neutralization and perturbation of LPS outer membrane integrity may perhaps facilitate cell-cell associations and agglutinations. Taken together, the atomic resolution structures and mode of interactions of thanatin presented in this work can be potentially used for further development of novel cell agglutinating antimicrobial agents.

Chapter 5

Structure – Functional Analyses of Thanatin Mutants in Presence of LPS

In this chapter, various gain-in and loss-in function mutations of thanatin are analysed. Improved aromatic-aromatic stacking interactions in the β-sheet of the gain-in function mutant, thanatin M21F leads to an enhanced antimicrobial activity. Interestingly, the inactive mutant, thanatin R13R14AA adopts a dimeric conformation in presence of LPS. This suggest that thanatin has an intrinsic tendency to form a multi stranded β-sheet structure in complex with LPS. MD simulation studies in LPS-DPPE bilayer demonstrate that the dimeric thanatin interact with multiple LPS molecules at a time. Finally, an illustrative model of thanatin interacting with various bacterial cells demonstrates the mechanism of agglutination.

5.1 Introduction

Natural AMPs are host defense peptides that play a key role in combating invading pathogens. These AMPs are extremely diverse in terms of amino acid composition, 3D structure, net charge, hydrophobicity and mechanism of action[65]. Most AMPs adopt a defined conformation in presence of a hydrophobic membrane environment. Cationic AMPs interact with anionic bacterial cell membrane electrostatically and hydrophobically. However, in order to clearly understand the mechanism of antimicrobial action, it is pivotal to comprehend the structure-activity correlation for these AMPs[109]. Modifying certain amino acids in order to alter their 3D conformation, hydrophobicity and net charge is an effective means to understand their mode of antimicrobial action. For instance, replacing critical amino acids of an AMP with their D-enantiomers would shed some light on the role of stereospecificity in the mechanism while combating pathogens. Pore formation is a non-stereospecific mechanism. Hence, both natural pore forming AMP and its D form would be equally active. However, if an AMP targets intra-cellular components where only its L-isomer can interact with the target, replacing the critical amino acids with their D-form would completely inhibit the antimicrobial action[74]. Furthermore, numerous studies have been conducted on the modification of natural AMPs either to improve their activity or to gain insight on their mechanism of action[74].

Protegrin without a disulphide bond is inactive against HSV. On the other hand, addition of a disulphide bond in CP-11 derivative of indolicin, made it more stable against protease activity but with no difference in its antimicrobial activity[125, 126]. Amidation of the carboxyl end of PAMP-23 makes it orient perpendicularly instead of parallelly to the bacterial membrane. This modification increased its cellular uptake by ten folds, led to faster interaction with Gram-negative bacterial cell membrane and deeper insertion into the inner membrane[127]. Incorporation of an unnatural amino acid β-didehydrophenylalanine is used to improve the conformational stability of the AMPs. Its incorporation in the primary sequence of VSI imparted a higher stability against proteases[128].

Modifying AMPs by altering one or more residues is also an effective strategy to identify critical residues important for antimicrobial activity and to understand the physiological characteristics that play an important role in the activity and target spectrum of the AMP. LL-37 or human cathelicidin was modified by replacing neutral amino acids Gln and Asn with cationic Arg residues. The new mutant peptide (named P60.4) is used successfully in nasal applications against MRSA[129].

Furthermore, deleting residues from C/N-terminus of an AMP or replacing certain residues in its primary sequence with Ala and analysing the changes in its structure and in its interaction with bacterial cell membrane is also a well followed strategy to determine its structure-activity correlation. A lot of modifications have been made in thanatin in an attempt to understand its mechanism and to further improve its activity. In one study, two cysteine residues were chemically modified with tert-butyl group (C11tBu/C18tBu)[130]. This mutant lacked the ability to form disulphide bonds. However, the stability of the loop was compensated by strong hydrophobic interaction between the modified cysteine residues. This chemically modified thanatin mutant exhibited a four-fold higher activity against *M. luteus*. However, its activity decreased considerably against *E. coli*[130]. This implies that the disulphide bond in thanatin is dispensible for its activity against *M. luteus*. In another study, T15 in thanatin was replaced by serine. This mutant (s-thanatin) exhibited LPS neutralizing properties and reduced plasma endotoxin levels[131]. It was also found to restore the susceptibility of resistant bacteria to common antibiotics *in vivo*. Another mutant R-thanatin (IYNCRRRFCKQR) was synthesized and evaluated for antimicrobial efficacy. It exhibited low toxicity, good stability in plasma and a high efficacy in inhibiting biofilm formation in MRSE-caused urinary tract infection[132].

Various truncated forms of thanatin were synthesized and their activities were tested against fungi, Gram-positive and Gram-negative bacteria[74]. These truncated isoforms of thanatin, their sequence and relative activities are illustrated in Table 5.1. As seen, 21-residue long thanatin is required for antifungal activity. However, the absence of the first three N-terminus residues (K18M) does not have any effect on its antibacterial activity. The antibacterial activity is halved after removing first five N-terminus residues (V16M). Furthermore, if the next two residues are also truncated (I14M), activity against Gram-negative bacteria decreases dramatically with no further effect on the activity against Gram-positive bacteria. Finally, the absence of three C-terminus residues decreases the overall antimicrobial activity to a large extent. Hence, it can be concluded that the C-terminus residues and the N-terminus residues from the fourth amino acid (K18M) is important for effective antibacterial activity. However, all the N-terminus residues are necessary for full antifungal activity of thanatin[74].

Table 5.1| Antimicrobial activities of thanatin derivatives. Relative activities of truncated isoforms of thanatin, taking the percentage activity of wild type thanatin as 100%. Table taken from ref.[74]

Peptide	Amino acid sequence	*A.viridans* & *M.luteus*	*E. coli* D31 & *E. coli* D22	*N.crassa*
Thanatin	GSKKPVPIIYCNRRTGKCQRM	100	100	100
I11C	IIYCNRRTGKC	0.5	0	0
Y12M	YCNRRTGKCQRM	3	0	0
G18C	GSKKPVPIIYCNRRTGKC	25	0	5
I14M	IIYCNRRTGKCQRM	50	15	3
V16M	VPIIYCNRRTGKCQRM	50	50	5
K18M	KPVPIIYCNRRTGKCQRM	100	100	25

Aforementioned studies suggest that the stability of the β-sheet at the C-terminus is an important factor contributing to its antimicrobial activity. Furthermore, in the previous chapter, we have hypothesized that the two Arg residues present in the β-turn play a critical role in interacting with LPS micelles. In the current chapter various thanatin mutants were designed based on the following factors:

Stability of the anti-parallel β-sheet:

Gain-in-function mutation: Designed to improve the hydrophobic packing in the β-sheet between Tyr10 and Phe21

Thanatin M21F – GSKKPVPIIVCNRRTGKCQRF

Loss-in-function mutation: Designed to decrease the stability of the β-sheet by disrupting the hydrophobic packing.

Thanatin Y10M21AA – GSKKPVPIIACNRRTGKCQRA

Replacing the cationic residues in the β-turn with Ala to gain an insight on its structure-activity correlation:

Loss-in-function mutations:

Thanatin R13A – GSKKPVPIIYCNARTGKCQRM

Thanatin R14A – GSKKPVPIIYCNRATGKCQRM

Thanatin R13R14AA – GSKKPVPIIYCNAATGKCQRM

Atomic resolution 3D structures of these mutant peptides were determined in presence and absence of LPS. Their Antimicrobial activities were studied against four Gram-positive and four Gram-negative bacteria. Finally, various biophysical characterizations were performed to elucidate the role of critical residues and stability of the β-sheet on its interaction with LPS.

5.2 Results

5.2.1 Structure of free thanatin M21F

3D structure of thanatin M21F was determined in free solution at 298 K and pH 5 using NMR spectroscopy. SPARKY was used to analyse the two dimensional ^{1}H-^{1}H TOCSY and NOESY spectra. 2D NOESY spectra of free thanatin M21F is shown in Figure 5.1. Structure was determined based on 152 NOE driven distance constraints and 32 dihedral angle constraints. NMR derived 3D structure of thanatin M21F in aqueous solution and an ensemble of 20 energy minimized structures are illustrated in Figures 5.2 and 5.3, respectively. Like free thanatin, thanatin M21F also assumes a β-hairpin structure with an extended seven residue long N-terminus. The two anti-parallel β-strands comprising residues I8 to N12 and K17 to F21 are connected by a loop consisting of residues R13 to G16. The disulphide bond present between C11 and C18 and strong hydrophobic interactions between Y10 and F21 further stabilizes the β-hairpin structure. A summary of structural statistics is shown in Table 5.6.

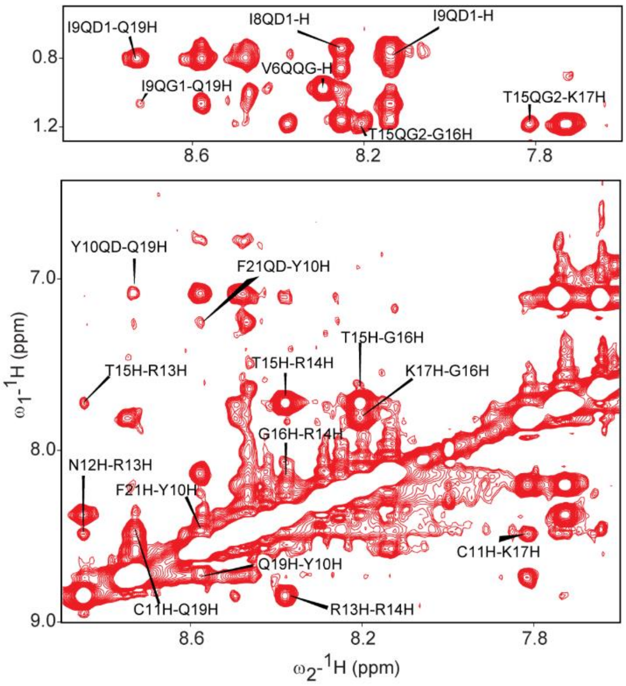

Figure 5.1| 2D ^{1}H-^{1}H NOESY spectra of free thanatin M21F. Long range NOEs between I9/Q19, Y10/Q19, C11/K17 and F21/Y10 are critical for determination of β-hairpin structure.

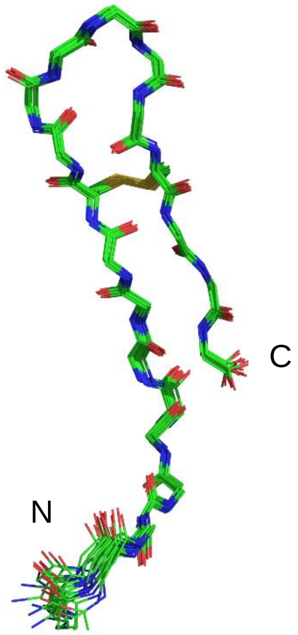

Figure 5.2| Representative structure of free thanatin M21F in aqueous solution. NMR derived 3D structure of free thanatinM21F at 298 K, pH 5. Strong hydrophobic interaction between Y10 and F21 further increases the β-sheet characteristic in thanatin M21F.

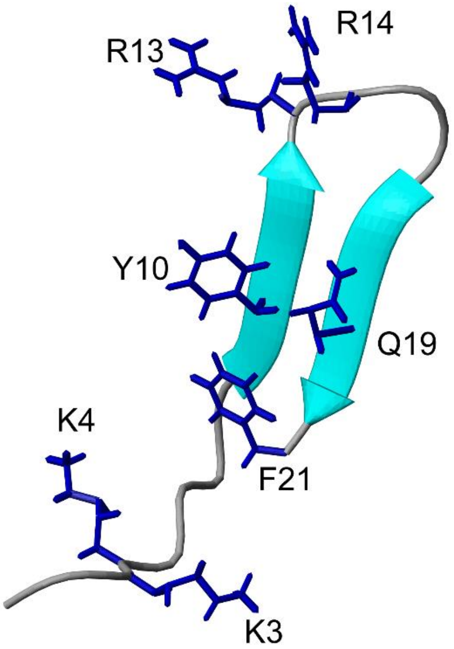

Figure 5.3| NMR derived structure of free thanatin M21F. Superposition of backbone atoms of 20 lowest energy structures of thanatin M21F in aqueous solution.

5.2.2 Structure of thanatin M21F in presence of LPS

Transferred nuclear Overhauser effect spectroscopy (tr-NOESY) was analysed to determine atomic-resolution 3D structure of thanatin M21F in presence of LPS. The 2D ^{1}H-^{1}H tr-NOESY spectra of thanatin M21F in presence of LPS has more long range and sidechain/sidechain NOE connectivities (Figure 5.4) when compared to free thanatin M21F (Figure 5.1). Figure 5.5 illustrates number of NOE constraints per residue for both thanatin M21F in free solution and in presence of LPS. Furthermore, in comparison to thanatin, the number of NOE connectivities of the last residue in thanatin M21F has increased because of enhanced aromatic stacking interactions between Y10 and M21F. A number of unique long range NOEs were detected (Figure 5.4, Table 5.2) in the tr-NOESY spectra which were found to be incompatible with the monomeric structure and were incorporated as intermonomer NOEs to determine the structure of thanatin M21F in presence of LPS. Furthermore, 368 NOE driven distance constrains, including 78 long range NOEs were utilized to in structure determination. Ensemble of 20 energy minimized structure is illustrated in Figure 5.6. Thanatin M21F in presence of LPS has adopted a dimeric conformation wherein the long N-terminal region of the two monomers are oriented in anti-parallel fashion.

Figure 5.7 elucidates the hydrophobic interaction present in the two sub-units wherein F21 and F21’ showed enhanced close aromatic-aromatic stacking interactions with residues Y10 and Y10’. Such aromatic interactions are known to be involved in LPS interactions and results in superior antimicrobial activity. Furthermore, a number of cationic residues in the dimeric structure of thanatin M21F, namely R13 and R14 present in the β-turn of one sub-unit and K3, K4 present at the N-terminus of the other sub-unit are situated in spatially proximal orientation (Figure 5.7).

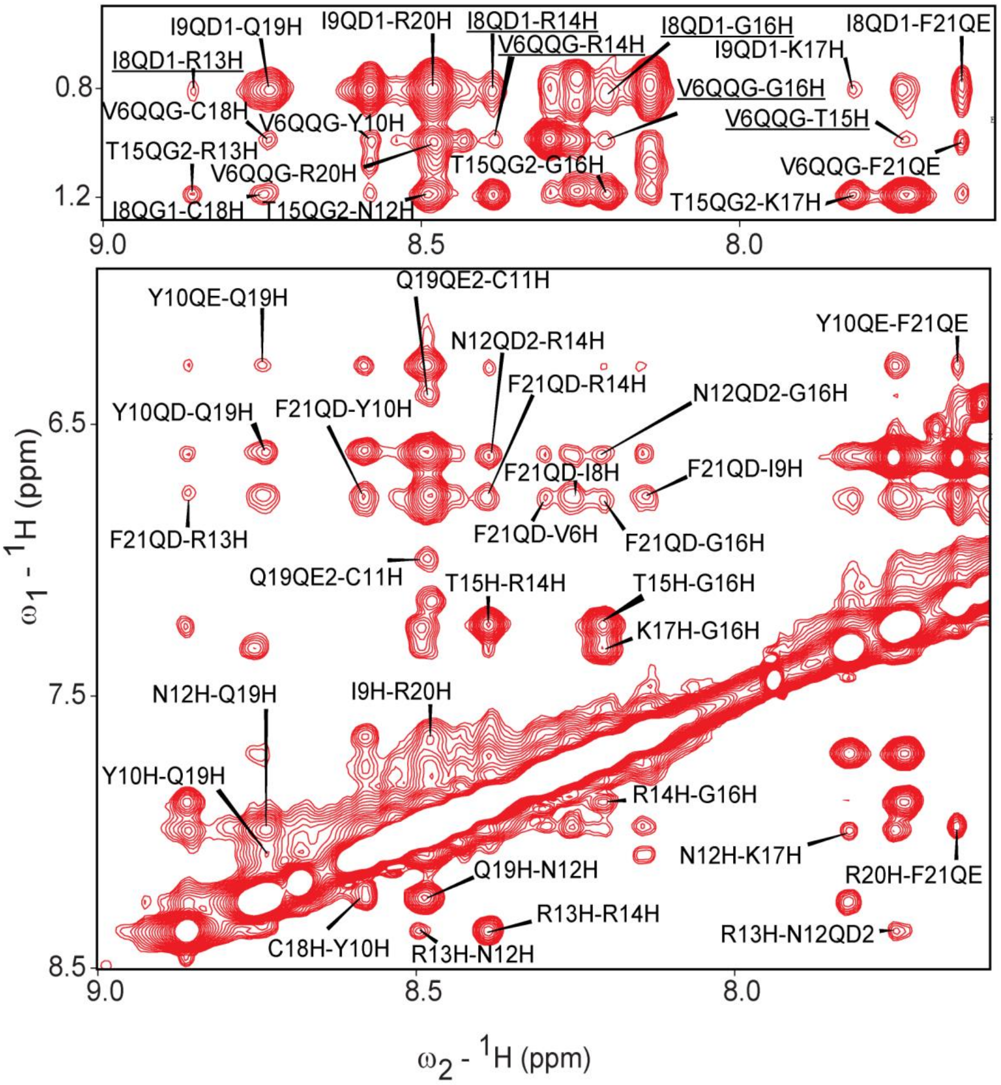

Figure 5.4| tr-NOESY spectrum of thanatin M21F in presence of LPS. NOEs highlighted with an underline are incompatible with the monomeric structure and are used as inter-monomeric NOEs to determine the dimeric structure of thanatin M21F in presence of LPS.

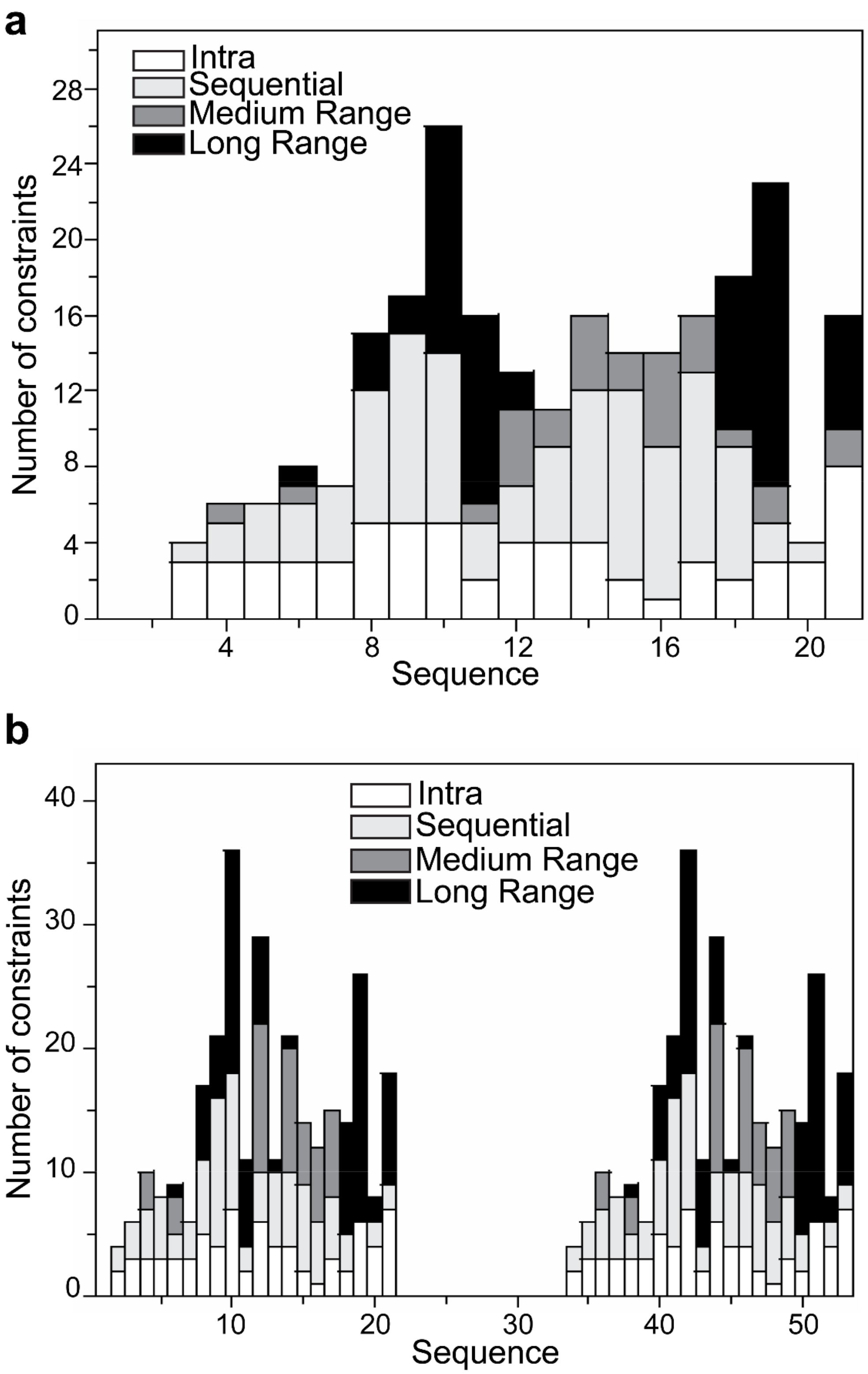

Figure 5.5| No. of NOE connectivities per residue. Bar diagrams showing number and type of NOE constraints for **a,** free thanatin M21F and **b,** thanatin M21F in presence of LPS. Thanatin M21F/LPS has a lot more long range NOE constraints than free thanatin M21F.

Table 5.2| Inter-monomer long-range NOEs for thanatin M21F dimer. A list of long range NOEs that were deemed incompatible with the monomeric structure and were further used as inter-monomeric NOEs for structure calculation.

Thanatin M21F dimer in complex with LPS
8 ILE QD1 – 12 ASN' QD2
6 VAL QQG – 12 ASN' QD2
8 ILE QD1 – 13 ARG' H
8 ILE QD1 – 14 ARG' H
6 VAL QQG – 14 ARG' H
8 ILE' QD1 – 12 ASN QD2
6 VAL' QQG – 12 ASN QD2
8 ILE' QD1 – 13 ARG H
8 ILE' QD1 – 14 ARG H
6 VAL' QQG – 14 ARG H

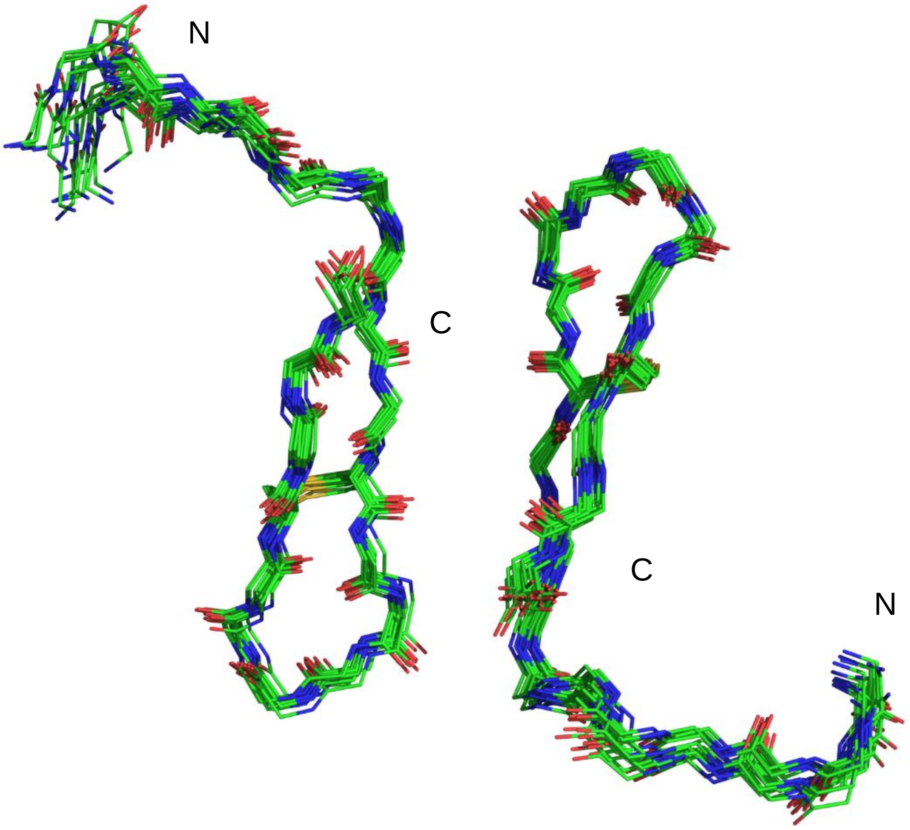

Figure 5.6| Thanatin M21F adopts a dimeric conformation in presence of LPS. Superposition of backbone atoms of 20 lowest energy dimeric structures of thanatin M21F in complex with LPS.

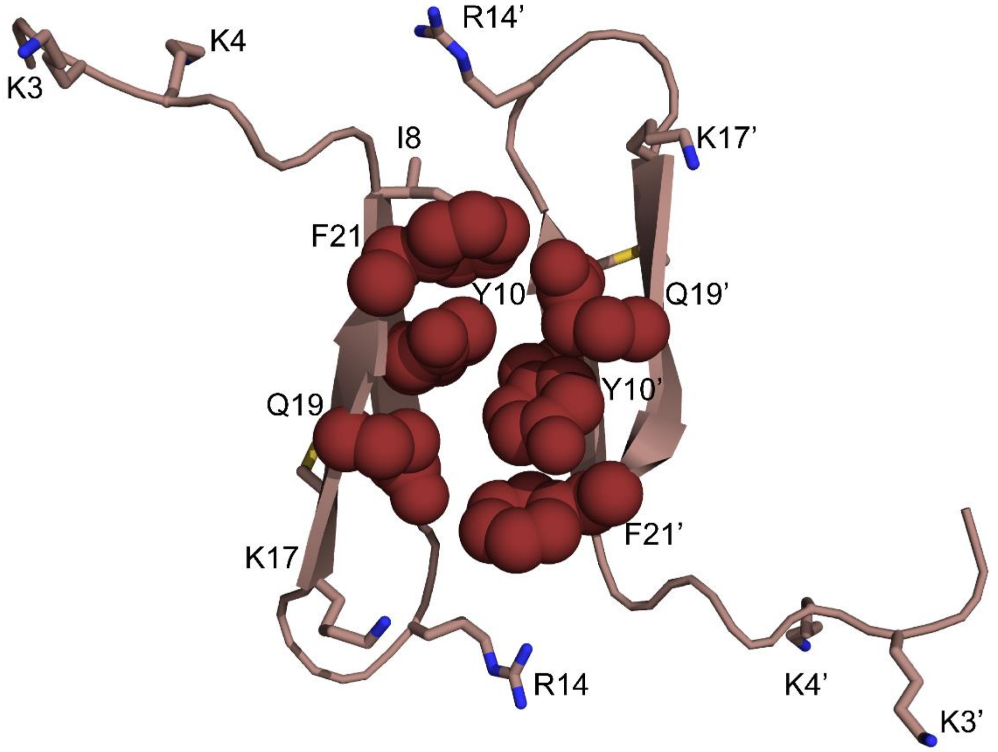

Figure 5.7| Representative structure of thanatin M21F in presence of LPS. The residues F21 and F21’ has enhanced close aromatic-aromatic stacking interactions with residues Y10 and Y10’.

5.2.3 Structure of free thanatinY10M21AA

Ala mutation was done at the 10th and 21st positions of thanatin in order to disturb and decrease the stability of the β-hairpin. This would in turn allow us to understand the role of hydrophobic packing in agglutination. 2D ^{1}H-^{1}H TOCSY and NOESY spectra were analysed and 107 NOE derived distance constrains were incorporated while determining its structure. NOESY spectra of thanatin are illustrated in Figure 5.8 As compared to thanatin and thanatin M21F, number of NOE peaks observed in the NOESY spectra of thanatin Y10M21AA was decreased to a large extent. Furthermore, only 5 long-range NOEs were incorporated while determining its structure (Table 5.6). This is due to the decrease in hydrophobic interactions amongst the residues in the β-strands. Figures 5.9 and 5.10 illustrate the representative structure of thanatin Y10M21AA and an ensemble of 20 energy minimized structures, respectively. Despite a decreased hydrophobic interaction, thanatin Y10M21AA still assumes a β-hairpin conformation with an extended N-terminus. This clearly suggests that the β-strands in thanatin are extremely stable.

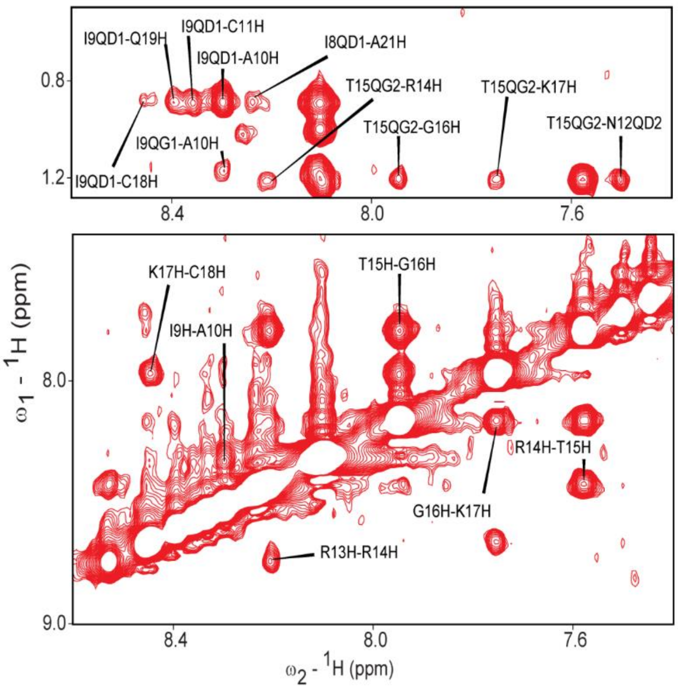

Figure 5.8| 2D ^{1}H-^{1}H NOESY spectra of free thanatin Y10M21AA. Replacing the aromatic residue Y10 and residue M21 in the β-strands by Ala residues decreases the hydrophobic interactions and disturbs the stability of β-hairpin.

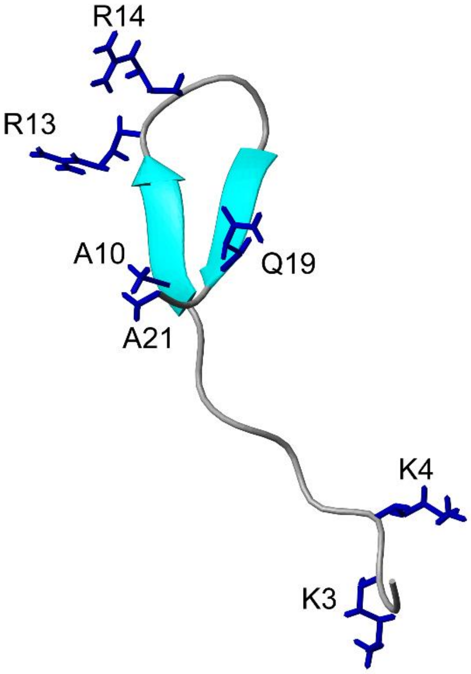

Figure 5.9| Representative structure of free thanatin Y10M21AA in aqueous solution. NMR derived 3D structure of free thanatin Y10M21AA at 298K, pH 5. Thanatin Y10M21AA assumes a β-hairpin conformation with an extended N-terminus.

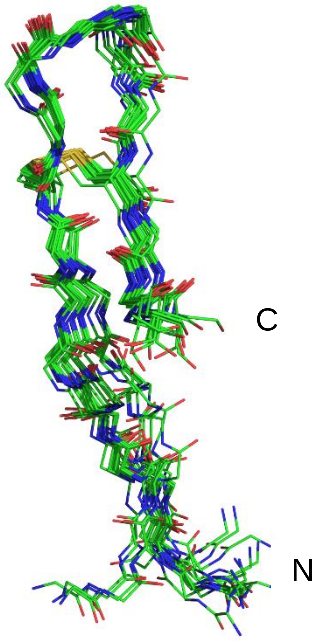

Figure 5.10| NMR derived structure of free thanatin Y10M21AA. Superposition of backbone atoms of 20 lowest energy structures of free thanatin Y10M21AA in aqueous solution.

5.2.4 Structure of thanatin Y10M21AA in presence of LPS

Atomic-resolution 3D structure of thanatin Y10M21AA was determined by analysing ^{1}H-^{1}H TOCSY and tr-NOESY spectra. tr-NOESY spectra of thanatin Y10M21AA in presence of LPS (figure 5.11) yielded more long range and sidechain/sidechain NOE connectivities when compared to that in free state (Figure 5.8). Moreover, certain NOEs demonstrated a close proximity between the residues I8/G16, I8/K1, I8/T15, I8/R13 and V6/G16. These NOEs (Table 5.3) were deemed incompatible with the monomeric structure and were further used as inter-monomer NOEs to determine its dimeric structure. Number of NOE connectivities and long range NOEs per residue for thanatin Y10M21AAin free solution and in presence of LPS (figure 5.12) has reduced dramatically in comparison to that of thanatin (Figure 4.23) and thanatin M21F (Figure 5.5). 226 NOE driven distance constraints and 52 angle constraints were incorporated to determine the structure of thanatin Y10M21AA in presence of LPS. Representative structure of thanatin Y10M21AA and an ensemble of 20 energy minimized structures are illustrated in Figures 5.13 and 5.14, respectively. Like thanatin, thanatin Y10M21AA also assumed a dimeric conformation with its N-terminus region oriented in an anti-parallel fashion.

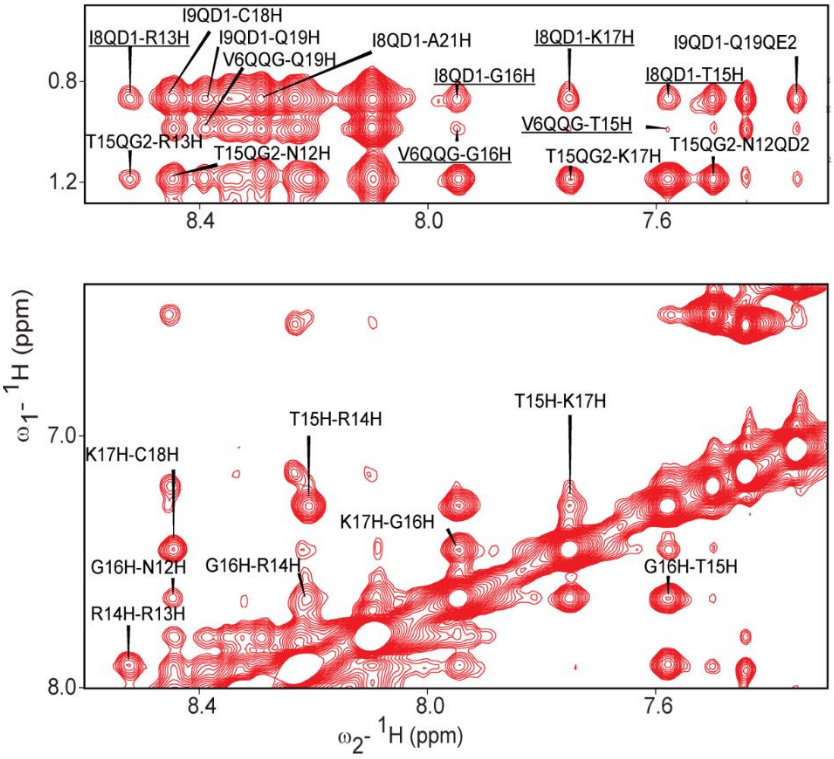

Figure 5.11| tr-NOESY spectrum of thanatin Y10M21AA in presence of LPS. NOEs highlighted with an underline are incompatible to the monomeric structure and were used as inter-monomer NOEs to determine the dimeric structure of thanatin Y10M21AA in presence of LPS.

Table 5.3| Inter-monomer long range NOEs for thanatin Y10M21AA dimer. A list of long range NOEs that were deemed incompatible with the monomeric structure and were further used as inter-monomeric NOEs for structure calculation.

Thanatin Y10M21AA dimer
6 VAL QQG – 12 ASN’ QD2
8 ILE QD1 – 12 ASN’ QD2
8 ILE QD1 – 13 ARG’ H
8 ILE QD1 – 15 THR’ H
8 ILE QD1- 16 GLY’ H
8 ILE QD1 – 17 LYS’ H
6 VAL’ QQG – 12 ASN QD2
8 ILE’ QD1 – 12 ASN QD2
8 ILE’ QD1 – 13 ARG H
8 ILE’ QD1 – 15 THR H
8 ILE’ QD1- 16 GLY H
8 ILE’ QD1 – 17 LYS H

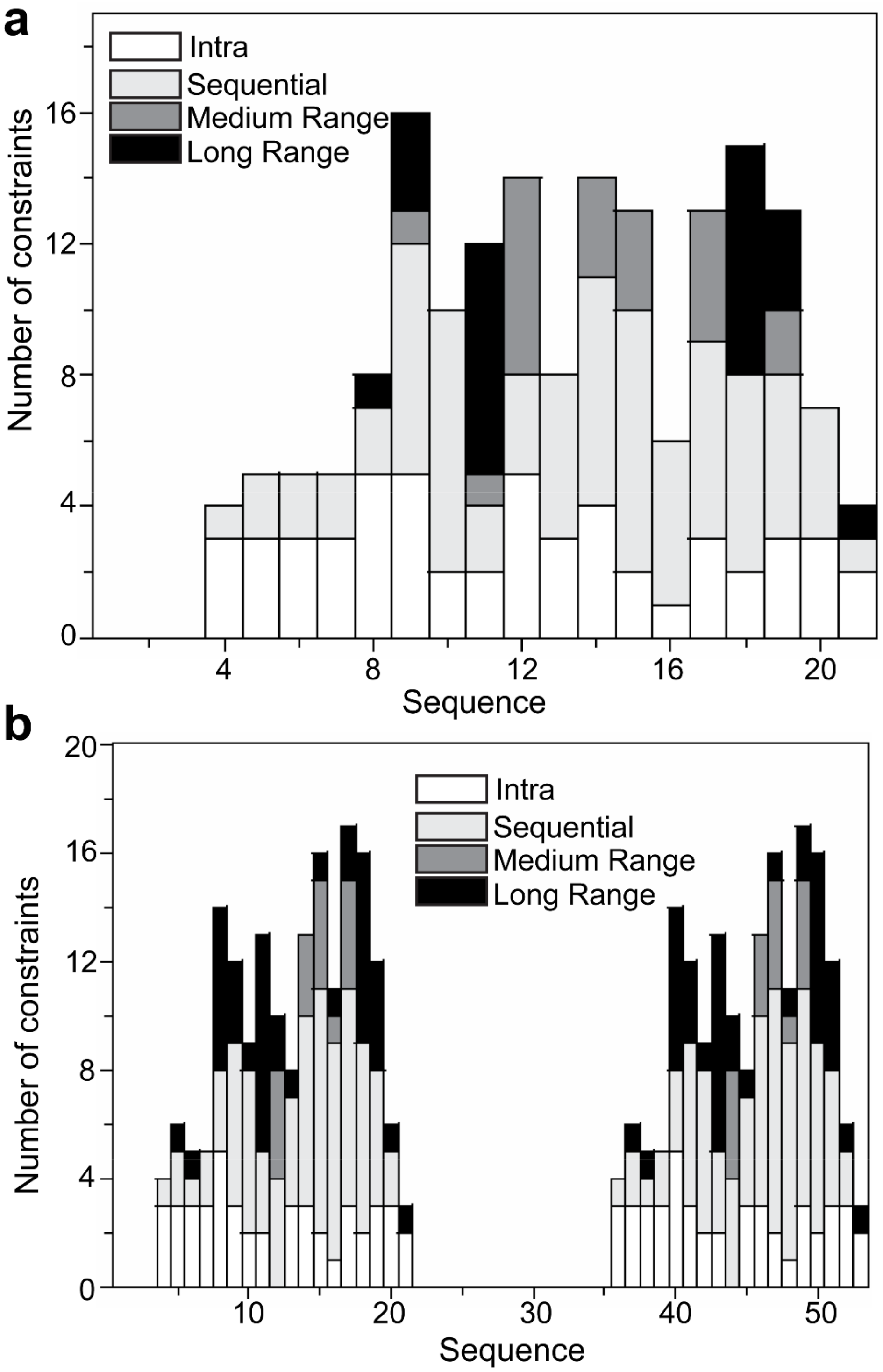

Figure 5.12| Number of NOE connectivities per residue. Bar diagrams illustrating number and type of NOE constraints for **a,** free thanatin Y10M21AA and **b,** thanatinY10M21AA in presence of LPS.

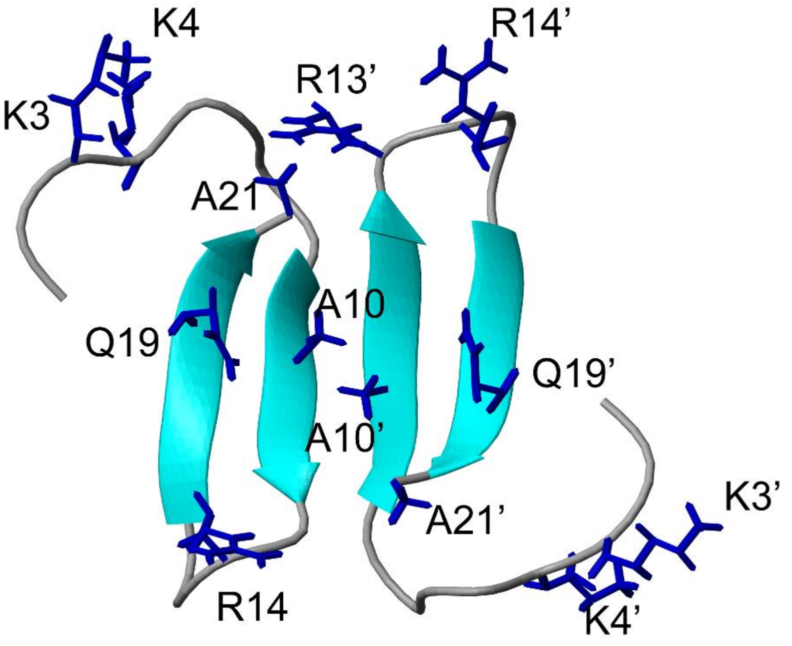

Figure 5.13| Representative structure of thanatin Y10M21AA in presence of LPS. Thanatin Y10M21AA assumes a dimeric conformation in presence of LPS. However, Ala mutation at the 10th and 21st positions decreases the stability of the β-sheet.

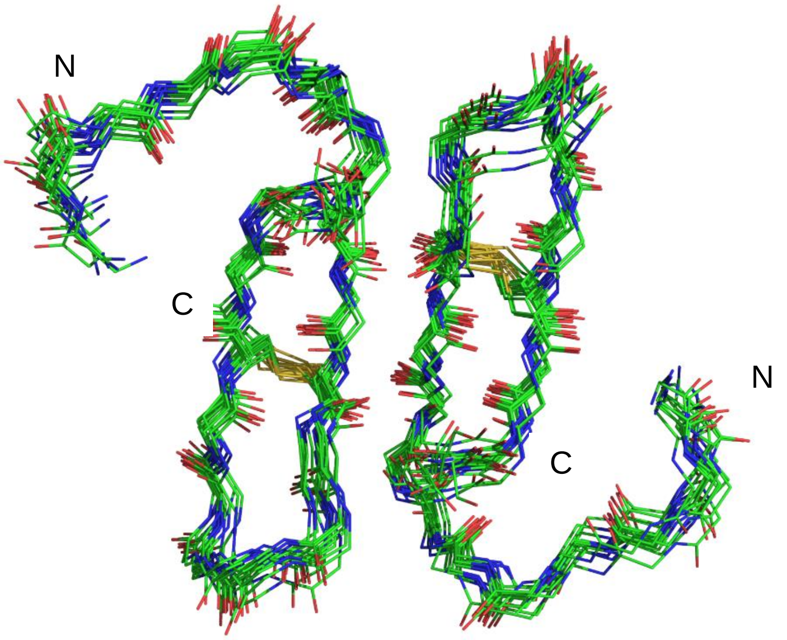

Figure 5.14| NMR derived structure of thanatin Y10M21AA in presence of LPS. Superposition of backbone atoms of 20 lowest energy structures of dimeric thanatin Y10M21AA in presence of LPS.

5.2.5 Minimum Inhibitory Concentration

MIC for the gain-in function mutation thanatin M21F and loss-in function mutation thanatin Y10M21AA was determined against four Gram-positive and four Gram-negative bacteria. The values are shown in Table 5.4. The MIC of thanatin M21F is decreased as compared to thanatin. Despite disturbing the hydrophobic packing in the β-hairpin of thanatin Y10M21AA, it is still moderately active against all 8 tested bacterial strains.

Furthermore, Ala mutation was done on the two arginine residues present in the β-turn. Three loss-in function mutations, namely thanatin R13A, thanatin R14A and thanatin R13R14AA were designed and their MIC values were determined (Table 5.4). Interestingly, single Ala mutation halved the antimicrobial activity. However, replacing both the Arg residues by Ala completely impaired the-activity against all 8 bacterial strains. This clearly indicates that presence of at least one of the Arg residues in the β-turn is pivotal for thanatin's antimicrobial activity and is critical for binding to LPS.

Table 5.4| Antimicrobial activity of thanatin mutants. Minimum inhibitory concentration (µM) against EC: *Escherichia coli*; PA: *Pseudomonas aeruginosa*; SE: *Salmonella enterica*; KP: *Klebsiella pneumoniae*; SA: *Staphylococcus aureus*; BS: *Bacillus subtilis*; SP: *Streptococcus pyogenes*; EF: *Enterococcus faecalis*.

Peptide	**MIC (µM)**							
	Gram-Negative				**Gram-Positive**			
	EC	**PA**	**SE**	**KP**	**SA**	**BS**	**SP**	**EF**
Thanatin	0.5	1	1	1	1	2	0.5	0.5
Thanatin M21F	0.5	0.5	0.5	0.5	0.5	1	<0.25	<0.25
Thanatin Y10M21AA	6	4	4	2	4	8	6	2
Thanatin R13A	2	2	2	4	2	2	2	2
Thanatin R14A	2	2	4	2	2	2	2	1
Thanatin R13R14AA	>100	>100	>100	>100	>100	>100	>100	>100

5.2.6 Structure of thanatin R13R14AA in presence of LPS

The activity of thanatin R13R14AA was completely impaired due to Ala mutations in the β-turn. In order to analyse the structure-activity correlation of this loss-in function mutation, atomic resolution 3D structure was determined in presence of LPS. 2D ^{1}H-^{1}H TOCSY and tr-NOESY spectra (Figure 5.15) were analysed to acquire the NOE drive distance constraints. Surprisingly, this inactive mutant peptide also yielded NOEs between the residues I8/N12, I8/A13, I8/A15, I8/T15, I8/K17, V6/N12 and V6/A13. Close proximity between these residues is not possible in a monomeric structure. Hence, these NOEs were incorporated as inter-monomeric NOEs while determining its dimeric structure (Table 5.5). Furthermore, analysis of tr-NOESY yielded 418 NOE driven distance constraints that were used in the structure determination. Number of NOE connectivities per residue is illustrated in Figure 5.16. Unlike thanatin Y10M21AA (Figure 5.12), tr-NOESY of thanatin R13R14AA a lot more long range NOEs. Representative structure of thanatin R13R14AA and an ensemble of 20 lowest energy structures are illustrated in Figures 5.17 and 5.18, respectively. A summary of structural statistics is elucidated in Table 5.6.

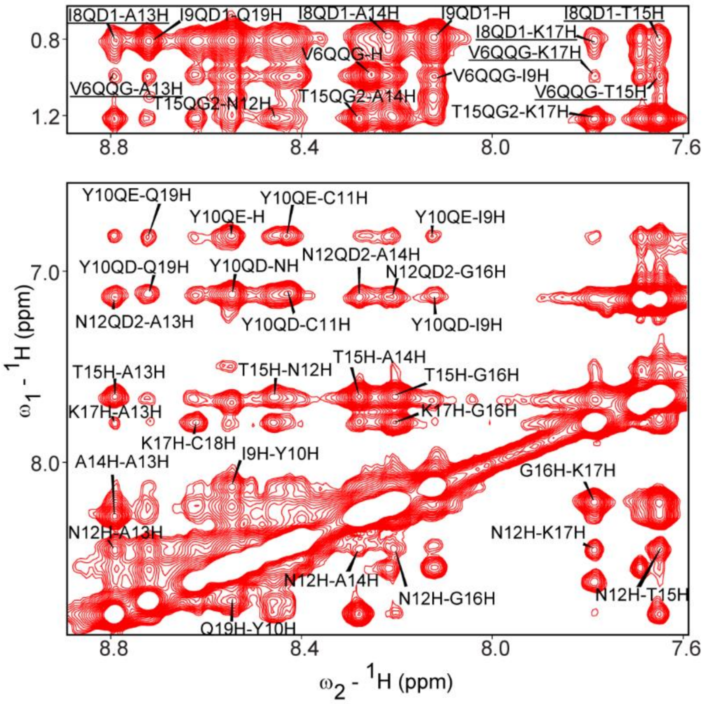

Figure 5.15| tr-NOESY spectrum of thanatin R13R14AA in presence of LPS. NOEs highlighted with an underline are incompatible to the monomeric structure and were used as inter-monomer NOEs to determine the dimeric structure of thanatin Y10M21AA in presence of LPS.

Table 5.5| Inter-monomer long range NOEs for thanatin R13R14AA dimer. A list of long range NOEs that were deemed incompatible with the monomeric structure and were further used as inter-monomeric NOEs for structure calculation.

Thanatin R13R14AA dimer
6 VAL QQG – 12 ASN’ QD2
6 VAL QQG – 13 ALA’ H
8 ILE QD1 – 12 ASN’ H
8 ILE QD1 – 12 ASN’ QD2
8 ILE QD1 – 13 ALA’ H
8 ILE QD1 – 14 ALA’ H
8 ILE QD1 – 15 THR’ H
8 ILE QD1 – 17 LYS’ H
6 VAL’ QQG – 12 ASN QD2
6 VAL’ QQG – 13 ALA H
8 ILE’ QD1 – 12 ASN H
8 ILE’ QD1 – 12 ASN QD2
8 ILE’ QD1 – 13 ALA H
8 ILE’ QD1 – 14 ALA H
8 ILE’ QD1 – 15 THR H
8 ILE’ QD1 – 17 LYS H

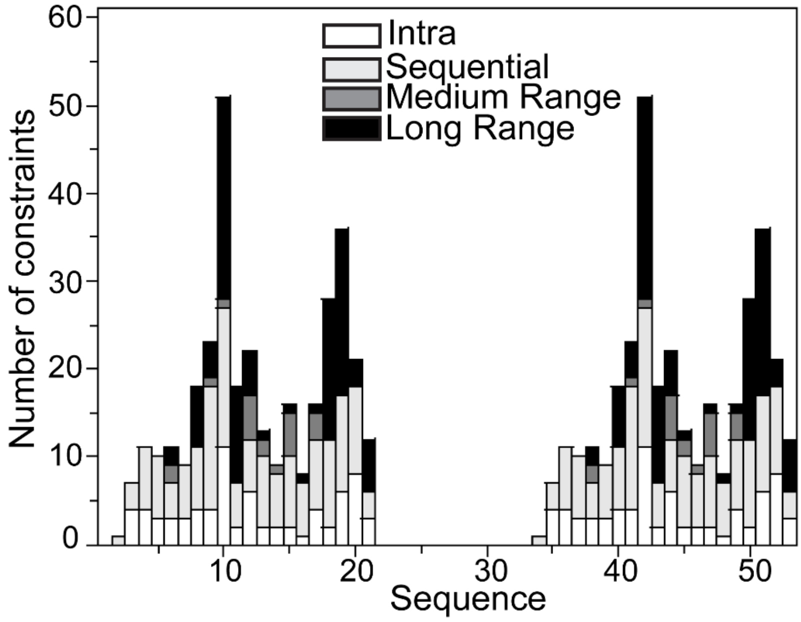

Figure 5.16| No. of NOE connectivities per residue. Bar diagrams illustrating number and type of NOE constraints for dimeric thanatin R13R14AA in presence of LPS.

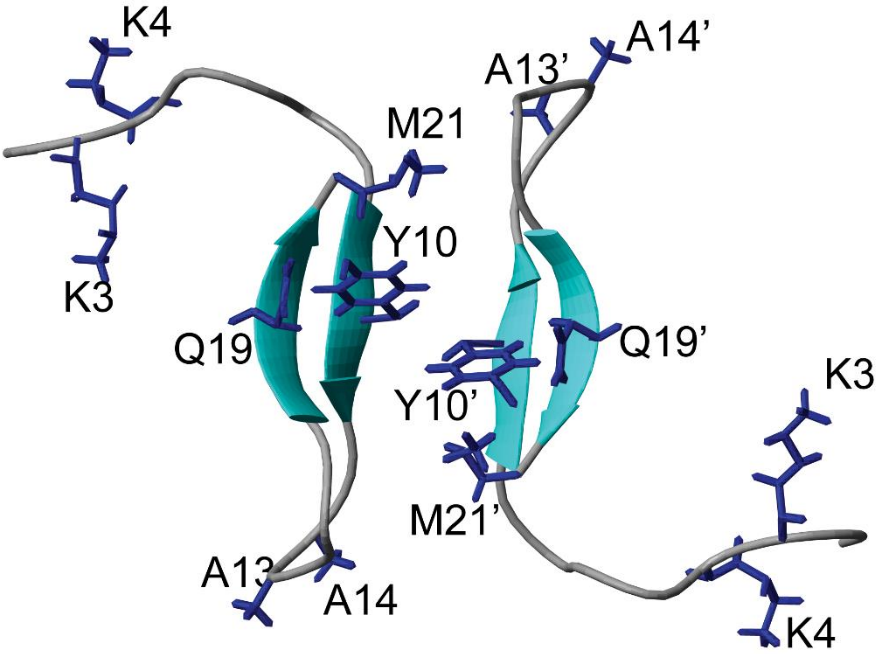

Figure 5.17| Representative structure of thanatin R13R14AA in presence of LPS. Although the antimicrobial activity of thanatin R13R14AA is completely impaired, the mutant still adopts a dimeric conformation.

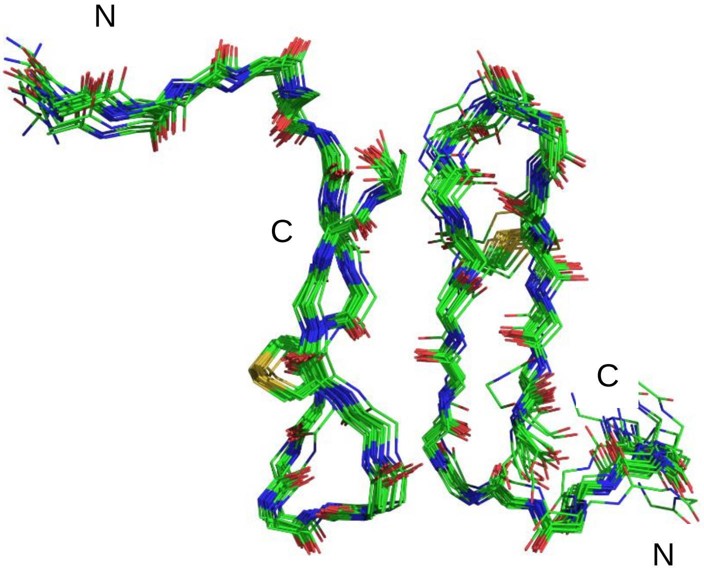

Figure 5.18| NMR derived structure of thanatin R13R14AA in presence of LPS. Superposition of backbone atoms of 20 lowest energy structures of dimeric thanatin Y10M21AA in presence of LPS.

Table 5.6| Summary of structural statistics. 1, Thanatin M21F in free solution. **2,** Thanatin M21F in presence of LPS. **3,** Thanatin Y10M21AA in free solution. **4,** Thanatin Y10M21AA in presence of LPS. **5,** Thanatin R13R14AA in presence of LPS.

	1	**2**	**3**	**4**	**5**
Distance constraints					
Sequential [|i-j|= 1]	48	90	38	78	146
Medium range [1 <|i-j|< 4]	10	36	10	16	14
Long range [|i-j|≥ 4]	28	78	5	14	82
Inter monomer	-	10	-	12	16
Total	152	368	107	226	418
Dihedral-angle constraints	32	64	32	52	64
Deviation from mean structure (Å)					
All backbone atoms	0.23	0.69	1.43	0.98	0.7
All heavy atoms	0.94	1.39	1.72	1.94	1.03
Ramachandran plot for the mean structure (%residues)					
Most favoured region	56.3	62.5	62.5	62.5	43.8
Additional allowed region	37.5	37.5	37.5	37.5	50
Generously allowed region	6.2	0	0	0	6.2
Disallowed region	0	0	0	0	0

The dimeric structures of the impaired analogs, Y10M21AA and R13R14AA in presence of LPS were unexpected. However, structural analyses indicated that the dimeric β-sheet structures of the analogs delineated significant variations from thanatin dimer (Figure 5.19). Regardless, these observations strongly suggest that the β-hairpin structure of thanatin contains an intrinsic tendency to form multi-stranded β-sheet structures in complex with LPS.

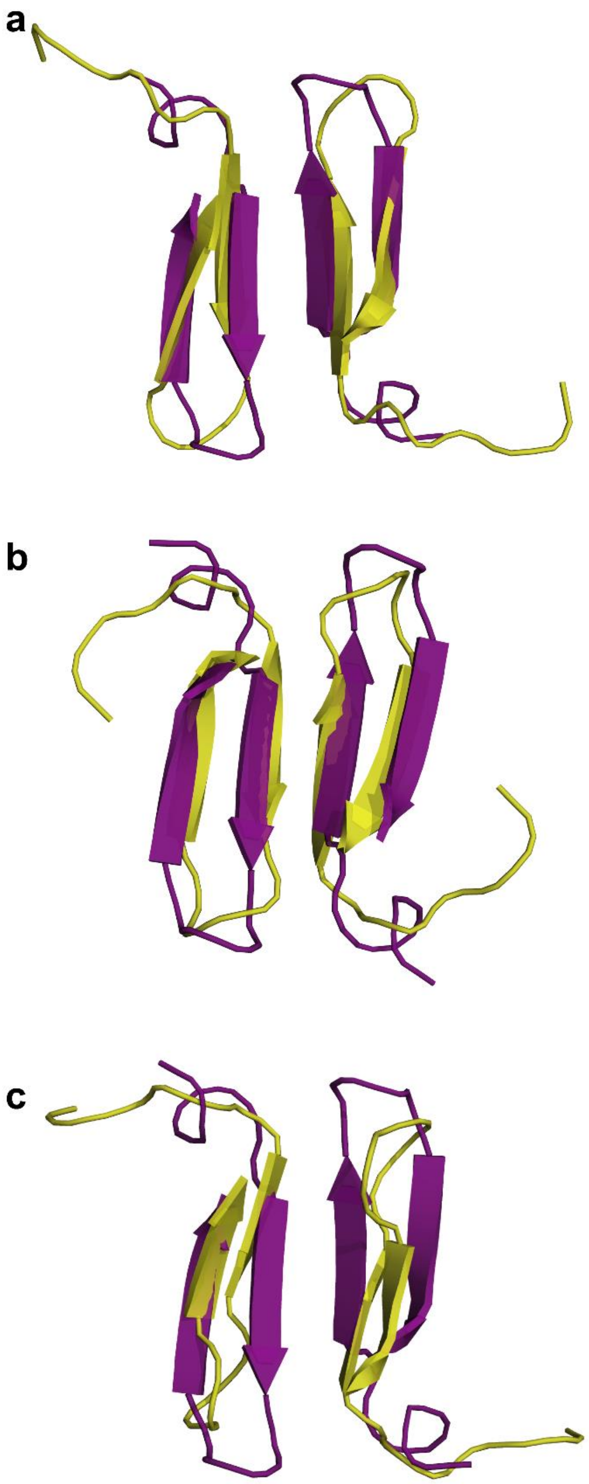

Figure 5.19| Differences in the dimeric β-sheet structures of thanatin and its analogs. Superposition of thanatin dimer (purple) and **a,** thanatin M21F dimer (yellow) with RMSD of 7.1; **b,** thanatin Y10M21AA dimer (yellow) with RMSD of 4.3; **c,** thanatin R13R14AA dimer (yellow) with RMSD of 5.5.

5.2.7 Interactions of thanatin analogs with LPS

N-terminal dansylated thanatin analogs or dans-thanatin analogs were used to study their interaction with *E. coli* 0111:B4 LPS. The change in fluorescence intensity (ΔF) at λ_{max} was then plotted as a function of concentration of LPS (Figure 5.20). Plots were fitted with Hill's equation to yield dissociation constant (K_d). Dansyl fluorescence analyses of thanatin analogs in presence of varying LPS concentrations showed that all of these mutants were able to bind to LPS with comparable affinity with similar Hill coefficient, indicating potential plasticity in LPS/thanatin interactions (Table 5.7).

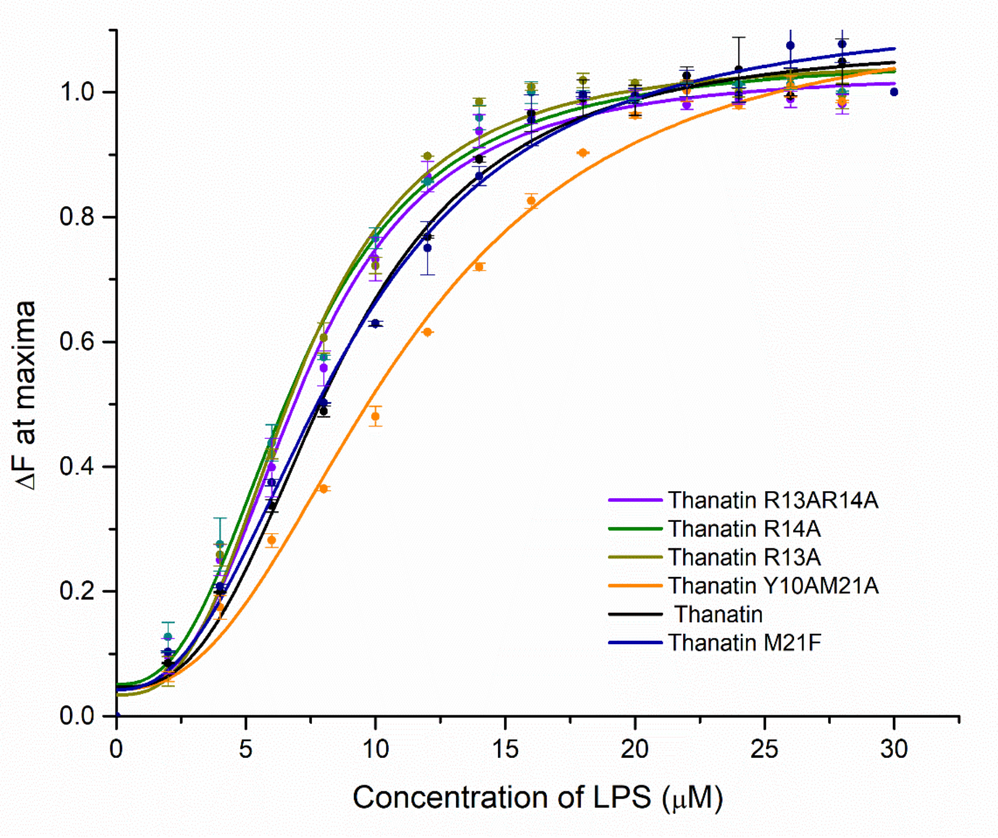

Figure 5.20| Hill's plot to calculate dissociation constant. Changes in fluorescence emission intensity of N-terminal dansylated thanatin in presence of varying concentrations of LPS reveal that thanatin analog/LPS interaction is cooperative in nature.

Table 5.7| Kd calculation. Dissociation constant and Hill's coefficient for N-terminally dansylated thanatin and its analogs in presence of varying concentrations of LPS.

Peptides	Dissocation Constant, Kd (μM)	Hill's Coefficient (n)
Thanatin	8.6	2.75
Thanatin M21F	8.84	2.37
Thanatin Y10M21AA	11.03	2.42
Thanatin R13A	7.01	2.84
Thanatin R14A	7.05	2.62
Thanatin R13R14AA	7.24	2.82

5.2.8 BODIPY-Cadaverine Displacement Assay

ED_{50} for the thanatin analogs were examined using BODIPY cadaverine as a fluorescent probe. The peptide with a higher affinity to LPS would replace BC fluorescent probe from the lipid A domain. BC occupancy factor was calculated and was plotted against concentration of the peptide (Figure 5.21). BC probe displacement data demonstrated ED50 of the following order Thanatin>M21F>Y10M21AA>R13R14AA (Table 5.8). The least active peptide R13R14AA disclosed the highest ED50 of 3.2 μM.

Table 5.8| Mean effective dose for thanatin analogs. A comparison of ED_{50} of thanatin and its analogs, calculated as the efficacy of the peptides in binding to LPS by displacing BODIPY- cadaverine probe.

Peptides	ED50 (μM)
Thanatin	0.87
Thanatin M21F	0.99
Thanatin Y10M21AA	1.22
Thanatin R13R14AA	3.20

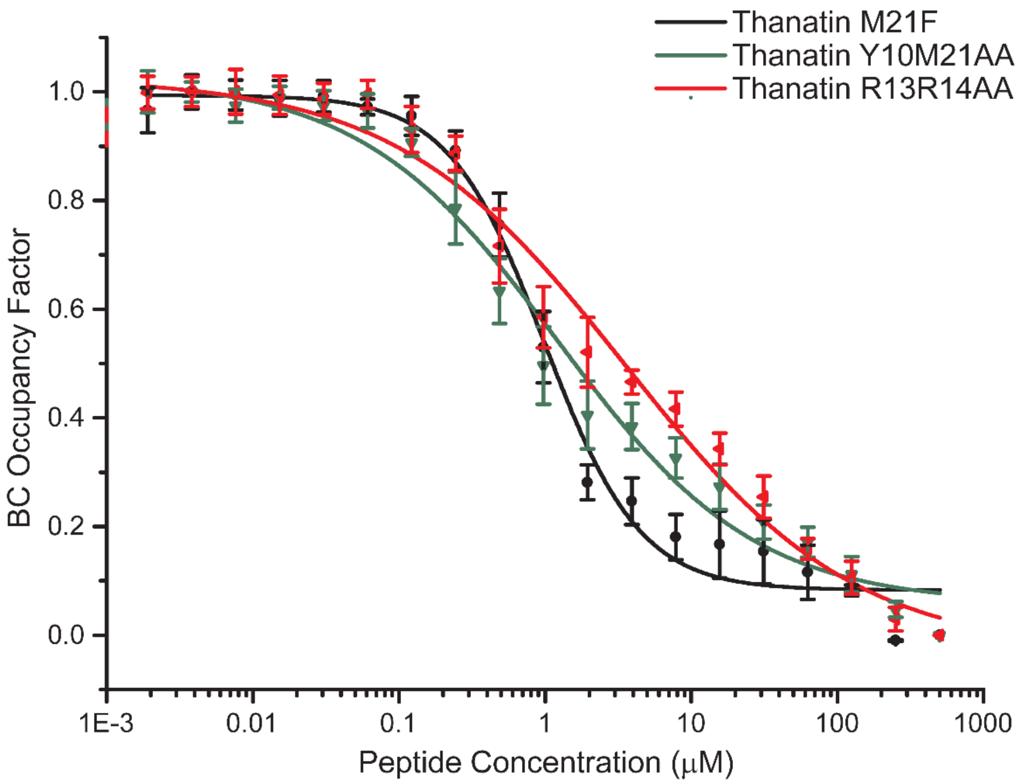

Figure 5.21| BC occupancy factor. Comparison of BC probe displacement by thanatin and PMB. A lower BC occupancy factor at a particular mediator concentration indicates a more efficient binding of the mediator to LPS**.**

5.2.9 Isothermal Titration Calorimetry

To further understand the interaction of thanatin analogs with LPS, binding affinity and thermodynamic parameters were analysed using ITC. The downward position of the titration peaks and integrated heat values (Figures 5.22, 5.23 & 5.24) suggest that LPS/thanatin analog interactions are exothermic in nature. ITC derived LPS/thanatin analog binding parameters are shown in Table 5.9. It is interesting to note that only thanatin (Table 4.3) and its gain-in function mutant thanatin M21F has an enthalpy-driven binding. -TΔS for other loss-in function mutants (thanatin Y10M21AA and thanatin R13R14AA) is more negative when compare to ΔH and contributes more towards the -ΔG.

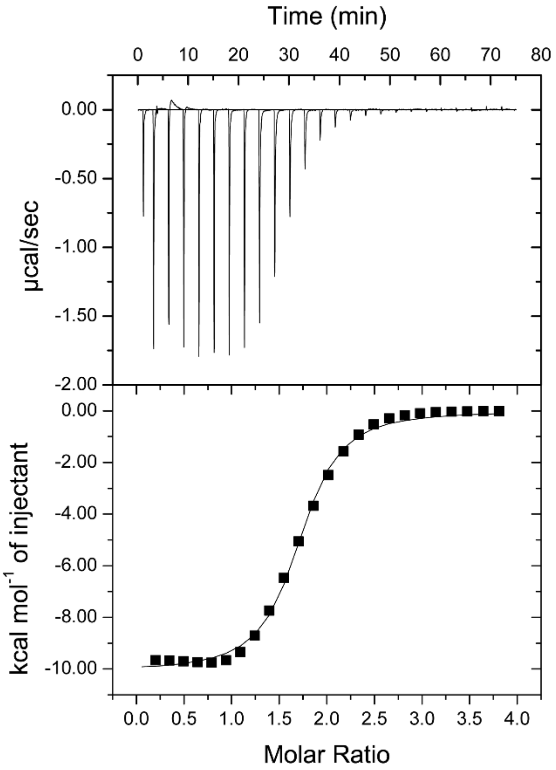

Figure 5.22| ITC thermogram: LPS/thanatin M21F interaction. ITC derived binding parameters of thanatin M21F titrated against 50 µM LPS in 10 mM phosphate buffer, pH 7.

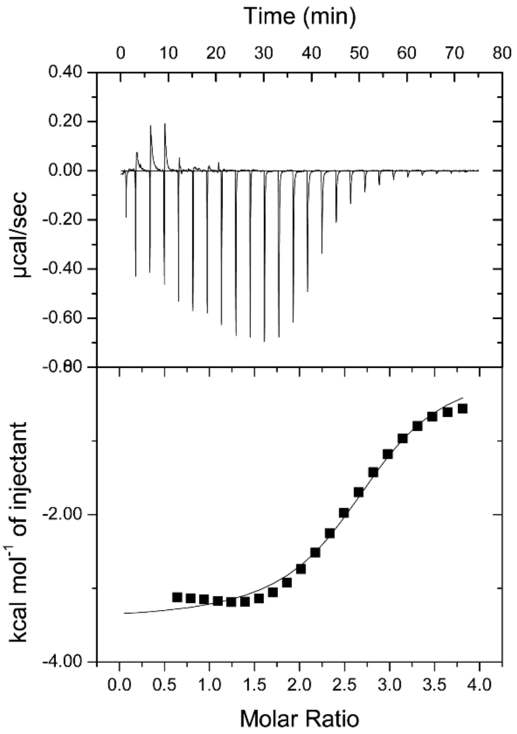

-

Figure 5.23| ITC thermogram: LPS/thanatin Y10M21AA interaction. ITC derived binding parameters of thanatin Y10M21AA titrated against 50µM LPS in 10 mM phosphate buffer, pH 7.

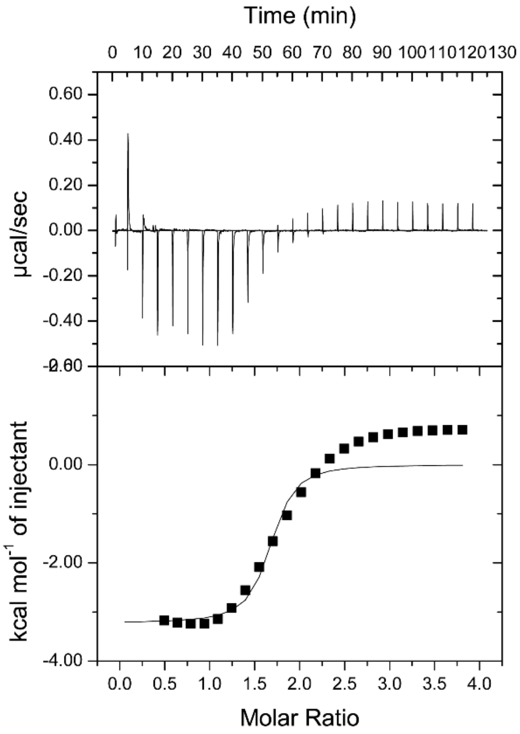

Figure 5.24| ITC thermogram: LPS/thanatin R13R14AA interaction. ITC derived binding parameters of thanatin R13R14AA titrated against 50 µM LPS in 10 mM phosphate buffer, pH 7.

Table 5.9| Thermodynamic Parameters. ITC derived binding parameters of thanatin analogs titrated against 50µM LPS in 10 mM phosphate buffer, pH 7.

	Kd (µM)	**ΔH (Kcal/mol)**	**TΔS (Kcal/mol)**	**ΔG (Kcal/mol)**
Thanatin M21F	1.43	-10.09	-2.11	-7.98
Thanatin Y10M21AA	3.90	-3.44	3.93	-7.37
Thanatin R13R14AA	0.55	-3.22	5.31	-8.53

5.2.10 Zeta Potential Measurements

Surface charge neutralization of *E. coli* 0111:B4 in presence of increasing thanatin analog concentrations was studied by measuring its zeta potential. On addition of increasing concentrations of cationic pore-forming AMPs, zeta potential would first neutralize and then further reach to a plateau at a higher positive value of ~ 5mV. However, the mutant peptides are not able to neutralize the zeta potential of the cells (Figure 5.25). Moreover, the inactive peptide is the least effective in neutralizing the zeta potential, indicating that there is a decrease in electrostatic interactions with the anionic cell membrane due to the loss-in function mutation.

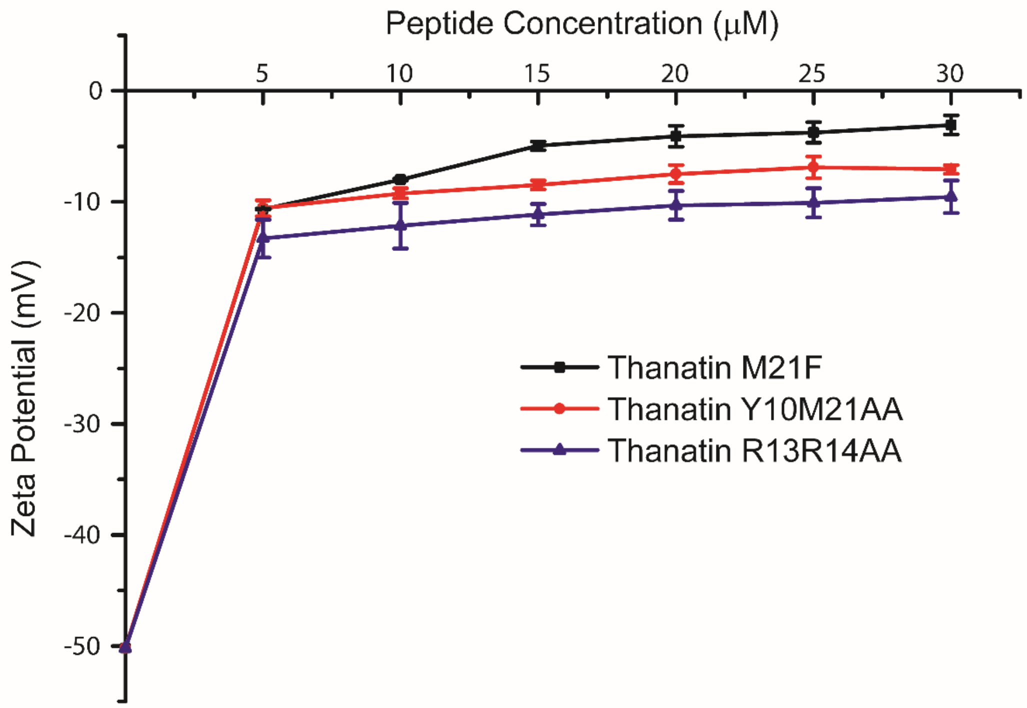

Figure 5.25| Zeta Potential Measurement. Thanatin analogs are not able to completely neutralize the zeta potential of *E. coli* cells.

5.2.11 FITC-LPS Fluorescence Assay

In order to examine the differences in the structural changes in LPS micelles due to mutations in critical residues of thanatin, FITC-LPS was examined in presence of varying concentrations of thanatin analogs in fluorescence spectrometer.

Dissociation of LPS micelles on binding with pore forming antimicrobial peptides results in FITC emission intensity. On the other hand, the emission intensity of FITC-LPS is quenched due to FRET among the fluorophore in an aggregated LPS micelle structure. As can be observed from Figure 5.26, there is a significant quenching in emission intensity of FITC-LPS in presence of increasing thanatin M21F concentrations. Such diminution in the fluorescence intensity of FITC-LPS in complex with the gain-in function mutant suggests a higher degree of FRET amongst the fluorophore FITC. Hence, from the FITC-LPS fluorescence data it can be concluded that LPS micelles undergo a higher order of association upon binding with thanatin M21F when compared to thanatin Y10M21AA and thanatin R13R14AA. The inactive peptide yielded the least quenching in emission intensity of FITC-LPS, indicating its inefficiency in agglutinating the micelles.

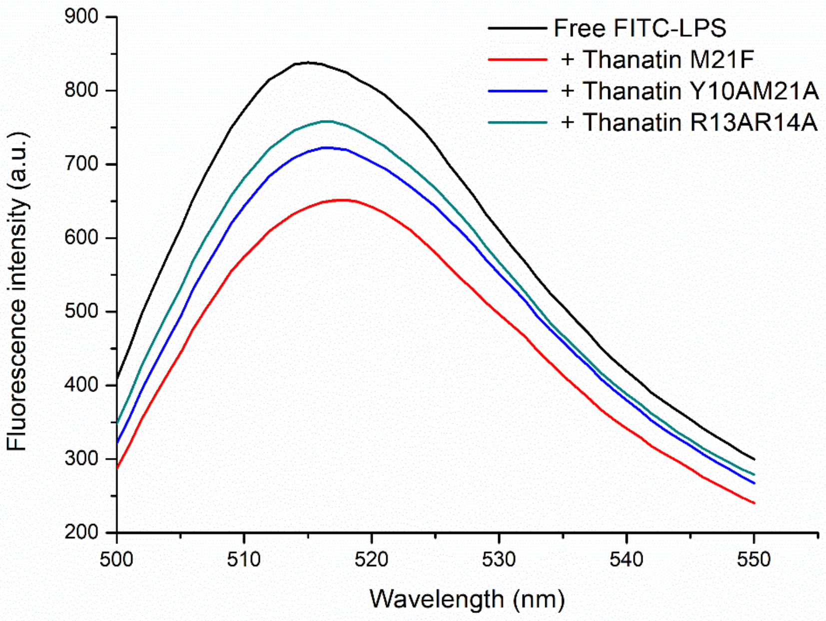

Figure 5.26| Emission intensity spectra of FITC-LPS. Unlike in presence of pore forming AMPs, emission intensity spectra of FITC-LPS demarcates a marked quenching in presence of increasing concentrations of bacterial cell agglutinating AMP.

5.2.12 Transmission Electron Microscopy

Tendency of the active thanatin M21F peptide to agglutinate bacterial cells were further demonstrated by TEM. Changes in the morphology of the *E.coli* cells in presence of thanatin M21F are shown in Figure 5.27.

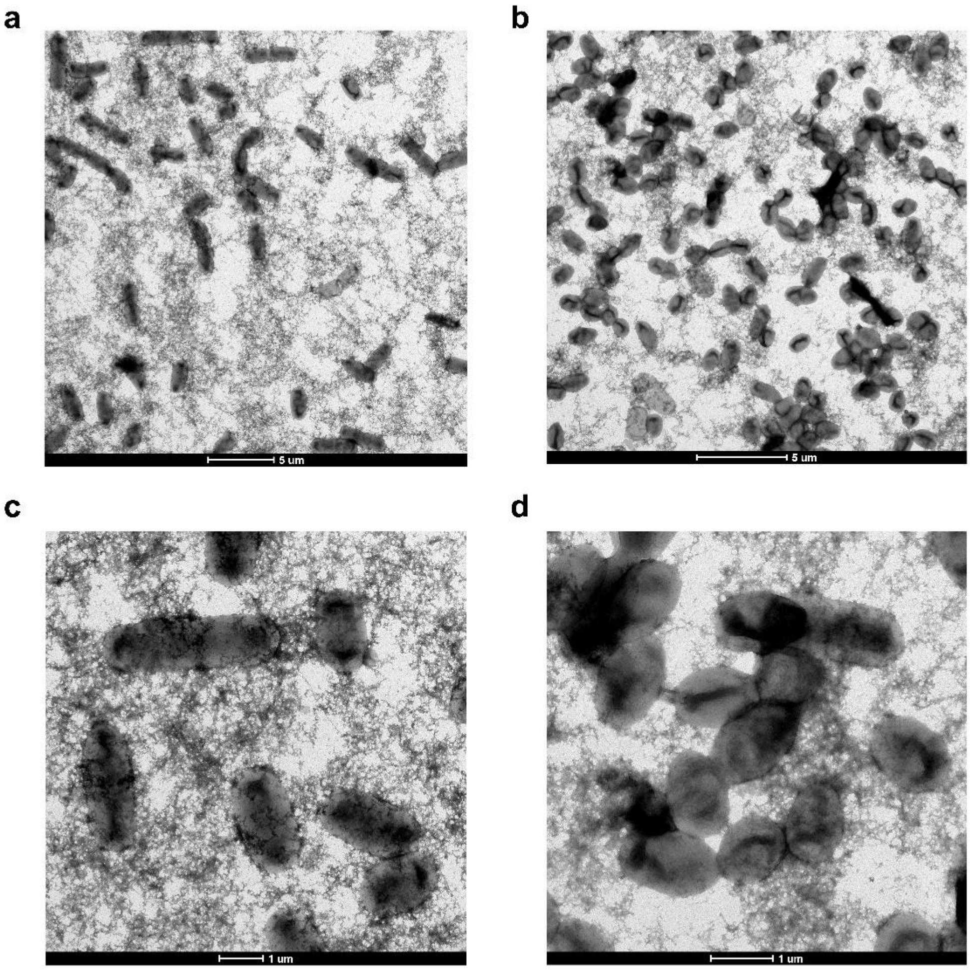

Figure 5.27| Transmission Electron Microscopy. TEM images of *E.coli* cells in absence of (a,c) and in presence of thanatin M21F (b,d). Changes in morphology of the *E.coli* cells clearly indicates agglutination.

5.2.13 ^{31}P NMR Spectroscopy

Perturbation of LPS micelle structure by thanatin analogs was further examined by 31P NMR experiments. ^{31}P NMR spectra of LPS were acquired in free solution and at 1:1 molar ratios of LPS and thanatin M21F, thanatin Y10M21AA, thanatin R13R14AA (Figure 5.28). Free LPS micelles produce two well resolved NMR signal at ~ -1 ppm and -2 ppm. As illustrated in Figure 5.28, both the phosphate groups demonstrate extensive line broadening and changes in chemical shifts when in complex with thanatin M21F. This suggests involvement of the phosphate head groups in binding with the gain-in function mutant. Such resonance broadening effect may potentially arise from slower tumbling motion of aggregated LPS micelles in complex with thanatin M21F. However, thanatin Y10M21AA and thanatin R13R14AA do not render such line broadening effect and are probably inefficient in imparting structural changes in LPS micelles.

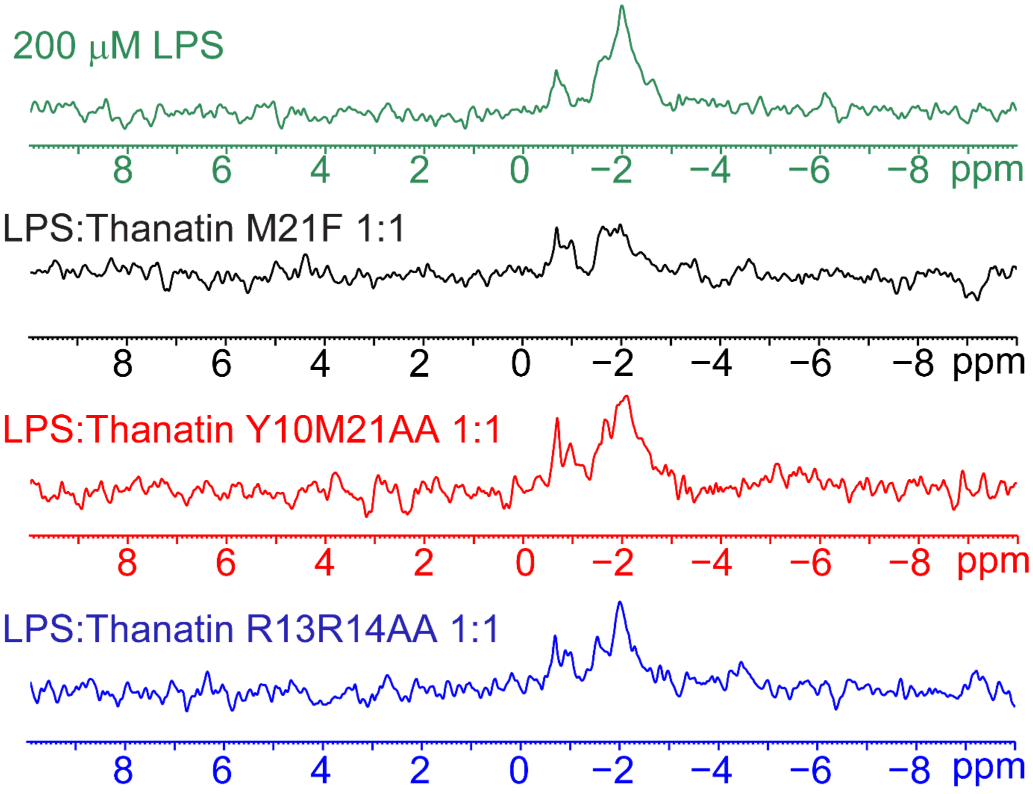

Figure 5.28| ^{31}P NMR spectra of LPS. ^{31}P NMR spectra of 200 µM LPS in free solution (green), LPS in presence of thanatin M21F (black) in the ratio 1:1, LPS in presence of thanatin Y10M21AA (red) in the ratio 1:1 and LPS in presence of thanatin R13R14AA (blue) in the ratio 1:1. Thanatin M21F demonstrates extensive line broadening at both -1 ppm (mono-phosphate group) and -2 ppm (di-phosphate group) indicating that unlike the other analogs of thanatin, thanatin M21F interacts with both the phosphate groups more efficiently and renders changes to the LPS micelle structure.

5.2.14 Modelling of LPS-dimeric thanatin complex by MD simulations

In order to gain further insights on LPS-thanatin interactions, MD simulations were carried out for 3 repeats of 400 ns each in LPS/DPPE bilayer and dimeric thanatin. The LPS/DPPE bilayer can be considered as a mimic of outer membrane of Gram negative bacteria where the outer-leaflet of the outer membrane is predominantly occupied by LPS molecules. Interactions between dimeric thanatin and LPS lipids during MD simulations revealed a rapid (within 40–50 ns) encountering and stabilization of the LPS-thanatin complex (Figure 5.29). Both the subunits of the dimeric thanatin were found to form a network of interactions with multiple LPS molecules, primarily with the head regions through multiple electrostatics, polar and van der Waals contacts (Figures 5.30 and 5.31). Residues at the N terminal tail from one subunit and cationic residues R13 and R14 from the middle loop of another subunit appeared to establish interactions with LPS molecules (Figures 5.30 and 5.31). As seen, residues R13 and R14 form multiple hydrogen bonds with hydroxyl groups of LPS (Figure 5.31). Moreover, residues, P5′, V6′, P7′ and I8′ interact with the sugar rings of LPS through non-polar contacts (Figure 5.30).

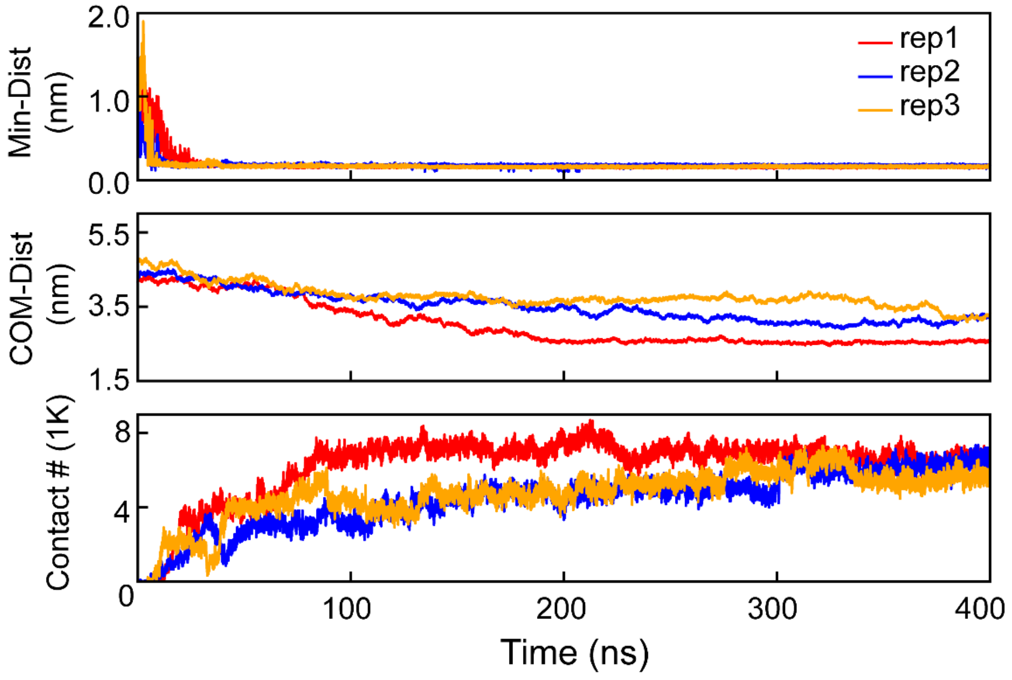

Figure 5.29| MD Simulation: LPS/thanatin interactions. Time revolutions of thanatin-LPS minimum distances, center of mass distances (in z direction) and the number of contacts in LPS/DPPE bilayer during MD simulations reveal that dimeric thanatin rapidly binds to LPS lipid surface.

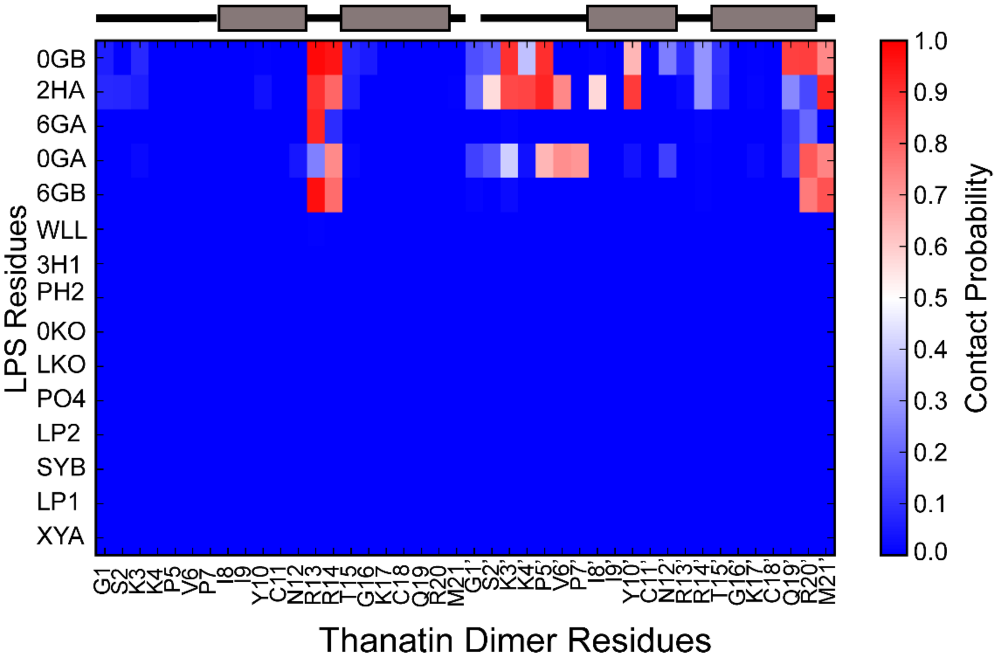

Figure 5.30| Contact Probability: LPS/thanatin dimer residues. Contact plot showing probability of each residue in dimeric thanatin with various LPS residues indicates that N terminal residues interact with the sugar rings of LPS molecules. The secondary structures of thanatin have been shown at the top of the panel, thick bars (in light black) represent β-strands whereas other structural elements are in thin black line.

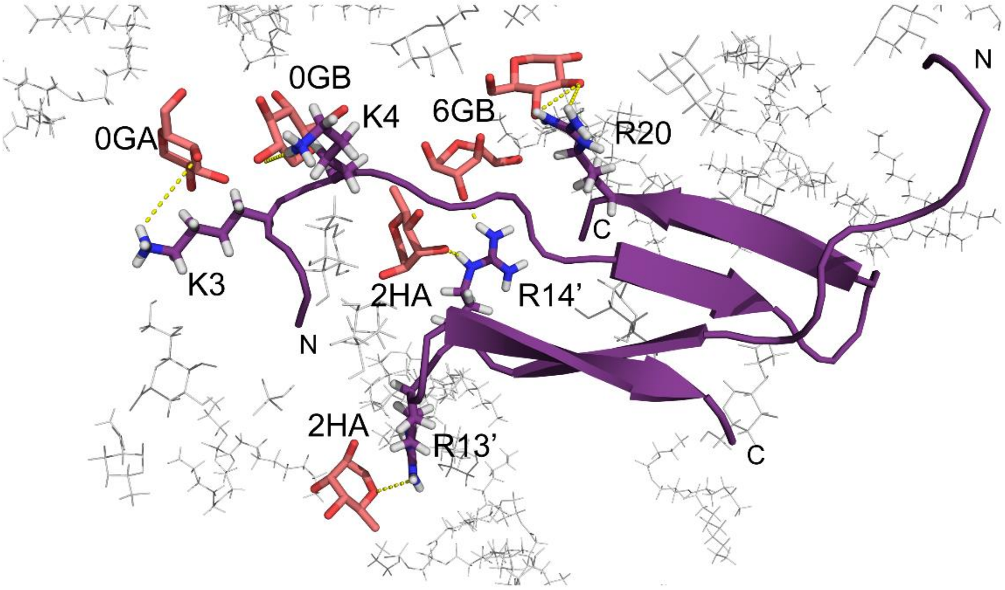

Figure 5.31| Binding model of thanatin dimer and LPS. Dimeric thanatin interacts with LPS molecules utilizing residues at the N terminus of one subunit and residues in the turn from another subunit.

5.3 Discussion

In order to correlate LPS-thanatin structures and activity, critical residues Y10, M21, R13 and R14 of thanatin, involved in β-sheet dimerization and LPS recognition were mutated and antimicrobial activities of these analogs were examined against Gram-negative and Gram-positive bacteria (Table 5.4). Replacements of aromatic/hydrophobic packing residues Y10 and M21 to Ala has substantially decreased antimicrobial activity as indicated by higher MIC values of the analog peptide Y10M21AA (Table 5.4). Interestingly, thanatin analog M21F, containing a substitution of residue M21 to Phe, demonstrated lower MICs compared to the native thanatin. As seen, MICs ranging from 1 to 4 μM for the analogs R13A, R14A delineated somewhat lower antibacterial activity compared to the native thanatin. However, R13R14AA analog was found to be largely inactive. Further, the analog peptides M21F, Y10M21AA and R13R14AA assumed monomeric β-hairpin structure in free solution (Figures 5.2 & 5.9). However, dimeric structures were obtained in complex with LPS (Figures 5.7, 5.13 and 5.17). As expected, the dimeric structure of M21F revealed that the Phe residues, F21 and F21' showed enhanced close aromatic-aromatic stacking interactions with residues Y10 and Y10' (Figure 5.7). Such aromatic stacking interactions are known to be involved in LPS interactions and results in superior antimicrobial activity. The dimeric structures of the analogs with impaired activity, Y10M21AA and R13R14AA in LPS may be rather surprizing. However, structural analyses indicated that the dimeric β-sheet structures of the analogs delineated significant variations (Fig. 5.19). Regardless, these observations strongly demonstrated that the β-hairpin structure of thanatin contains an intrinsic tendency to form multi-stranded β-sheet structures in complex with LPS. Dansyl fluorescence analyses of thanatin analogs in presence of varying LPS concentrations showed that all of these mutants were able to bind to LPS with comparable affinity with similar Hill coefficient, indicating potential plasticity in LPS/thanatin interactions (Figure 5.20 and Table 5.7). However, BC probe displacement data demonstrated ED_{50} of the following order Thanatin>M21F>Y10M21AA>R13R14AA (Figure 5.21 and Table 5.8). The least active peptide R13R14AA disclosed the highest ED_{50} of 3.2 μM. Binding affinity and thermodynamic parameters of thanatin and its analogs were analysed using ITC. Thanatin and thanatin M21F showed a negative change in entropy as opposed to loss-in function mutants (Table 5.9 & 4.3). Zeta potential measurement illustrated in Figure 5.25 showed that thanatin analogs were inefficient in completely neutralizing the zeta potential of *E. coli* cells. FITC-LPS fluorescence spectra (Figure 5.26) of LPS were obtained in presence of analogs of thanatin. The M21F peptide demonstrated more quenching of FITC-LPS fluorescence as compared to the Y10M21AA and R13R14AA analogs. Perturbation of LPS micelles by analog peptides were further investigated using ^{31}P NMR. The M21F analog had rendered extensive changes in terms of line width and chemical shifts of the ^{31}P resonances of LPS, whereas limited changes of ^{31}P signals were detected in case of Y10M21AA and R13R14AA analogs (Figure 5.28). The aforementioned investigations clearly established that the structural states of LPS are more influenced or perturbed upon binding to the active peptides thanatin and M21F. By contrast, the inactive analogs Y10M21AA and R13R14AA demonstrated binding to LPS but they were unable to generate structural changes to the LPS structures.

MD simulation studies in LPS-DPPE bilayer demonstrated that dimeric thanatin can interact with multiple LPS molecules and is dynamical in nature. Thanatin interactions were predominantly observed with the sugar and phosphate head groups of LPS molecules (Figure 5.30). The basic residues e.g. K3, K4, R13, R14 and K17, belonging to the cationic patches were found to be primarily involved in LPS recognition (Figure 5.31). Antibacterial activity and biophysical studies of the analog peptide R13R14AA indicated critical involvement of residues R13 and R14. The atomic-resolution structure of thanatin solved in complex with LPS micelles thus provides mechanistic insights on bacterial cell agglutination. The antiparallel topology of the dimeric structure of thanatin would potentially allow binding of two or more LPS molecules at the distal ends. An agglutination model by dimeric thanatin is illustrated in Figure 5.32.

In conclusion, bacterial cell killing by agglutination have been reported for a number of antimicrobial peptides, proteins and recently for amyloid Aβ peptides[100-102]. However, the mechanism of cell agglutination remains largely unclear. One of the key steps in cell agglutination of Gram-negative bacteria is the binding of AMPs with the outer membrane LPS. Self-assembly of AMPs and antimicrobial proteins in LPS are thought be an essential event in cell agglutination mechanism. The atomic structure, mutational analyses and MD simulations of thanatin in LPS lipid bilayer provided molecular insights on its interaction with LPS-outer membrane and into bacterial cell agglutination mechanism. The detailed mechanism of action of thanatin and its analogs can be used as a template for further development of novel cell agglutinating antimicrobial peptides.

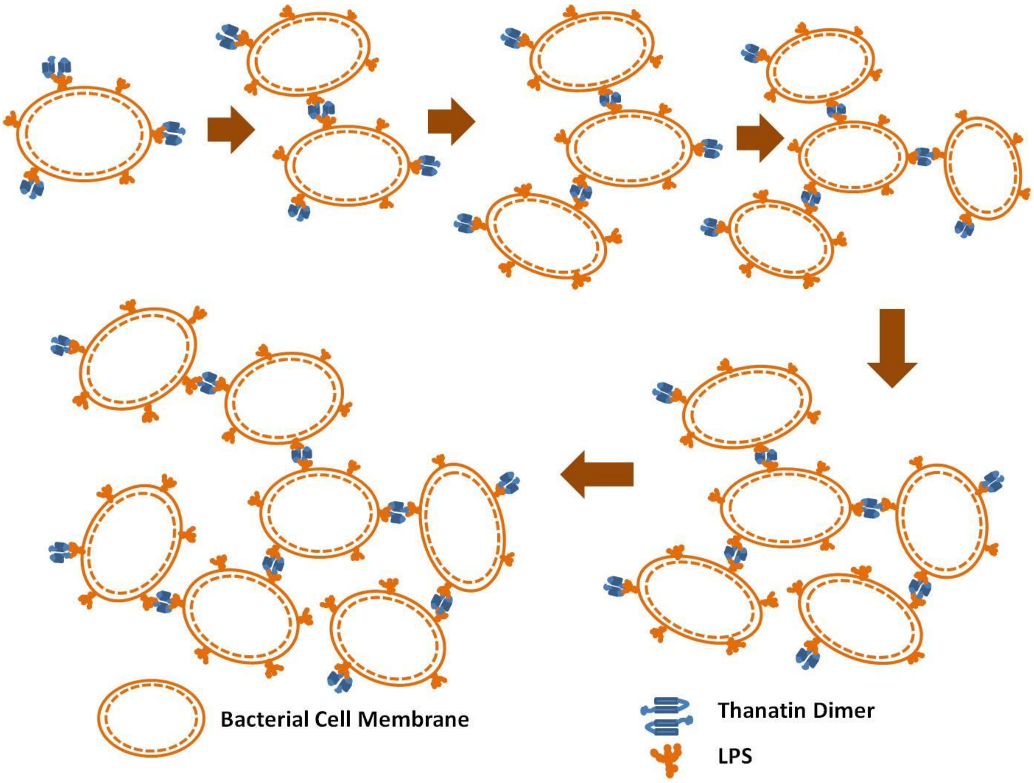

Figure 5.32| Mechanism of agglutination by thanatin. A schematic illustration of bacterial cell agglutination by thanatin. Thanatin dimerizes in presence of LPS, providing multiple binding sites. Therefore, it can interact with multiple bacterial cells at its distal ends. Furthermore, each bacterial cell can interact with multiple thanatin dimers. This leads to aggregation of a number of bacterial cells in to large clumps

Chapter 6

Antimicrobial Properties in Furin Prodomain

Furin prodomain is known for exhibiting anti-cancerous properties. In this chapter, various truncations from the prodomain are screened for their antimicrobial properties. Interestingly, the peptide YR26, derived from the central region of furin prodomain exhibits broad-range antimicrobial properties and non-toxicity towards mammalian cells. Further, various truncations are made in YR26 to optimize high antimicrobial and low cytotoxic properties of the peptides. To gain mechanistic insight on the mode of action, cell membrane permeabilization assays and other biophysical characterizations in presence of LPS and cell mimicking liposomes are conducted. Analyses of the biophysical characterizations of furin prodomain derived active peptides strongly indicate agglutination as their mode of action. Moreover, 3D structure of YR26 in presence if SDS micelles is determined to understand the mechanism of action and structural – function correlation. Finally, a simulation model of YR26/LPS complex is presented to elucidate the mechanism of agglutination.

6.1 Introduction

Furin is the first discovered mammalian proprotein convertase (PC)[133, 134]. It is also gaining interest as a target for drug development to inhibit the processing of proproteins which are involved in a number of human diseases such as Alzheimer's disease and cancer[135]. Furin is enriched in the Golgi apparatus where it activates other proteins by cleaving them downstream of a basic amino acid target sequence (Arg-X-(Arg/Lys)-Arg')[136]. The proprotein form of furin itself undergoes a two-step autocatalytic removal of the prodomain to activate the furin endoprotease. The RER-localized cleavage at the site R_{78}-T-K-R_{81}~ is a necessary but not a sufficient condition to activate furin. Following the cleavage in RER, the prodomain still remains associated with the enzyme and still inhibits the function of furin. A second cleavage downstream of a P6 arginine site (R_{44}-G-V-T-K-R_{49}~) at acidic pH in TGN is required for complete removal of the furin inhibiting prodomain and activate the enzyme (Figure 6.1)[137, 138]. This compartment-dependent activation of furin and the delay in proteolytic activation inhibits the enzyme to cleave substrates prematurely[137].

NMR spectroscopy was used to determine the backbone conformations of 81-residues long prodomain of furin in presence of 50% TFE (v/v). The prodomain encompasses four helical segments comprising residues V3-A9 in helix 1, A17-H26 in helix 2, L31-R44 in helix 3 and Q66-K80 in helix 4[137]. The interim residues R11-G15 between helix 1&2 show a propensity towards β-strand. Residues between helices 2&3, 3&4 assume a flexible conformation. Figure 6.2 illustrates a well-defined helix-loop-helix conformation of helix2-loop-helix3 in the pro-domain[137].

Furin prodomain is of therapeutic value also. Overexpression of furin prosegment is known to decrease and abolish the invasive and proliferative abilities of four malignant HNSCC cell lines[139]. Furthermore, this affects the activation of crucial proteases, growth factors and growth factor receptors involved. In this work, prodomain region of furin was studied to further exploit its therapeutic value as a potential antimicrobial agent[139].

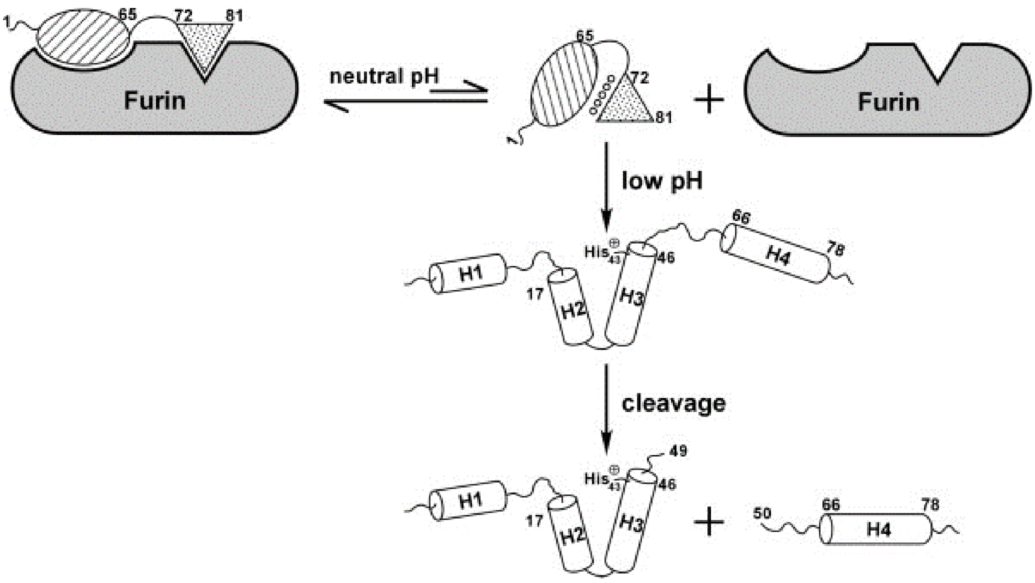

Figure 6.1| Activation of furin. The catalytically active C-terminus region (residues 72-81) prefers a different conformation to bind from the N- terminal region (residues 17-49) which prefers a helix-loop-helix conformation. At neutral pH, the prodomain segment forms extensive contacts with furin. However, in the acidic environment of TGN, the equilibrium shifts towards a partially folded conformational state of prodomain which is then cleaved by the released furin into permanent peptide fractions.

Figure taken from ref.[137]

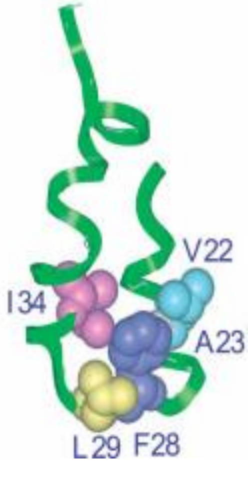

Figure 6.2| Helix2-loop-helix3 conformation in furin prodomain. Representative structure of N-terminus region (P16-R49) of the furin prodomain. The figure illustrates the sidechain-sidechain interactions involving residues V22, A23, F28, L29 and I34 in the helix-loop-helix conformation of the prodomain.
Figure taken from ref.[137]

A number of antimicrobial peptides have been derived from N-terminus region of human proteins in recent years[140]. Lactoferrin is a glycoprotein which is present in most biological fluids of mammals. It is released as an inflammatory response from activated neutrophils and is considered to be an effective broad-spectrum host defense peptide against pathogens[140]. Inhibition of bacterial growth by sequestering iron from the bacterial pathogens is a widely believed mode of action of lactoferrin[140]. However, a single active peptide was isolated from the N-termius region of human lactoferrin, following gastric pepsin cleavage[141]. This region is distinct from its iron-binding sites and is devoid of the Tyr and His residues which are responsible for chelating metal ions in peptides and proteins. The active peptide mainly consists of a loop of 18 amino acid residues having a disulphide bond between residues Cys20-Cys37. Furthermore, its synthetic analogs also demonstrated potent antimicrobial activity against both Gram-positive and Gram-negative bacteria[141]. Similarly, an active peptide from the N-terminus region of bovine lactoferrin was also derived. This active peptide from bovine lactoferrin showed a higher efficacy in killing bacteria than that derived from human lactoferrin[141]. This region of lactoferrin might also contribute to its antimicrobial activity by a mechanism distinct from metal chelation.

Lysozyme is an antimicrobial enzyme and is a part of the innate immune system. It is abundantly found in biological fluids such as tears, saliva, human milk and mucus[142]. Pepsin cleaves chicken lysozyme in conditions relevant to the stomach of a new born and generates five antimicrobial peptide motifs[143]. Corresponding peptides were derived from human lysozymes and were found to be extremely potent against Gram-negative and Gram-positive bacteria and the fungus *Candida albicans*[143]. Human milk lysozyme is considered to be crucial in defending the gastrointestinal tract of the newborns against bacterial infections[143]. Multiple antimicrobial peptide motifs within its N-terminal domain can facilitate in development of new drugs treating infectious diseases[143].

In the present study, different regions of the furin prodomain were truncated and tested for antimicrobial activity. Various membrane permeabilization tests and other biophysical experiments were conducted on the active segment to gain insight on the mechanism of antimicrobial action. Furthermore, the most active segment was expressed and purified to carry out NMR experiments and determine its 3D structure in presence of anionic SDS micelles.

6.2 Results

6.2.1 Minimum Inhibitory Concentration

Various truncations in furin prodomain were made (Figure 6.3) and MIC values for the different segments were determined in order to screen the antimicrobial region in the prodomain. MIC values of the truncated segments against four Gram-positive and four Gram-negative bacteria are shown in Table 6.1.

Figure 6.3| Screening furin prodomain for antimicrobial activity. Different truncations of prodomain from the N-terminus, C-terminus and central regions were synthetically prepared in order to screen for antimicrobial activity.

Table 6.1| Minimum Inhibitory Concentration to screen various prodomain truncations. Minimum inhibitory concentration (µM) against EC: *Escherichia coli*; PA: *Pseudomonas aeruginosa*; SE: *Salmonella enterica*; KP: *Klebsiella pneumoniae*; SA: *Staphylococcus aureus*; BS: *Bacillus subtilis*; SP: *Streptococcus pyogenes*; EF: *Enterococcus faecalis*.

	Gram – negative (µM)				**Gram – positive (µM)**			
	EC	**PA**	**SE**	**KP**	**BS**	**SA**	**SP**	**EF**
VR15	>100	>100	>100	>100	>100	>100	>100	>100
QR20	>100	>100	>100	>100	>100	>100	>100	>100
RR25	>100	>100	>100	>100	>100	>100	>100	>100
SR30	>100	>100	>100	>100	>100	>100	>100	>100
TR35	>100	>100	>100	>100	>100	>100	>100	>100
YR26	2	4	4	2	2	4	4	4
RV23	4	>100	>100	>100	>100	>100	>100	>100
QF35	20	>100	>100	>100	>100	>100	>100	>100

As evident from Table 6.1, all the peptides derived from the C-terminus region of furin prodomain are inactive against both Gram-positive and Gram-negative bacteria. Peptides from the N-terminus region are moderately active only against *E. coli*. Interestingly, the peptides derived from the central region of furin prodomain demonstrate extremely potent bactericidal activity against all 8 types of tested bacteria.

In order to further optimize the antimicrobial activity, various truncations were made in the active region (Figure 6.4) and MIC was determined against four Gram-positive and four Gram-negative bacteria (Table 6.2).

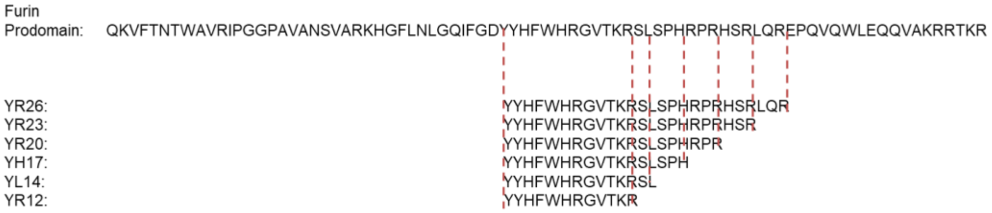

Figure 6.4| Truncations made in the active region of furin prodomain. These truncated peptides were further tested for MIC to optimize the antimicrobial activity.

Table 6.2| Antimicrobial activity in furin prodomain. Minimum inhibitory concentration (µM) against EC: *Escherichia coli*; PA: *Pseudomonas aeruginosa*; SE: *Salmonella enterica*; KP: *Klebsiella pneumoniae*; SA: *Staphylococcus aureus*; BS: *Bacillus subtilis*; SP: *Streptococcus pyogenes*; EF: *Enterococcus faecalis*.

	Gram – negative (µM)				**Gram – positive (µM)**			
	EC	**PA**	**SE**	**KP**	**BS**	**SA**	**SP**	**EF**
YR12	40	40	40	40	40	30	70	30
YL14	30	60	80	70	60	80	>100	70
YH17	30	>100	>100	>100	>100	>100	>100	>100
YR20	6	8	8	6	6	6	15	6
YR23	4	4	4	2	4	4	6	4
YR26	2	4	4	2	2	4	4	4

Peptides YR26 and YR23 are extremely potent against all 8 bacterial strains. YR20 is moderately active against the tested strains. However, on further truncating the antimicrobial peptide, the activity gets highly impaired.

6.2.2 Hemolysis Assay

The selectivity of the truncated peptides in the active region of the prodomain was examined by testing them on human erythrocytes. To check their hemolytic activity, desired concentrations of the peptides were incubated with erythrocytes at 37°C for 1 hr. Figure 6.5 illustrates % hemolysis of erythrocytes by these peptides in varying concentrations. Peptides were found to be non-hemolytic till 150 μM concentration. Even at a concentration as high as 300 μM, the active peptide YR26 is 25% hemolytic. Furthermore, YR23 – an equally active peptide shows no % hemolysis at 300 μM concentration. It is interesting to note that this concentration is 75 times its MIC value.

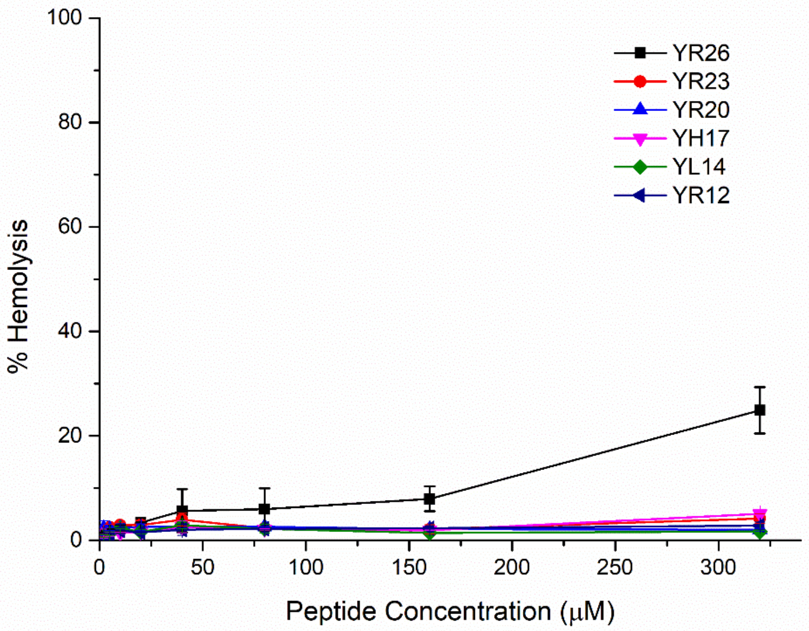

Figure 6.5| Hemolysis assay. Low % hemolysis of the active furin prodomain derived peptides emphasizes on the high selectivity of these peptides against broad range of bacterial strains.

6.2.3 Cytotoxicity Test

The active peptides YR26, YR23 and YR20 were further incubated with NIH3T3 mouse cell line for 4 hours at selected test concentrations and % cell viability for each peptide was calculated respectively (Figure 6.6). At ~10 times the MIC concentration (50 μM), the cells are 100% viable in presence of both YR26 and YR23. On further increasing the concentration of YR26, the cell viability decreases drastically. Interestingly, at all the test concentrations of YR23, the cell viability was observed to be greater than 90%. The cell viability for the moderately active peptide YR20 was greater than 70% for all test concentrations. Taken together, the MIC, hemolysis and cytotoxicity data strongly implies that the peptide YR23 is extremely selective towards bacterial cells and is not toxic for mammalian cells.

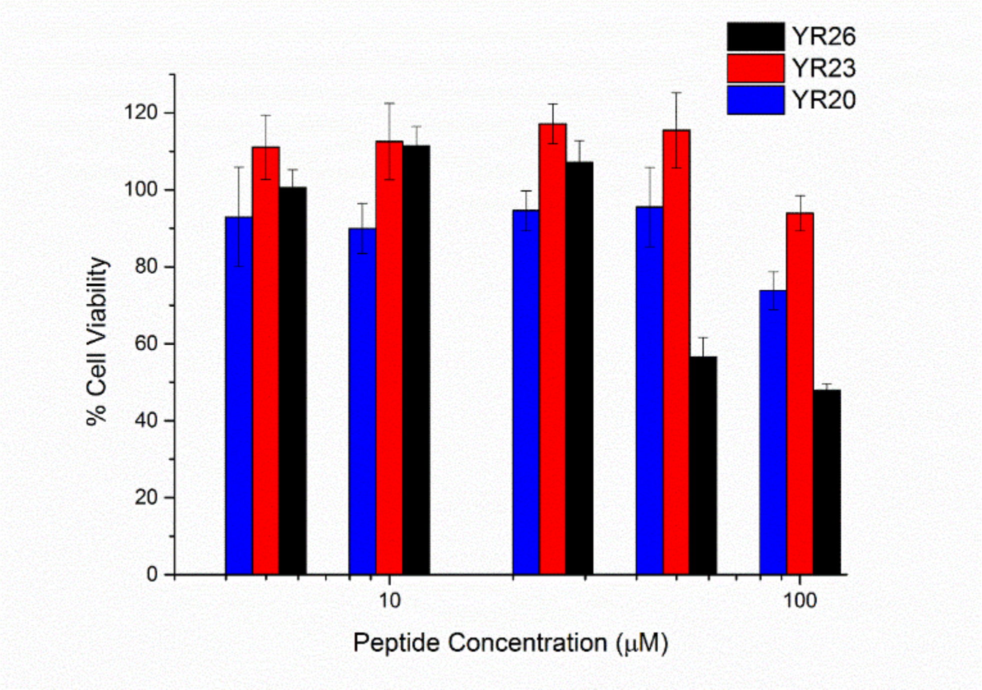

Figure 6.6| % cell viability. The figure illustrates low cytotoxicity of all the three active peptides against NIH3T3 mammalian cell line.

In order to gain insights on the mode of action, outer and inner membrane permeabilization by the truncated peptides in *E. coli* cells was examined using fluorescence spectroscopy. Furthermore, binding of these peptides to LPS, SDS and DPC micelles were examined by observing the intrinsic tryptophan fluorescence emission spectra in presence and absence of the aforementioned micelles.

6.2.4 Outer Membrane Permeabilization Assay

The ability of the furin prodomain derived peptides was assessed with the help of a fluorescent probe, NPN. N-phenyl-1-naphthylamine turns fluorescent in hydrophobic environment[144]. An intact outer membrane excludes hydrophobic NPN. However, once the outer membrane loses its integrity, NPN can easily enter in the phospholipid bilayer resulting in a substantial increase in fluorescence. The increase in the fluorescence intensity in the emission spectra of NPN in presence of increasing peptide concentrations indicates that these peptides are able to permeabilize the outer cell membrane of the tested *E. coli* strain. As expected, the least active peptide YR12 is the least efficient in permeabilizing the outer cell membrane.

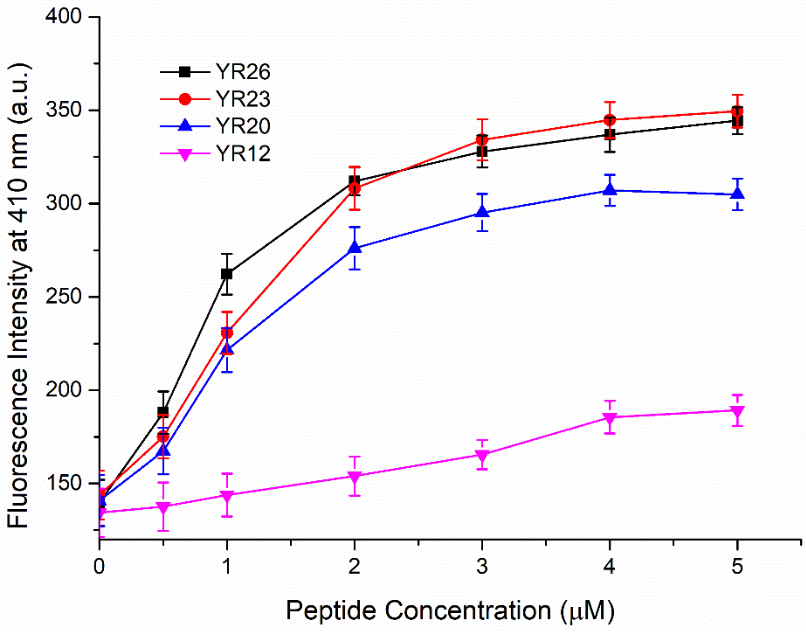

Figure 6.7| Outer membrane permeability. The ability of the peptides to permeabilize the outer membrane of *E. coli* cells was tested by examining the fluorescence intensity of the NPN fluorescent probe in presence of the bacterial cells and varying peptide concentrations. The increase in fluorescence emission intensity of the probe indicates that these peptides permeabilize the outer membrane of the tested bacterial strain.

6.2.5 Inner Membrane Permeabilization Assay

SYTOX green is a dye that fluoresces strongly after exclusively binding to nucleic acids. Inner membrane permeabilizing ability of the antimicrobial peptides was tested by using SYTOX green as a fluorescent probe. Addition of pore-forming AMPs to a mixture of the fluorescent dye and *E. coli* cells would lead to an increase in the fluorescence intensity of the emission spectra of the probe[144]. However, in presence of the active peptides derived from furin prodomain, the fluorescence intensity is quenched (Figure 6.8). This diminution of the intensity indicates a higher order of association of the *E. coli* cells upon binding with the active peptides. The percentage reduction in the emission intensity of SYTOX green is depicted in the Table 6.3. Interestingly, the most active peptide is able to quench the fluorescence intensity most effectively. The results indicate that these furin derived peptides have a non-membranolytic mode of action.

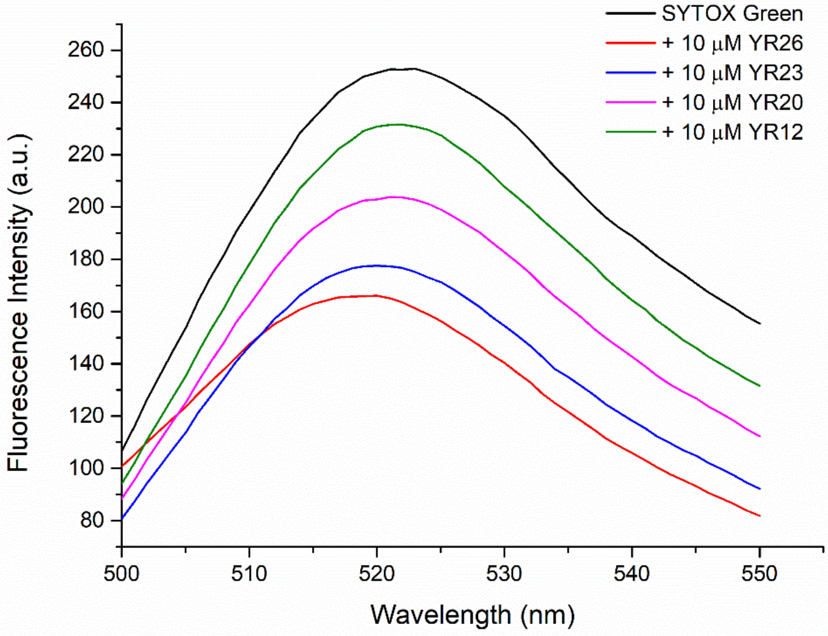

Figure 6.8| Inner membrane permeability. The ability of the peptides to permeabilize the iiner membrane of *E. coli* cells was tested by examining the fluorescence intensity of SYTOX green in presence of the bacterial cells and varying peptide concentrations. The diminution of fluorescence emission intensity of the dye indicates that these peptides follow a non-membranolytic mode of action.

Table 6.3| Inner membrane permeability. The diminution of fluorescence emission intensity of the dye indicates that these peptides aggregate the bacterial cells into larger clumps.

Peptide	% Reduction in Intensity
YR12	16.1
YR20	20.3
YR23	32.9
YR26	34.3

6.2.6 Intrinsic Tryptophan Fluorescence Assay

Tryptophan is an excellent intrinsic fluorescent probe to study the binding of a peptide with hydrophobic micelles such as LPS, SDS and DPC. In aqueous solution, tryptophan has an emission maxima at 356-360 nm. However, in hydrophobic environment, there is a concomitant blue shift in the fluorescence emission maxima[144]. To study the binding of the active peptides to LPS, peptides were titrated with LPS and the fluorescence for each LPS concentration was recorded. Figure 6.9 shows concomitant blue shift in fluorescence emission maxima of intrinsic tryptophan of YR26 in presence of higher LPS concentrations. Normalized change in fluorescence intensity maxima was calculated as change in intensity maxima divided by basal fluorescence intensity maxima. The normalized change was plotted against LPS concentration and dissociation constant was determined by fitting the plot in Hill’s equation. Figure 6.10 illustrates Hill’s plot for the active peptides YR26, YR23 and YR20. It is interesting to note that Hill’s coefficient is ~2 for all the peptides, indicating that they bind to 2 LPS units at a time (Table 6.4). Furthermore, the shift in fluorescence emission intensity maxima was examined in presence of anionic SDS micelles and zwitterionic DPC micelles. In each case, the peptides exhibit a blue shift, confirming the micelle-peptide binding (Table 6.5). The inactive peptide TR35 from the C-terminus region of the furin prodomain showed little to no change in the wavelength of fluorescence intensity maxima.

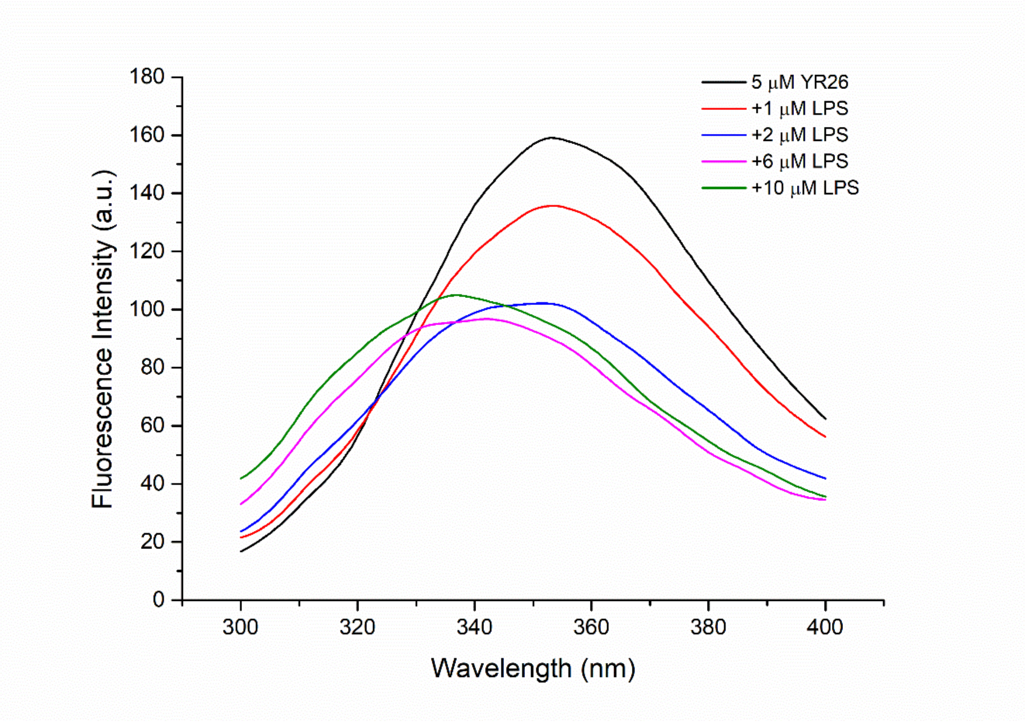

Figure 6.9| Intrinsic tryptophan fluorescence emission spectra of YR26. The concomitant blue shift in presence of higher LPS concentrations confirms binding of YR26 with LPS.

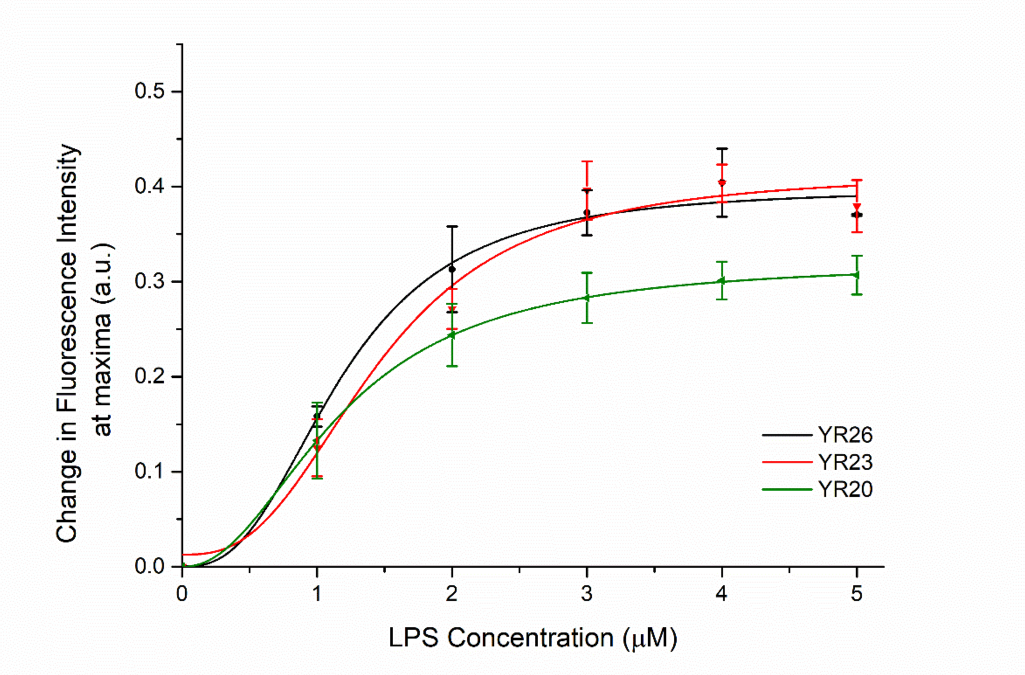

Figure 6.10| Hill's plot. Normalized change in fluorescence emission intensity of intrinsic tryptophan was plotted against LPS concentration and the plot was fitted with Hill's equation to calculate K_d.

Table 6.4| Calculation of dissociation constant. Intrinsic tryptophan fluorescence assay was examined to acquire the input data for the Hill's equation to determine LPS/peptide binding parameters.

Peptide	**Dissociation Constant, K_d (μM)**	**Hill's Cosfficient, n**
YR26	1.18	2.65
YR23	1.45	2.71
YR20	1.17	2.15

Table 6.5| Intrinsic tryptophan fluorescence assay. The blue shift in the emission intensity maxima suggests binding of the peptides with the micelles.

Peptide	**With LPS ($\Delta\lambda_{max}$, nm)**	**With DPC ($\Delta\lambda_{max}$, nm)**	**With SDS ($\Delta\lambda_{max}$, nm)**
YR12	14	14	12
YR20	17	12	16
YR23	18	18	16
YR26	21	18	22
RV23	13	16	18
TR35	1	2	2

6.2.7 Isothermal Titration Calorimetry

Thermodynamic parameters governing the interaction of LPS and the active peptides were determinted using ITC. The binding profiles of the peptides with LPS are depicted in Figure 6.11. 500 μM stock solution of the test peptide was titrated in 50 μM LPS in the titration cell to determine the binding parameters. The inverted titration peaks and high negative change in enthalpy suggest that the binding is an enthalpy driven exothermic process. The negative change in entropy suggests higher order or association. The exothermic profile of binding suggests predominant electrostatic interactions. Table 6.6 illustrates the thermodynamic parameters and the dissociation constant for LPS/peptide interactions. The moderately active peptide YR12 showed the poorest binding to LPS.

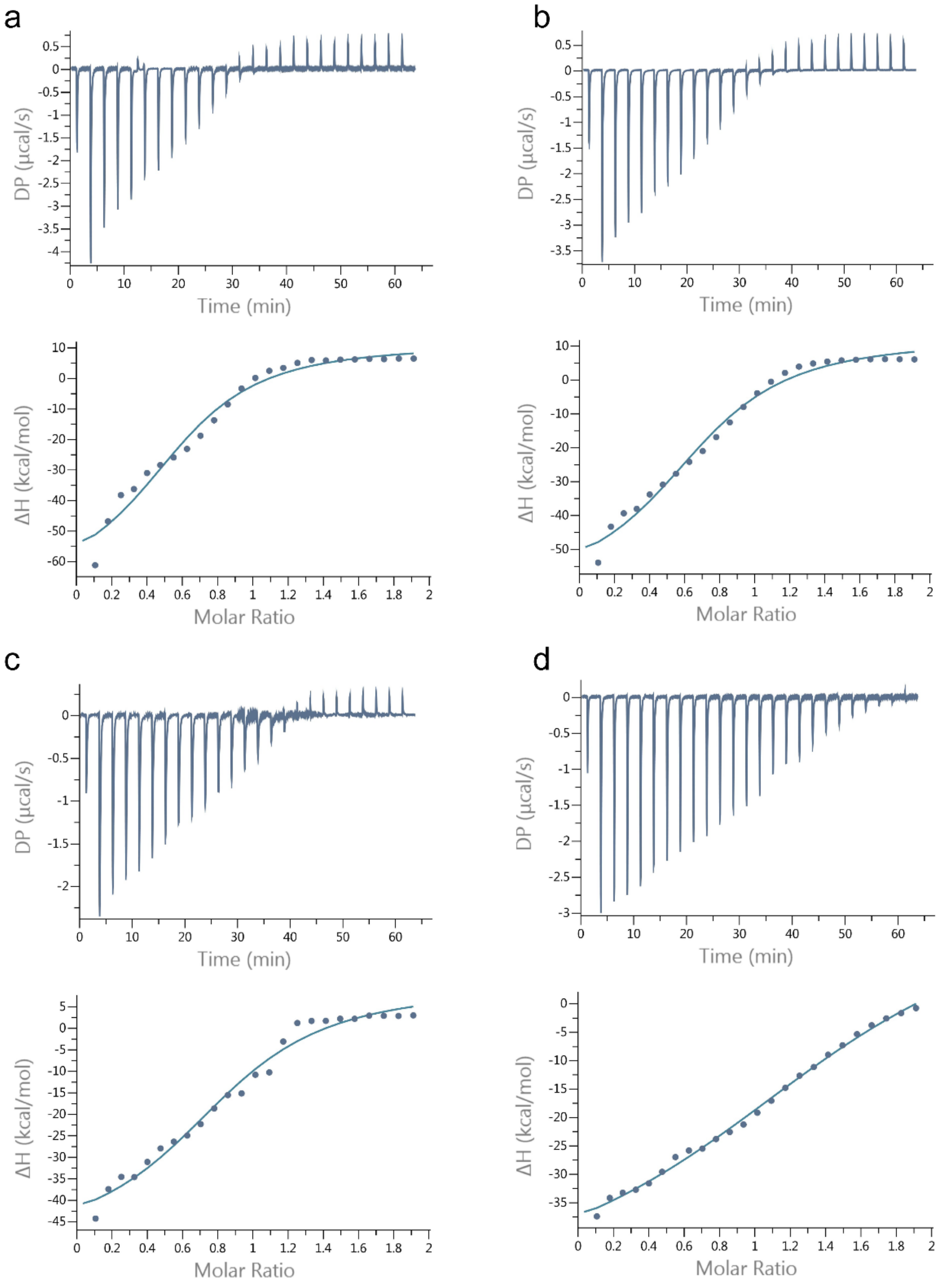

Figure 6.11| Isothermal titration calorimetry. ITC binding profiles for **a.** YR26/LPS, **b.** YR23/LPS, **c.** YR20/LPS and **d.** YR12/LPS.

Table 6.6| ITC binding parameters. 500 µM of test peptide in syringe was titrated in 50 µM LPS in titration cell at 37°C, pH 7.

Peptide	K_d (µM)	ΔH (Kcal/mol)	ΔG (Kcal/mol)	-TΔS (Kcal/mol)
YR26	6.98	-80	-7.32	72.7
YR23	7.09	-74	-7.31	66.7
YR20	7.65	-59.5	-7.26	52.2
YR12	19.00	-69	-6.70	62.3

6.2.8 FITC-LPS Fluorescence Assay

FITC is a fluorescent probe which is situated in the hydrophobic core of the LPS micelles. However, upon interaction with pore-forming AMPs, the probe gets exposed leading to an increase in its fluorescence emission intensity[112]. On the other hand, diminution of the emission intensity indicates a higher order of association. Figure 6.12 illustrates the quenching of emission intensity signal of FITC in presence of increasing concentrations of YR26. This observation strongly suggests that interaction with these peptides leads to aggregation of FITC-LPS micelles in large agglutinates. The % reduction in fluorescence emission intensity of FITC-LPS in presence of the active furin prodomain derived peptides as compared to the emission intensity of free FITC-LPS is tabulated in Table 6.7. All the active and moderately active peptides are extremely potent in quenching the emission intensity and thereby, aggregating LPS micelles. However, the inactive peptide from C-terminus of furin prodomain, TR 35 is not able to decrease the emission intensity of the fluorescent probe and is therefore, not able to agglutinate LPS micelles.

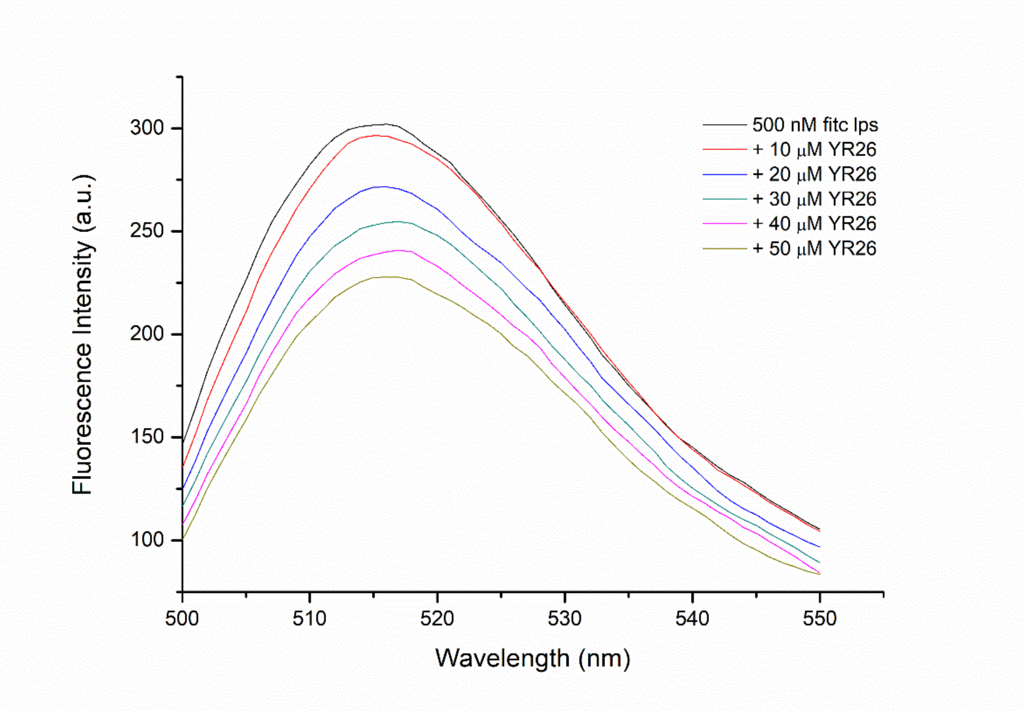

Figure 6.12| FITC-LPS fluorescence assay. The decrease in intensity of the fluorescence emission intensity of FITC-LPS in presence of increasing YR26 concentration clearly indicates its ability to agglutinate LPS micelles.

Table 6.7| Diminution in emission intensity of FITC-LPS. The fluorescence emission intensity of FITC-LPS decreases as the peptides interact to agglutinate the LPS-micelles.

Peptide	**% Reduction in Intensity**
YR12	22
YR20	24
YR23	25
YR26	25
TR35	5

6.2.9 Zeta Potential

The surface charge of *E. coli* cells in absence and presence of LPS was determined by examining their zeta potential. Gram-negative bacteria exhibit a high negative zeta potential due to the presence of phosphate and carboxylate groups in the outer membrane surface. On interaction with pore-forming AMPs, the zeta potential of the bacterial cells should increase, eventually neutralize them and may reach a high positive value. Figure 6.13 illustrates the zeta potential of the *E. coli* cells in presence of the furin prodomain derived active AMPs. The active peptides YR26 and YR23 are able to effectively neutralize the surface charge of the bacterial cells. However, the moderately active peptide is not potent in surface charge neutralization. Instead, it stabilizes the zeta potential of the tested *E. coli* cells at a lower negative value. These observations corroborate the analysis from outer membrane permeability assay wherein, the active peptides were able to permeabilize the outer membrane of the *E. coli* cells and increase the emission intensity of NPN many folds. However, the moderately active peptide YR12 was not so potent in doing so.

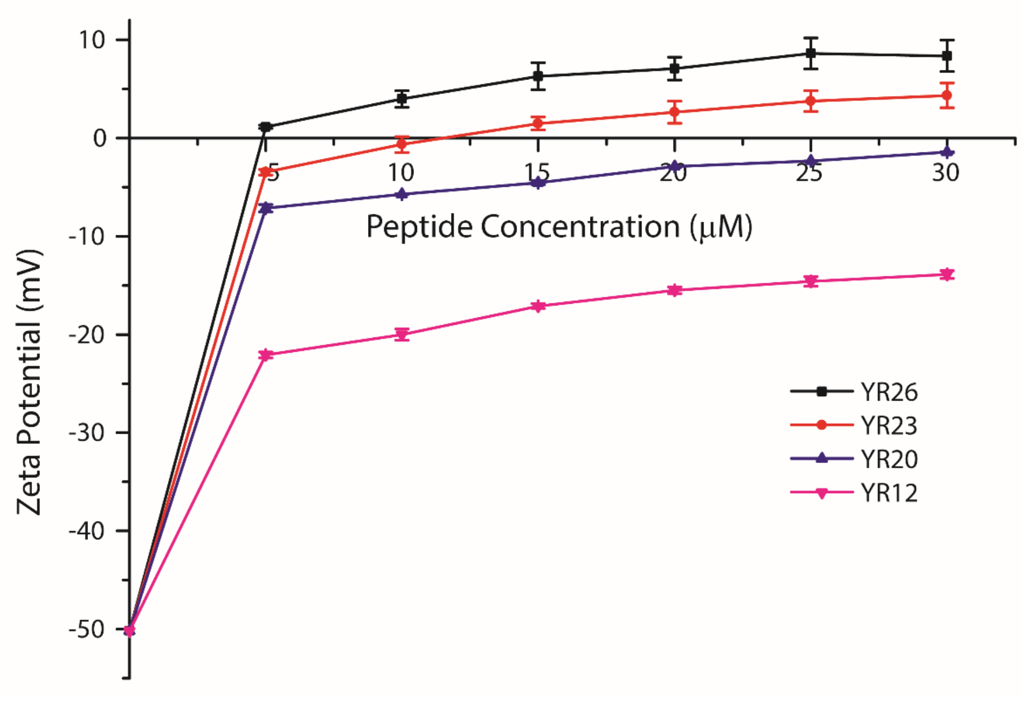

Figure 6.13| Zeta potential measurement. The active peptides are able to efficiently neutralize the zeta potential of *E. coli* cells in phosphate buffer, pH 7.

6.2.10 Interaction of the AMPs with liposomes

To further gain insights on the mechanism of action and selectivity, POPC-POPG (3:1) liposomes mimicking bacterial cells and POPC liposome mimicking mammalian cells were prepared and their interaction with the AMPs were examined. The concomitant blue shift in the intrinsic tryptophan fluorescence emission intensity of YR26 in presence of increasing POPC-POPG liposome concentration indicates binding of YR26/POPC-POPG (Figure 6.14). However, there is little to no shift in the tryptophan emission intensity of YR26 in presence of zwitterionic POPC (Figure 6.15). Table 6.8 depicts shift in fluorescence intensity maxima of furin prodomain derived active peptides in presence of POPC and POPC-POPG. All the tested peptides interact with the bacterial cell mimicking POPC-POPG liposomes. Whereas, there are little or no interactions with the zwitterionic mammalian cell mimicking POPC liposomes. This observation is consistent with the high selectivity that these peptides present towards bacterial cells.

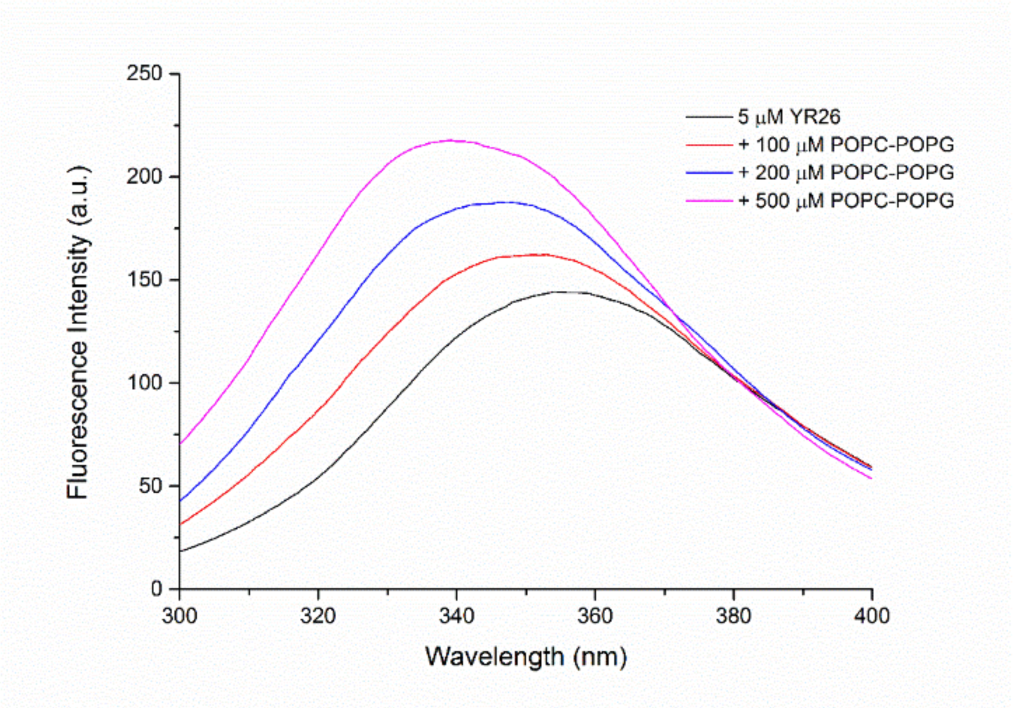

Figure 6.14| YR26/POPC-POPG interaction. Intrinsic tryptophan fluorescence was used to examine the interaction of the peptide with the bacterial cell mimicking liposomes. The blue shift in the emission intensity maxima suggest a strong peptide/liposome binding.

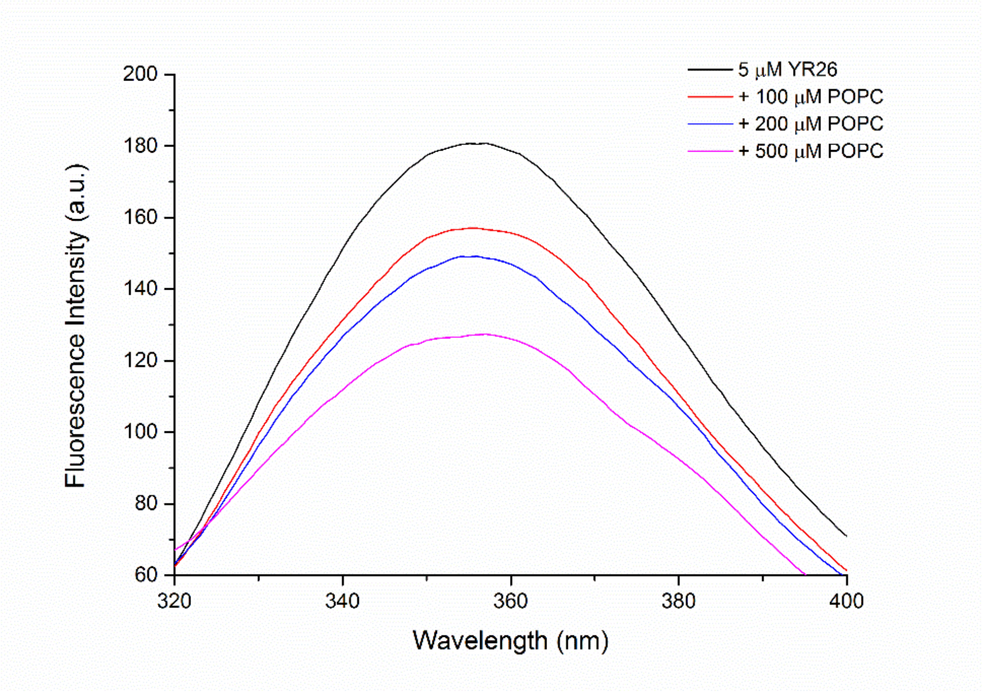

Figure 6.15| YR26/POPC interaction. Intrinsic tryptophan fluorescence was used to examine the interaction of the peptide with zwitterionic POPC liposomes. No significant shift in the emission intensity maxima suggest that these peptides do not interact and hence, are not toxic to the mammalian cells.

Table 6.8| Intrinsic tryptophan fluorescence assay with liposomes. Blue shift of emission maxima in presence of anionic POPC-POPG liposomes and negligible shift in presence of zwitterionic POPC liposomes indicate the high selectivity of the tested AMPs towards bacterial cells.

	$\Delta\lambda_{max}$ (nm)	
	POPC-POPG	**POPC**
YR26	21	4
YR23	19	1
YR20	20	3
YR12	19	1

6.2.11 Calcein Leakage Assay

POPC-POPG and POPC liposomes entrapped with the fluorescent dye, calcein were used to examine the membrane permeabilization ability of the active AMPs. If a peptide is able to permeabilize the liposomes, entrapped calcein leaks out resulting in an enhanced emission intensity[145]. The change in fluorescene emission intensity of calcein entrapped in POPC-POPG and POPC liposomes in presence of the active peptides are illustrated in Figures 6.16 and 6.17, respectively. In presence of peptides, the fluorescence emission intensity of calcein has been diminished. This indicates that these peptides are not able to permeabilize the liposomes. The marked reduction of fluorescence intensity in case of POPC-POPG liposomes also directs towards a higher order of association of these liposomes in presence of the active peptides. Moreover, the diminution of the emission intensity is several folds more in case of anionic POPC-POPG liposomes when compared to mammalian cell mimic POPC liposomes. The result strongly suggests that these peptides follow a non-membranolytic mode of action.

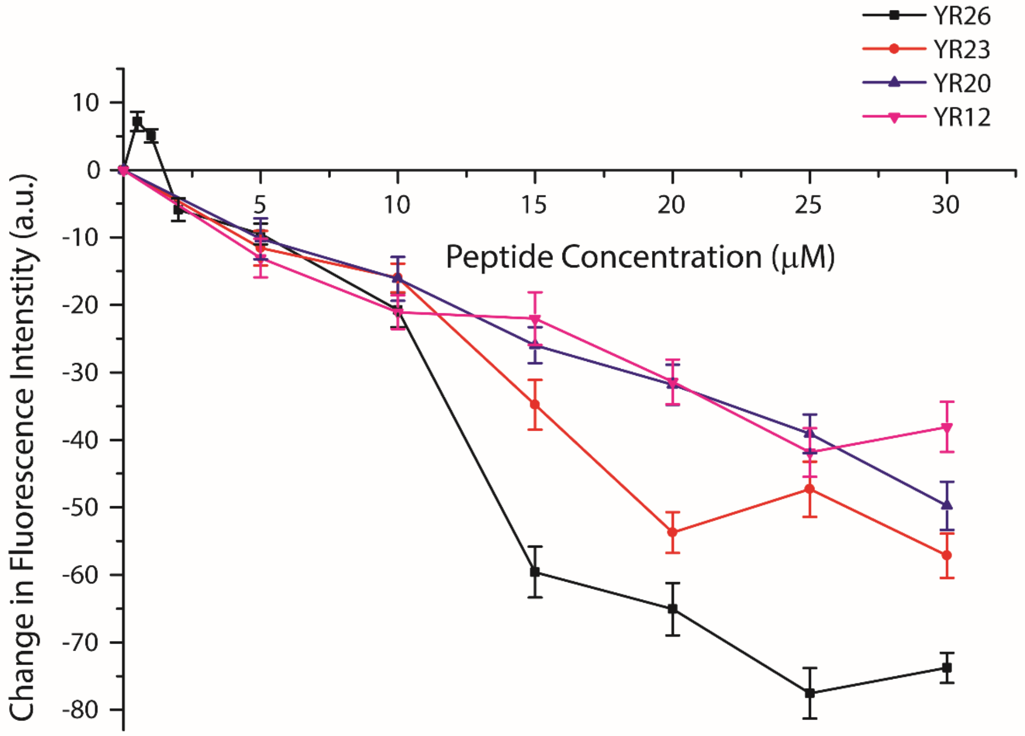

Figure 6.16| Calcein leakage assay: POPC-POPG liposomes. The quenching of fluorescence intensity of POPC-POPG liposomes in presence of increasing peptide concentration indicates a non-membranolytic mode of action.

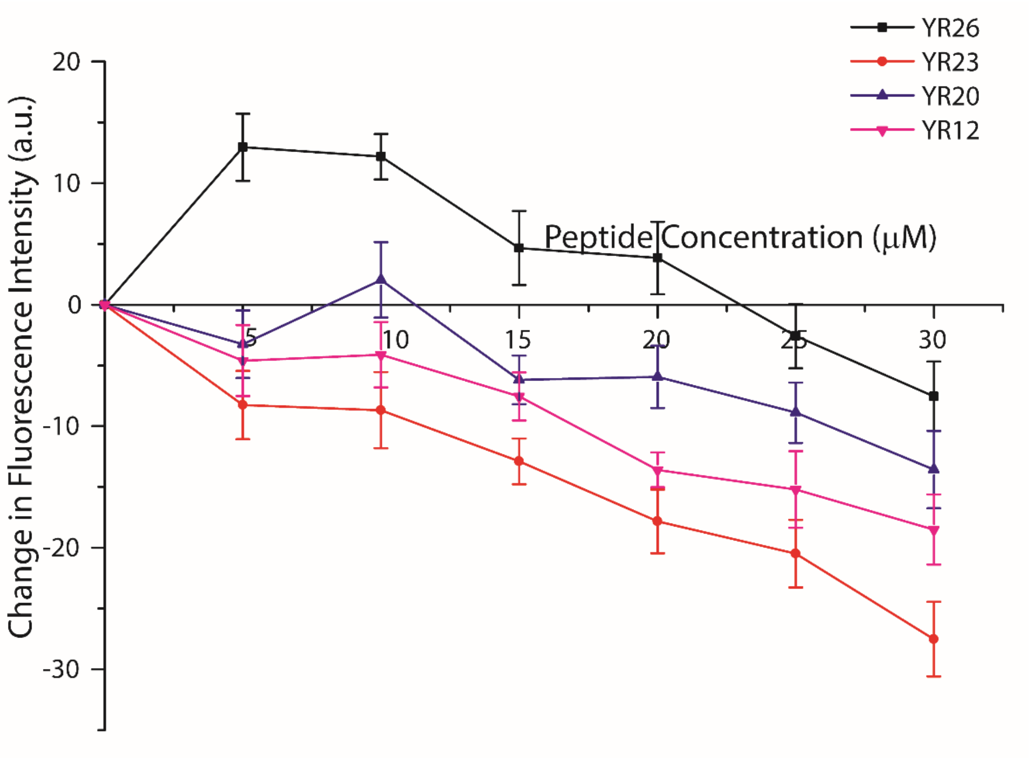

Figure 6.17| Calcein leakage assay: POPC liposomes. No significant increase in fluorescence intensity of calcein in presence of AMPs suggest that the peptides do not permeabilize the POPC liposomes.

6.2.12 DLS Particle Size Analysis

To further validate the mechanism of action, particle size measurements of POPC-POPG and POPC liposomes were carried out using dynamic light scattering technique. The mean diameter of POPC-POPG and POPC liposomes were observed to be 192.3 nm and 370.8 nm, respectively. Mean diameters of the liposomes in presence of the active AMPs in liposome:peptide ratios of 1:1, 1:2 and 1:4 are depicted in tables 6.9 and 6.10. It is clearly evident that the peptides are able to aggregate the POPC-POPG liposomes in large agglutinates. The mean diameter of the POPC-POPG liposome in presence of high YR26 and YR23 concentration increases to twelve folds and eight folds, respectively. Moreover, no significant change in the mean diameter of the POPC liposomes is observed even at high peptide concentrations. This along with the observations from calcein leakage assay clearly suggested that the mode of action of the peptides derived from furin prodomain is agglutination.

Table 6.9| Particle size analysis: POPC-POPG liposomes. The multiple folds increase in the mean diameter of POPC-POPG at higher peptide concentrations strongly suggests agglutination as a mechanism of action for these peptides. The mean diameter of free POPC-POPG liposome was observed to be 192.3 nm.

Peptides	POPC-POPG: Peptide		
	1:1	1:2	1:4
YR26	488.1	1193.5	2311.2
YR23	521.5	938.4	1515.9
YR20	420.2	658.6	1063.9
YR12	198.2	227.4	430.8

Table 6.10| Particle size analysis: POPC liposomes. There is no significant change in the mean diameter of zwitterionic POPC liposomes even in presence of high peptide concentrations. This suggests that the tested peptides are highly selective and do not interact with these mammalian cell mimicking liposomes. The mean diameter of free POPC liposome was observed to be 370.8 nm.

Peptides	POPC: Peptide		
	1:1	1:2	1:4
YR26	379.2	351.3	406
YR23	362.5	374.3	352.4
YR20	375.8	382.9	412
YR12	368.9	385.7	337.1

6.2.13 Transmission Electron Microscopy

To validate agglutination as the mechanism of action, TEM images of *E.coli* cells were taken in presence and absence of YR26. The aggregated morphology of the bacterial cells (Figure 6.18) clearly indicate agglutination as the mode of action.

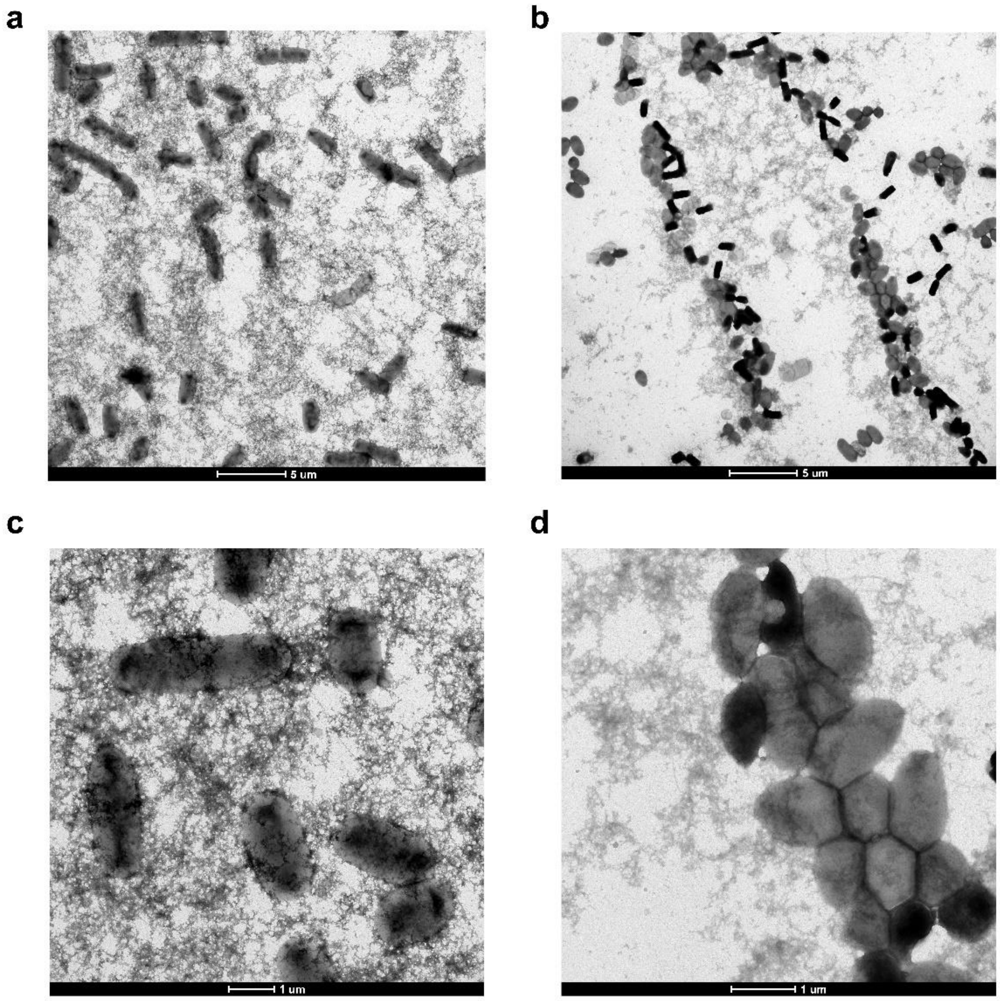

Figure 6.18| Transmission Electron Microscopy. Morphology of the *E.coli* cells in absence of (a,c) and in presence of YR26 (b,d) suggests agglutination as the mode of action.

6.2.14 Expression & Purification of ^{15}N YR26

YR26 was ^{15}N labelled to facilitate ^{15}N- ^{1}H HSQC NMR experiments. YR26 was successfully overexpressed as a fusion protein comprising KSI as a hydrophobic fusion tag (Figure 6.19). The fusion protein was further purified in using Ni-NTA chromatography in denaturing conditions (8M urea). The fusion protein was cleaved at D-P site using 50% formic acid for 24 hours. Formic acid was removed using rotary evaporator. And the cleaved protein and fusion tag were re-dissolved in DI water. KSI being hydrophobic easily separates out from the solution. YR26 was further purified using HPLC (Figure 6.20). The major peak obtained during purification was confirmed using MALDI-ToF and NMR spectroscopy (Figure 6.21).

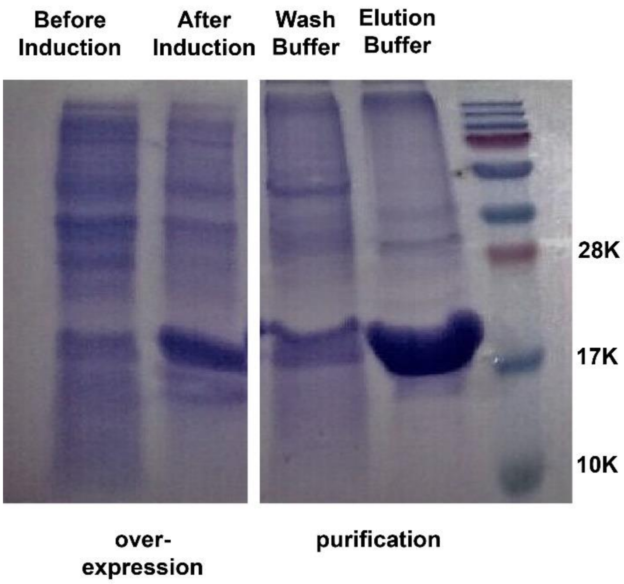

Figure 6.19| Expression and Purification of ^{15}N YR26. The fusion protein was successfully overexpressed using LB and M9 media. The protein was purified using Ni-NTA column in presence of 8M urea.

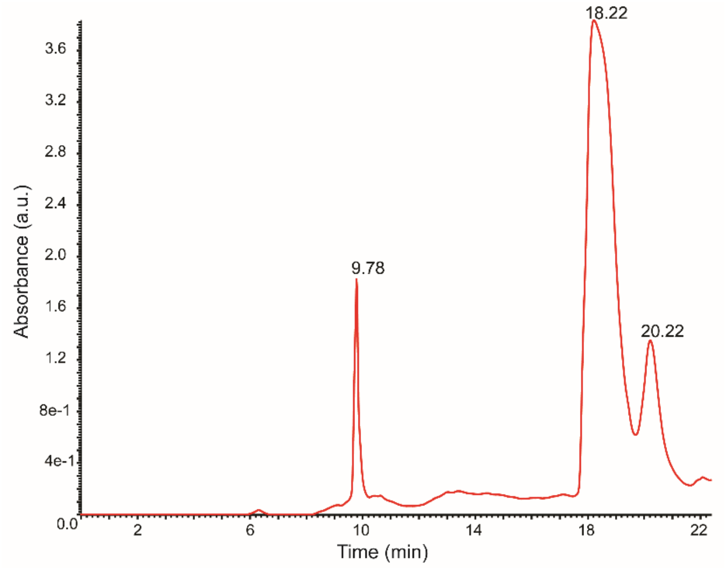

Figure 6.20| Purification profile of ^{15}N YR26. After formic acid cleaving of the fusion protein, the cleaved peptide was further purified using a reverse phase HPLC.

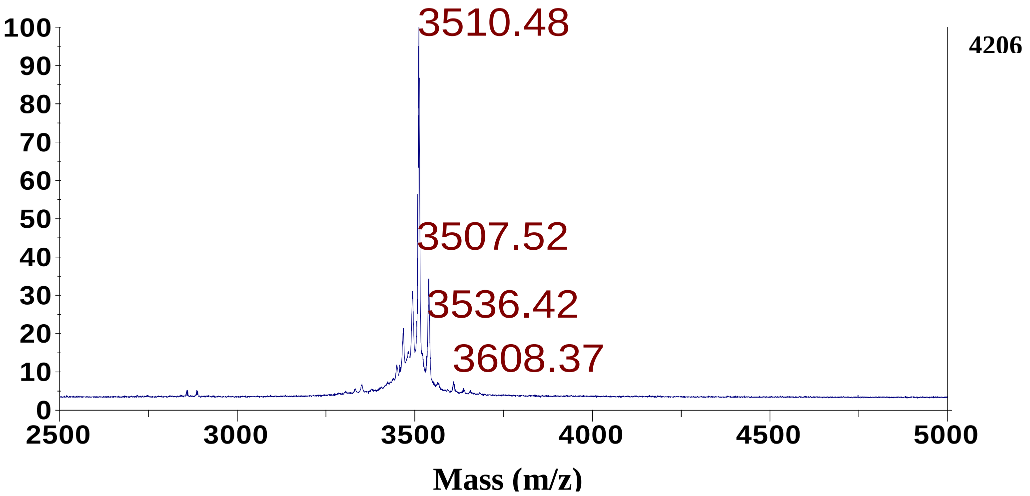

Figure 6.21| Mass spectrometry of the purified ^{15}N YR26. The peptide exuding thom the column at 18 mins was collected and the fraction was checked for purity using MALDI ToF. The spectrum shows expected molecular weight for YR26.

6.2.15 Interaction of YR26 with LPS micelles

Since the peptide YR26 demonstrates outer membrane permeabilization (Figure 6.7), its interaction with LPS micelles was further scrutinized by NMR. ^{15}N-^{1}H HSQC spectra of YR26 in absence and presence of varying LPS concentrations were recorded. It is observed that the peaks for most amino acids are either shifted or diminished indicating a strong YR26/LPS interaction. Figure 6.22 depicts ^{15}N-^{1}H HSQC spectra of YR26 in absence of LPS (red) and in presence of 20 μM (green), 40 μM (blue) and 60 μM (yellow) LPS.

6.2.16 Backbone Motional Characteristics of YR26

Backbone dynamics of YR26 in presence of anionic SDS micelles were examined by determining ^{15}N longitudinal (R1=1/T1) and transverse (R2=1/T2) relaxation rates and ^{1}H-^{15}N steady state heteronuclear NOEs. ^{15}N R1, R2 and ^{1}H-^{15}N NOE were plotted against residue number (Figure 6.23). High heteronuclear

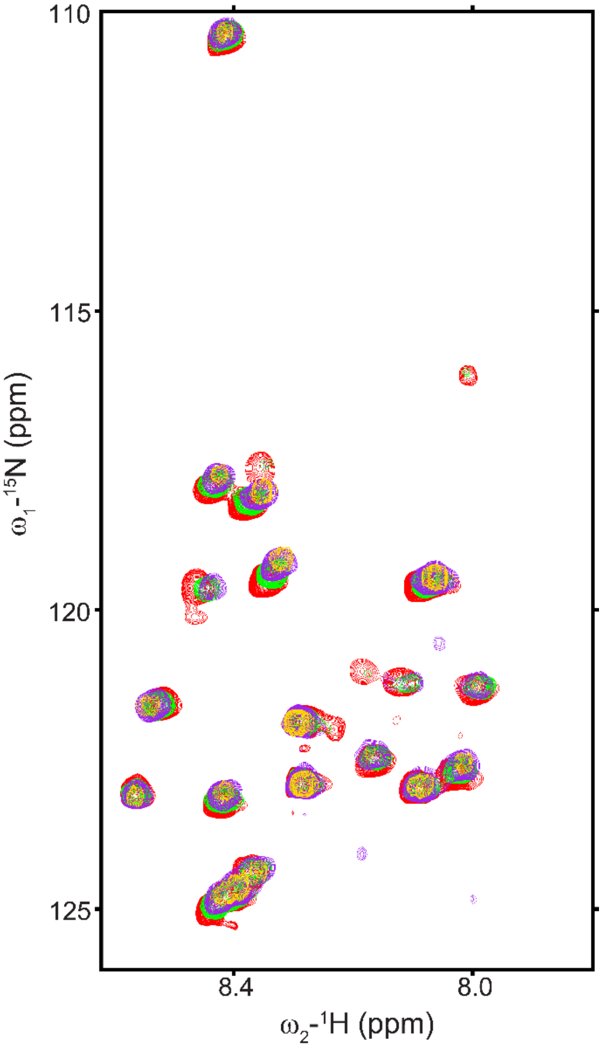

Figure 6.22| YR26/LPS Interactions. ^{15}N-^{1}H HSQC spectra of YR26 in presence of varying LPS concentrations. Red: 0 μM, green: 20 μM, blue: 40 μM and yellow: 60 μM.

NOE values (0.45-0.62) can be seen for most of the residues (Figure 6.23c), suggesting that almost all the residues are in well folded conformation[137]. Residues. Residues Arg12 and Ser15 have comparatively lower NOE values (0.38-0.41) indicating that the region may be relatively mobile. Residues Tyr2 and Gln25 near the terminals have much lesser NOE values of 0.17 and 0.24, respectively. This suggests that the residues near the terminal are flexible, as expected. Figure 6.23a and b illustrates R1 and R2 relaxation rates for each residue. However, there are no significant variations in the relaxation rates amongst the residues. Thus, conformational preferences cannot be determined using this parameter.

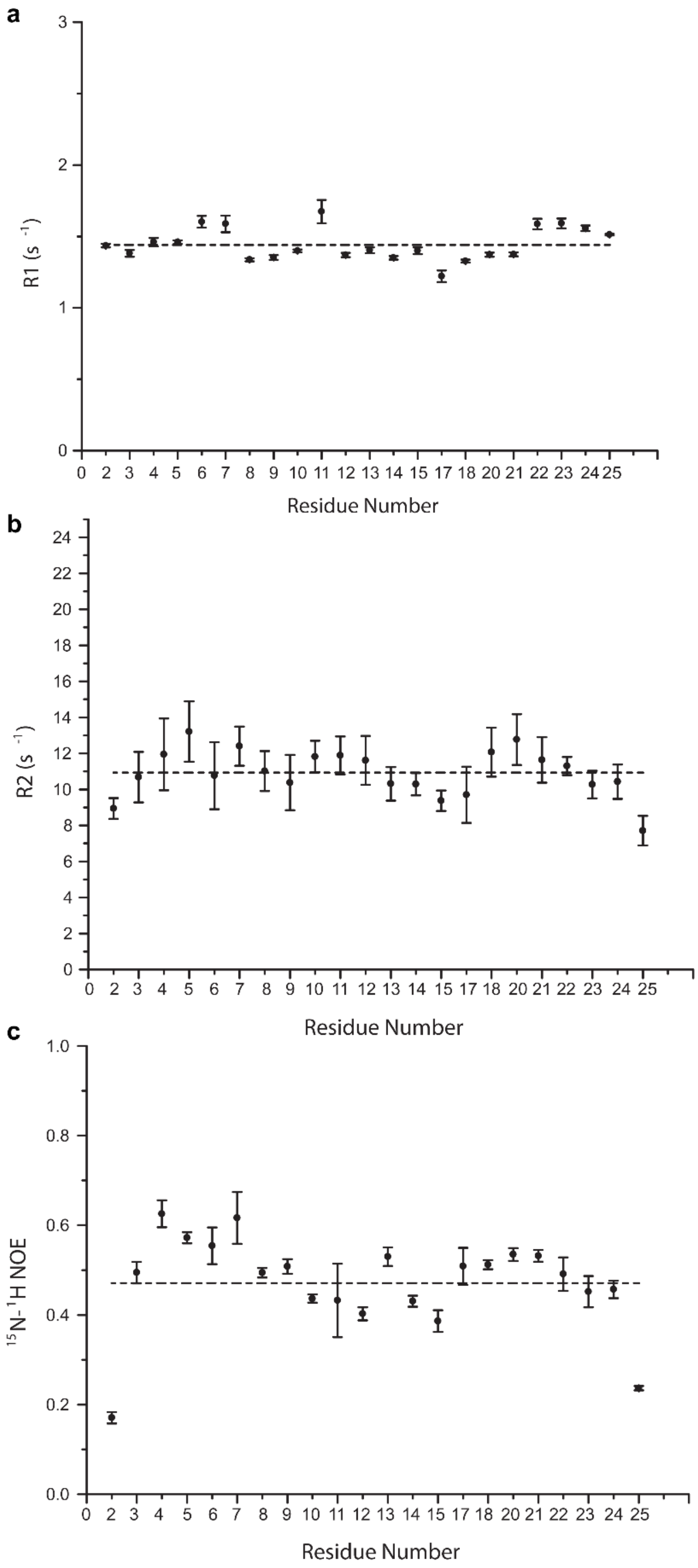

Figure 6.23| Backbone motional characteristics of YR26. a. Longitudinal (R1) relaxation rate with an average of 1.44 s^{-1}, **b.** Transverse (R2) relaxation rate with an average of 10.93 s^{-1}, **c.** 1H-15N heteronuclear NOEs with an average of 0.47.

6.2.17 Paramagnetic Relaxation Enhancement

YR26/SDS interaction was further analysed by observing the resonance perturbation caused in the ^{15}N-^{1}H HSQC by spin-labelled doxyl lipids, 5-DSA and 16-DSA. High remaining amplitudes (RA) for 5-DSA and low RA values in presence of 16-DSA suggest that the amino acids are localized in the hydrophobic core of the SDS micelles (Figure 6.24). Zero RA values for amino acids His3, Phe4, Trp5, His6, Arg12, His17 and Arg23 indicate that they are localized near the micelle centre of SDS.

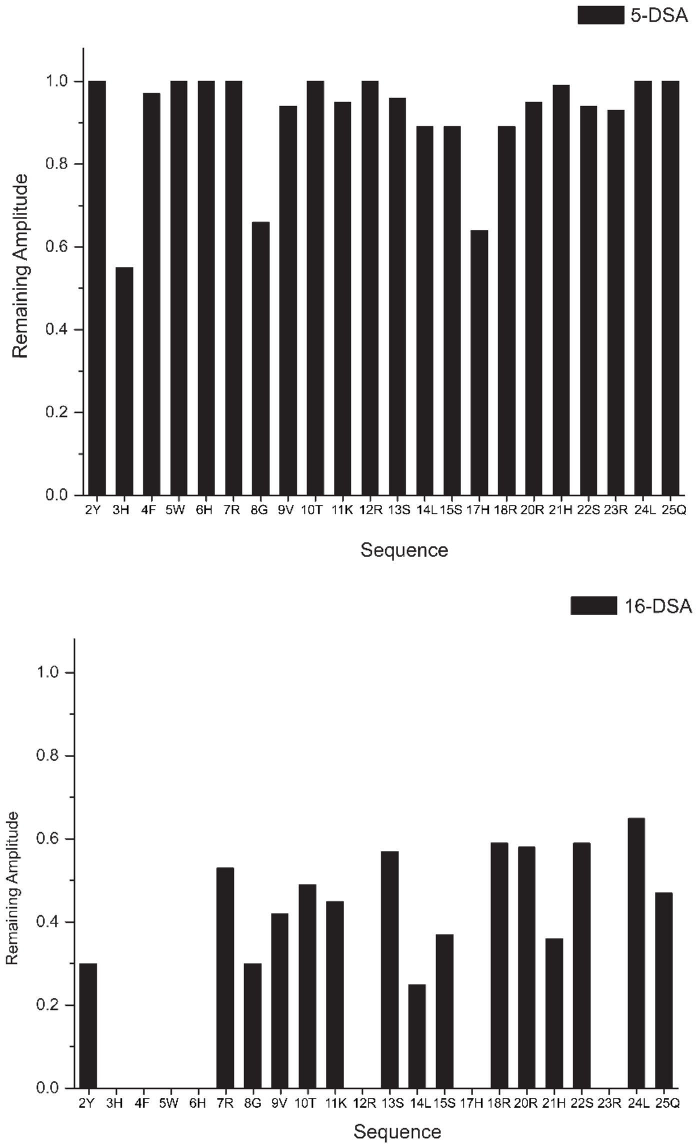

Figure 6.24| Paramagnetic Relaxation Enhancement. Resonance perturbations in ^{15}N-^{1}H HSQC spectrum of YR26 in presence of SDS micelles by spin labelled 5-DSA and 16-DSA lipids.

6.2.18 Three-dimensional structure of YR26 in presence of SDS

Sodium dodecyl sulphate (SDS) is a membrane mimic detergent which is frequently used to determine the structure of AMPs in anionic environment. ^{1}H-^{1}H TOCSY and NOESY experiments of YR26 were carried out in presence of SDS at 298 K, pH 5. Figure 6.25 illustrates representative NOESY spectra of YR26 in the abovementioned conditions. A total of 191 NOE driven distance constraints were utilized to determine the structure of YR26 in presence of SDS. As observed with most alpha helical conformations, the residues mostly have medium range (1<|i-i+1|<4) and sequential connectivities (Figure 6.26). ^{15}N-^{1}H HSQC (Figure 6.27) and ^{13}C-^{1}H HSQC spectra were analyzed and the chemical shift deviations were utilized to determine the angle constraints for structure determination. Figures 6.28 and 6.29 depict the representative structure of YR26 in presence of SDS and an ensemble of its 20 lowest energy structures, respectively. Structural statistics and RMSDs are provided in table 6.11.

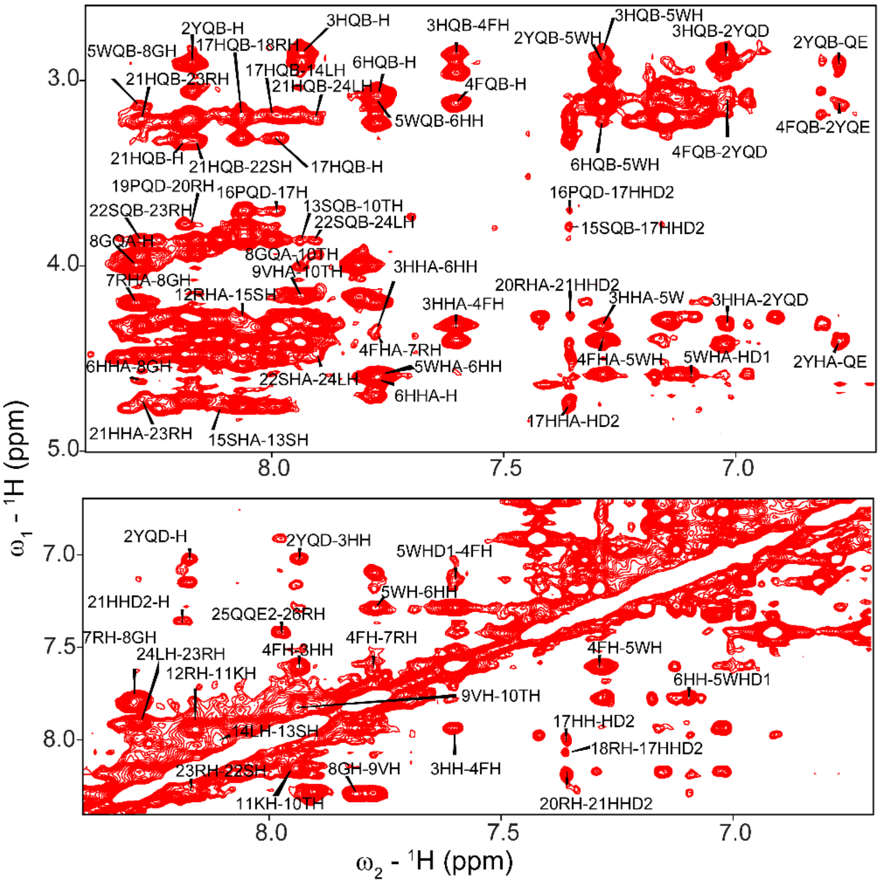

Figure 6.25| Two dimensional NOESY spectra of YR26 is presence of SDS. ^{1}H-^{1}H NOESY NMR experiment of 0.300 mM YR26 was carried out in presence of 150 mM SDS at 298 K, pH 5.

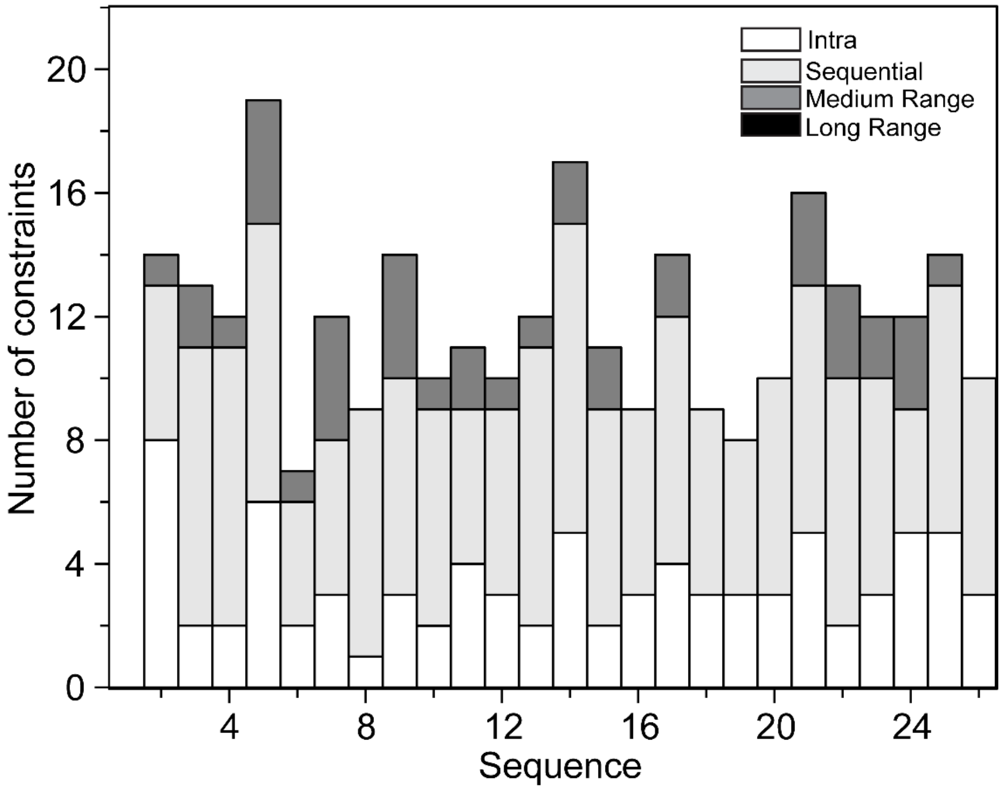

Figure 6.26| Number of NOE connectivities per residue. Residues 1-15 and 20-26 show a number of medium range NOEs, characteristic to an α-helix conformation.

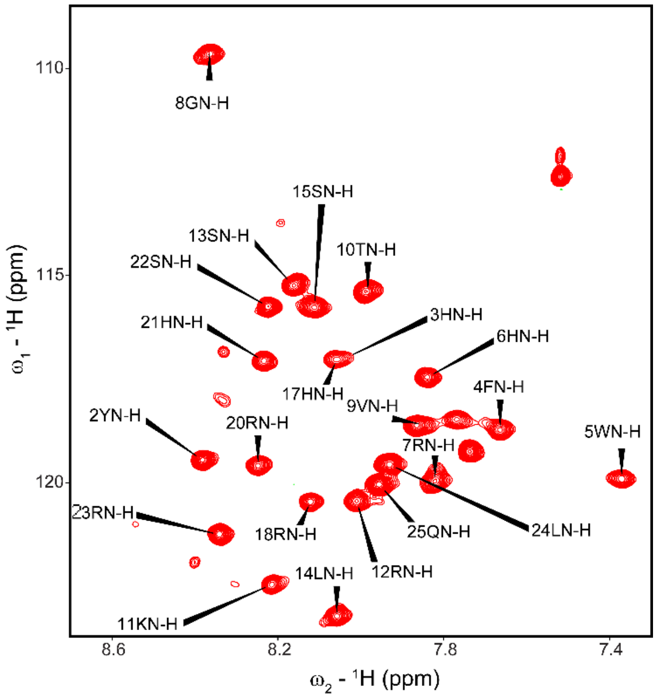

Figure 6.27| ^{15}N-^{1}H HSQC spectrum of YR26 in presence of SDS. The chemical shift deviation of the ^{15}N NOEs were analysed and were utilized to determine angle constraints. A total of 40 angle constraints were utilized for structure determination.

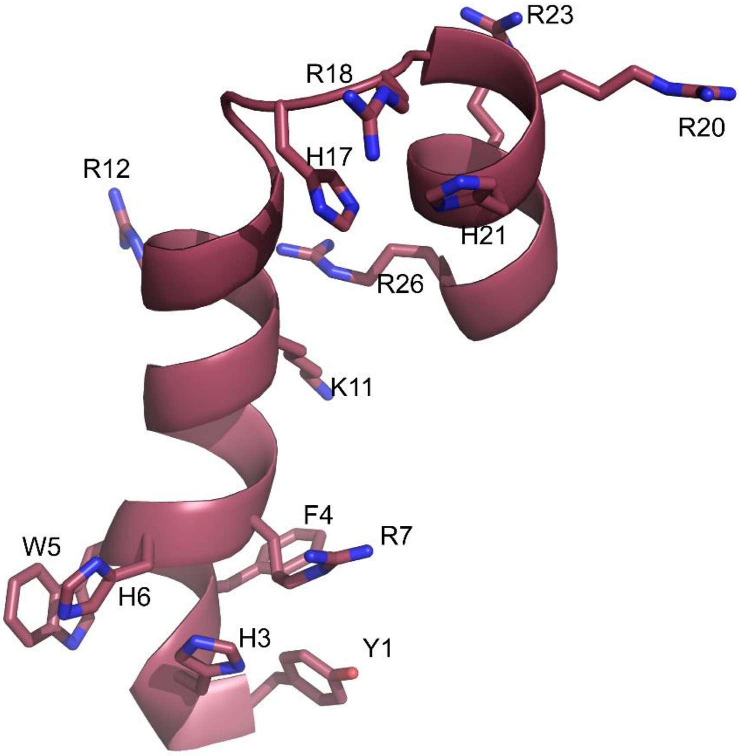

Figure 6.28| Representative structure of YR26 in presence of SDS. YR26 consists of a long helical region comprising residues 1-15 and another shorter helical region comprising residues 20-26. Both the helices are arranged in an anti-parallel fashion with a loop linking the two regions.

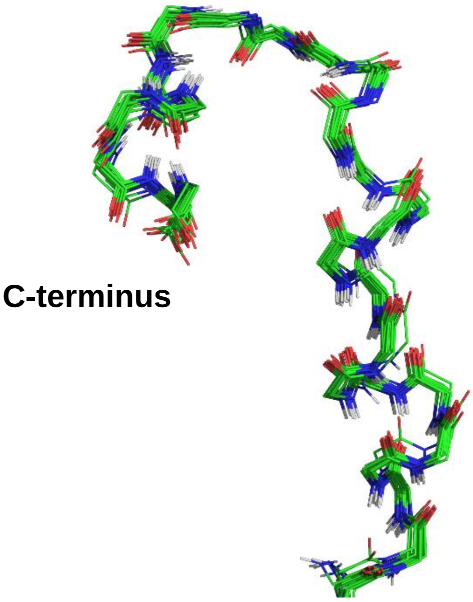

Figure 6.29| NMR derived structure of YR26 in presence of SDS. Superposition of backbone atoms of 20 lowest energy structures of YR26 in presence of anionic SDS micelles.

Table 6.11| Structural statistics. A summary of structural statistics of YR26 in presence of anionic SDS micelles.

	YR26 in presence of SDS
Distance constraints	
Sequential [|i-j|= 1]	87
Medium range [1 <|i-j|< 4]	19
Long range [|i-j|≥ 4]	1
Total	191
Dihedral-angle constraints	40
Deviation from mean structure (Å)	
All backbone atoms	0.27
All heavy atoms	1.20
Ramachandran plot for the mean structure (%residues)	
Most favoured region	76.2
Additional allowed region	23.8
Generously allowed region	0
Disallowed region	0

YR26 comprises two well-folded helices consisting of residues Y1 to S15 and R18 to R26 (Figure 6.28). Proline is a known ‘helix breaker’. The residues from P16 to P19 adopt an extended loop structure connecting the two helices in an anti-parallel fashion. N-terminus of YR26 is stabilized by stacking aromatic interactions of Tyr1/Phe4 and Trp5/His6. There is a possible interaction between His17 and His21 to further stabilize the structure. Figure 6.30 illustrates the Ramachandran plot for YR26 in presence of SDS. As expected, most of the residues are in α-helical conformation. The electrostatic potential surface of YR26 in presence of SDS is shown in Figure 6.31. Three distinct cationic patches comprising residues H3/H6/R7, K11/R12/R26 and R18/R20/R23 can electrostatically interact with the anionic phosphate head groups present in LPS, thereby providing multiple LPS binding sites.

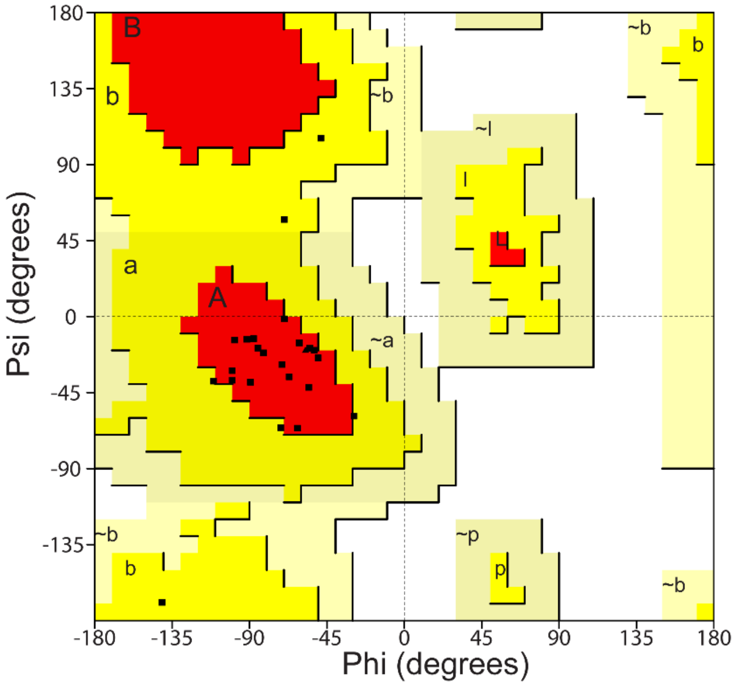

Figure 6.30| Ramachandran plot for YR26 in presence of SDS. Most of the residues in YR26 are in α-helical conformation.

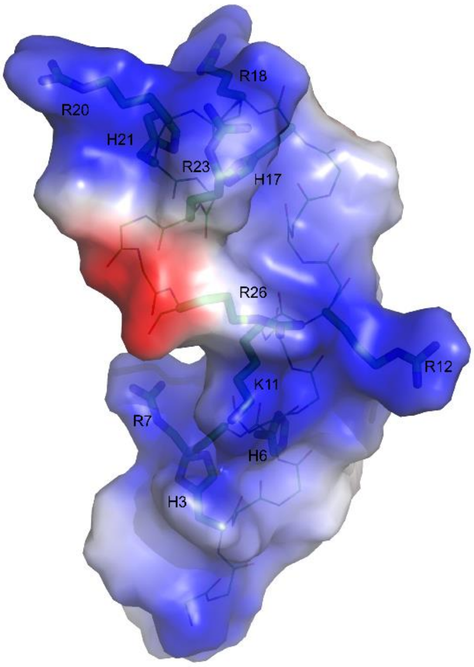

Figure 6.31| Electrostatic surface potential of YR26 in presence of SDS. Distinct cationic patches interact with the negatively charged phosphate head groups in LPS electrostatically, thereby providing multiple LPS binding sites.

6.2.19 Docking YR26 in LPS micelles

Energy calculations were performed in Discover module of Insight II (Biosym). Constraints were set between the cationic residues of YR26 and anionic phosphate groups in LPS unit. The cationic residues H3/H6R7, K11/R12/R26 and R18/R20/R23 form three distinct local cluster of cationic charges. Therefore, these residue pairs serve as the perfect binding pockets for multiple LPS units. For energy minimization, dielectric constant was set to 1. To start, initial constraints were set between one binding pocket and one unit of LPS. The system was then subjected to Steepest Descent energy minimization. In order to release the initial model from bad contacts, Conjugated energy minimization was further used. Similarly, energy minimization was done for other binding sites. Figure 6.32 elucidates plausible LPS binding sites present in YR26.

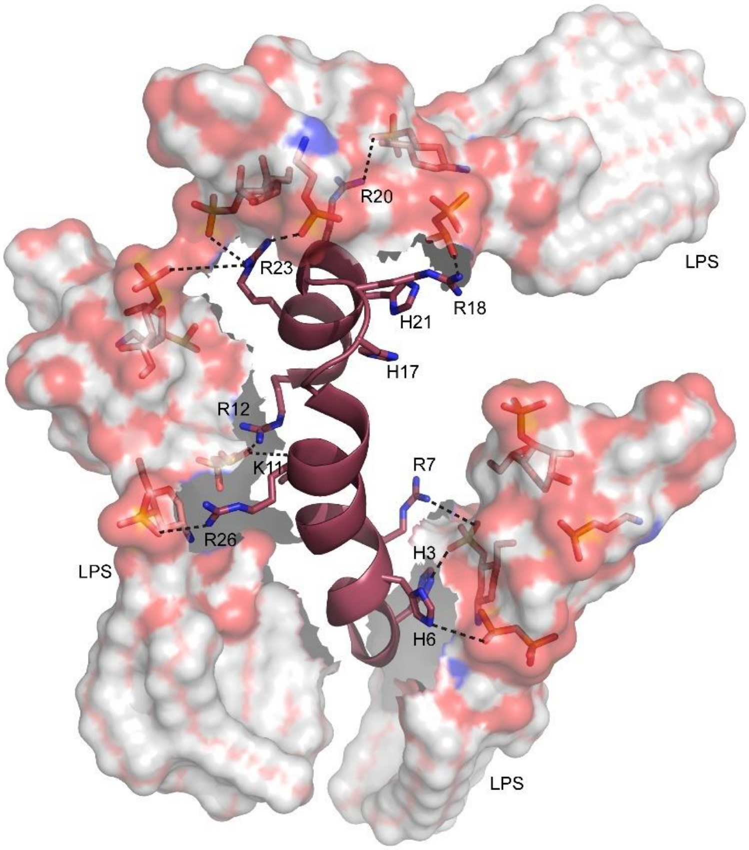

Figure 6.32| Docked model of YR26/LPS complex. Multiple possible LPS binding sites present in YR26 facilitates agglutination.

6.3 Discussion

Furin is a calcium dependent serine endoprotease, which is enriched in golgi[136]. It is activated after a two-step autocatalytic cleavage of the furin preprotein[137, 138]. Anti-cancerous properties of furin prodomain have been exploited in recent years[139]. In this work, a number of peptide segments derived from the N-terminus, C-terminus and the central region of the prodomain were examined for their antimicrobial activity. Interestingly, the peptide derived from the central region of the prodomain (residues 38-63) showed potent and wide-spectrum antimicrobial activity (Table 6.1). The peptide YR26 was further truncated into different segments to optimize the active region in the prodomain. Truncation of three residues from the C-terminus did not affect the activity. However, truncation of more than six residues rendered the peptide completely inactive (Table 6.2). Furthermore, it can be concluded from the hemolysis and cytotoxicity tests (Figures 6.5 & 6.6) that the active peptides are highly selective and non-toxic to mammalian cells. Membrane permeabilization assays suggested that the peptides are able to permeabilize the outer cell membrane of *E. coli* cells (Figure 6.7). However, they are incapable of permeabilizing the inner cell membrane of the tested *E. coli* strain. Furthermore, quenching of fluorescence intensity of FITC-LPS in presence of increasing concentrations of the active peptides suggested a higher order of association of LPS micelles in presence of these peptides (Figure 6.12). Intrinsic tryptophan fluorescence data indicated that the active peptides interact with LPS, SDS and DPC micelles (Table 6.5). Furthermore, it can be inferred from the ITC data that the binding of the tested AMPs with LPS is an enthalpy driven exothermic process (Figure 6.11).

The interactions of these AMPs with bacterial cell mimicking liposome (POPC-POPG) and mammalian cell mimicking liposome (POPC) were analysed to gain further insights on their mechanism of action. Intrinsic tryptophan fluorescence revealed that the peptides interact with POPC-POPG liposomes but not with POPC liposomes, further corroborating their selectivity towards bacterial cells (Table 6.8). An analysis of calcein leakage from POPC-POPG and POPC liposomes indicated that the liposomes form a higher order of association in presence of the active peptides (Figures 6.16 & 6.17). Particle size analysis of the POPC-POPG liposomes demonstrated their agglutination in presence of higher peptide concentrations (Table 6.9). Taken together, it can be concluded that these peptides follow a non-membranolytic mechanism of action and kill bacteria by agglutination.

3D structure of YR26 in presence of SDS micelles revealed two α-helical regions arranged in an antiparallel topology (Figure 6.28). Electrostatic surface potential illustrated three distinct cationic patches (Figure 6.31) that are present in YR26 that can electrostatically interact with anionic phosphate head groups in LPS unit. Finally, the energy minimized simulation model of YR26/LPS complex elucidated the multiple possible LPS binding sites facilitating agglutination (Figure 6.32).

Chapter 7

Conclusion & Future Work

In this chapter, a conclusion for the overall thesis work is provided. A discussion on the overall mechanism of action of thanatin, thanatin analogs and furin prodomain derived active peptides is provided. Mechanistic insights on agglutination are summarized. Furthermore, a summary of possible future applications and directions is provided.

7.1 Conclusion

Decline of the golden age of antibiotics witnessed an emergence of drug resistant bacteria[1]. With an exponential increase in multi-drug resistant bacteria and a decline in FDA approval of new antimicrobials[7], it is crucial to discover new drugs with alternate mode of action. Membrane permeabilization and targeting intra-cellular components by cationic AMPs are well perceived mechanisms of antimicrobial action. However, agglutination of bacterial cells by AMPs is poorly understood. In this thesis, two different systems of AMPs with agglutination as a mode of antimicrobial action has been elucidated.

Thanatin is known to kill bacteria by agglutination. In this work, first 3D structure of thanatin in complex with LPS has been elucidated. Thanatin dimerizes in presence of LPS and adopts a four stranded antiparallel β-sheet conformation with 'head-tail' topology. The dimeric structure of thanatin provides multiple LPS binding sites to facilitate agglutination. MD simulation of thanatin dimer/LPS complex gave a mechanistic insight on LPS/thanatin interaction and agglutination. Futhermore, structure-activity correlation of thanatin and mutant peptides provided further insights on the mode of antimicrobial action. The gain-in function mutant, thanatin M21F has an improved antimicrobial activity as compared to the wild type thanatin due to enhanced aromatic-aromatic stacking interactions. On the other hand, on mutating both Arg13 and Arg14 to Ala residues completely rendered the peptide inactive. Thus, atleast one Arg in the β-turn region is necessary for LPS binding and antimicrobial activity. Dissociation constant and ED50 were determined for thanatin and mutant peptides in complex with LPS via various biophysical techniques. The quenching of FITC-LPS fluorescence spectra in presence of active thanatin and mutant peptide indicated a higher order of association of these micelle, thus corroborating agglutination. Extensive line broadening of the ^{31}P signals for phosphate groups of LPS at higher peptide concentrations indicated that thanatin and the gain-in function mutant thanatin M21F bind with the phosphate head groups of LPS. Finally, an illustrative model of thanatin agglutinating the bacterial cells was prepared to explain its mechanism of action.

YR26 was derived from the central region of furin prodomain and is shown to possess a broad spectrum of antimicrobial activity. Various truncations were made from the C-terminus of the peptide and was observed that truncating more than six residues renders the peptide inactive. Moreover, the active peptides YR26, YR23 and YR20 were found to be highly selective to bacterial cells and non-hemolytic and non-toxic to mammalian cells. In order to study their mode of antimicrobial action, various biophysical experiments were conducted. The peptides were able to permeabilize the outer membrane but not the inner membrane of *E. coli* cells. Further, the experiments indicated a higher order of association of LPS micelles/*E. coli* cells in presence of these peptides. Particle size analysis of bacterial cell mimicking POPC-POPG liposomes in presence of higher peptide concentration confirmed agglutination as their mode of antimicrobial action. Furthermore, 3D structure of YR26 was determined in presence of SDS. YR26 adopts an antiparallel α-helical conformation whereby, the two helical regions are connected by an extended loop. YR26 possesses multiple cationic patches that can interact electrostatically with LPS. An energy minimized simulation model of YR26/LPS was prepared to elucidate the interaction of YR26 with multiple LPS units and agglutination.

It is interesting to note that thanatin and YR26 are structurally very different. YR26 has α-helical-loop-α-helical structure in presence of SDS micelles, whereas thanatin has β-hairpin dimer structure in presence of LPS. However, both the peptides provide multiple LPS docking sites to enable agglutination. Moreover, in YR26 all the docking sites are in one monomeric unit. On the other hand, thanatin needs to dimerize to provide for multiple LPS binding pockets to facilitate agglutination.

7.2 Future Work

The mechanistic insight on agglutination as a mode of antimicrobial action can be used as a template to develop new antimicrobial drugs. The furin prodomain derived peptide, YR26 has high selectivity towards bacterial cells *in vitro*. In furture, the peptide or its analog can be tested *in vivo* and can be developed into an antimicrobial drug. These antimicrobial peptides can also be tagged on nanoparticles for infection targeted drug delivery. For enhanced selectivity, these peptides can also be grafted on a biopolymer like chitosan and polymer/peptide complex can be tested for antimicrobial activity.

References

1. Phoenix, D.A., Dennison, S.R. & Harris, F. Antimicrobial peptides: their history, evolution, and functional promiscuity. *Antimicrobial peptides,* 1-37 (2013).
2. Cabello, F.C. Heavy use of prophylactic antibiotics in aquaculture: a growing problem for human and animal health and for the environment. *Environmental microbiology* **8**, 1137-1144 (2006).
3. Economou, V. & Gousia, P. Agriculture and food animals as a source of antimicrobial-resistant bacteria. *Infection and drug resistance* **8**, 49 (2015).
4. Penders, J. & Stobberingh, E. Antibiotic resistance of motile aeromonads in indoor catfish and eel farms in the southern part of The Netherlands. *International journal of antimicrobial agents* **31**, 261-265 (2008).
5. Perron, G.G. *et al.* Functional characterization of bacteria isolated from ancient arctic soil exposes diverse resistance mechanisms to modern antibiotics. *PLoS ONE* **10** (2015).
6. von Wintersdorff, C.J. *et al.* Dissemination of antimicrobial resistance in microbial ecosystems through horizontal gene transfer. *Frontiers in microbiology* **7** (2016).
7. Schäberle, T.F. & Hack, I.M. Overcoming the current deadlock in antibiotic research. *Trends in microbiology* **22**, 165-167 (2014).
8. Zasloff, M. Antimicrobial peptides of multicellular organisms. *nature* **415**, 389-395 (2002).
9. Zasloff, M. Antimicrobial peptides in health and disease. *New England Journal of Medicine* **347**, 1199-1199 (2002).
10. Brogden, K.A. Antimicrobial peptides: pore formers or metabolic inhibitors in bacteria? *Nature reviews microbiology* **3**, 238-250 (2005).
11. Nicolas, P. & El Amri, C. The dermaseptin superfamily: a gene-based combinatorial library of antimicrobial peptides. *Biochimica et Biophysica Acta (BBA)-Biomembranes* **1788**, 1537-1550 (2009).
12. Nicolas, P., Vanhoye, D. & Amiche, M. Molecular strategies in biological evolution of antimicrobial peptides. *Peptides* **24**, 1669-1680 (2003).
13. Vanhoye, D., Bruston, F., Nicolas, P. & Amiche, M. Antimicrobial peptides from hylid and ranin frogs originated from a 150-million-year-old ancestral precursor with a conserved signal peptide but a hypermutable antimicrobial domain. *The FEBS Journal* **270**, 2068-2081 (2003).
14. Nguyen, L.T., Haney, E.F. & Vogel, H.J. The expanding scope of antimicrobial peptide structures and their modes of action. *Trends in biotechnology* **29**, 464-472 (2011).
15. Cudic, M. & Otvos Jr, L. Intracellular targets of antibacterial peptides. *Current drug targets* **3**, 101-106 (2002).
16. Maher, S. & McClean, S. Investigation of the cytotoxicity of eukaryotic and prokaryotic antimicrobial peptides in intestinal epithelial cells in vitro. *Biochemical pharmacology* **71**, 1289-1298 (2006).
17. Kagan, B.L., Ganz, T. & Lehrer, R.I. Defensins: a family of antimicrobial and cytotoxic peptides. *Toxicology* **87**, 131-149 (1994).

18. Yount, N.Y. & Yeaman, M.R. Structural congruence among membrane-active host defense polypeptides of diverse phylogeny. *Biochimica et Biophysica Acta (BBA)-Biomembranes* **1758**, 1373-1386 (2006).
19. Yeaman, M.R. & Yount, N.Y. Unifying themes in host defence effector polypeptides. *Nature Reviews Microbiology* **5**, 727-740 (2007).
20. Holland, L.Z. *et al.* The amphioxus genome illuminates vertebrate origins and cephalochordate biology. *Genome research* **18**, 1100-1111 (2008).
21. Erwin, D.H. & Davidson, E.H. The last common bilaterian ancestor. *Development* **129**, 3021-3032 (2002).
22. Panopoulou, G. & Poustka, A.J. Timing and mechanism of ancient vertebrate genome duplications–the adventure of a hypothesis. *TRENDS in Genetics* **21**, 559-567 (2005).
23. Das, S. *et al.* Comparative genomics and evolution of the alpha-defensin multigene family in primates. *Molecular biology and evolution* **27**, 2333-2343 (2010).
24. Ghosh, J. *et al.* Invertebrate immune diversity. *Developmental & Comparative Immunology* **35**, 959-974 (2011).
25. Fleming, A. On a remarkable bacteriolytic element found in tissues and secretions. *Proceedings of the Royal Society of London B: Biological Sciences* **93**, 306-317 (1922).
26. Fleming, A. On the antibacterial action of cultures of a penicillium, with special reference to their use in the isolation of B. influenzae. *British journal of experimental pathology* **10**, 226 (1929).
27. Brown, K. The history of penicillin from discovery to the drive to production. *Pharmaceutical historian* **34**, 37 (2004).
28. Hirsch, J.G. Phagocytin: a bactericidal substance from polymorphonuclear leucocytes. *Journal of Experimental Medicine* **103**, 589-611 (1956).
29. Zeya, H. & Spitznagel, J. Cationic proteins of polymorphonuclear leukocyte lysosomes II. Composition, properties, and mechanism of antibacterial action. *Journal of bacteriology* **91**, 755-762 (1966).
30. Hultmark, D., STEINER, H., Rasmuson, T. & Boman, H.G. Insect immunity. Purification and properties of three inducible bactericidal proteins from hemolymph of immunized pupae of Hyalophora cecropia. *The FEBS Journal* **106**, 7-16 (1980).
31. Zasloff, M. Magainins, a class of antimicrobial peptides from Xenopus skin: isolation, characterization of two active forms, and partial cDNA sequence of a precursor. *Proceedings of the National Academy of Sciences* **84**, 5449-5453 (1987).
32. Agerberth, B. *et al.* The human antimicrobial and chemotactic peptides LL-37 and α-defensins are expressed by specific lymphocyte and monocyte populations. *Blood* **96**, 3086-3093 (2000).
33. Durán, N. *et al.* Mechanistic aspects in the biogenic synthesis of extracellular metal nanoparticles by peptides, bacteria, fungi, and plants. *Applied microbiology and biotechnology* **90**, 1609-1624 (2011).
34. Ntwasa, M., Goto, A. & Kurata, S. Coleopteran antimicrobial peptides: prospects for clinical applications. *International journal of microbiology* **2012** (2012).

35. Lee, J.K., Jeon, J.-K., Kim, S.-K. & Byun, H.-G. 4 Characterization of Bioactive Peptides Obtained from Marine Invertebrates. *Advances in food and nutrition research* **65**, 47 (2012).
36. Wang, G., Li, X. & Wang, Z. APD2: the updated antimicrobial peptide database and its application in peptide design. *Nucleic acids research* **37**, D933-D937 (2008).
37. Piotto, S.P., Sessa, L., Concilio, S. & Iannelli, P. YADAMP: yet another database of antimicrobial peptides. *International journal of antimicrobial agents* **39**, 346-351 (2012).
38. Kohanski, M.A., Dwyer, D.J. & Collins, J.J. How antibiotics kill bacteria: from targets to networks. *Nature Reviews Microbiology* **8**, 423-435 (2010).
39. Drlica, K. & Zhao, X. DNA gyrase, topoisomerase IV, and the 4-quinolones. *Microbiology and Molecular Biology Reviews* **61**, 377-392 (1997).
40. Chen, C.R., Malik, M., Snyder, M. & Drlica, K. DNA gyrase and topoisomerase IV on the bacterial chromosome: Quinolone-induced DNA cleavage. *Journal of Molecular Biology* **258**, 627-637 (1996).
41. Drlica, K., Malik, M., Kerns, R.J. & Zhao, X. Quinolone-mediated bacterial death. *Antimicrobial Agents and Chemotherapy* **52**, 385-392 (2008).
42. Campbell, E.A. *et al.* Structural mechanism for rifampicin inhibition of bacterial RNA polymerase. *Cell* **104**, 901-912 (2001).
43. Hartmann, G., Honikel, K.O., Knüsel, F. & Nüesch, J. The specific inhibition of the DNA-directed RNA synthesis by rifamycin. *BBA Section Nucleic Acids And Protein Synthesis* **145**, 843-844 (1967).
44. Losick, R. & Chamberlin, M. *RNA Polymerase* (1976).
45. McClure, W.R. & Cech, C.L. On the mechanism of rifampicin inhibition of RNA synthesis. *Journal of Biological Chemistry* **253**, 8949-8956 (1978).
46. Höltje, J.V. Growth of the stress-bearing and shape-maintaining murein sacculus of Escherichia coli. *Microbiology and Molecular Biology Reviews* **62**, 181-203 (1998).
47. Wise Jr, E.M. & Park, J.T. Penicillin: its basic site of action as an inhibitor of a peptide cross-linking reaction in cell wall mucopeptide synthesis. *Proceedings of the National Academy of Sciences of the United States of America* **54**, 75-81 (1965).
48. Tomasz, A., Albino, A. & Zanati, E. Multiple antibiotic resistance in a Bacterium with suppressed autolytic System. *Nature* **227**, 138-140 (1970).
49. Patel, U. *et al.* Oxazolidinones Mechanism of Action: Inhibition of the First Peptide Bond Formation. *Journal of Biological Chemistry* **276**, 37199-37205 (2001).
50. Menninger, J.R. & Otto, D.P. Erythromycin, carbomycin, and spiramycin inhibit protein synthesis by stimulating the dissocation of peptidyl-tRNA from ribosomes. *Antimicrobial Agents and Chemotherapy* **21**, 811-818 (1982).
51. Davis, B.D. Mechanism of bactericidal action of aminoglycosides. *Microbiological Reviews* **51**, 341-350 (1987).

52. Davies, J., Gorini, L. & Davis, B.D. Misreading of RNA codewords induced by aminoglycoside antibiotics. *Molecular pharmacology* **1**, 93-106 (1965).
53. Barlow, M. & Hall, B.G. Phylogenetic analysis shows that the OXA β-lactamase genes have been on plasmids for millions of years. *Journal of Molecular Evolution* **55**, 314-321 (2002).
54. Martínez, J.L. Antibiotics and antibiotic resistance genes in natural environments. *Science* **321**, 365-367 (2008).
55. Hawkey, P.M. The origins and molecular basis of antibiotic resistance. *BMJ: British Medical Journal* **317**, 657 (1998).
56. Chopra, I. & Roberts, M. Tetracycline antibiotics: mode of action, applications, molecular biology, and epidemiology of bacterial resistance. *Microbiology and molecular biology reviews* **65**, 232-260 (2001).
57. Garcia-Bustos, J. & Tomasz, A. A biological price of antibiotic resistance: major changes in the peptidoglycan structure of penicillin-resistant pneumococci. *Proceedings of the National Academy of Sciences* **87**, 5415-5419 (1990).
58. Michel, M. & Gutmann, L. Methicillin-resistant Staphylococus aureus and vancomycin-resistant enterococci: therapeutic realities and possibilities. *The Lancet* **349**, 1901-1906 (1997).
59. Smillie, C., Garcillán-Barcia, M.P., Francia, M.V., Rocha, E.P.C. & De La Cruz, F. Mobility of plasmids. *Microbiology and Molecular Biology Reviews* **74**, 434-452 (2010).
60. Wozniak, R.A.F. & Waldor, M.K. Integrative and conjugative elements: Mosaic mobile genetic elements enabling dynamic lateral gene flow. *Nature Reviews Microbiology* **8**, 552-563 (2010).
61. Alexander, H.E., Hahn, E. & Leidy, G. On the specificity of the desoxyribonucleic acid which induces streptomycin resistance in Hemophilus. *The Journal of experimental medicine* **104**, 305-320 (1956).
62. Alexander, H.E. & Leidy, G. Induction of streptomycin resistance in sensitive Hemophilus influenzae by extracts containing desoxyribonucleic acid from resistant Hemophilus influenzae. *The Journal of experimental medicine* **97**, 17-31 (1953).
63. Modi, S.R., Lee, H.H., Spina, C.S. & Collins, J.J. Antibiotic treatment expands the resistance reservoir and ecological network of the phage metagenome. *Nature* **499**, 219-222 (2013).
64. Brown-Jaque, M., Calero-Cáceres, W. & Muniesa, M. Transfer of antibiotic-resistance genes via phage-related mobile elements. *Plasmid* **79**, 1-7 (2015).
65. Bhattacharjya, S. & Ramamoorthy, A. Multifunctional host defense peptides: Functional and mechanistic insights from NMR structures of potent antimicrobial peptides. *FEBS Journal* **276**, 6465-6473 (2009).
66. Haney, E.F., Nazmi, K., Lau, F., Bolscher, J.G.M. & Vogel, H.J. Novel lactoferrampin antimicrobial peptides derived from human lactoferrin. *Biochimie* **91**, 141-154 (2009).
67. Holt, A. & Killian, J.A. Orientation and dynamics of transmembrane peptides: The power of simple models. *European Biophysics Journal* **39**, 609-621 (2010).

68. Pino-Angeles, A., Leveritt III, J.M. & Lazaridis, T. Pore structure and synergy in antimicrobial peptides of the magainin family. *PLoS computational biology* **12**, e1004570 (2016).
69. Lee, C.-C., Sun, Y., Qian, S. & Huang, H.W. Transmembrane pores formed by human antimicrobial peptide LL-37. *Biophysical journal* **100**, 1688-1696 (2011).
70. Nicolas, P. Multifunctional host defense peptides: Intracellular-targeting antimicrobial peptides. *FEBS Journal* **276**, 6483-6496 (2009).
71. Lan, Y. *et al.* Structural contributions to the intracellular targeting strategies of antimicrobial peptides. *Biochimica et Biophysica Acta - Biomembranes* **1798**, 1934-1943 (2010).
72. Tang, M. & Hong, M. Structure and mechanism of β-hairpin antimicrobial peptides in lipid bilayers from solid-state NMR spectroscopy. *Molecular BioSystems* **5**, 317-322 (2009).
73. Gifford, J.L., Hunter, H.N. & Vogel, H.J. Lactoferricin: A lactoferrin-derived peptide with antimicrobial, antiviral, antitumor and immunological properties. *Cellular and Molecular Life Sciences* **62**, 2588-2598 (2005).
74. Fehlbaum, P. *et al.* Structure-activity analysis of thanatin, a 21-residue inducible insect defense peptide with sequence homology to frog skin antimicrobial peptides. *Proceedings of the National Academy of Sciences* **93**, 1221-1225 (1996).
75. Su, L.Y., Willner, D.L. & Segall, A.M. An antimicrobial peptide that targets DNA repair intermediates in vitro inhibits Salmonella growth within murine macrophages. *Antimicrobial Agents and Chemotherapy* **54**, 1888-1899 (2010).
76. Mattila, J.P., Sabatini, K. & Kinnunen, P.K.J. Oxidized phospholipids as potential molecular targets for antimicrobial peptides. *Biochimica et Biophysica Acta - Biomembranes* **1778**, 2041-2050 (2008).
77. Rokitskaya, T.I., Kolodkin, N.I., Kotova, E.A. & Antonenko, Y.N. Indolicidin action on membrane permeability: Carrier mechanism versus pore formation. *Biochimica et Biophysica Acta - Biomembranes* **1808**, 91-97 (2011).
78. Marchand, C. *et al.* Covalent binding of the natural antimicrobial peptide indolicidin to DNA abasic sites. *Nucleic Acids Research* **34**, 5157-5165 (2006).
79. Vila, J.A., Baldoni, H.A., Ripoll, D.R., Ghosh, A. & Scheraga, H.A. Polyproline II helix conformation in a proline-rich environment: a theoretical study. *Biophysical journal* **86**, 731-742 (2004).
80. Epand, R.M. & Epand, R.F. Lipid domains in bacterial membranes and the action of antimicrobial agents. *Biochimica et Biophysica Acta (BBA)-Biomembranes* **1788**, 289-294 (2009).
81. Ebenhan, T., Gheysens, O., Kruger, H.G., Zeevaart, J.R. & Sathekge, M.M. Antimicrobial peptides: their role as infection-selective tracers for molecular imaging. *BioMed research international* **2014** (2014).
82. Jäkel, C.E., Meschenmoser, K., Kim, Y., Weiher, H. & Schmidt-Wolf, I.G. Efficacy of a proapoptotic peptide towards cancer cells. *in vivo* **26**, 419-426 (2012).

83. Martinez de Tejada, G. *et al.* Bacterial cell wall compounds as promising targets of antimicrobial agents I. Antimicrobial peptides and lipopolyamines. *Current drug targets* **13**, 1121-1130 (2012).
84. Cross, A.S. & Opal, S.M. Endotoxin's role in Gram-negative bacterial infection. *Current Opinion in Infectious Diseases* **8**, 156-163 (1995).
85. Brown, L., Wolf, J.M., Prados-Rosales, R. & Casadevall, A. Through the wall: extracellular vesicles in Gram-positive bacteria, mycobacteria and fungi. *Nature Reviews Microbiology* **13**, 620-630 (2015).
86. Salditt, T., Li, C. & Spaar, A. Structure of antimicrobial peptides and lipid membranes probed by interface-sensitive X-ray scattering. *Biochimica et Biophysica Acta (BBA)-Biomembranes* **1758**, 1483-1498 (2006).
87. Cézard, C., Silva-Pires, V., Mullié, C. & Sonnet, P. Antibacterial peptides: a review. *Science against Microbial Pathogens: Communicating Current Research and Technological Advances: Formatex Research Center* (2011).
88. Podda, E. *et al.* Dual mode of action of Bac7, a proline-rich antibacterial peptide. *Biochimica et Biophysica Acta (BBA)-General Subjects* **1760**, 1732-1740 (2006).
89. Huang, H.W. Action of antimicrobial peptides: two-state model. *Biochemistry* **39**, 8347-8352 (2000).
90. Scocchi, M., Tossi, A. & Gennaro, R. Proline-rich antimicrobial peptides: converging to a non-lytic mechanism of action. *Cellular and Molecular Life Sciences* **68**, 2317-2330 (2011).
91. Roy, R.N., Lomakin, I.B., Gagnon, M.G. & Steitz, T.A. The mechanism of inhibition of protein synthesis by the proline-rich peptide oncocin. *Nature structural & molecular biology* **22**, 466-469 (2015).
92. Fabbretti, A. *et al.* Inhibition of translation initiation complex formation by GE81112 unravels a 16S rRNA structural switch involved in P-site decoding. *Proceedings of the National Academy of Sciences* **113**, E2286-E2295 (2016).
93. Park, C.B., Kim, H.S. & Kim, S.C. Mechanism of action of the antimicrobial peptide buforin II: buforin II kills microorganisms by penetrating the cell membrane and inhibiting cellular functions. *Biochemical and biophysical research communications* **244**, 253-257 (1998).
94. Rosenberger, C.M., Gallo, R.L. & Finlay, B.B. Interplay between antibacterial effectors: a macrophage antimicrobial peptide impairs intracellular Salmonella replication. *Proceedings of the National Academy of Sciences of the United States of America* **101**, 2422-2427 (2004).
95. Scocchi, M., Mardirossian, M., Runti, G. & Benincasa, M. Non-membrane permeabilizing modes of action of antimicrobial peptides on bacteria. *Current topics in medicinal chemistry* **16**, 76-88 (2016).
96. Otvos, L. *et al.* Interaction between heat shock proteins and antimicrobial peptides. *Biochemistry* **39**, 14150-14159 (2000).
97. Kragol, G. *et al.* The antibacterial peptide pyrrhocoricin inhibits the ATPase actions of DnaK and prevents chaperone-assisted protein folding. *Biochemistry* **40**, 3016-3026 (2001).

98. Kragol, G. *et al.* Identification of crucial residues for the antibacterial activity of the proline-rich peptide, pyrrhocoricin. *The FEBS Journal* **269**, 4226-4237 (2002).
99. Wenzel, M. *et al.* Small cationic antimicrobial peptides delocalize peripheral membrane proteins. *Proceedings of the National Academy of Sciences* **111**, E1409-E1418 (2014).
100. Jung, S. *et al.* Macin family of antimicrobial proteins combines antimicrobial and nerve repair activities. *Journal of Biological Chemistry* **287**, 14246-14258 (2012).
101. Spitzer, P. *et al.* Amyloidogenic amyloid-β-peptide variants induce microbial agglutination and exert antimicrobial activity. *Scientific reports* **6**, 32228 (2016).
102. Gorr, S.-U., Sotsky, J.B., Shelar, A.P. & Demuth, D.R. Design of bacteria-agglutinating peptides derived from parotid secretory protein, a member of the bactericidal/permeability increasing-like protein family. *Peptides* **29**, 2118-2127 (2008).
103. Pulido, D. *et al.* Antimicrobial action and cell agglutination by the eosinophil cationic protein are modulated by the cell wall lipopolysaccharide structure. *Antimicrobial agents and chemotherapy* **56**, 2378-2385 (2012).
104. Harris, F., Dennison, S.R. & Phoenix, D.A. Anionic antimicrobial peptides from eukaryotic organisms. *Current Protein and Peptide Science* **10**, 585-606 (2009).
105. Burian, M. & Schittek, B. The secrets of dermcidin action. *International Journal of Medical Microbiology* **305**, 283-286 (2015).
106. Cassone, M. & Otvos Jr, L. Synergy among antibacterial peptides and between peptides and small-molecule antibiotics. *Expert review of anti-infective therapy* **8**, 703-716 (2010).
107. Laskowski, R.A., Rullmann, J.A.C., MacArthur, M.W., Kaptein, R. & Thornton, J.M. AQUA and PROCHECK-NMR: programs for checking the quality of protein structures solved by NMR. *Journal of biomolecular NMR* **8**, 477-486 (1996).
108. Kirschner, K.N., Lins, R.D., Maass, A. & Soares, T.A. A glycam-based force field for simulations of lipopolysaccharide membranes: parametrization and validation. *Journal of chemical theory and computation* **8**, 4719-4731 (2012).
109. Bhattacharjya, S. NMR structures and interactions of antimicrobial peptides with lipopolysaccharide: connecting structures to functions. *Current topics in medicinal chemistry* **16**, 4-15 (2016).
110. Robert, E.m. *et al.* Mimicking and Understanding the Agglutination Effect of the Antimicrobial Peptide Thanatin Using Model Phospholipid Vesicles. *Biochemistry* **54**, 3932-3941 (2015).
111. Mandard, N. *et al.* Solution structure of thanatin, a potent bactericidal and fungicidal insect peptide, determined from proton two-dimensional nuclear magnetic resonance data. *The FEBS Journal* **256**, 404-410 (1998).
112. Bhunia, A. *et al.* NMR structure of pardaxin, a pore-forming antimicrobial peptide, in lipopolysaccharide micelles mechanism of outer membrane permeabilization. *Journal of biological chemistry* **285**, 3883-3895 (2010).

113. Bhunia, A., Bhattacharjya, S. & Chatterjee, S. Applications of saturation transfer difference NMR in biological systems. *Drug discovery today* **17**, 505-513 (2012).
114. Meyer, B. & Peters, T. NMR spectroscopy techniques for screening and identifying ligand binding to protein receptors. *Angewandte Chemie International Edition* **42**, 864-890 (2003).
115. Bhunia, A., Mohanram, H. & Bhattacharjya, S. Lipopolysaccharide bound structures of the active fragments of fowlicidin-1, a cathelicidin family of antimicrobial and antiendotoxic peptide from chicken, determined by transferred nuclear overhauser effect spectroscopy. *Peptide Science* **92**, 9-22 (2009).
116. Saravanan, R. *et al.* NMR structure of temporin-1 ta in lipopolysaccharide micelles: mechanistic insight into inactivation by outer membrane. *PloS one* **8**, e72718 (2013).
117. Bhunia, A., Ramamoorthy, A. & Bhattacharjya, S. Helical Hairpin Structure of a Potent Antimicrobial Peptide MSI-594 in Lipopolysaccharide Micelles by NMR Spectroscopy. *Chemistry-A European Journal* **15**, 2036-2040 (2009).
118. Domadia, P.N., Bhunia, A., Ramamoorthy, A. & Bhattacharjya, S. Structure, interactions, and antibacterial activities of MSI-594 derived mutant peptide MSI-594F5A in lipopolysaccharide micelles: role of the helical hairpin conformation in outer-membrane permeabilization. *Journal of the American Chemical Society* **132**, 18417-18428 (2010).
119. Bhunia, A., Saravanan, R., Mohanram, H., Mangoni, M.L. & Bhattacharjya, S. NMR Structures and Interactions of Temporin-1Tl and Temporin-1Tb with Lipopolysaccharide Micelles MECHANISTIC INSIGHTS INTO OUTER MEMBRANE PERMEABILIZATION AND SYNERGISTIC ACTIVITY. *Journal of Biological Chemistry* **286**, 24394-24406 (2011).
120. Yu, L., Tan, M., Ho, B., Ding, J.L. & Wohland, T. Determination of critical micelle concentrations and aggregation numbers by fluorescence correlation spectroscopy: aggregation of a lipopolysaccharide. *Analytica chimica acta* **556**, 216-225 (2006).
121. Snyder, D.S. & McIntosh, T.J. The lipopolysaccharide barrier: correlation of antibiotic susceptibility with antibiotic permeability and fluorescent probe binding kinetics. *Biochemistry* **39**, 11777-11787 (2000).
122. Beutler, B. & Rietschel, E.T. Innate immune sensing and its roots: the story of endotoxin. *Nature Reviews Immunology* **3**, 169-176 (2003).
123. Schultz, M.J. *et al.* Current challenges in the management of sepsis in ICUs in resource-poor settings and suggestions for the future. *Intensive Care Medicine*, 1-13 (2017).
124. Faraj, T.A., McLaughlin, C.L. & Erridge, C. Host defenses against metabolic endotoxaemia and their impact on lipopolysaccharide detection. *International Reviews of Immunology*, 1-20 (2017).
125. Ösapay, K. *et al.* Formation and characterization of a single Trp-Trp cross-link in indolicidin that confers protease stability without altering antimicrobial activity. *Journal of Biological Chemistry* **275**, 12017-12022 (2000).

126. Rozek, A., Powers, J.-P.S., Friedrich, C.L. & Hancock, R.E. Structure-based design of an indolicidin peptide analogue with increased protease stability. *Biochemistry* **42**, 14130-14138 (2003).

127. Kim, J.-Y., Park, S.-C., Yoon, M.-Y., Hahm, K.-S. & Park, Y. C-terminal amidation of PMAP-23: translocation to the inner membrane of Gram-negative bacteria. *Amino acids* **40**, 183-195 (2011).

128. Torino, D. *et al.* Synthesis and evaluation of new endomorphin-2 analogues containing (Z)-α, β-didehydrophenylalanine (ΔZPhe) Residues. *Journal of medicinal chemistry* **53**, 4550-4554 (2010).

129. Göblyös, A. *et al.* Development of a Nose Cream Containing the Synthetic Antimicrobial Peptide P60. 4Ac for Eradication of Methicillin-Resistant Staphylococcus aureus Carriage. *Journal of pharmaceutical sciences* **102**, 3539-3544 (2013).

130. Imamura, T. *et al.* NMR based structure–activity relationship analysis of an antimicrobial peptide, thanatin, engineered by site-specific chemical modification: Activity improvement and spectrum alteration. *Biochemical and biophysical research communications* **369**, 609-615 (2008).

131. Wu, G. *et al.* Selective toxicity of antimicrobial peptide S-thanatin on bacteria. *Peptides* **31**, 1669-1673 (2010).

132. Hou, Z. *et al.* R-thanatin inhibits growth and biofilm formation of methicillin-resistant Staphylococcus epidermidis in vivo and in vitro. *Antimicrobial agents and chemotherapy* **57**, 5045-5052 (2013).

133. Fuller, R.S., Brake, A.J. & Thorner, J. Intracellular targeting and structural conservation of a prohormone-processing endoprotease. *Science* **246**, 482-487 (1989).

134. Roebroek, A. *et al.* Characterization of human c-fes/fps reveals a new transcription unit (fur) in the immediately upstream region of the proto-oncogene. *Molecular biology reports* **11**, 117-125 (1986).

135. Thomas, G. Furin at the cutting edge: from protein traffic to embryogenesis and disease. *Nature reviews Molecular cell biology* **3**, 753-766 (2002).

136. Anderson, E.D., VanSlyke, J.K., Thulin, C.D., Jean, F. & Thomas, G. Activation of the furin endoprotease is a multiple-step process: requirements for acidification and internal propeptide cleavage. *The EMBO journal* **16**, 1508-1518 (1997).

137. Bhattacharjya, S., Xu, P., Wang, P., Osborne, M.J. & Ni, F. Conformational analyses of a partially-folded bioactive prodomain of human furin. *Biopolymers* **86**, 329-344 (2007).

138. Bhattacharjya, S. *et al.* pH-induced conformational transitions of a molten–globule–like state of the inhibitory prodomain of furin: Implications for zymogen activation. *Protein Science* **10**, 934-942 (2001).

139. De Cicco, R.L., Bassi, D.E., Zucker, S., Seidah, N.G. & Klein-Szanto, A.J. Human carcinoma cell growth and invasiveness is impaired by the propeptide of the ubiquitous proprotein convertase furin. *Cancer research* **65**, 4162-4171 (2005).

140. Jenssen, H. & Hancock, R.E. Antimicrobial properties of lactoferrin. *Biochimie* **91**, 19-29 (2009).

141. Bellamy, W. *et al.* Identification of the bactericidal domain of lactoferrin. *Biochimica et Biophysica Acta (BBA)-Protein Structure and Molecular Enzymology* **1121**, 130-136 (1992).
142. Jollès, P. & Jollès, J. What's new in lysozyme research? *Molecular and cellular biochemistry* **63**, 165-189 (1984).
143. Ibrahim, H.R., Imazato, K. & Ono, H. Human lysozyme possesses novel antimicrobial peptides within its N-terminal domain that target bacterial respiration. *Journal of agricultural and food chemistry* **59**, 10336-10345 (2011).
144. Mohanram, H. & Bhattacharjya, S. Resurrecting inactive antimicrobial peptides from the lipopolysaccharide trap. *Antimicrobial agents and chemotherapy* **58**, 1987-1996 (2014).
145. Mohanram, H. & Bhattacharjya, S. Salt-resistant short antimicrobial peptides. *Peptide Science* **106**, 345-356 (2016).